

ACYL-HOMOSERINE LACTONE BASED MODULATORS FOR RHLI, A QUORUM  
SENSING SIGNAL SYNTHASE IN *PSEUDOMONAS AERUGINOSA*

by

Daniel D. Shin

A thesis

submitted in partial fulfillment

of the requirements for the degree of

Master of Science in Chemistry

Boise State University

December 2017

© 2017

Daniel D. Shin

ALL RIGHTS RESERVED

BOISE STATE UNIVERSITY GRADUATE COLLEGE

**DEFENSE COMMITTEE AND FINAL READING APPROVALS**

of the thesis submitted by

Daniel D. Shin

Thesis Title: Acyl-Homoserine Lactone Based Modulators for RhII, a Quorum Sensing Signal Synthase in *Pseudomonas aeruginosa*

Date of Final Oral Examination: 13 October 2017

The following individuals read and discussed the thesis submitted by student Daniel D. Shin, and they evaluated his presentation and response to questions during the final oral examination. They found that the student passed the final oral examination.

Rajesh Nagarajan, Ph.D. Chair, Supervisory Committee

Henry A. Charlier, Ph.D. Member, Supervisory Committee

Michael P. Callahan, Ph.D. Member, Supervisory Committee

The final reading approval of the thesis was granted by Rajesh Nagarajan, Ph.D., Chair of the Supervisory Committee. The thesis was approved by the Graduate College.

## ACKNOWLEDGEMENTS

I would like to show my gratitude to Boise State University and the Department of Chemistry and Biochemistry for the opportunity of pursuing research. I thank Mila Lam, Levi Mitchell, John Taffin, and Neil Rexrode for their help with enzyme purification and small molecule synthesis. I have deep appreciation for Dr. Eric Brown, who was crucial in synthesizing small-molecules, and Dr. Shin Pu and Matthew Turner, who were pivotal in identifying the said compounds. The generous contribution of small molecule compounds from Dr. Helen Blackwell of University of Wisconsin made this work possible. My graduate committee members, Dr. Henry Charlier and Dr. Michael Callahan, provided the needed criticism to look at my work again from third and fourth angles so that the objective of this work became better focused. Most importantly, I would like to thank Dr. Rajesh Nagarajan for all the time, patience, concern, guidance, and dedication he has showed to me, not just as a student and a scientist, but as a human being.

## ABSTRACT

Gram-negative bacteria use *N*-acyl-homoserine lactone (AHL) autoinducer based signal system, known as quorum sensing (QS), to modulate the gene expression for such traits as biofilm formation, toxin production, and antibiotic resistance. Therefore, there is great potential in pursuing quorum sensing inhibition (QSI) as a means of achieving antivirulence. *Pseudomonas aeruginosa*, an opportunistic pathogen commonly found in healthcare-related infections, use two LuxI/R type systems to regulate AHL-based quorum sensing: LasI/R and RhII/R. LasI (initiator protein/signal synthase) and LasR (receptor) use 3-oxododecanoyl-L-homoserine lactone signal molecule while RhII and RhIR use butanoyl-L-homoserine lactone autoinducer. Thus far, most of the studies have focused on inhibiting the Las system, in particular by using AHL signal analogs to interfere with signal-receptor binding. Recently, RhII/R system has gained attention as potentially having greater effect in *P. aeruginosa* virulence. In this study, we have tested the effect of AHL analogs on RhII, as product inhibitors with the goal of targeting both RhII and RhIR for increased potency. Screening of compounds have revealed three variations to have the greatest effect on RhII inhibition: longer/bulkier acyl- chain, D-stereocenter in the headgroup, and a less polar thiolactone head-group. Surprisingly, the addition of a carbonyl at the C3 position was found to activate the enzyme. Moreover, we measured kinetic constants of RhII with various acyl-substrates and performed inhibition assays with inert acyl-substrate analogs to determine how RhII activity changes to variations in the acyl-chain length. We found that the catalytic efficiency of acyl-

substrate and inhibition potency of the corresponding inert acyl-substrate analogs surges with increase in the length of the acyl-chain. These patterns suggest that long acyl-chains most likely bind to an alternate binding site with marked increase in both  $k_{on}$  and  $k_{off}$  rate constants. Our findings with AHL derivatives provide a basis for rational design of quorum sensing inhibitors to better combat *P. aeruginosa* bacterial infections.

## TABLE OF CONTENTS

ACKNOWLEDGEMENTS .....	iv
ABSTRACT .....	v
LIST OF TABLES .....	xi
LIST OF FIGURES .....	xii
LIST OF ABBREVIATIONS .....	xviii
CHAPTER ONE: INTRODUCTION.....	1
The Antibiotic Crisis.....	1
Quorum Sensing.....	3
Proposed AHL synthase mechanism .....	8
RhII, QS signal synthase in <i>Pseudomonas aeruginosa</i> .....	9
AHL synthase Kinetics .....	11
DCPIP Assay .....	11
Enzyme Kinetics .....	12
Thesis objective .....	25
CHAPTER TWO: MATERIALS AND METHODS .....	31
Materials and Equipment .....	31
Methods.....	33
HPLC Methods .....	33
RhII Purification.....	34

Apo-ACP Purification.....	36
Alkyl-CoA Synthesis .....	37
Alkyl-/Acyl-ACP synthesis .....	38
Purification of D-homocysteine thiolactone .....	40
Synthesis of <i>N</i> -acyl-D-homocysteine thiolactones .....	41
Synthesis of <i>N</i> -(3-Oxoacyl)-D-homocysteine thiolactones .....	44
Mass Spectrometry.....	46
Kinetics Assays.....	47
<b>CHAPTER THREE: RESULTS AND DISCUSSION.....</b>	<b>52</b>
Enzyme Purification.....	52
RhII purification.....	52
Apo-ACP Purification.....	53
Alkyl-CoA Synthesis .....	53
Acyl/Alkyl-ACP Synthesis .....	54
Small Molecule Synthesis.....	56
D-Homocysteine Thiolactone (Figure 19, Chapter 2) .....	56
<i>N</i> -Acyl-D-Homocysteine Thiolactone (Figure 20, Chapter 2) .....	57
<i>N</i> -(3-Oxoacyl)-D-Homocysteine Thiolactone (Figure 21, Chapter 2) .....	58
Spectral Data.....	58
AHL Analog Kinetics .....	58
Background rate .....	58
The Effects of AHL analogs on RhII enzymatic rate.....	59
Acyl-L-homoserine lactone (L-HSL) .....	60



Acyl-D-homoserine lactone (D-HSL).....	61
3-oxoacyl-D-HSL .....	62
Acyl- and 3-oxoacyl-L-homocysteine thiolactone.....	64
Acyl- and 3-oxoacyl-D-thiolactone .....	65
Acyl-Cyclopentanamide .....	66
Non-lactone derivatives .....	67
Headgroup vs Tail chain effects .....	68
Determining the mode of inhibition.....	69
AHL analog Trends.....	71
Chain length effect.....	71
Acyl-chain vs 3-oxoacyl-chain effects.....	73
Headgroup chirality effect .....	76
Headgroup hydrophilicity effect.....	77
Determining Kinetic Constants with various Acyl-ACPs .....	78
Alkyl-ACP Inhibition.....	83
Alkyl-CoA Inhibition.....	88
Conclusion .....	89
REFERENCES .....	94
APPENDIX A.....	99
Mass Spectra .....	100
APPENDIX B .....	109
NMR spectra .....	110
APPENDIX C .....	130

UV-Vis Spectra.....	131
---------------------	-----

## LIST OF TABLES

Table 1.	Types of QS signal molecules.....	6
Table 2.	Structures of 1 <sup>st</sup> generation AHL-based small molecules tested for RhII inhibition. ....	26
Table 3.	Variations in the acyl-chains for 2 <sup>nd</sup> generation of AHL-based small molecules tested for RhII inhibition.....	27
Table 4.	2 <sup>nd</sup> generation of AHL-based small molecules tested for RhII inhibition.	28
Table 5.	Nonlactone derivatives tested for RhII inhibition.....	29
Table 6.	Acyl-ACP, alkyl-ACP, and alkyl-CoA derivatives .....	29
Table 7.	Alkyl-CoA separation method .....	34
Table 8.	ACP separation method .....	34
Table 9.	C6-ACP separation method .....	34
Table 10.	Determining best fit model for the mode of inhibition using AIC .....	71
Table 11.	Effect of AHL analogs on RhII initial enzyme rate .....	71
Table 12.	Trends with variations in the acyl-chain length/size.....	73
Table 13.	Patterns in varying effects of acyl- and 3-oxoacyl-chain derivatives. ....	75
Table 14.	Effects of varying the headgroup chirality from L to D stereoisomer. ....	76
Table 15.	The effect of headgroup hydrophobicity on RhII inhibition.....	78
Table 16.	RhII initial enzyme rate with various acyl-ACP substrates .....	81
Table 17.	Effect of IACP on RhII initial enzyme rate. ....	84
Table 18.	Determining best fit model for the mode of inhibition using AIC .....	87
Table 19.	Effect of ICoA on RhII initial enzyme rate.....	89

## LIST OF FIGURES

Figure 1.	Timeline of the effective-lifetime of antibiotics .....	2
Figure 2.	Decrease in new antibiotic development .....	3
Figure 3.	The typical quorum sensing system found in Gram-negative bacteria.....	5
Figure 4.	Species-specific signal molecules.....	6
Figure 5.	The proposed mechanism of AHL-synthases .....	8
Figure 6.	QS system regulation in <i>P. aeruginosa</i> .....	11
Figure 7.	DCPIP assay mechanism .....	12
Figure 8.	The Substrate-Velocity Curve.....	13
Figure 9.	Typical Lineweaver-Burk plot.....	14
Figure 10.	Kinetic mechanism for bisubstrate enzyme .....	15
Figure 11.	Double reciprocal plot of sequential vs ping-pong reaction mechanism..	17
Figure 12.	Cleland diagram of RhlI catalyzed ordered bi-ter reaction.....	17
Figure 13.	Modes of inhibition.....	19
Figure 14.	Representative IC <sub>50</sub> curve .....	23
Figure 15.	Representative EC <sub>50</sub> curve .....	25
Figure 16.	Structures of Acyl-ACP and CoA.....	30
Figure 17.	Synthesis of alkyl-CoA.....	38
Figure 18.	<i>Sfp</i> catalyzed acyl-pantetheine transfer reaction.....	39
Figure 19.	Purification of pure D-homocysteine thiolactone .....	41
Figure 20.	Acylation of D-thiolactone headgroup.....	42

Figure 21.	Synthesis and purification of 3-oxoacyl-D-thiolactones .....	45
Figure 22.	SDS-PAGE gel of RhII protein.....	52
Figure 23.	SDS-PAGE gel of apo-ACP .....	53
Figure 24.	Elution time of various alkyl-CoAs .....	54
Figure 25.	Elution time of various acyl-/alkyl-ACPs.....	56
Figure 26.	DCPIP background rate progress curve.....	59
Figure 27.	Initial set of AHL-analogs and their effects.....	60
Figure 28.	Effects of acyl-L-homoserine lactones .....	61
Figure 29.	Effects of acyl-D-homoserine lactones.....	62
Figure 30.	Effects of 3-oxoacyl-D-homoserine lactones.....	63
Figure 31.	Effects of L and D sulfonamides .....	63
Figure 32.	Effects of acyl- and 3-oxoacyl-L-homocysteine thiolactones .....	64
Figure 33.	Effects of acyl- and 3-oxoacyl-D-homocysteine thiolactones .....	66
Figure 34.	Effects of acyl-cyclopentanamide on RhII activity.....	67
Figure 35.	Effects of non-lactone AHL analogs on RhII activity .....	68
Figure 36.	Effects of headgroup and tail moieties in isolation on RhII initial rate ....	69
Figure 37.	Cleland diagram of RhII catalyzed reaction.....	70
Figure 38.	Double Reciprocal Plot of RhII activity with varying C4-ACP concentrations and various fixed AHL analog concentrations .....	71
Figure 39.	Substrate-velocity curves of RhII with native and nonspecific acyl-ACP substrates.....	80
Figure 40.	Trends in $k_{cat}$ , $K_m$ , and $k_{cat}/K_m$ values of RhII with various acyl substrates .....	81
Figure 41.	Alignment of amino acid sequence of <i>P. aeruginosa</i> ACP1, ACPP, ACP3, and <i>E. coli</i> ACP.....	83

Figure 42.	Various AHL products of LasI .....	83
Figure 43.	Designing inactive acyl-ACP analog .....	84
Figure 44.	IC <sub>50</sub> test of various IACPs.....	85
Figure 45.	Double Reciprocal Plot of RhII activity with varying C4 -CP concentrations and various fixed IACP concentrations .....	87
Figure 46.	Time-dependency of IACP inhibition.....	88
Figure 47.	IC <sub>50</sub> test of various ICoAs.....	89
Figure 48.	Moieties of interest for improved AHL-based RhII modulators.....	90
Figure 49.	Specificity vs. Potency in targeting RhII. ....	91
Figure A1.	Mass Spectrum of Compound 56.....	100
Figure A2.	Mass Spectrum of Compound 57.....	100
Figure A3.	Mass spectrum of Compound 58 .....	101
Figure A4.	Mass Spectrum of Compound 59.....	101
Figure A5.	Mass Spectrum of Compound 60.....	102
Figure A6.	Mass Spectrum of Compound 61.....	102
Figure A7.	Mass Spectrum of Compound 62.....	103
Figure A8.	Mass Spectrum of Compound 63.....	103
Figure A9.	Mass Spectrum of Compound 64.....	104
Figure A10.	Mass Spectrum of Compound 88.....	104
Figure A11.	Mass Spectrum of Compound 89.....	105
Figure A12.	Mass Spectrum of Compound 90.....	105
Figure A13.	Mass Spectrum of Compound 91.....	106
Figure A14.	Mass Spectrum of Compound 92.....	106
Figure A15.	Mass Spectrum of Compound 93.....	107

Figure A16.	Mass Spectrum of Compound 94.....	107
Figure A17.	Mass Spectrum of Compound 95.....	108
Figure B1.	D-homocysteine thiolactone <sup>1</sup> H NMR.....	110
Figure B2.	Compound 56 <sup>1</sup> H NMR .....	110
Figure B3.	Compound 56 COSY NMR.....	111
Figure B4.	Compound 56 HSQC NMR.....	111
Figure B5.	Compound 56 HMBC NMR.....	112
Figure B6.	Compound 56 <sup>13</sup> C NMR .....	112
Figure B7.	Compound 57 <sup>1</sup> H NMR .....	113
Figure B8.	Compound 57 COZY NMR.....	113
Figure B9.	Compound 57 <sup>13</sup> C NMR .....	114
Figure B10.	Compound 58 <sup>1</sup> H NMR .....	114
Figure B11.	Compound 58 COSY NMR.....	115
Figure B12.	Compound 58 HSQC NMR.....	115
Figure B13.	Compound 58 HMBC NMR.....	116
Figure B14.	Compound 58 <sup>13</sup> C NMR .....	116
Figure B15.	Compound 59 <sup>1</sup> H NMR .....	117
Figure B16.	Compound 59 COSY NMR.....	117
Figure B17.	Compound 59 HSQC NMR.....	118
Figure B18.	Compound 59 HMBC NMR.....	118
Figure B19.	Compound 59 <sup>13</sup> C NMR .....	119
Figure B20.	Compound 60 <sup>1</sup> H NMR .....	119
Figure B21.	Compound 60 COSY NMR.....	120

Figure B22.	Compound 60 HSQC NMR .....	120
Figure B23.	Compound 60 HMBC NMR.....	121
Figure B24.	Compound 60 <sup>13</sup> C NMR .....	121
Figure B25.	Compound 61 <sup>1</sup> H NMR .....	122
Figure B26.	Compound 61 COSY NMR.....	122
Figure B27.	Compound 61 HSQC NMR.....	123
Figure B28.	Compound 61 HMBC NMR.....	123
Figure B29.	Compound 61 <sup>13</sup> C NMR .....	123
Figure B30.	Compound 62 <sup>1</sup> H NMR .....	124
Figure B31.	Compound 62 COSY NMR.....	124
Figure B32.	Compound 62 HSQC NMR.....	125
Figure B33.	Compound 62 HMBC NMR.....	125
Figure B34.	Compound 62 <sup>13</sup> C NMR .....	125
Figure B35.	Compound 63 <sup>1</sup> H NMR .....	126
Figure B36.	Compound 63 COSY NMR.....	126
Figure B37.	Compound 63 HSQC NMR.....	127
Figure B38.	Compound 63 HMBC NMR.....	127
Figure B39.	Compound 64 <sup>13</sup> C NMR .....	127
Figure B40.	Compound 64 <sup>1</sup> H NMR .....	128
Figure B41.	Compound 64 COSY NMR .....	128
Figure B42.	Compound 64 HSQC NMR.....	129
Figure B43.	Compound 64 HMBC NMR.....	129
Figure B44.	Compound 64 <sup>13</sup> C NMR .....	129



Figure C1.	IC <sub>50</sub> of First generation of AHL analogs.....	131
Figure C2.	IC <sub>50</sub> of L-HSL derivatives.....	132
Figure C3.	IC <sub>50</sub> of acyl-D-HSL analogs.....	133
Figure C4.	IC <sub>50</sub> and EC <sub>50</sub> of 3-oxoacyl-D-HSL analogs.....	133
Figure C5.	IC <sub>50</sub> of DL-sulfonamide analog .....	134
Figure C6.	IC <sub>50</sub> of acyl- and 3-oxoacyl-L-homocysteine thiolactones .....	135
Figure C7.	IC <sub>50</sub> and EC <sub>50</sub> of acyl- and 3oxoacyl-D-homocysteine thiolactones .....	136
Figure C8.	IC <sub>50</sub> of cyclopentyl derivatives .....	136
Figure C9.	IC <sub>50</sub> of non-lactone AHL analogs .....	137
Figure C10.	IC <sub>50</sub> of headgroup and tail moieties .....	138
Figure C11.	Substrate-velocity curve of RhII with various acyl-ACP substrates.....	139
Figure C12.	IC <sub>50</sub> of various alkyl-ACPs.....	139
Figure C13.	RhII Inhibition assays with various alkyl-ACPs.....	140
Figure C14.	Double reciprocal plot for RhII inhibition with various alkyl-ACPs.....	140
Figure C15.	IC <sub>50</sub> of IACPs at different time points.....	141
Figure C16.	IC <sub>50</sub> of ICoA derivatives .....	141
Figure C17.	DMSO Inhibition .....	141

## LIST OF ABBREVIATIONS

CDC	Center for Disease Control and Prevention
WHO	World Health Organization
QS	Quorum Sensing
QSI	Quorum Sensing Inhibition
AHL	<i>N</i> -Acyl-Homoserine Lactone
AI-1	Autoinducer-1
SAM	<i>S</i> -adenosyl-L-methionine
ACP	Acyl Carrier Protein
Apo-ACP	Apo-Acyl Carrier Protein
Acyl-ACP	Acyl-Acyl Carrier Protein
CoA	Coenzyme A
Acyl-CoA	Acyl-Coenzyme A
AIP	Autoinducer Peptide
AI-2	Autoinducer-2
MTA	5'-Deoxy-5'-methylthioadenosine
PQS	Pseudomonas Quinolone Signal
HSL	Homoserine lactone
3oxoC12-HSL	3-Oxododecanoyl-homoserine lactone
C4-HSL	Butanoyl-homoserine lactone
DCPIP	2,6-Dichloroindophenol

V	Enzyme initial rate
$V_{\max}$	Maximum enzyme initial rate
$K_m$	Michaelis constant
$k_{\text{cat}}$	Turnover rate
$K_i$	Inhibition constant
[S]	Substrate concentration
[I]	Inhibitor concentration
AIC	Akaike's Information Criterion
IC <sub>50</sub>	Half maximal inhibitory concentration
EC <sub>50</sub>	Half maximal effective concentration
Alkyl-ACP	Alkyl-Acyl Carrier Protein
Alkyl-CoA	Alkyl-Coenzyme A
MPA	(S)-(+)- $\alpha$ -Methoxyphenylacetic acid
MES	2-( <i>N</i> -Morpholino)ethanesulfonic acid hydrate
Meldrum's acid	2,2-Dimethyl-1,3-dioxane-4,6-dione
HEPES	4-(2-Hydroxyethyl)piperazine-1-ethanesulfonic acid
EDTA	Ethylenediaminetetraacetic acid
MgSO <sub>4</sub>	Magnesium sulfate anhydrous
EDC	<i>N</i> -(3-Dimethylaminopropyl)- <i>N'</i> -ethylcarbodiimide hydrochloride
TLCK	<i>N</i> <sub><math>\alpha</math></sub> -Tosyl-L-lysine chloromethyl ketone hydrochloride
PMSF	Phenylmethanesulfonyl fluoride
C4-CoA	Butanoyl-CoA

C6-CoA	Hexanoyl-CoA
C8-CoA	Octanoyl-CoA
C10-CoA	Decanoyl-CoA
C12-CoA	Dodecanoyl-CoA
DNase	Deoxyribonuclease I
RNase	Ribonuclease I
IPA	2-Propanol
B-PER	Bacterial protein extraction reagent
DMF	Dimethylformamide
DMSO	Dimethyl sulfoxide
HCl	Hydrochloric acid
IPTG	Isopropyl $\beta$ -D-1-thiogalactopyranoside
MnSO <sub>4</sub>	Manganese sulfate
TFA	Trifluoroacetic acid
MgCl <sub>2</sub>	Magnesium chloride
kD	Kilodalton
<i>Sfp</i>	Surfactin-synthetase activating protein/phosphopantetheinyl transferase
UV-Vis	Ultraviolet-visible light
HPLC	High performance liquid chromatography
UHPLC	Ultra high performance liquid chromatography
QTOF	Quadrupole time-of-flight
ACN	Acetonitrile

Buffer A	50 mM Tris-HCl, pH 7.5, 0.2 M NaCl, 1 mM EDTA, 0.1 mM PMSF, 0.1 mM TLCK, 0.4 M sucrose, and 2.5% (v/v) glycerol
Psi	Pounds per square inch
OD <sub>600</sub>	Optical density at 600 nm
w/v	weight to volume ratio
RT	Retention time
C6-ACP	Hexanoyl-ACP
C4-ACP	Butanoyl-ACP
IACP	Inert-ACP/alkyl-ACP
C4-IACP	Butyl-ACP
C6-IACP	Hexyl-ACP
C8-ACP	Octanoyl-ACP
C8-IACP	Octyl-ACP
C10-ACP	Decanoyl-ACP
C10-IACP	Decyl-ACP
C12-ACP	Dodecanoyl-ACP
NaHCO <sub>3</sub>	Sodium bicarbonate
KHSO <sub>4</sub>	Potassium bisulfate
HPLC-MS	High performance liquid chromatography mass spectrometry
MS	Mass spectrometry
LC-MS	Liquid chromatography-mass spectrometry

ESI	Electrospray ionization
LC	Liquid chromatography
TLC	Thin layer chromatography
3-oxoC8-D-HSL	3-Oxooctanoyl-D-homoserine lactone
3-oxoC6-D-HSL	3-Oxohexanoyl-D-homoserine lactone
C12-D-thiolactone	Dodecanoyl-D-homocysteine thiolactone
3-oxoC12-D-thiolactone	3-Oxododecanoyl-D-homoserine lactone
C12-L-thiolactone	Dodecanoyl-L-homocysteine thiolactone
3-oxoC12-L-thiolactone	3-Oxododecanoyl-L-homoserine lactone
3-oxoC6-D-thiolactone	3-Oxohexanoyl-D-homoserine lactone
3-oxoC8-D-thiolactone	3-Oxooctanoyl-D-homoserine lactone
3-oxoC10-D-thiolactone	3-Oxodecanoyl-D-homoserine lactone
C4-ICoA	Butyl-CoA
C6-ICoA	Hexyl-CoA
C8-ICoA	Octyl-CoA

## CHAPTER ONE: INTRODUCTION

### **The Antibiotic Crisis**

The modern age of medicine was made possible, in large parts, by the discovery and the proliferation of antibiotics. However, mankind has been slowly disarmed by the rise and the spread of antibiotic resistant superbugs. In the U.S. alone, antibiotic-resistant bacteria are responsible for at least two million infections, resulting in 23,000 lives and cost \$35 billion annually.<sup>1</sup> In response to this rise in antibiotic resistance, the White House has named it a threat to national security.<sup>2</sup> Despite efforts to curb the tide, both CDC and WHO warn of a post-antibiotic age.<sup>1,3</sup>

The rise of superbugs highlights a fundamental problem with antibiotics; the use of antibiotics is an all-or-nothing treatment in which all the drug-sensitive strains are eliminated while the resistant ones are untouched. This dichotomy places enormous selective pressure for resistant bacteria to propagate throughout the entire population. In a controlled environment, a strain of sensitive bacteria can be pressured to withstand ever-increasing concentrations of antibiotics in less than two-weeks.<sup>4</sup> Even in the real-world setting, resistance often develops within a few years of the release of a new antibiotic (Figure 1).<sup>5</sup> Therefore, drug companies are shying away from continuing to put resources into R&D of a drug that could become irrelevant soon after its commercialization (Figure 2).<sup>6,7</sup> The resulting decrease in supply combined with the increase in demand have led to the investigation of novel methods to fight bacteria, such as predatory bacteria, bacteriophage, antimicrobial peptides, gene-editing enzymes, and quorum sensing.<sup>8-13</sup> Of

these alternatives, most follow the pattern of antibiotics in that they kill sensitive strains, leaving behind resistant strains to flourish; however, quorum sensing (QS) provide a unique means of avoiding the pitfalls of antibiotics by targeting virulence rather than the organism directly.<sup>14</sup>

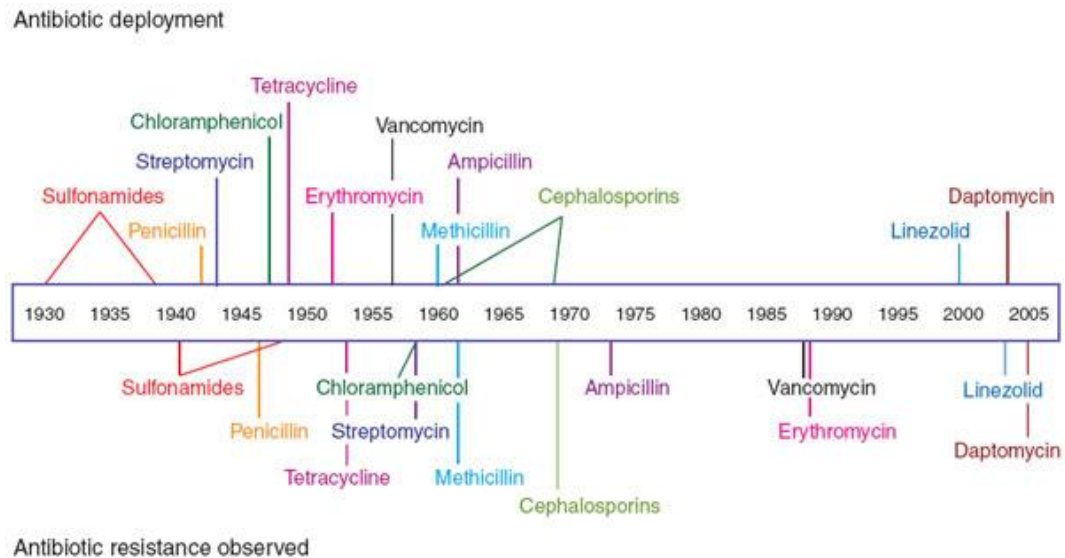


**Figure 1.<sup>5</sup> Timeline of the effective-lifetime of antibiotics.** The labels above the timeline indicates the year different antibiotics were released, whereas the year resistance to each antibiotic was first observed is shown below the timeline. In many cases, resistance developed within a few years of deployment of new antibiotics.



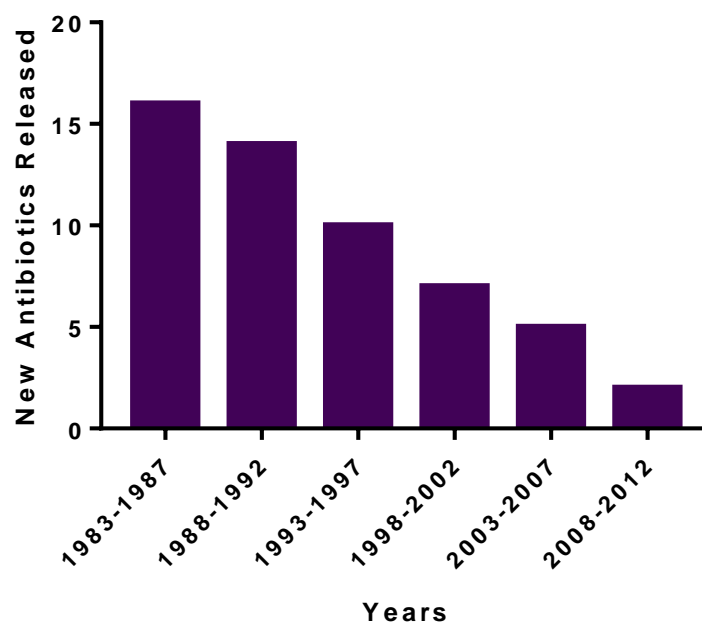


**Figure 2. Decrease in new antibiotic development.** In the heydays of antibiotic development in the 1980's, more than 3 new drugs were released annually; however, in recent years, that number has been reduced to just two new antibiotics in five years.

### Quorum Sensing

Once known mainly for their single-cellular life, bacteria are now known to communicate via chemical signals to approximate multicellular behavior in a process termed quorum sensing.<sup>15</sup> The concentration of the signal molecules, called autoinducers, correlate to the number of bacteria in the area. Therefore, by monitoring the concentrations of the autoinducers, bacteria can detect the concentration of local bacteria population.<sup>16,17</sup> Typically, when signal concentration is low, indicative of limited cell count, bacteria operate individually. However, once a certain concentration, or “quorum,” is reached, QS-controlled genes are turned on, activating group behaviors, which includes biofilm formation, virulence, antibiotic resistance, protease production, and siderophores.<sup>18</sup> Therefore, theoretically, QS inhibitors could be used as combination drug with antibiotics since antibiotic resistance associated with QS inhibition (QSI) would be

reduced. Additionally, inhibiting quorum sensing should prevent virulent traits from emerging.<sup>19</sup> Indeed, studies have shown QS-knockout strains to be incapable of colonial behaviors characteristic of pathogenicity.<sup>20</sup> As an anti-virulence treatment, contrary to the lethal (to the bacteria) antibiotic therapy, QS inhibition (QSI) could potentially pave the path to an “evolution-proof” method of dealing with bacterial infections.<sup>19</sup> It has been shown that QSI resistance does not lead to survival advantage. The study showed that since the majority of the population are unable to produce autoinducer signal molecules, the few resistant strains could not produce sufficient AHLs to reach “quorum” and induce QS-controlled gene expression; however, even if the resistance strains are able to express QS-controlled traits, many of which are group-beneficial, the benefits of those traits are shared with the inhibited strains, thus limiting any survival advantage QSI resistance could offer.<sup>19</sup>

Quite contrary to the notion of being “simple” creatures, bacteria have complex communication system with different QS system for various types of bacteria. Gram-negative bacteria have LuxI (initiator/synthase) and LuxR (receptor) type proteins responsible for the synthesis and the uptake of *N*-acyl-homoserine lactone (AHL/AI-1) autoinducers (Figure 3; Table 1). In this communication system, AHL synthases release AHL autoinducers and release them to the environment. The binding of the signal with the designated receptor protein starts the upregulation of QS-controlled genes such as increased AHL synthase activity, biofilm formation, toxin production, and antibiotic resistance.

AHL synthases are bi-substrate enzymes that use *S*-adenosyl-L-methionine (SAM) and an acyl substrate (acyl-ACP or acyl-CoA) to synthesize AHL signal

molecule. Whereas SAM is a conserved substrate among various AHL synthases, preferential usage of an acyl substrate of certain acyl-chain moiety results in enzyme-specific signal molecules, allowing each species to speak its own unique “language,” or differentiated AHLs (Figure 4).<sup>21</sup> Many AHL synthases have been shown to discriminate against non-native acyl-chain and only use a specific acyl substrate to produce enzyme-specific AHL signal, thus increasing the signal to noise ratio.<sup>22</sup> Different receptor proteins likewise preferentially bind with their designated AHLs so that bacteria can conduct intra-specie communication without interference.

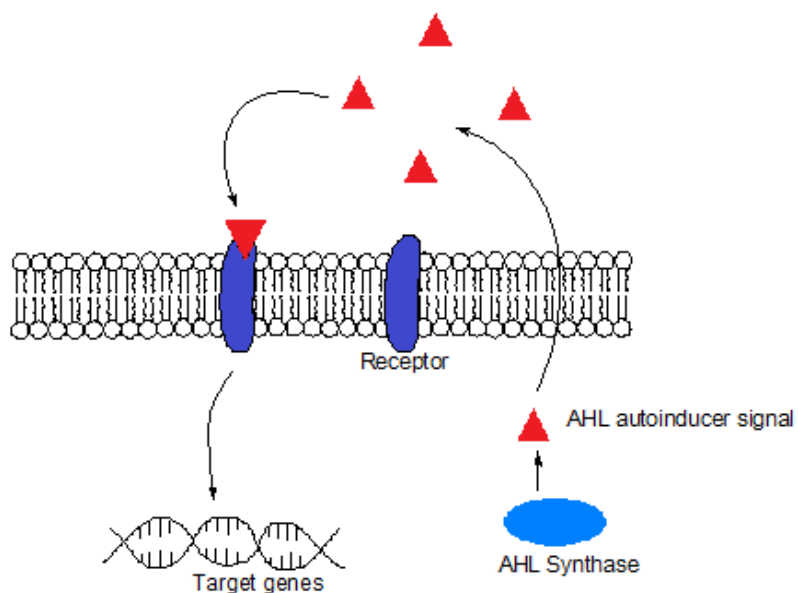


**Figure 3. The typical quorum sensing system found in Gram-negative bacteria.** A LuxI-type signal synthase produces AHL signal molecules which then binds to LuxR-type receptor proteins. The signal-receptor binding promotes the expression of QS-controlled genes, which includes further activation of the synthase.

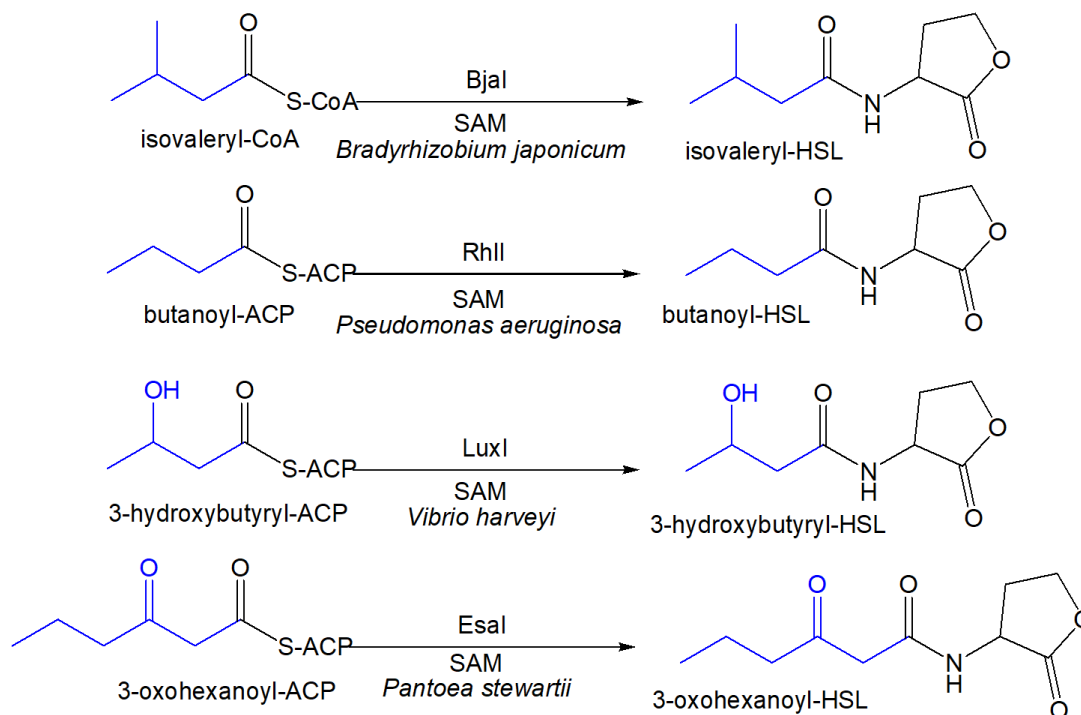


**Figure 4. Species-specific signal molecules.** The different “languages” used by each Gram-negative bacteria species are dependent on the variations in the acyl-chain which is derived from the acyl substrate.

**Table 1. Types of QS signal molecules**

Signal Type	Organism	Structure
AI-1/AHL	Gram-negative	
AIP	Gram-positive	
AI-2	Universal	

Gram-positive bacteria, on the other hand, use short peptides, linear or cyclic, as QS signals (Table 1). As with Gram-negative QS system, the specificity comes from varying the signal molecules by modifying the peptide sequence and shape.<sup>23</sup> Synthesized in the cytoplasm and actively transported out of the cell, these autoinducer peptides (AIP) bind to membrane-bound histidine kinase, leading to a phosphorylation cascade, activating QS regulator proteins for gene expression.<sup>24</sup>

In addition to the species-specific AHL/AI-1 and AIP based QS for interspecies-communications, a universal signal-based QS system has also been discovered. This interspecies-communication QS is based on AI-2 signal molecule (Table 1). Like the AIP-based system, AI-2 binding event starts a phosphorylation cascade to regulate gene expression.<sup>25</sup>

In light of the antibiotic crisis, of these three systems (AHL, AIP, AI-2), AHL-based QS found in human-pathogen-causing Gram-negative bacteria is of great interest. Four-main principles of targeting AHL communication system have been proposed: synthase inhibition, receptor inhibition, quorum-quenching enzymes, and AHL-sequestering antibodies.<sup>26-29</sup> Most studies thus far have explored receptor inhibition; however, due to high affinity of native AHLs to AHL-receptor proteins, it is a difficult task to design a molecule that could out compete the binding of native autoinducer to LuxR-type proteins to disrupt QS.<sup>30-33</sup> The progress towards developing synthase inhibitors, on the other hand, is hampered because most AHL synthases are yet to be characterized. Nevertheless, AHL synthase-knockout studies have led to elimination of virulence traits, supporting AHL synthase modulation as a means of QS control.<sup>34</sup>

Efforts toward understanding the mechanism of AHL synthesis are important to design potent and selective AHL synthase inhibitors.

### Proposed AHL synthase mechanism

AHL synthases are bi-ter enzymes that catalyzes the conversion of S-adenosyl-L-methionine (SAM) and acyl-acyl-carrier protein (acyl-ACP) or acyl-coenzyme A (acyl-CoA) to AHL autoinducer, 5'-deoxy-5'-methylthioadenosine (MTA), and holo-ACP or free-CoA (Figure 5).<sup>35-38</sup> During catalysis, nucleophilic attack from the amine group of SAM to the carbonyl carbon of acyl-ACP cleaves the thioester bond, thereby releasing holo-ACP and transferring the fatty acid tail to SAM in the acylation half-reaction. In the lactonization reaction, SAM undergoes intramolecular ring closure, forming the lactone head-group and producing MTA side product.

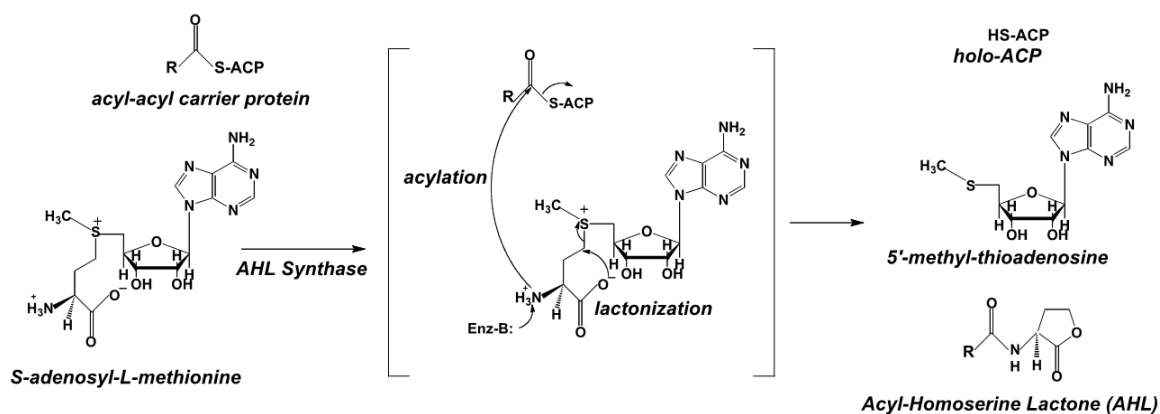


**Figure 5.** The proposed mechanism of AHL-synthases. SAM is a conserved substrate amongst all AHL synthases. The variation comes from the R-group of the acyl substrate.

As with any other enzyme, AHL synthases can be inhibited by interference in the substrate binding, the catalysis, or the product release steps. However, each approach has its corresponding challenges. To disrupt substrate binding, substrate analogs would be the ideal starting point, yet SAM and acyl-ACP are commonly used in human enzymes,

SAM as a common methyl donor and acyl-ACP as a key player in fatty-acid biosynthesis.<sup>39, 40</sup> Therefore, SAM or acyl-ACP based design of inhibitors have the potential to target all SAM or acyl-ACP using enzymes, thereby increasing the risk of unwanted side-effects. Moreover, how an AHL synthase preferentially bind to its native substrate over similarly shaped analogs, such as acyl-ACPs of different chain length, is not well understood, which impedes the design of substrate analogs that would out-compete the native substrates binding to the enzyme. Mechanism-based covalent inhibitors act by forming covalent bonds with certain active site residues; however, as most AHL synthases remain uncharacterized the active site residues to target remain unknown.

As holo-ACP and MTA are both relevant in human biology, holo-ACP in fatty acid synthesis and MTA in polyamine synthesis, product inhibitors based on those compounds carry the dangers of serious side-effects.<sup>41, 42</sup> AHL-based inhibitors, on the other hand, has qualities suitable for pharmaceutical uses; AHL-analogs would have the potential of targeting both the synthase and the receptor, be QS-specific, have favorable cell-membrane diffusion characteristics, and have long shelf-life.<sup>30, 31, 33</sup> There have been no reports of AHL-based modulators tested on AHL-synthases; however, studies reveal their great effect on AHL receptors, both as agonists and antagonists.<sup>43-45</sup>

### **RhII, QS signal synthase in *Pseudomonas aeruginosa***

*Pseudomonas aeruginosa* is a specie of common Gram-negative bacteria that can cause diseases in both animals and plants. It is categorized as opportunistic bacteria commonly associated with healthcare-associated infections, infecting 51,000 every year in American hospitals, killing 400.<sup>46</sup> In humans, it can cause pneumonia, cystic fibrosis,

bacterial meningitis, septic shock, urinary tract infection, GI infection, and skin and soft tissue infections.<sup>6, 46, 47</sup> *P. aeruginosa* infections are becoming harder to treat due their increasing resistance to antibiotics, so much so that the CDC labeled it as a “serious threat” in their report on “Antibiotic Resistance Threats in the United States, 2013.”<sup>46</sup>

The virulence and antibiotic resistance in *P. aeruginosa* is controlled by its QS system comprised of AHL-quinolone system. Its AHL system is comprised of LasI/R and RhlI/R systems whereas the Pseudomonas quinolone signal (PQS) is under Pqs receptor (PqsR) control (Figure 6).<sup>48</sup> The two AHL-based systems use very different signal molecules. LasI synthesizes 3-oxo-dodecanoyl-homoserine lactone (3OC12HSL) signal molecule, which binds with LasR to activate several QS-controlled genes, which includes the Rhl and Pqs system. The RhlI/R proteins, in contrast, use butanoyl-homoserine lactone (C4HSL) autoinducers as the signal molecule. Under normal conditions, LasI/R pair is thought to activate the Rhl and the Pqs system, though both the Rhl and the Pqs have been observed acting independent of the Las system under certain circumstances. Furthermore, Pqs generally activates Rhl whereas Rhl typically suppresses Pqs via mechanisms not completely understood. Studies have shown that inhibiting any of these three QS systems significantly reduces *Pseudomonas aeruginosa* virulence. Studies thus far have focused primarily on Las-system inhibition and Rhl-specific inhibitors have yet to be studied in great detail. However, Rhl-system inhibition merit further examination for Rhl knockout strains strain to display pathogenic phenotype.<sup>49, 50</sup>



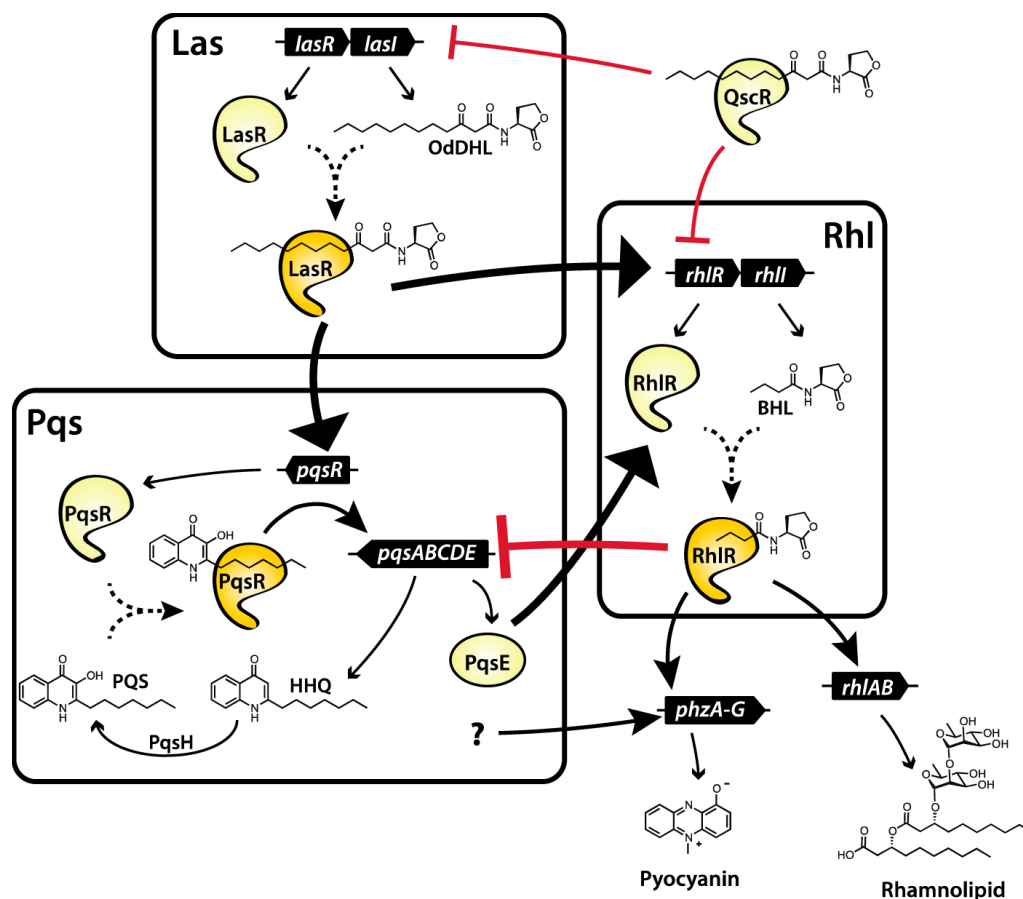


**Figure 6.**<sup>48</sup> QS system regulation in *P. aeruginosa*. LasI/R promotes both the Rhl and Pqs systems. Whereas Pqs induces Rhl activity, Rhl inhibits Pqs via unknown methods.

### AHL synthase Kinetics

#### DCPIP Assay

DCPIP colorimetric assay is a well-established assay used to determine AHL synthase activity by monitoring the enzyme-dependent rate of release of holo-ACP/CoA thiol product over time (Figure 7).<sup>51-53</sup> DCPIP, in its oxidized form, is a blue compound that absorbs at 600 nm ( $\epsilon_{600} = 21,000 \text{ M}^{-1}\text{cm}^{-1} = 2.1 \times 10^{-2} \mu\text{M}^{-1} \text{cm}^{-1}$ ). The holo-ACP thiol released upon acylation of SAM reduces the DCPIP dye to a colorless form, DCPIPH<sub>2</sub>. By monitoring the change in the absorbance of DCPIP at 600 nm, the enzyme rate can be determined by the following equation:

$$Abs_{600} = \epsilon_{600} l c = (2.1 \times 10^{-2} \mu M^{-1})(cm^{-1})(c) \quad (1)$$

$$c = \frac{Abs_{600}}{\epsilon_{600} l} = \frac{Abs_{600}}{l} (\epsilon_{600}^{-1}) = \frac{Abs_{600} \mu M DCPIP \cdot cm}{cm \cdot 2.1 \times 10^{-2}} \quad (2)$$

$$rate = \frac{c}{t} = \left( \frac{Abs}{\epsilon \cdot l} \right) t^{-1} = \left( \frac{Abs}{cm} \right) \left( \frac{\mu M DCPIP \cdot cm}{2.1 \times 10^{-2}} \right) (s^{-1}) \left( \frac{2 \mu M thiol}{1 \mu M DCPIP} \right) \left( \frac{60 s}{1 min} \right) \quad (3)$$

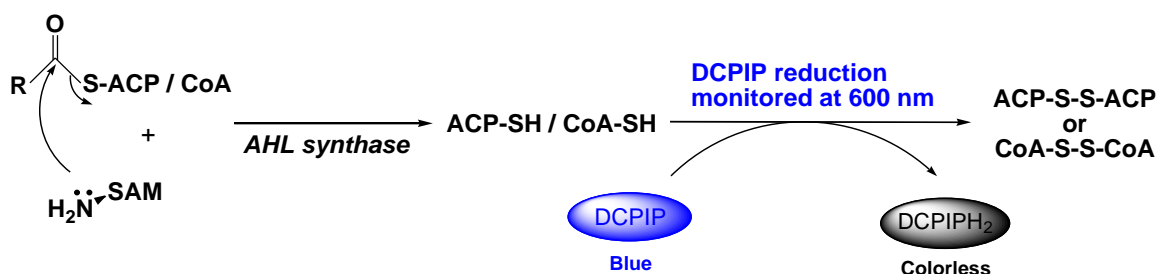


**Figure 7. DCPIP assay mechanism.** DCPIP, in its oxidized form, is a blue compound that turns colorless upon reduction with two thiols released from acylation reaction in AHL synthesis. By monitoring the decrease of absorbance at 600 nm, AHL synthase rate can be determined.

### Enzyme Kinetics

Initial rate of enzyme activity as a function of substrate concentration follows a hyperbolic curve (Figure 8). When the substrate is present in saturating concentrations, maximum initial rate is achieved, denoted by  $V_{max}$ . The concentration of the substrate required to reach half-maximal velocity is termed  $K_m$ .

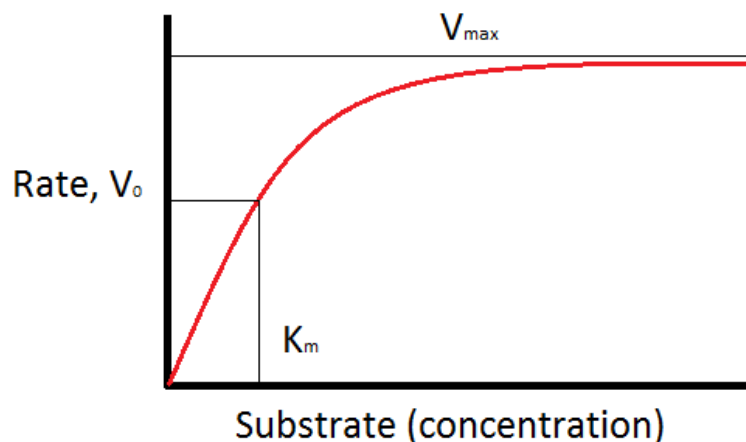


**Figure 8. The Substrate-Velocity Curve.** This curve represents the relationship of enzyme rate as a function of substrate concentration.

This plot, also called the substrate-velocity curve, is commonly analyzed using the Michaelis-Menten equation. In the simplest situation where one substrate is converted to one product, the reaction can be summarized as:



where E is the enzyme, S the substrate, ES the enzyme-substrate complex (Michaelis complex), P the product, and v the reaction rate. The rate of the reaction (v) can be described with the equation:

$$V = \frac{V_{max}[S]}{[S] + K_m} \quad (5)$$

where  $V_{max}$  is the highest reaction rate that the enzyme can achieve at saturating substrate concentration, [S] the substrate concentration, and  $K_m$  the substrate concentration required for half-maximal rate. The  $V_{max}$  and  $K_m$  of an enzyme can be determined by measuring the initial enzyme rate with various substrate concentrations and fitting the resulting plot with the Michaelis-Menten equation. For easier interpretation, this hyperbolic curve can be linearized by taking the inverse of both sides of the equation,

thereby converting the Michaelis-Menten equation to the double-reciprocal or Lineweaver-Burke equation (Figure 9):

$$\frac{1}{v} = \frac{K_m}{V_{max}} [S] + \frac{1}{V_{max}} \quad (6)$$

where independent axis (x-axis) represents the substrate concentration and the dependent axis (y-axis), the inverse rate. In this form, a change in the  $V_{max}$  would lead to a shift in the y-intercept (intercept-effect) and a change in the  $\frac{K_m}{V_{max}}$  (inverse of catalytic efficiency,  $k_{cat}/K_m$ ) ratio would cause a change in the slope (slope-effect).

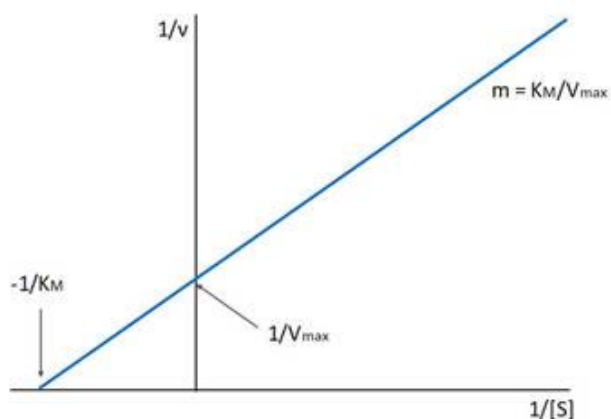


**Figure 9. Typical Lineweaver-Burk plot.** Taking the inverse of the hyperbolic Michaelis-Menten plot linearizes the data. In the  $1/V$  vs  $1/[S]$  plot, the y-intercept corresponds to  $1/V_{max}$ , the x-intercept to  $-1/K_m$ , and the slope to  $K_m/V_{max}$ .

However, AHL synthases are bi-ter enzymes (2 substrates, 3 products). The order of substrate binding and product release (the kinetic mechanism) can follow one of three patterns (Figure 10). 1) Ordered sequential mechanism: substrates bind to the enzyme in a specific order before the products are released in a defined sequence. 2) Random sequential mechanism: substrates all bind before the first product is released but the order of substrate addition or the product release, or both, is random. 3) Ping-pong sequential mechanism: the first product is released before the second substrate binds with the enzyme.

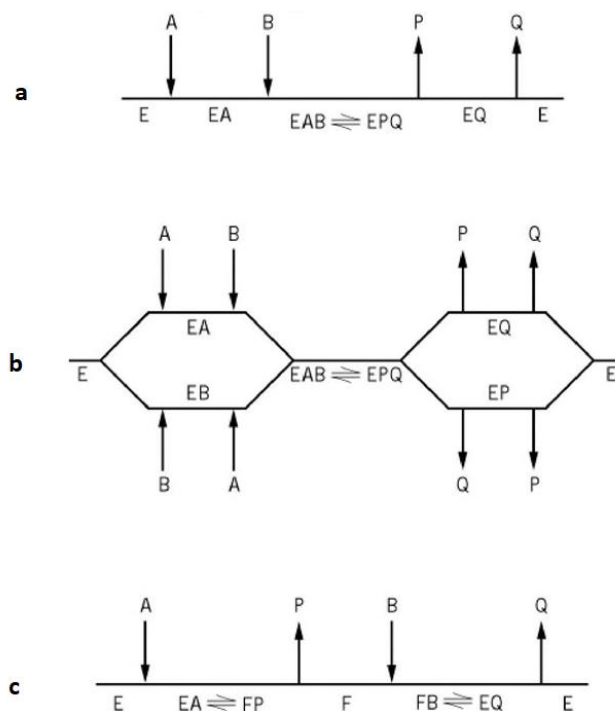


**Figure 10. Kinetic mechanism for bisubstrate enzyme.** (a) Ordered sequential: substrate binding occurs before product release and follow definite order. (b) Random sequential: substrate binding occurs before product release and follow random order. (c) Ping-pong: first product release step occurs before the second substrate addition.

Bi-substrate enzyme kinetics is represented by a more complicated Cleland equation as shown:

$$v = \frac{v_{max}[A][B]}{K + K_m^B[A] + K_m^A[B] + [A][B]} \quad (7)$$

where  $K_m^A$  is the Michaelis constant for substrate A at saturating concentrations of B,  $K_m^B$  the Michaelis constant for substrate B at saturating concentrations of A, and K depends on the reaction type (sequential vs ping-pong). In a sequential mechanism, the Cleland equation becomes:

$$v = \frac{v_{max}[A][B]}{K_i^A K_m^B + K_m^B[A] + K_m^A[B] + [A][B]} \quad (8)$$

where the  $K_i^A$  is the dissociation constant for the EA complex in the absence of the second substrate, B. If the enzyme undergoes ping-pong mechanism, the K term drops and the Cleland equation becomes:

$$v = \frac{v_{max}[A][B]}{K_m^B[A] + K_m^A[B] + [A][B]} \quad (9)$$

The double reciprocal of the Cleland equation for sequential mechanism is:

$$\frac{1}{v} = \frac{1}{v_{max}} \left[ \left( 1 + \frac{K_m^B}{[B]} \right) + \frac{1}{[A]} \left( K_m^A + K_i^A \cdot \frac{K_m^b}{[B]} \right) \right] \quad (10)$$

and for the ping-pong mechanism:

$$\frac{1}{v} = \frac{1}{v_{max}} \left[ \left( 1 + \frac{K_m^B}{[B]} \right) + \frac{1}{[A]} (K_m^A) \right] \quad (11)$$

at constant [B] and variable [A], the slope of sequential equation is:

$$\frac{1}{v_{max}} \left( K_m^A + K_i^A \cdot \frac{K_m^b}{[B]} \right) \quad (12)$$

which indicates that the slope depends on the concentration of substrate B (slope-effect).

For the ping-pong equation, the slope is:

$$\frac{K_m^A}{v_{max}} \quad (13)$$

indicating that the slope is independent of the substrate B concentration (no slope-effect).

For both the sequential and the ping-pong mechanism equation, the intercept of this is:

$$\frac{1}{v_{max}} \left( 1 + \frac{K_m^B}{[B]} \right) \quad (14)$$

showing that the intercept always depends on B concentration (intercept-effect). This dependence on [B] indicates that saturation with A does not cut off the effect of adding more B. Therefore, at saturating A concentration, the addition of B always increases the rate (increases the apparent  $V_{max}$ ).

For sequential mechanism, since both the slope and the intercept are dependent on the fixed concentration of substrate B, the double reciprocal plot of  $\frac{1}{v}$  vs  $\frac{1}{[A]}$  at various

fixed [B] would feature a set of lines intersecting in quadrant II (Figure 11 a). For ping-pong mechanism, since only the intercept is affected by the concentration of B, the double reciprocal plot of  $\frac{1}{v}$  vs  $\frac{1}{[A]}$  at various fixed [B] would feature a set of parallel lines (Figure 11 b).

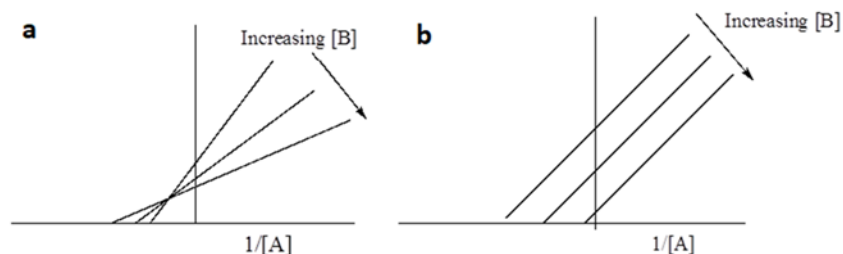


**Figure 11. Double reciprocal plot of sequential vs ping-pong reaction mechanism.** Enzyme reactions at various fixed B concentrations and varying A concentration are observed. (a) If A and B both bind before product release, sequential addition, both the slope and the intercept drop as [B] increases and the lines intersect in the second quadrant. (b) If the enzyme follows ping-pong mechanism, only the intercept decreases as [B] increases and the lines remain parallel.

Work by Greenberg showed that RhII is an ordered bi-ter enzyme with SAM binding first followed by C4-ACP binding and the ordered release of holo-ACP, C4-HSL, and MTA (Figure 12). Therefore, RhII reaction will follow equations 11 and 13 and the double reciprocal plot of  $\frac{1}{v}$  vs  $\frac{1}{[SAM]}$  at various fixed [C4-ACP] would show both slope and intercept-effects.



**Figure 12. Cleland diagram of RhII catalyzed ordered bi-ter reaction.** “E” denotes free RhII enzyme while “A,” “B,” “P,” “Q,” and “R” represents SAM, C4-ACP, holo-ACP, C4-HSL, and MTA, respectively.

However, to simplify the equation, if one of the substrates were to be at saturating concentrations (e.g.  $[A] \gg [B]$ ,  $K_m^A$ ), any term not including the  $[A]$  term would drop out to form:

$$V = \frac{V_{max}[A][B]}{K_m^B[A] + [A][B]} \quad (15)$$

then the  $[A]$  term in the remaining equation would cancel out, simplifying the equation to:

$$V = \frac{V_{max}[B]}{K_m^B + [B]} \quad (16)$$

which is mathematically identical to the Michaelis-Menten equation. Therefore, by keeping one substrate, “A”, at a saturating concentration and varying the concentration of the other substrate, “B”, the apparent  $K_m$ ,  $V_{max}$ , and  $k_{cat}$  values of the enzyme associated with “B” substrate can be determined, which will be referred to as “V vs [S]” kinetics. In this study, substrate “A” corresponds to SAM and substrate “B” corresponds to C4-ACP

### Enzyme Inhibition

Inhibitors can decrease enzyme activity in one of three ways: competitive inhibition, uncompetitive inhibition, and mixed mode of inhibition (Figure 13). In competitive mode of inhibition, the inhibitor is competing with the substrate for the same enzyme form; in uncompetitive mode of inhibition, the inhibitor is not competing with the substrate and binds to a different enzyme form; and in mixed mode of inhibition, the inhibitor binds with both the same and different forms of the enzyme.



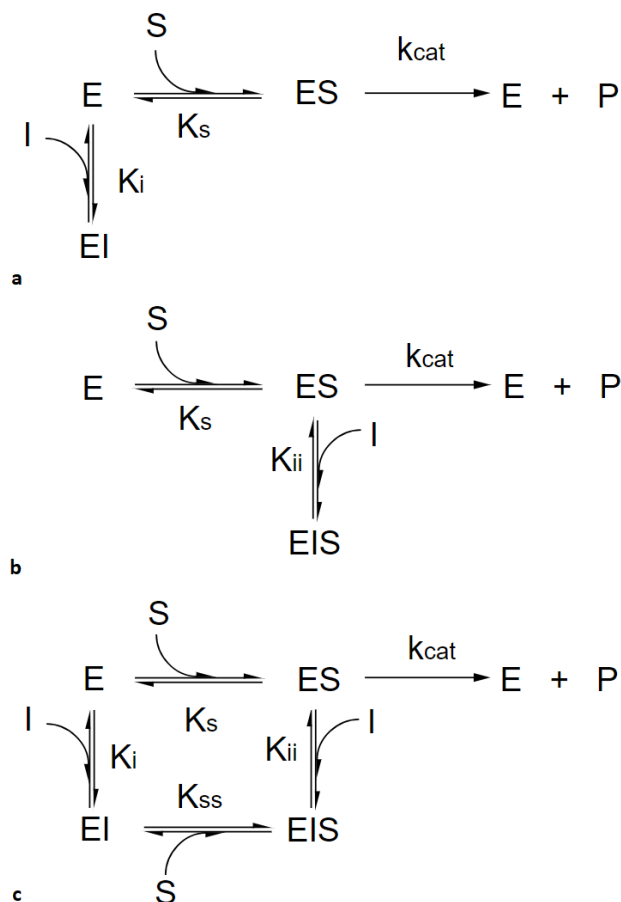


**Figure 13. Modes of inhibition.** (a) Competitive mode of inhibition: the inhibitor competes with the substrate for the same enzyme form. (b) Uncompetitive mode of inhibition: the inhibitor and the substrate bind to different enzyme form. (c) Mixed mode of inhibition: the inhibitor binds to both the same and different enzyme forms. Noncompetitive inhibition is a special case of mixed mode when the  $K_i$  and  $K_{ii}$  values are equal.

The mode of inhibition can be determined by conducting the  $V$  vs  $[S]$  kinetics assay at different inhibitor concentration and the resulting rate curves will fit to the following form of the Michaelis-Menten equation:

$$V = \frac{V_{max}^{app}[S]}{K_m^{app} + [S]} \quad (17)$$

If the inhibitor is targeting the same form of the enzyme to which the variable substrate binds, it would be inhibiting the enzyme competitively and mathematically, the  $V_{max}^{app}$  and the  $K_m^{app}$  would be:

$$V_{max}^{app} = V_{max} \quad (18)$$

$$K_m^{app} = K_m \left(1 + \frac{[I]}{K_{is}}\right) \quad (19)$$

since  $K_m^{app}$  changes while  $V_{max}^{app}$  remains unaffected, according to the Lineweaver-Burk equation, the inhibition produces a slope-effect, denoted by  $K_{is}$  (binding affinity of the inhibitor to E form). Mechanistically, as substrate concentration increases, Le Chatlier's principle predicts that the reaction would be pushed forward to form more EA complex, which would decrease the concentration of free enzyme, E. The decrease in E concentration would push the EI complex to revert to E + I. Therefore, the substrate can outcompete the inhibitor at high concentrations (closer to the y-axis of the double reciprocal plot) and reach  $V_{max}$  (no intercept-effect). However, the interference in binding increases the concentration of substrate for half-maximal rate ( $K_m$ ), thus increasing the  $\frac{K_m}{V_{max}}$ , or the slope (slope-effect). This inhibition pattern can be generalized to the following observation: if the inhibitor binds with the same form of the enzyme, "E," as the variable substrate or binds with an enzyme form reversibly connected to "E" form, there is slope-effect.

If the inhibitor is targeting a different form of the enzyme as the variable substrate, it would be inhibiting the enzyme uncompetitively and the  $V_{max}^{app}$  and the  $K_m^{app}$  would be:

$$V_{max}^{app} = \frac{V_{max}}{\left(1 + \frac{[I]}{K_{ii}}\right)} \quad (20)$$

$$K_m^{app} = \frac{K_m}{\left(1 + \frac{[I]}{K_{ii}}\right)} \quad (21)$$

since  $V_{max}^{app}$  changes, the Lineweaver-Burk equation dictates that this inhibition would cause an intercept-effect, denoted by  $K_{ii}$  (binding affinity of the inhibitor to the ES form).

Moreover, as both the  $K_m^{app}$  and the  $V_{max}^{app}$  are changed by the same ratio,  $(1 + \frac{[I]}{K_{ii}})$ , the slope,  $\frac{K_m}{V_{max}}$ , remains the same. Mechanistically, since the inhibitor is binding to a different enzyme form than the substrate binding to, increasing the substrate concentration cannot overcome the inhibition; therefore, even at saturating substrate concentration (near y-axis), the apparent  $V_{max}$  is lower than true  $V_{max}$  (intercept-effect). As noted above, slope-effect is only observed if the inhibitor and the variable substrate are binding to the same enzyme form or reversibly connected enzyme forms; in uncompetitive inhibition, the inhibitor binds to a different form of the enzyme and no slope-effect is observed. This inhibition pattern can be generalized as: if the inhibitor and the variable substrate bind with different forms of the enzyme, there is intercept-effect.

If the inhibitor is targeting both the same and a different form of the enzyme as the variable substrate, it would be inhibiting the enzyme via mixed model inhibition and the  $V_{max}^{app}$  and the  $K_m^{app}$  would be:

$$V_{max}^{app} = \frac{V_{max}}{(1 + \frac{[I]}{K_{ii}})} \quad (22)$$

$$K_m^{app} = \frac{K_m(1 + \frac{[I]}{K_{is}})}{(1 + \frac{[I]}{K_{ii}})} \quad (23)$$

since  $K_m^{app}$  and  $V_{max}^{app}$  change by differing ratios, the Lineweaver-Burk equation indicates that the inhibition would cause both slope and intercept-effects, denoted by having both  $K_{is}$  and  $K_{ii}$ . In this case, since the inhibitor also binds with a different form of the enzyme,  $V_{max}$  is affected and there is intercept-effect. Since the inhibitor and the substrate are binding to the same form of the enzyme, there is also slope-effect. In a special case of mixed model inhibition, in which the inhibitor binds to two different enzyme forms

equally well, the  $K_{ii}$  value would equal  $K_{is}$  value and the  $K_m^{app}$  value would be equal to the  $K_m$  value and only the  $V_{max}$  would be affected.

Once the V vs [S] assays in varying [I] is conducted, the data can be fitted to all the models and the best fit can be determined by Akaike's information criterion method (AIC), which compares the scatter about the fit and the degrees of freedom associated with each model and assay. In this model, the different inhibition models are listed in order of increasing complexity in the following manner: competitive, noncompetitive, uncompetitive, and mixed model. The AIC model compares two inhibition patterns at a time, the simpler model (fewer parameters) assigned "model 1" and the more complex model (more parameters) assigned "model 2," with the following equation:

$$\Delta AIC = N \cdot \ln \frac{SS2}{SS1} + 2\Delta DF = AIC_1 - AIC_2 \quad (24)$$

in which SS1 and SS2 refers to sum of the square of the scatter about the fit in inhibition models 1 and 2 and  $\Delta DF$ , the difference in the degrees of freedom due to the parameters associated with the inhibition models. The simpler model is expected to have bigger/more scatter and higher degree of freedom; therefore, the  $\ln \frac{SS2}{SS1}$  term is expected to be negative and the  $\Delta DF$  term, positive. If the  $\Delta AIC$  is negative, it would indicate that the scatter in the simpler model 1 was greater than expected thus model 2 would be a better fit, and if the  $\Delta AIC$  is positive, the opposite would be true and model 1 would be a better fit. The overall probability of one model being the better fit over the other is determined by the following equation:

$$probability = \frac{e^{0.5\Delta AIC}}{1 + e^{0.5\Delta AIC}} \quad (25)$$

By repeating the AIC comparison between each of the inhibition models, the best fit can be determined, thereby identifying the mode of inhibition.

Although assaying the enzyme with various fixed inhibitor concentration and variable substrate concentration is useful in determining the mode of inhibition and the binding affinity of the inhibitor to the enzyme, it is a laborious and time-consuming process. To quickly determine whether a compound is inhibiting, the enzyme is assayed at fixed substrate concentration and variable inhibitor concentration. The kinetics data from this test shows the potency of the inhibitor as the concentration of the inhibitor required to reduce the enzyme initial rate by half, or the  $IC_{50}$  value; however, the  $IC_{50}$  value alone cannot be used to determine the mechanistic mode of inhibition or the binding affinity of the inhibitor for the enzyme. The  $IC_{50}$  value can be calculated by the following equation:

$$V = \frac{V_{max} - V_{min}}{\left(1 + \frac{[I]^h}{IC_{50}^h}\right)} \quad (26)$$

in which  $V_{max}$  and  $V_{min}$  refers to the starting and the minimum activities, respectively;  $[I]$ , the inhibitor concentration; and  $h$ , the hill constant (Figure 14).<sup>54</sup>

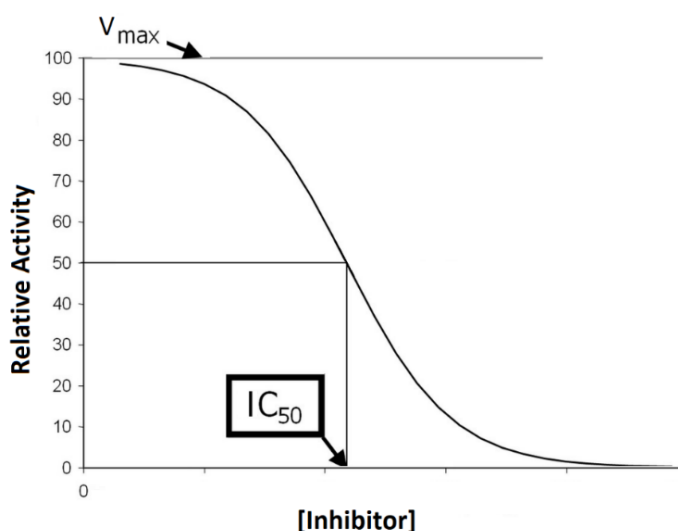


**Figure 14. Representative  $IC_{50}$  curve.** The enzyme rate with no inhibitor is the baseline, denoted  $V_{max}$ . The concentration of the inhibitor required to reach half  $V_{max}$  rate is  $IC_{50}$ .

Under competitive mode of inhibition, the  $K_i$  and the  $IC_{50}$  values are related by:

$$K_i = \frac{IC_{50}}{\left(1 + \frac{S}{K_m}\right)} \quad (27)$$

under uncompetitive mode:

$$K_i = \frac{IC_{50}}{\left(1 + \frac{K_m}{S}\right)} \quad (28)$$

and under noncompetitive mode:

$$K_i = IC_{50} \quad (29)$$

However, if a compound were to bind at an allosteric site and alter the enzyme structure to promote product release (increase  $k_{cat}$  and maybe decrease  $K_m$ ) or substrate binding (decrease  $K_m$ ), the enzymatic rate would increase. If the enzyme is assayed with fixed concentration of the substrate and variable concentration of the agonist,  $EC_{50}$  is the concentration of the activator at which the enzyme rate is half way between the baseline and the maximum. and this agonistic effect would be modeled by the  $EC_{50}$  equation:

$$V = V_{min} + \frac{[A]^h \cdot (V_{max} - V_{min})}{([A]^h + EC_{50}^h)} \quad (30)$$

where  $V_{min}$  and  $V_{max}$  refers to the starting and the maximum rates, respectively;  $[A]$ , the activator concentration; and  $h$ , the hill constant (Figure 15).<sup>55</sup>

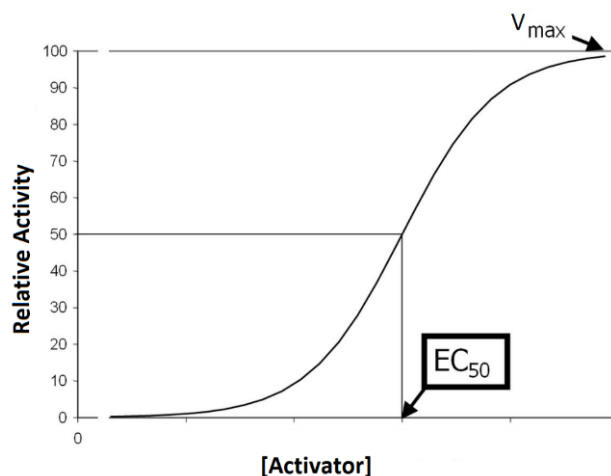


**Figure 15. Representative EC<sub>50</sub> curve.** The enzyme rate with no activator is the baseline and the maximum enzyme rate reached with addition of the activator is denoted  $V_{\max}$ . The concentration of the activator required to reach halfway between the baseline and  $V_{\max}$  is EC<sub>50</sub>.

### Thesis objective

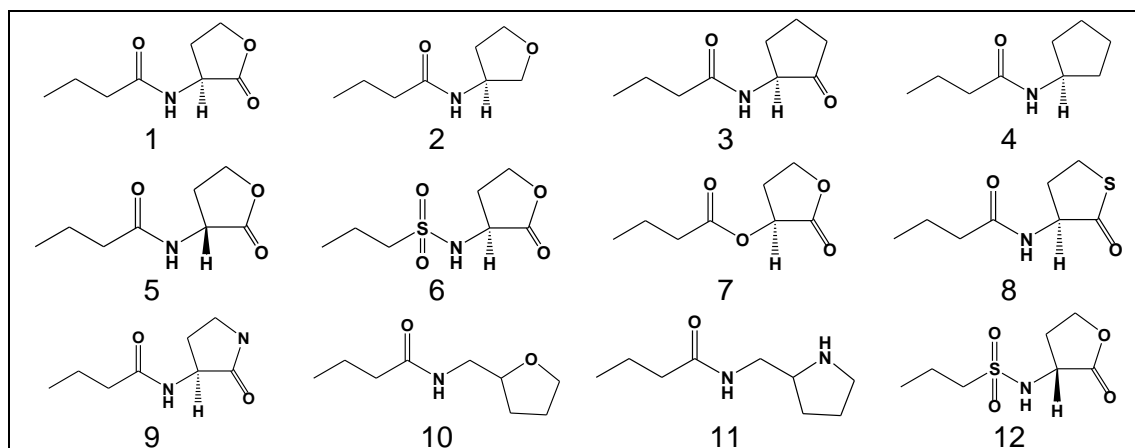
The objective of this thesis is to determine how altering the acyl-chain, chirality, and the head-group polarity of native AHL signal molecule changes the activity of RhII to determine the moieties of greatest importance and understand the mechanism of their effect.

The native AHL product, butanoyl-L-homoserine lactone, was used as the control. The L-homoserine lactone headgroup alteration was the focus of the first generation of AHL analogs (compounds 1-12; Table 2). Modifications to the lactone ring (compounds: 2-4, 8-12), the chirality (compounds: 5, 12), and the tail-headgroup linkage (compounds: 6, 7, 10-12). Variations in the acyl-chains were introduced in the next generation of AHL analogs (Table 3) which was combined with the lessons learned from the first generation of AHL derivative to target headgroup hydrophobicity with thiolactone, cyclopentyl, and non-lactone compounds (compounds 8, 43-64, 76, 77; 4, 65-68; 2-3, 9-11, 69-73; 76-77; Table 4, 5), D vs L headgroup chirality (compounds 5, 28-36; 12, 41-42; 56-64, 75, 77;

Table 4), sulfonamide linkage (compounds 6, 37-40; 12, 41-42; Table 4), and acyl-chain length and substitution at the C3 position (Compounds 13-55, 57-68, 70-73, 78-82; Table 4, 5). The acyl-chain effects were further correlated by testing RhII activity with acyl-ACP substrates of varying acyl-chain moieties (compounds 83-87; Table 4; Figure 16) and testing the activity in the presence of alkyl-ACP (inactive acyl-ACP analogs; compounds 88-91; Table 6; Figure 16). Finally, the importance of the ACP moiety in binding was tested by observing RhII activity in the presence of alkyl-CoAs (compounds 92-94; Table 4; Figure 16).

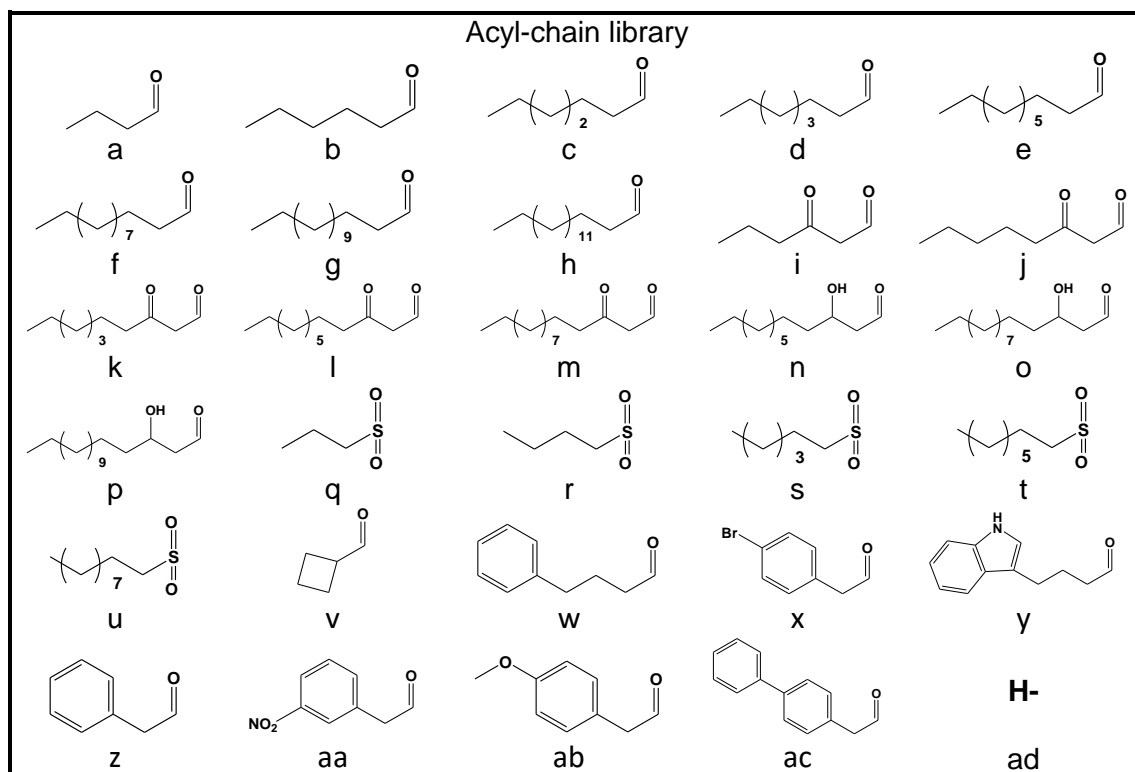
This is the first study to test the effects of modified AHLs on AHL synthases. The work described in this thesis is the basis upon which future of rational inhibitor design can be based.

**Table 2. Structures of 1<sup>st</sup> generation AHL-based small molecules tested for RhII inhibition.**

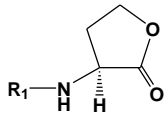
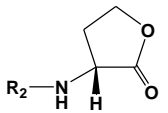
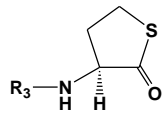
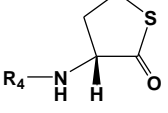
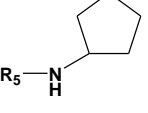




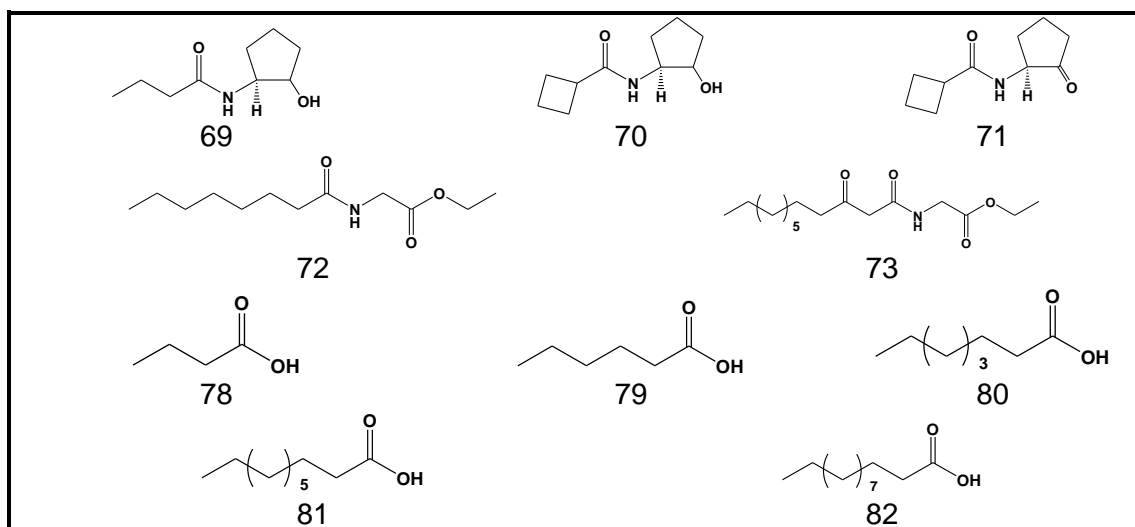
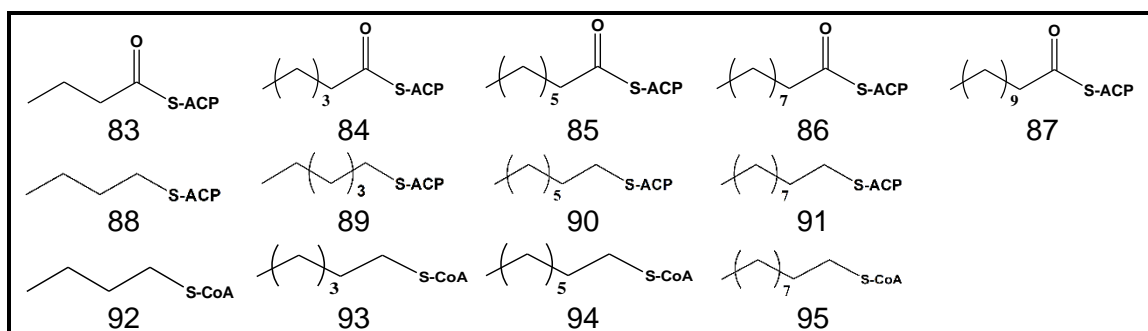
**Table 3. Variations in the acyl-chains for 2<sup>nd</sup> generation of AHL-based small molecules tested for RhII inhibition.**



**Table 4.** 2<sup>nd</sup> generation of AHL-based small molecules tested for RhII inhibition.<sup>a</sup>

L-HSL		D-HSL		LTL	
					
Compound	R <sub>1</sub>	Compound	R <sub>2</sub>	Compound	R <sub>3</sub>
1	a	5	a	8	a
6	q	12	r	43	b
13	b	28	b	44	c
14	c	29	d	45	d
15	d	30	v	46	f
16	e	31	w	47	v
17	f	32	x	48	z
18	g	33	y	49	x
19	h	34	i	50	aa
20	i	35	j	51	ab
21	j	36	l	52	ac
22	k	41	s	53	i
23	l	42	u	54	j
24	m	75	ad	55	l
25	n			76	ad
26	o				
27	p				
37	r			Cyclopentyl	
38	s				
39	t	Compound	R <sub>4</sub>	Compound	R <sub>5</sub>
40	u	56	a	65	l
74	ad	57	b	66	v
		58	d	67	z
		59	e	68	aa
		60	f		
		61	i		
		62	j		
		63	k		
		64	l		
		77	ad		

<sup>a</sup> a = letter notations for R-groups refer to structures listed in Table 3

**Table 5. Nonlactone derivatives tested for RhlI inhibition****Table 6. Acyl-ACP, alkyl-ACP, and alkyl-CoA derivatives**

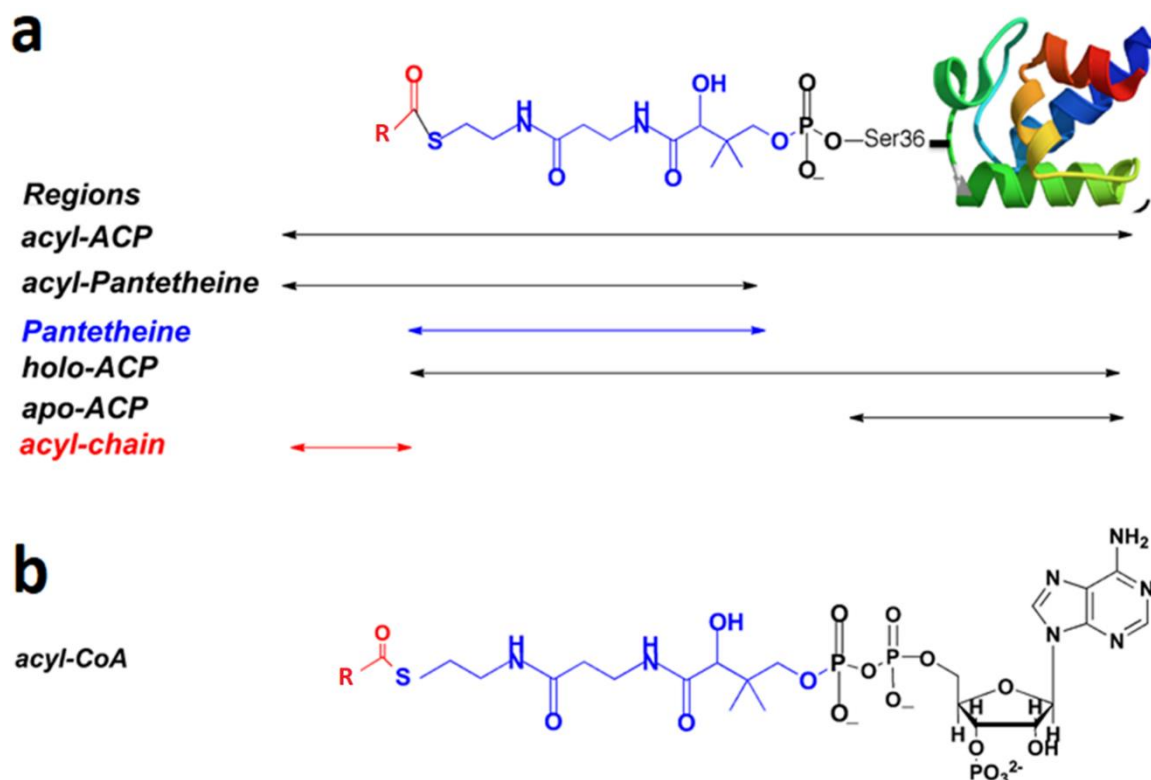


**Figure 16. Structures of Acyl-ACP and CoA.** (a) Apo-ACP is a relatively small protein made up of four helices. When apo-ACP is linked with a pantetheine linker, it is called holo-ACP. Acylated holo-ACPs are called acyl-ACPs. (b) Free coenzyme A consists of a nucleotide connected to the pantetheine linker. Acylated CoAs are called acyl-CoAs.

## CHAPTER TWO: MATERIALS AND METHODS

### Materials and Equipment

The following reagents were purchased from Sigma Aldrich: (*S*)-(+)- $\alpha$ -methoxyphenylacetic acid (MPA), 2-(*N*-morpholino)ethanesulfonic acid hydrate (MES), 2,2-dimethyl-1,3-dioxane-4,6-dione (Meldrum's acid), 2,6-dichloroindophenol (DCPIP), 4-(2-hydroxyethyl)piperazine-1-ethanesulfonic acid (HEPES), ammonium sulfate, D-homoserine lactone hydrochloride, DL-homocysteine thiolactone, ethylenediaminetetraacetic acid (EDTA), glycerol, L-homoserine lactone hydrochloride, magnesium sulfate anhydrous (MgSO<sub>4</sub>), maltose, *N*-(3-dimethylaminopropyl)-*N'*-ethylcarbodiimide hydrochloride (EDC), *N*-hydroxysuccinimide, *N* <sub>$\alpha$</sub> -tosyl-L-lysine chloromethyl ketone hydrochloride (TLCK), phenylmethanesulfonyl fluoride (PMSF), protamine sulfate, *S*-(5'-adenosyl)-L-methionine chloride (SAM), sucrose, toluene, trichloroacetic acid, coenzyme A free acid (CoA-SH), butanoyl-coenzyme A (C4-CoA), hexanoyl-coenzyme A (C6-CoA), octanoyl-coenzyme A (C8-CoA), decanoyl-coenzyme A (C10-CoA), dodecanoyl-coenzyme A (C12-CoA), deoxyribonuclease I (DNase), ribonuclease A (RNase), lysozyme, ampicillin, kanamycin, chloramphenicol, kanamycin, spectinomycin, and streptomycin. Thermo Fisher Scientific supplied the following: 2-propanol (IPA), acetonitrile, agar, ammonium acetate, bacterial protein extraction reagent (B-PER), chloroform, diethyl ether, dimethylformamide (DMF), dimethyl sulfoxide (DMSO), ethyl acetate, hydrochloric acid (HCl), imidazole, isopropyl  $\beta$ -D-1-thiogalactopyranoside (IPTG), Lennox broth, manganese sulfate (MnSO<sub>4</sub>), methanol,

hexane, potassium carbonate, silica, sodium bicarbonate, tricine, and tris base. Butyric acid, hexanoic acid, octanoic acid, decanoic acid, dodecanoic acid, and trifluoroacetic acid (TFA) were obtained from Acros Organics. Alfa Aesar provided bromobutane, bromohexane, bromooctane, bromodecane, magnesium chloride (MgCl<sub>2</sub>), and triethyl amine. The 3kD and 10kD spin filter columns and celite were purchased from EMD. Amylose resin, ethanol, and 0.22 μm sample filters were provided by NEB, Ultra Pure, and Costar, respectively. Dr. Peter Tipton (University of Missouri, Columbia), Dr. E. Peter Greenberg (University of Washington), and Dr. Michael Burkart (University of California-San Diego) provided clones for purifying RhII, apo-ACP, and *Sfp*, respectively. *Sfp* was purified by Levi Mitchell and Nhu Lam (Both from Nagarajan lab, Boise State University). Various AHL analogs were supplied by Dr. Helen Blackwell (University of Wisconsin, Madison; compounds 1, 3-9, 12-55, 65-73), Dr. Eric Brown (Boise State University; compounds 2, 10, 11), and Neil Rexrode (Nagarajan lab, Boise State University; compounds 34, 36).

All UV-Vis spectrophotometric data was collected with Thermo Scientific Evolution 260 Bio UV-Vis spectrophotometer using Fisher 1 cm path length quartz cuvettes (14-385-928C). HPLC data was obtained with Thermo Scientific Dionex UltiMate 3000 UHPLC<sup>+</sup> focused HPLC with Dionex UltiMate 3000 Automated Fraction Collector using Thermo Scientific Hypersil Gold C18 reverse-phase UHPLC column (25002-054630) or Thermo Scientific Hypersil Gold C18 reverse-phase preparative column (25005-159070). All mass spectrometry data was collected with Bruker maXis Quadrupole Time-of-Flight (QTOF) mass spectrometry and analyzed with the Bruker

Compass Data Analysis software. All the kinetics data were processed using GraphPad Prism 7.

## Methods

### HPLC Methods

HPLC and the fraction collector was used to isolate and collect alkyl-CoA and to monitor the synthesis and purity of acyl-ACP synthesis. Solvent “A” consisted of 25 mM ammonium acetate pH 5 solution. Solvent “B” is acetonitrile (ACN) + 0.1% trifluoroacetic acid (TFA), and solvent “C” is H<sub>2</sub>O + 0.1% TFA. To isolate alkyl-CoA, the filtered sample was injected into a C18 reverse-phase preparatory column equilibrated with the initial solvent condition of 95.0% solvent A and 5.0% solvent B. The analyte was analyzed using a solvent gradient of 95.0% solvent A and 5.0% solvent B to 30.0% solvent A and 70.0% solvent B over 11 minutes at a flow rate of 3.0 mL/min (Table 7). To monitor acyl-ACP synthesis, the analyte sample was injected into a C18 reverse-phase UHPLC column equilibrated with 25.0% solvent B and 75.0% solvent C. The acyl-ACP peaks were separated from apo-ACP peak with a solvent gradient of 25.0% solvent B and 75.0% solvent C to 75.0% solvent B and 25.0% solvent C over 10 minutes at a flow rate of 600  $\mu$ L/min (Table 8). Due to the similar retention time for hexanoyl/hexyl-ACP and apo-ACP, a shallower gradient of 25.0% solvent B and 75.0% solvent C to 75.0% solvent B and 25.0% solvent C over 60 minutes at a flow rate of 200  $\mu$ L/min was used (Table 9). The column and the sample loop were washed with methanol for 5 minutes between each run.

**Table 7. Alkyl-CoA separation method<sup>a</sup>**

Time (min)	Flow (mL/min)	%A <sup>b</sup>	%B <sup>c</sup>
-3.00	3.000	95.0	5.0
0.00 <sup>d</sup>	3.000	95.0	5.0
1.00	3.000	95.0	5.0
11.00	3.000	30.0	70.0
a = Preparatory column			
b = 25 mM ammonium acetate pH 5			
c = acetonitrile (ACN) + 0.1% trifluoroacetic acid (TFA)			
d = sample injection at Time 0.00			

**Table 8. ACP separation method<sup>a</sup>**

Time (min)	Flow (mL/min)	%B <sup>b</sup>	%C <sup>c</sup>
-3.00	0.600	25.0	75.0
0.00 <sup>d</sup>	0.600	25.0	75.0
10.00	0.600	75.0	25.0
a = UHPLC column			
b = ACN + 0.1% TFA			
c = H <sub>2</sub> O + 0.1% TFA			
d = sample injection at Time 0.00			

**Table 9. C6-ACP separation method<sup>a</sup>**

Time (min)	Flow (mL/min)	%B <sup>b</sup>	%C <sup>c</sup>
-3.00	0.200	25.0	75.0
0.00 <sup>d</sup>	0.200	25.0	75.0
60.00	0.200	75.0	25.0
a = UHPLC column			
b = ACN + 0.1% TFA			
c = H <sub>2</sub> O + 0.1% TFA			
d = sample injection at time 0.00			

### RhII Purification

RhII was purified via a previously described method with modifications.<sup>52</sup> *E. coli* with RhII plasmid was grown on an agar plate (20 g Lennox broth and 10 g agar per 1 L of medium) with ampicillin (100 µg/mL) for 12 hours at 37°C. A colony was isolated and was used to inoculate 25 mL of Lennox broth with ampicillin (100 µg/mL) and incubated



at 37°C with shaking (225 rpm) for 8-12 hours or until visible turbidity. The “mini-growth” was then transferred over to 1 L of Lennox broth (20 g broth/L) with ampicillin (100 µg/mL). The broth was incubated with shaking (225 rpm) at 37°C. When the OD<sub>600</sub> value reached 0.6-0.8, IPTG was added to 0.5 mM final concentration to promote protein expression. The cell culture was incubated for 3 hours at room temperature. The growth media was then spun down at 5,000 x g at 4°C for 15 minutes to collect cell paste. The cell pellet was resuspended in “Buffer A,” which is composed of 200 mL of 50 mM Tris-HCl, pH 7.5, containing 0.2 M NaCl, 1 mM ethylenediaminetetraacetic acid (EDTA), 0.1 mM phenylmethanesulfonyl fluoride (PMSF), 0.1 mM *N*<sub>α</sub>-tosyl-L-lysine chloromethyl ketone hydrochloride (TLCK), 0.4 M sucrose, and 2.5% (v/v) glycerol. The resuspended mixture was then lysed via sonication at 15,000 psi. The lysate was spun down for 40 minutes at 10,000 x g and at 4°C. Protamine sulfate was added to the supernatant to a final concentration of 6 mg/ g of cell pellet to cause nucleic acids to precipitate. The nucleic acid precipitates were removed via centrifugation for 20 minutes at 10,000 x g and at 4°C. The supernatant was then loaded onto an amylose column that has been equilibrated with 5x bed volume with buffer A. The column was washed with 5x bed volume with buffer A. RhII was eluted out using buffer A with 10 mM maltose added. The presence and purity of RhII was checked with SDS-PAGE gel electrophoresis. The protein sample was concentrated using 10 kD spin filter, the concentration checked via UV-Vis spectrophotometry ( $\epsilon_{280} = 107510 \text{ M}^{-1}\text{cm}^{-1}$ ), and stored in buffer A with 20% glycerol at -80 °C.

### Apo-ACP Purification

Apo-ACP was purified with a well-established method.<sup>22</sup> *E. coli* DK574 with pJT94 was grown on an agar plate (20 g Lennox broth and 10 g agar per 1 L of medium) with kanamycin (25 µg/mL), streptomycin (50 µg /mL), spectinomycin (50 µg /mL), and chloramphenicol (25 µg /mL) for 12 hours at 37°C. An isolated colony was used to inoculate 25 mL of Lennox broth with kanamycin (25 µg/mL), streptomycin (50 µg /mL), spectinomycin (50 µg /mL), and chloramphenicol (25 µg /mL) and incubated at 37°C with shaking (225 rpm) for 8-12 hours or until visible turbidity. The “mini-growth” was then transferred over to 1 L of Lennox broth (20 g broth/L) with kanamycin (25 µg/mL), streptomycin (50 µg /mL), spectinomycin (50 µg /mL), and chloramphenicol (25 µg /mL) and incubated at 37°C with stirring until OD<sub>600</sub> value reached 0.6-0.8. IPTG was then added to a final concentration of 1 mM to promote protein expression. The cell culture was incubated at 37°C for a further 3 hours then collected via centrifugation at 5,000 x g for 15 minutes. The cell paste was resuspended in 2 mL of B-PER reagent, 1 mL of lysozyme (2 mg/mL) 20 µL each of DNase (1 mg/mL) and RNase (1 mg/mL) and 25 µL of phenylmethylsulfonyl fluoride (13 mg/750 µL 2-propanol) to lyse the cells and their nucleic acids. The lysate mixture was incubated with gentle shaking at room temperature for 20 minutes. The lysate was spun down for 30 minutes at 20,000 x g and at 4°C. The supernatant was collected and was added MgCl<sub>2</sub> and MnSO<sub>4</sub> to final concentrations of 25 mM and 1.2 mM, respectively and incubated at 37°C for 4 hours. Extraneous proteins were precipitated by slow addition of 2-propanol to 50% initial volume while on ice. The precipitates were removed via centrifugation at 14,000 x g for 30 minutes. The supernatant was stirred with 2 g of DE52 diaminoethyl cellulose resin

overnight at 4°C. The mixture was packed in to a column and washed with 10 x bed volume with 10 mM lithium 4-morpholineethane-sulfonate (MES) pH 6.1 and 0.25 mM LiCl. The protein was eluted out using 10 mM lithium MES pH 6.1 and 0.5 M LiCl. The presence and purity of apo-ACP was checked via Tris/Tricine SDS-PAGE gel electrophoresis. Apo-ACP samples were pooled and the protein was precipitated with the addition of 0.02% (0.2 mg/mL) sodium deoxycholate and 5% (50 mg/mL) trichloroacetate (w/v). The mixture was incubated at 37°C with gentle shaking for 30 minutes. The mixture was then spun at 21,000 x g for 30 minutes to collect ACP pellet. The ACP pellet was resuspended in 60 mL of 0.5 M Tris-HCl pH 8.0 and concentrated using 3 kD spin filter. The concentration was determined via UV-Vis spectrophotometry ( $\epsilon_{280} = 1490 \text{ M}^{-1}\text{cm}^{-1}$ ), and stored in 10 mM MES pH 6.1 + 20 % glycerol at -80 °C.

#### Alkyl-CoA Synthesis

To a solution of coenzyme A, free acid (CoA-SH; 50 mg, 65.1  $\mu\text{mol}$ ) and alkyl bromide (120.2  $\mu\text{mol}$ ) in 2mL of 1:1 water:DMF, potassium carbonate was added to pH 8-9 (Figure 17). The reaction was stirred under nitrogen overnight and the completion of the reaction was tested by checking for the reduction of DCPIP by unreacted CoA-SH. The reaction mixture was diluted with water to a final volume of 5 mL and extracted with 5 mL of diethyl ether. The aqueous mixture was filtered with 0.2  $\mu\text{m}$  filter and the alkyl-CoA was isolated and collected with semi-prep HPLC using the Alkyl-CoA separation method (Table 5). Organic solvent was removed via evaporation by a gentle stream of nitrogen through the product solution and the aqueous solution was lyophilized to yield alkyl-CoA powder.

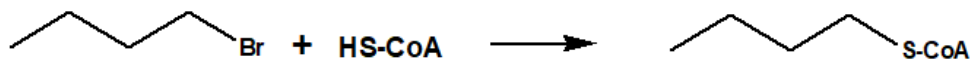


**Figure 17. Synthesis of alkyl-CoA.** Alkyl bromide was reacted with free-CoA in basic solution to produce alkyl-CoA.

**92. Butyl-Coenzyme A.** ESI-TOF: expected  $m/z$   $[M + H^+] = 824.1851$ ,

observed  $[M + H^+] = 824.1835$ . (Appendix Figures A14)

**93. Hexyl-Coenzyme A.** ESI-TOF: expected  $m/z$   $[M + H^+] = 852.2164$ ,

observed  $[M + H^+] = 852.2147$ . (Appendix Figures A15)

**94. Octyl-Coenzyme A.** ESI-TOF: expected  $m/z$   $[M + H^+] = 880.2477$ ,

observed  $[M + H^+] = 880.2444$ . (Appendix Figures A16)

**95. Decyl-Coenzyme A.** ESI-TOF: expected  $m/z$   $[M + H^+] = 908.2790$ ,

observed  $[M + H^+] = 908.2733$ . (Appendix Figures A17)

#### Alkyl-/Acyl-ACP synthesis

Alkyl-/acyl-pantetheine was transferred from CoA to apo-ACP via phosphopantetheinyl transferase (*Sfp*) catalyzed reaction (Figure 18).<sup>22</sup> The reaction mixture consisted of 50 mM Tris-HCl pH 6.8, 10 mM magnesium chloride, 600  $\mu$ M apo-ACP, 750  $\mu$ M alkyl-/acyl-CoA, and 10  $\mu$ M *Sfp*, with the CoA-substrate being the last to be added. Alkyl-/acyl-CoAs with aliphatic chains of 6 and fewer carbons were added all at once. Alkyl-/acyl-CoAs with aliphatic chains of 8 or more carbons were added in three equal portions every 15 minutes to prevent CoA precipitating and crashing out of the predominantly aqueous reaction mixture. The reaction was incubated at 37 °C and checked via HPLC every 30 minutes for completion using ACP separation method (Table 6). However, C6-ACP separation method was used to check hexyl- and hexanoyl-ACP synthesis since C6-ACP, C6-IACP, and apo-ACP have similar retention time (Table 7). For completion, reactions lasted 2 hours for C4-ACP and C4-IACP, between 4 and 5

hours for C6-ACP and C6-IACP, and 6 to 7 hours for C8- to C12-ACP and IACPs. Upon completion, ammonium sulfate was added to the reaction to 75% saturation and kept at 4 °C for 1 hour to precipitate *Sfp*.<sup>56</sup> The *Sfp* precipitates were pelleted by centrifugation at 15,000 x g for 15 minutes. The supernatant was desalted and concentrated by 3 kD spin filter spun at 5,000 x g at 4 °C. The concentration was determined via UV-Vis spectrophotometry ( $\epsilon_{280} = 1490 \text{ M}^{-1}\text{cm}^{-1}$ ), and stored in 10 mM MES pH 6.1 + 20 % glycerol at -80 °C.

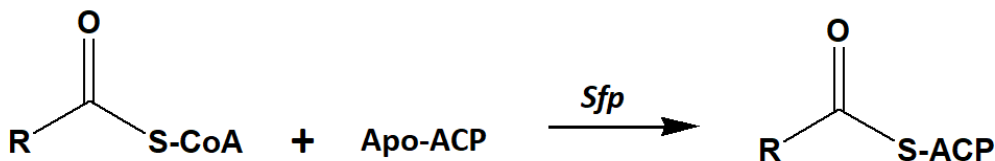


**Figure 18.** *Sfp* catalyzed acyl-pantetheine transfer reaction. *Sfp* catalyzes the transfer of pantetheine linker from a CoA to apo-ACP to produce alkyl-/acyl-ACP.

**83-87. Butanoyl-, Hexanoyl-, Octanoyl-, Decanoyl-, and Dodecanoyl-ACP.** Mass confirmed in previous work from Nagarajan laboratory.<sup>22</sup>

**88. Butyl-ACP.** ESI-TOF: expected mass = 8904.6, observed mass = 8904.3.

(Appendix Figures A10)

**89. Hexyl-ACP.** ESI-TOF: expected mass = 8932.6, observed mass = 8932.4.

(Appendix Figures A11)

**90. Octyl-ACP.** ESI-TOF: expected mass = 8960.7, observed mass = 8960.4.

(Appendix Figures A12)

**91. Decyl-ACP.** ESI-TOF: expected mass = 8988.7, observed mass = 8988.4.

(Appendix Figures A13)

### Purification of D-homocysteine thiolactone

Enantiomerically pure sample of D-homocysteine thiolactone was obtained using a published method with modification (Figure 19).<sup>57</sup> A solution of DL-homocysteine thiolactone (768.15 mg; 5.0 mmole), triethylamine (N(Et)<sub>3</sub>; 1.2 mL), *N*-hydroxysuccinimide (690.5 mg; 6 mmole), *S*-(+)-2-methoxyphenylacetic acid (MPA; 1.0 g; 6.0 mmole), and 1-ethyl-3-(3-dimethylaminopropyl)carbodiimide HCl (EDC; 1.150 g; 6 mmole) in 100 mL chloroform was stirred overnight at 4°C. This reaction resulted in the synthesis of L-homocysteine thiolactone-containing (3*S*,2'*S*)-3-(2'-methoxy-2'-phenyl-)acetamido-2-thiophenone and D-homocysteine thiolactone-containing (3*R*,2'*S*)-3-(2'-methoxy-2'-phenyl-)acetamido-2-thiophenone. The solution was then washed with water (50 mL), NaHCO<sub>3</sub> (5%, 20 mL), HCl (2M, 20 mL), and brine (saturated, 40 mL). After drying with MgSO<sub>4</sub>, the solvent was removed under low pressure. The two diastereomers were separated by silica gel column chromatography using hexane-ethyl acetate solution (7:3). The more polar, D-thiolactone-containing isomers were isolated and refluxed in ethanol-4M HCl (2:1; 15 mL) solution overnight. Ethanol was removed with rotary evaporation. Water was added to the resulting solution to make it 10 mL and washed with toluene (10 mL x 3). The aqueous layer was isolated and the solvent was removed under high vacuum. The resulting D-thiolactone-HCl mixture was recrystallized with anhydrous 2-propanol.

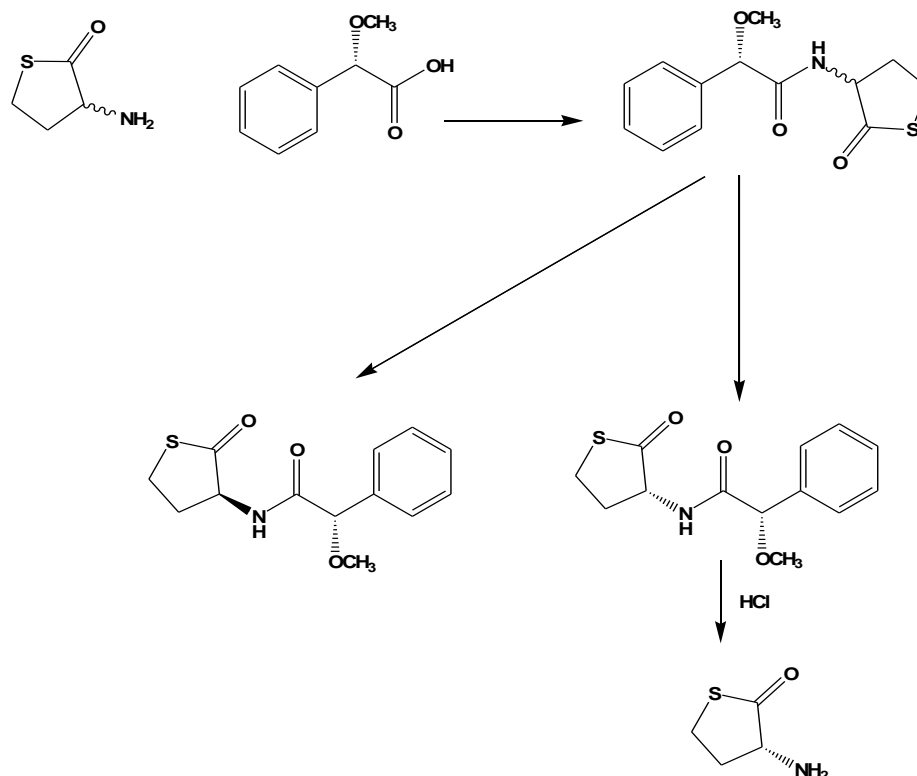


**Figure 19. Purification of pure D-homocysteine thiolactone.** A racemic mixture was acylated with MPA in an EDC-coupled reaction to form diastereomers with distinct polarity. The two diastereomers separated via silica gel column chromatography. D-Homocysteine thiolactone was obtained by removing the MPA by refluxing the compound in HCl.

**D-Homocysteine thiolactone HCl.** (comparable to literature value<sup>57</sup>) m.p. 176-178°C

$[\alpha]_D^{25}$  -36.3 (0.05 mg/mL in H<sub>2</sub>O). <sup>1</sup>H NMR (600 MHz, D<sub>2</sub>O):  $\delta$  2.10 (1H, m, 4 $\alpha$ -H), 2.62

(1H, m, 4 $\beta$ -H), 3.33 (1H, m, 5 $\alpha$ -H), 3.24 (1H, m, 5 $\beta$ -H), 4.29 (1H, s, 3-H). (Appendix

Figure B1)

#### Synthesis of N-acyl-D-homocysteine thiolactones

The D-thiolactone head-group was acylated using a previously published protocol with modification (Figure 20).<sup>43</sup> The thiolactone head-group (25 mg; 162.7  $\mu$ mole) was stirred overnight (12 hours) at room temperature with DCC (33.6 mg; 162.7  $\mu$ mole), N-hydroxysuccinimide (18.7 mg; 162.7  $\mu$ mole), triethylamine (50  $\mu$ L) in acetonitrile (10 mL) with the appropriate carboxylic acid (162.7  $\mu$ mole: butyric acid: 14.9  $\mu$ L; hexanoic

acid: 20.6  $\mu$ L; octanoic acid: 25.8  $\mu$ L; decanoic acid: 28 mg; dodecanoic acid: 32.6 mg).

The resulting mixture was cooled to 4 °C for an hour and then filtered with celite to remove *N,N'*-dicyclohexylurea precipitate. The filtrate solution was washed with water, HCl (2M), NaHCO<sub>3</sub> (saturated), and brine (saturated) (3x10 mL each). After drying with MgSO<sub>4</sub>, and removing the solvent under low pressure, the product was purified with a silica gel column using 7:3 hexane: ethyl acetate eluent.



**Figure 20. Acylation of D-thiolactone headgroup.** D-thiolactone headgroup was acylated by a DCC-coupled reaction in acetonitrile. Urea byproduct was removed via filtration and excess carboxylic acid was removed via silica gel column chromatography.

**56. *N*-Butanoyl-D-homocysteine thiolactone.** <sup>1</sup>H NMR (600 MHz, CDCl<sub>3</sub>):  $\delta$  0.93 (3H, t,  $J = 7.3$  Hz, CH<sub>3</sub>), 1.65 (2H, m, CH<sub>2</sub>), 1.90 (1H, m, -lac), 2.20, (2H, dt,  $J = 7.3, 3.9$  Hz, CH<sub>2</sub>), 2.93 (1H, m, -lac), 3.23 (1H, ddd,  $J = 11.4, 4.5, 1.0$  Hz, -lac), 3.33 (1H, ddd,  $J = 11.7, 11.7, 5.1$  Hz, -lac), 4.49 (1H, ddd,  $J = 12.9, 6.4, 6.4$  Hz, -lac), 5.92 (1H, s, NH); <sup>13</sup>C NMR (CDCl<sub>3</sub>, 600 MHz):  $\delta$  13.9, 19.2, 27.8, 32.4, 38.5, 59.7, 173.7, 205.8; ESI-TOF: expected  $m/z$  [M + H<sup>+</sup>] = 188.0734, observed [M + H<sup>+</sup>] = 188.0763. (Appendix Figures A1, B2-B6)

**57. *N*-Hexanoyl-D-homocysteine thiolactone.** <sup>1</sup>H NMR (600 MHz, CDCl<sub>3</sub>):  $\delta$  0.87 (3H, t, CH<sub>3</sub>), 1.29 (4H, m CH<sub>2</sub>), 1.64 (2H, m, CH<sub>2</sub>), 1.89 (1H, m, -lac), 2.22, (2H, dt,  $J = 7.5, 3.5$  Hz, CH<sub>2</sub>), 2.97 (1H, m, -lac), 3.24 (1H, ddd,  $J = 11.4, 6.9, 1.1$  Hz, -lac), 3.34 (1H, ddd,  $J = 11.7, 11.7, 5.3$  Hz, -lac), 4.48 (1H, ddd,  $J = 12.8, 6.4, 6.4$  Hz, -lac), 5.83 (1H, s, NH); <sup>13</sup>C NMR (CDCl<sub>3</sub>, 600 MHz):  $\delta$  13.9, 22.4, 25.2, 27.6, 31.4, 32.2, 36.4, 59.6,



173.7, 205.6; ESI-TOF: expected  $m/z$   $[M + H^+] = 216.1047$ , observed  $[M + H^+] = 216.1099$ . (Appendix Figures A2, B7-B9)

**58. *N*-Octanoyl-*D*-homocysteine thiolactone.**  $^1\text{H}$  NMR (600 MHz,  $\text{CDCl}_3$ ):  $\delta$  0.86 (3H, t,  $J = 6.9$  Hz,  $\text{CH}_3$ ), 1.26 (8H, m  $\text{CH}_2$ ), 1.62 (2H, m,  $\text{CH}_2$ ), 1.88 (1H, m, -lac), 2.22, (2H, dt,  $J = 7.5, 3.5$  Hz,  $\text{CH}_2$ ), 2.96 (1H, m, -lac), 3.23 (1H, ddd,  $J = 11.3, 4.4, 0.9$  Hz, -lac), 3.34 (1H, ddd,  $J = 11.7, 11.7, 5.2$  Hz, -lac), 4.48 (1H, ddd,  $J = 12.9, 6.4, 6.4$  Hz, -lac), 5.82 (1H, s, NH);  $^{13}\text{C}$  NMR ( $\text{CDCl}_3$ , 600 MHz):  $\delta$  14.3, 22.8, 25.7, 27.8, 29.4, 29.9, 31.9, 32.5, 36.7, 59.8, 173.9, 205.8; ESI-TOF: expected  $m/z$   $[M + H^+] = 244.1360$ , observed  $[M + H^+] = 244.1405$ . (Appendix Figures A3, B10-B14)

**59. *N*-Decanoyl-*D*-homocysteine thiolactone.**  $^1\text{H}$  NMR (600 MHz,  $\text{CDCl}_3$ ):  $\delta$  0.85 (3H, t,  $J = 6.9$  Hz,  $\text{CH}_3$ ), 1.25 (12H, m  $\text{CH}_2$ ), 1.61 (2H, m,  $\text{CH}_2$ ), 1.87 (1H, m, -lac), 2.21, (2H, dt,  $J = 7.4, 3.6$  Hz,  $\text{CH}_2$ ), 2.95 (1H, m, -lac), 3.23 (1H, ddd,  $J = 11.4, 4.5, 1.1$  Hz, -lac), 3.34 (1H, ddd,  $J = 11.5, 11.5, 5.1$  Hz, -lac), 4.48 (1H, ddd,  $J = 12.7, 6.3, 6.3$  Hz, -lac), 5.86 (1H, s, NH);  $^{13}\text{C}$  NMR ( $\text{CDCl}_3$ , 600 MHz):  $\delta$  14.0, 22.6, 25.5, 27.6, 29.2, 29.3, 29.4, 31.8, 32.2, 33.9, 36.4, 59.5, 173.6, 205.5; ESI-TOF: expected  $m/z$   $[M + H^+] = 272.1673$ , observed  $[M + H^+] = 272.1720$ . (Appendix Figures A4, B15-B19)

**60. *N*-Dodecanoyl-*D*-homocysteine thiolactone.**  $^1\text{H}$  NMR (600 MHz,  $\text{CDCl}_3$ ):  $\delta$  0.86 (3H, t,  $J = 6.8$  Hz,  $\text{CH}_3$ ), 1.25 (16H, m  $\text{CH}_2$ ), 1.62 (2H, m,  $\text{CH}_2$ ), 1.88 (1H, m, -lac), 2.21, (2H, dt,  $J = 7.5, 3.4$  Hz,  $\text{CH}_2$ ), 2.97 (1H, m, -lac), 3.23 (1H, ddd,  $J = 11.2, 4.4, 0.8$  Hz, -lac), 3.34 (1H, ddd,  $J = 11.7, 11.7, 5.3$  Hz, -lac), 4.47 (1H, ddd,  $J = 12.8, 6.2, 6.2$  Hz, -lac), 5.81 (1H, s, NH);  $^{13}\text{C}$  NMR ( $\text{CDCl}_3$ , 600 MHz):  $\delta$  14.1, 22.6, 24.9, 25.5, 27.6, 29.2, 29.3, 29.4, 29.6, 31.9, 32.2, 33.9, 36.4, 59.6, 173.6, 205.5; ESI-TOF: expected  $m/z$   $[M + H^+] = 300.1986$ , observed  $[M + H^+] = 300.2042$ . (Appendix Figures A5, B20-B24)

### Synthesis of *N*-(3-Oxoacyl)-D-homocysteine thiolactones

The synthesis of *N*-(3-oxoacyl)-D-homocysteine thiolactones has been developed previously (Figure 21).<sup>58</sup> A solution of Meldrum's acid (300.0 mg; 2.1 mmole), DCC (515.4 mg; 2.5 mmole), 4-(dimethylamino)pyridine (279.7 mg; 2.3 mmole), and the appropriate carboxylic acid (2.1 mmole: butyric acid: 191.0  $\mu$ L; hexanoic acid: 262.8  $\mu$ L; octanoic acid: 329.9  $\mu$ L; decanoic acid: 358.6 mg) in dichloromethane (10 mL) was stirred at room temperature overnight. The resulting mixture was cooled to 4 °C for an hour and then filtered with celite to remove *N,N'*-dicyclohexylurea precipitate. The filtrate was washed with HCl (2M, 20 mL). After drying with MgSO<sub>4</sub>, the solvent was removed under low pressure. A solution of D-homocysteine thiolactone HCl (30.0 mg; 0.2 mmole), triethylamine (35  $\mu$ L) and the appropriate acylated Meldrum's acid (0.2 mmole) in acetonitrile (10 mL) was prepared. The solution was stirred at room temperature for 1 hour and then refluxed overnight. The solvent was removed under low pressure and the product was then dissolved in ethyl acetate (10 mL). The solution was washed with NaHCO<sub>3</sub> (saturated), KHSO<sub>4</sub> (1M), and brine (saturated) (10 mL x 3 each). After drying with MgSO<sub>4</sub>, and removing the solvent under low pressure, the product was purified with a silica gel column using 7:3 hexane: ethyl acetate eluent.

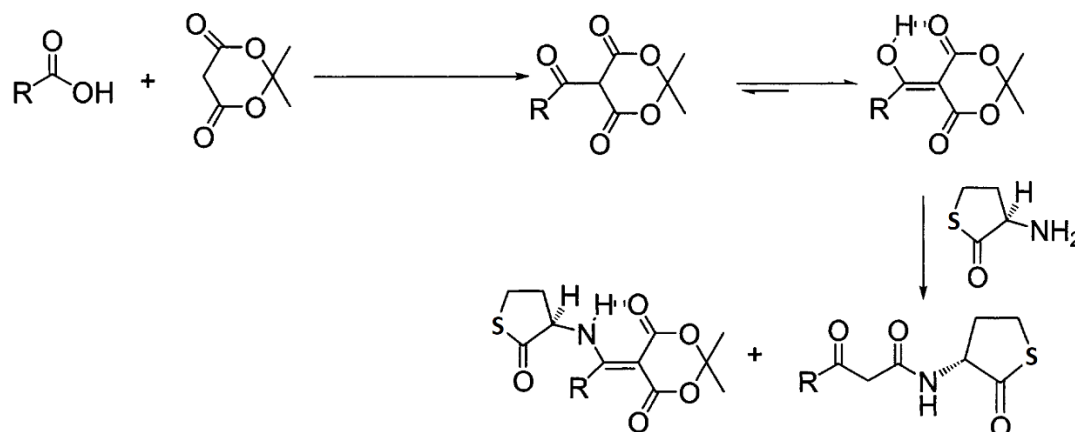


**Figure 21. Synthesis and purification of 3oxoacyl-D-thiolactones.** Carboxylic acid was attached to Meldrum's acid via DCC-coupled reaction. The acylated Meldrum's acid was reacted with thiolactone headgroup under heat. This reaction produced 3oxoacyl-thiolactone product and small amounts of a side product, which was removed via silica gel column chromatography.

**61. *N*-(3-Oxohexanoyl)-D-homocysteine thiolactone.** <sup>1</sup>H NMR (600 MHz, CDCl<sub>3</sub>): δ 0.91 (3H, t, *J* = 7.4 Hz, CH<sub>3</sub>), 1.61 (2H, m, CH<sub>2</sub>), 1.99 (1H, m, -lac), 2.49, (2H, t, *J* = 7.4 Hz, CH<sub>2</sub>), 2.83 (1H, m, -lac), 3.24 (1H, ddd, *J* = 11.5, 6.9, 1.0 Hz, -lac), 3.33 (1H, ddd, *J* = 11.7, 11.7, 5.2 Hz, -lac), 3.43 (2H, s, CH<sub>2</sub>) 4.56 (1H, ddd, *J* = 12.9, 6.8, 6.8 Hz, -lac), 7.43 (1H, s, NH); <sup>13</sup>C NMR (CDCl<sub>3</sub>, 600 MHz): δ 13.7, 17.1, 27.7, 31.8, 46.0, 48.6, 59.5, 166.4, 204.7, 206.6; ESI-TOF: expected *m/z* [M + H<sup>+</sup>] = 230.0845, observed [M + H<sup>+</sup>] = 230.0896. (Appendix Figures A6, B25-B29)

**62. *N*-(3-Oxoctanoyl)-D-homocysteine thiolactone.** <sup>1</sup>H NMR (600 MHz, CDCl<sub>3</sub>): δ 0.86 (3H, t, *J* = 7.1 Hz, CH<sub>3</sub>), 1.26 (4H, m CH<sub>2</sub>), 1.56 (2H, m, CH<sub>2</sub>), 1.99 (1H, m, -lac), 2.50, (2H, t, *J* = 7.4 Hz, CH<sub>2</sub>), 2.82 (1H, m, -lac), 3.23 (1H, ddd, *J* = 11.4, 7.0, 1.1 Hz, -lac), 3.33 (1H, ddd, *J* = 11.7, 11.7, 5.2 Hz, -lac), 3.43 (2H, s, CH<sub>2</sub>), 4.56 (1H, ddd, *J* = 13.0, 6.6, 6.6 Hz, -lac), 7.45 (1H, s, NH); <sup>13</sup>C NMR (CDCl<sub>3</sub>, 600 MHz): δ 14.0, 22.6, 23.3, 27.7, 31.3, 31.7, 44.1, 48.6, 59.5, 166.4, 204.7, 206.7; ESI-TOF: expected *m/z* [M + H<sup>+</sup>] = 244.1360, observed [M + H<sup>+</sup>] = 244.1433. (Appendix Figures A7, B30-B34)

**63. *N*-(3-Oxodecanoyl)-D-homocysteine thiolactone.**  $^1\text{H}$  NMR (600 MHz,  $\text{CDCl}_3$ ):  $\delta$  0.84 (3H, t,  $J = 7.1$  Hz,  $\text{CH}_3$ ), 1.24 (8H, m  $\text{CH}_2$ ), 1.55 (2H, m,  $\text{CH}_2$ ), 1.99 (1H, m, -lac), 2.49, (2H, t,  $J = 7.4$  Hz,  $\text{CH}_2$ ), 2.81 (1H, m, -lac), 3.23 (1H, ddd,  $J = 11.4, 7.1, 1.0$  Hz, -lac), 3.32 (1H, ddd,  $J = 11.8, 11.8, 5.3$  Hz, -lac), 3.42 (2H, s,  $\text{CH}_2$ ), 4.56 (1H, ddd,  $J = 12.9, 6.6, 6.6$  Hz, -lac), 7.46 (1H, s, NH);  $^{13}\text{C}$  NMR ( $\text{CDCl}_3$ , 600 MHz):  $\delta$  14.2, 22.8, 23.6, 27.7, 29.14, 29.17, 31.7, 31.8, 44.0, 48.6, 59.4, 166.5, 204.7, 206.6; ESI-TOF: expected  $m/z$   $[\text{M} + \text{H}^+] = 286.1471$ , observed  $[\text{M} + \text{H}^+] = 286.1472$ . (Appendix Figures A8, B35-B39)

**64. *N*-(3-Oxododecanoyl)-D-homocysteine thiolactone.**  $^1\text{H}$  NMR (600 MHz,  $\text{CDCl}_3$ ):  $\delta$  0.85 (3H, t,  $J = 7.1$  Hz,  $\text{CH}_3$ ), 1.24 (12H, m  $\text{CH}_2$ ), 1.56 (2H, m,  $\text{CH}_2$ ), 1.99 (1H, m, -lac), 2.50, (2H, t,  $J = 7.3$  Hz,  $\text{CH}_2$ ), 2.83 (1H, m, -lac), 3.24 (1H, ddd,  $J = 11.2, 6.9, 1.0$  Hz, -lac), 3.33 (1H, ddd,  $J = 11.7, 11.7, 5.2$  Hz, -lac), 3.43 (2H, s,  $\text{CH}_2$ ), 4.56 (1H, ddd,  $J = 12.9, 6.7, 6.7$  Hz, -lac), 7.45 (1H, s, NH);  $^{13}\text{C}$  NMR ( $\text{CDCl}_3$ , 600 MHz):  $\delta$  14.3, 22.9, 23.6, 27.7, 29.2, 29.4, 29.5, 29.6, 31.8, 32.1, 44.1, 48.5, 59.4, 166.4, 204.7, 206.7; ESI-TOF: expected  $m/z$   $[\text{M} + \text{H}^+] = 314.1784$ , observed  $[\text{M} + \text{H}^+] = 314.1791$ . (Appendix Figures A9, B40-B14)

### Mass Spectrometry

Molecular mass of ACP derivatives was determined by high performance liquid chromatography mass spectrometry (HPLC-MS) using a high resolution Quadrupole Time of Flight (QTOF) instrument with electrospray ionization (ESI). The ESI source was operated at positive ion mode, the nebulizer pressure at 1.2 bar, nitrogen drying gas flow at 8 L/min, drying temperature at 200 °C, and the voltage of the capillary and the end-plate offset to 3000 V to -500 V. The mass range was set from 250 to 2900  $m/z$  and

low concentration ESI tuning mix (Agilent Technologies, Santa Clara, California) was used to calibrate the instrument in the mass range. Ten microliters of samples were injected onto a Phenomenex Kinetex XB-C18 column (100 x 2.1 mm, 2.6 $\mu$ m) (Phenomenex Corporation, Torrance, California) at a flow rate of 0.3 mL/min followed by a simple linear gradient for sample desalting and separation. The initial eluent was 98% mobile phase A (99.9% water, 0.1% formic acid) and 2% B (99.9% acetonitrile, 0.1% formic acid) for 5 min and then mobile phase B was increased to 50% in 25 min. LC eluent was diverted to the waste during the first five minutes of the gradient to eliminate salts in the sample buffer.

Small molecule samples were prepared in concentrations of 0.5 mg/mL in methanol. Molecular mass of AHL analogs were determined with the instrument described above with direct sample injection via ESI inlet. The ESI source was operated at positive ion mode, the nebulizer pressure at 0.4 bar, nitrogen drying gas flow at 4 L/min, drying temperature at 200 °C, and the voltage of the capillary and the end-plate offset to 3000 V to -500 V. The mass range was set from 80 to 800 m/z and sodium formate was used to calibrate the instrument in this mass range.

The collected data was analyzed with the Bruker Compass Data Analysis software and the observed m/z values were compared to the theoretical monoisotopic mass calculated by Bruker Compass IsotopePattern software.

### Kinetics Assays

#### Determination of Background rate

A colorimetric DCPIP indirect assay was used to determine RhII activity.<sup>53</sup> Assay mixtures composed of HEPES buffer (100 mM, pH 7.3), SAM (300  $\mu$ M), butanoyl-ACP

(30  $\mu\text{M}$ ), DCPIP (30  $\mu\text{M}$ ), and sufficient nanopure water for a total volume of 100  $\mu\text{L}$  were tested, with DCPIP being added the last. Upon the addition of DCPIP, the absorbance of the mixture was observed at 600 nm for 30 minutes. The background rate was calculated by DCPIP reduction ( $\epsilon_{600}=21,000 \text{ M}^{-1}\text{cm}^{-1}$ ; see Chapter 1, equations 1-3). The time range at which the background rate was 5% of the lowest enzyme rate observed was used as the incubation time.

#### Determination of Kinetic Constants

Butanoyl- (C4), hexanoyl- (C6), octanoyl- (C8), decanoyl- (C10), and dodecanoyl- (C12) ACPs were tested (compounds 83-87; chapter 1, Table 3). The reaction mixture was composed of RhlI (0.3  $\mu\text{M}$  or 0.9  $\mu\text{M}$ ), DCPIP (300  $\mu\text{M}$ ), SAM (300  $\mu\text{M}$ ), HEPES buffer (100 mM, pH 7.3), varying concentrations of acyl-ACP (2-200  $\mu\text{M}$ ), and nanopure water for a total of 100  $\mu\text{L}$  reaction volume. The RhlI concentration was maintained at 0.3  $\mu\text{M}$  when working with C4-ACP native substrate and kept to 0.9  $\mu\text{M}$  when non-native substrates were tested. All components, sans enzyme, were incubated together for 10 minutes prior to initiation by RhlI. The absorbance was monitored for 300 seconds at 600 nm. The decrease in DCPIP absorbance in the 100 to 200 second range was converted to RhlI rate (equations 1-3, chapter 1) and fitted to Michaelis-Menten equation (equation 5, chapter 1) to determine the kinetic constants. Each run was conducted in triplicates and the spread used to determine error with GraphPad Prism 7.

#### IC<sub>50</sub>/EC<sub>50</sub> determination

Since AHLs are mostly hydrophobic, AHL derivatives were first dissolved in DMSO. The IC<sub>50</sub> value of DMSO was determined to identify the appropriate volume of

DMSO to use. The reaction mixture was composed of RhII (0.3  $\mu\text{M}$ ), DCPIP (300  $\mu\text{M}$ ), SAM (300  $\mu\text{M}$ ), C4-ACP (14  $\mu\text{M}$ ), HEPES buffer (100 mM, pH 7.3), varying concentrations of DMSO (10% – 25% total volume), and nanopure water for a total of 100  $\mu\text{L}$  reaction volume. All components, sans enzyme, were incubated together for 10 minutes prior to initiation by RhII. After enzyme addition, the absorbance was monitored for 300 seconds at 600 nm. The decrease in DCPIP absorbance in the 100 to 200 second range was converted to enzyme rate (equations 1-3, chapter 1) to determine the appropriate volume of DMSO to use for RhII enzyme assay.

The effects of various AHL analogs were tested by measuring their  $\text{IC}_{50}$  or  $\text{EC}_{50}$  values via DCPIP colorimetric assay. The reaction mixture was composed of RhII (0.3  $\mu\text{M}$ ), DCPIP (300  $\mu\text{M}$ ), SAM (300  $\mu\text{M}$ ), C4-ACP (14  $\mu\text{M}$ ), HEPES buffer (100 mM, pH 7.3), varying concentrations (0 -2 mM) of AHL analogs in DMSO (10% of total reaction volume as determined by above experiment; see Appendix Figure C17), and nanopure water for a total of 100  $\mu\text{L}$  reaction volume. All components, sans enzyme, were incubated together for 10 minutes prior to initiation by RhII. After enzyme addition, the absorbance was monitored for 300 seconds at 600 nm. The decrease in DCPIP absorbance in the 100 to 200 second range was converted to RhII rate (equations 1-3, chapter 1) and fitted to  $\text{IC}_{50}$  or  $\text{EC}_{50}$  equations depending on the effect (equations 26 and 30, chapter 1). Each run was conducted in triplicates and the spread used to determine error with GraphPad Prism 7.

The effects of IACPs and ICoAs were tested by measuring their  $\text{IC}_{50}$  values via DCPIP colorimetric assay. The reaction mixture was composed of RhII (0.3  $\mu\text{M}$ ), DCPIP (300  $\mu\text{M}$ ), SAM (300  $\mu\text{M}$ ), C4-ACP (14  $\mu\text{M}$ ), HEPES buffer (100 mM, pH 7.3), varying

concentrations (0 - 1 mM) of IACP or ICoA, and nanopure water for a total of 100  $\mu$ L reaction volume. All components, sans enzyme, were incubated together for 10 minutes prior to initiation by RhII. After enzyme addition, the absorbance was monitored for 300 seconds at 600 nm. The decrease in DCPIP absorbance in the 100 to 200 second range was converted to RhII rate (equations 1-3, chapter 1) and fitted to  $IC_{50}$  equation (equation 26, chapter 1) with GraphPad Prism 7.

#### Time-dependent $IC_{50}$ test

The inhibitory effects as a function of time was determined by incubating RhII with varying concentration of an inhibitor for 0, 10, 30, and 60 minutes. The reaction mixture was composed of RhII (0.3  $\mu$ M), DCPIP (300  $\mu$ M), SAM (300  $\mu$ M), C4-ACP (14  $\mu$ M), HEPES buffer (100 mM, pH 7.3), varying concentrations (10  $\mu$ M -2 mM) of the inhibitor. All components, sans RhII and the inhibitor, were incubated together for 10 minutes prior to initiation by RhII-inhibitor mixture. Upon reaction initiation, the absorbance was monitored for 300 seconds at 600 nm. The decrease in DCPIP absorbance in the 100 to 200 second range was converted to RhII rate (equations 1-3, chapter 1) and fitted to  $IC_{50}$  or  $EC_{50}$  equations depending on the effect (equations 26 and 30, chapter 1). Each run was conducted in triplicates and the spread used to determine error with GraphPad Prism 7.

#### Mode of Inhibition tests

The activity of RhII as a function of C4-ACP concentration was determined under varying amounts of an inhibitor. The inhibitor concentration was determined from the  $IC_{50}$  test, choosing two concentrations below, two above and one run with zero inhibitor. Each reaction mixture contained RhII (0.3  $\mu$ M), DCPIP (300  $\mu$ M), SAM (300  $\mu$ M),



HEPES buffer (100 mM, pH 7.3), and varying concentrations of C4-ACP (2-20  $\mu$ M) and of the inhibitor (0-400  $\mu$ M). The concentration of C4-ACP was varied while the inhibitor concentration constant. All components, sans enzyme, were incubated together for 10 minutes prior to initiation by RhII. The absorbance was monitored for 300 seconds at 600 nm. The decrease in DCPIP absorbance in the 100 to 200 second range was converted to RhII rate (equations 1-3, chapter 1) and fitted to modified Michaelis-Menten equation using  $V_{\max}^{\text{app}}$  and  $K_m^{\text{app}}$  to determine the apparent kinetic constants (equation 17, chapter 1). After determining the mode of inhibition, the  $V_{\max}^{\text{app}}$  and  $K_m^{\text{app}}$  values were used to calculate the inhibitor binding affinity,  $K_i$ , value (competitive mode of inhibition: equations 18, 19; uncompetitive mode of inhibition: equations 20, 21; and mixed or noncompetitive mode of inhibition: equations 22, 23; see chapter 1). Each data point was collected in single run and fitted to various inhibition models and the best model was determined by comparing each fit using Akaike's method (AIC) (equations 24 and 25, chapter 1).

## CHAPTER THREE: RESULTS AND DISCUSSION

**Enzyme Purification**RhII purification

Four hours of growth was required for the RhII-containing strains in 1 L medium to reach OD<sub>600</sub> value between 0.6 and 0.8 for sufficient cell density. Physical lysis via sonication and the subsequent centrifugation resulted in clear dull-yellow lysate. The RhII-containing plasmid also codes for maltose binding protein (MBP) for use with amylose affinity column. The RhII and MBP pair has a combined molecular weight of 65.5 kD, which was supported by the analysis of SDS-PAGE gel (Figure 22)

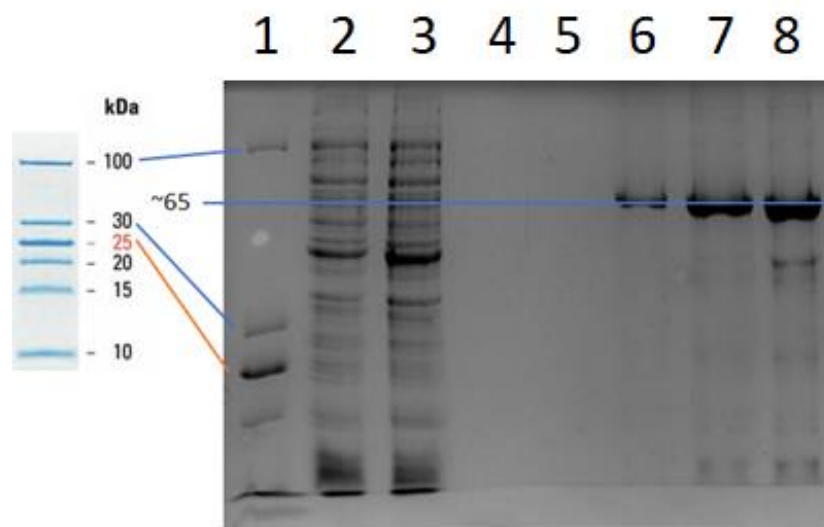


**Figure 22. SDS-PAGE gel of RhII protein isolated using amylose chromatography.** Lane 1: EZ prestained protein ladder; Lane 2: RhII column load run-through; Lane 3: load wash; Lanes 4-8: Buffer A (50 mM Tris-HCl, pH 7.5, 0.2 M NaCl, 1 mM EDTA, 0.1 mM PMSF, 0.1 mM TLCK, 0.4 M sucrose, and 2.5% (v/v) glycerol) +10 mM maltose elution fractions 1-5. RhII + MBP has a combined molecular weight of 65.5 kD. The 100 kD ladder is the first one from the top, followed by 30 kD marker. The thick bands in between the 100 and 30 kD marker, much closer to the 100 kD marker, are presumed to be containing purified RhII.

### Apo-ACP Purification

The cell culture reached optimal cell density indicated by  $OD_{600} = 0.6-0.8$  within 4 hours of growth. Chemical lysis via B-PER, DNase, RNase, Lysozyme, and PMSF followed by centrifugation was effective in producing clear dull-yellow lysate. Upon addition of  $MgCl_2$  and  $MnSO_4$  to activate ACP-hydrolase, co-coded with apo-ACP gene to convert holo-ACP to apo-ACP, the solution turned cloudy. A clear lysate was again achieved after precipitating ACP-hydrolase using 2-propanol followed by centrifugation. This solution was run through DE52 diaminoethyl cellulose anion exchange column for purification. SDS-PAGE gel confirmed the isolation of apo-ACP at ~9 kD (Figure 23).

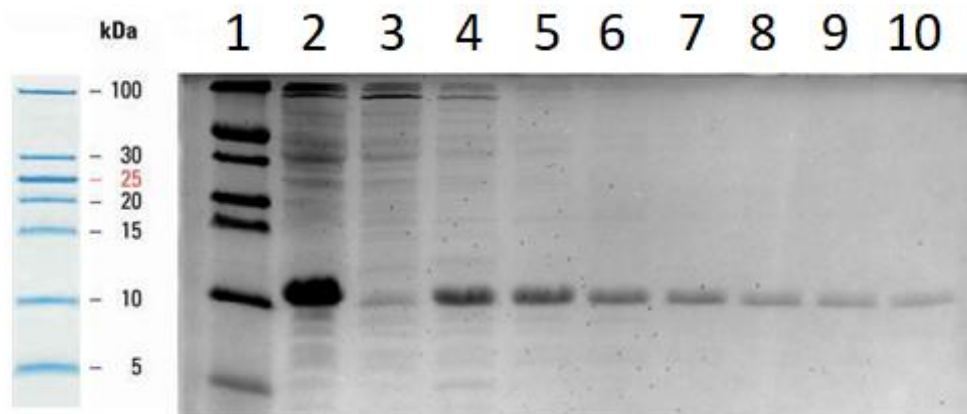


**Figure 23. SDS-PAGE gel of apo-ACP isolated with anion exchange chromatography.** Lane 1: EZ prestained protein ladder; Lane 2: Crude apo-ACP; Lane 3: load wash; Lanes 4-10: 10 mM lithium MES pH 6.1 + 0.5 M LiCl elution fractions 1, 3, 5, 7, 9, 11. The second-from-the-bottom ladder corresponds to 10 kD. The protein bands aligned with the 10 kD marker are presumed to be apo-ACP (8.6 kD).

### Alkyl-CoA Synthesis

In alkyl-CoA synthesis reaction, free-Coenzyme A (limiting reagent) is alkylated with alkyl-bromides. As described in Chapters 1 and 2, DCPIP turns colorless upon reaction with thiols. Therefore, upon adding a sample of the reaction mixture to an aliquot of DCPIP, if no color change is observed, it would indicate that free-CoA, a thiol,

was completely consumed and that the reaction went to completion. The alkyl-CoA (inactive-CoA; ICoA) was isolated via HPLC using the Alkyl-CoA separation method described in Chapter 2 and the fractions were collected using an automated fraction collector. Since the compounds are run through a reverse-phase column, compounds with longer alkyl-chain (more nonpolar) have longer retention time (RT) as compared to ICoAs with shorter, less hydrophobic, alkyl-chains (Figure 24).

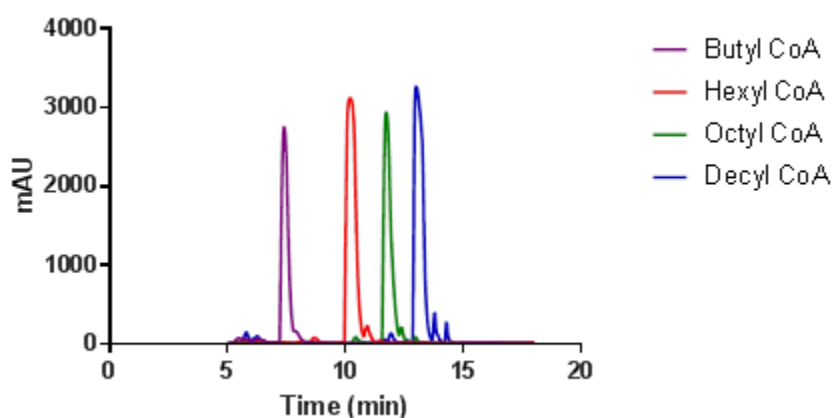


**Figure 24. Elution time of various alkyl-CoAs.** The reverse-phase preparatory column has higher affinity for more hydrophobic compounds, causing compounds with longer alkyl chain, thus greater hydrophobicity, to have greater retention time.

### Acyl/Alkyl-ACP Synthesis

Phosphopantetheinyl transferase, or *Sfp*, catalyzes the transfer of acyl-/alkyl-pantetheine from CoA nucleotide to ACP protein. Apo-ACP (limiting reagent) was reacted with acyl-/alkyl-CoA in the presence of *Sfp*. Due to precipitation of highly hydrophobic CoAs with acyl-/alkyl- chain of ten carbons or longer, C10-CoA and C12-CoA were added to the reaction in portions over a 90-minute period to avoid having the CoA crash out of the predominantly aqueous solvent. The synthesis of acyl-/alkyl-ACPs were monitored by HPLC using the ACP separation method as described in Chapter 2. Using the standard ACP separation method, apo-ACP elutes out at 7.8 minutes. The

addition of pantetheine linker greatly reduces its overall hydrophobicity, causing holo- and butanoyl-ACPs to have shorter RT than apo-ACP whereas acyl/alkyl-ACPs with eight or longer carbon chain nonpolar enough to have longer RT than apo-ACP (Figure 25a). Whereas apo-ACP elutes out at 7.8 minutes, butanoyl-, octanoyl-, decanoyl-, and dodecanoyl-ACPs elute out at 7.3, 8.0, 8.3, and 8.7 minutes, respectively. However, hexyl- and hexanoyl-ACPs have nearly identical RT as apo-ACP, necessitating separation using C6-ACP separation method with shallower solvent gradient (Figure 25b). In this method, apo-ACP elution time is 34 minutes, compared with 33 minutes for hexanoyl-ACP. There is virtually no difference in the elution time between an acyl-ACP and its alkyl-ACP counterpart (e.g. both butanoyl-ACP and butyl-ACP elutes out at 7.3 minutes). The reaction was deemed complete when the limiting reagent, apo-ACP, peak at 7.8 min was completely depleted, which occurred in 3 hours or less. However, the batch was deemed unusable if there was a significant peak present at 6.5 minutes, corresponding to holo-ACP contamination. The solution became cloudy when ammonium sulfate was added to precipitate *Sfp*. The precipitated transferase was then removed with centrifugation. The clear lysate was run through 3 kD spin filtration column to remove ammonium sulfate, CoA byproduct, and excess acyl-/alkyl-CoA. This filtration process was repeated until the peak at 280 nm (corresponding to ACP) was at least 10% greater than the peak at 260 nm (corresponding to CoA) as determined by the UV-vis spectrophotometer.

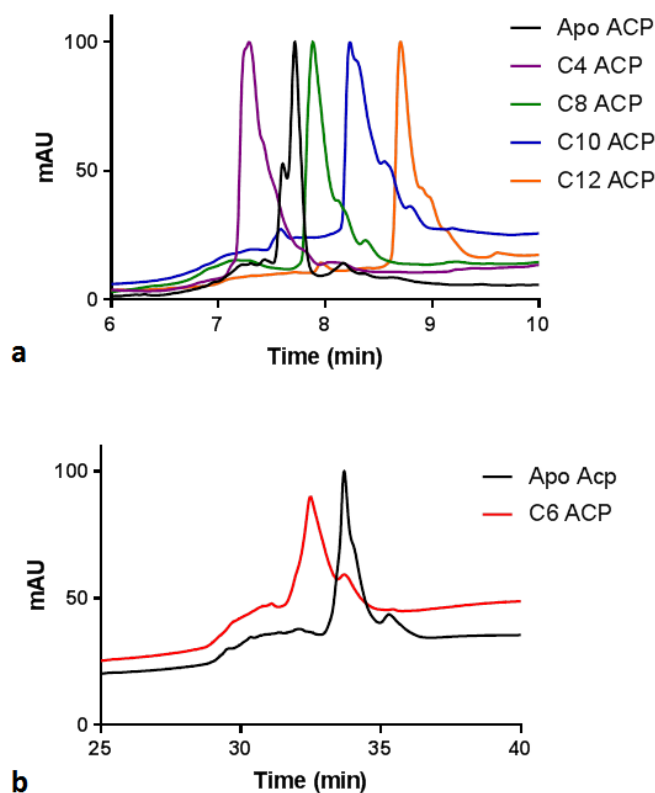


**Figure 25. Elution time of various acyl-/alkyl-ACPs.** The more hydrophobic compounds have higher affinity to the reverse-phase UHPLC column and have longer retention time. The addition of the pantetheine linker greatly reduces the hydrophobicity of ACP, (a) causing acyl-/alkyl-ACPs with four carbon chains or shorter to elute out before apo-ACP and those with chains of eight carbons or longer to elute out after apo-ACP. (b) Hexanoyl-/hexyl-ACP has nearly identical retention time as apo-ACP thus requiring the solvent gradient to shift over a longer time-period at a lower flowrate.

### Small Molecule Synthesis

#### D-Homocysteine Thiolactone (Figure 19, Chapter 2)

Stereoisomerically pure D-homocysteine thiolactone was purified from a racemic mixture of DL-homocysteine thiolactone by acylating the thiolactone headgroup with *S*-(+)-2-methoxyphenylacetic acid in a EDC-coupled reaction to produce two diastereomers with distinct differences in polarity that could be separated with column chromatography. The EDC-coupled reaction produced white crystalline product easily soluble in chloroform but not so much in the 7:3 hexane: ethyl acetate eluting solvent, thus the

diastereomer mixture was dissolved in minimal amount of chloroform and then loaded to the silica gel column. The separation of the diastereomers via silica gel column was confirmed with thin layer chromatography (TLC) with UV active silica with the 7:3 hexane: ethyl acetate eluent. Because there is only a small difference in the polarities of the diastereomers, there were significant number of fractions with both products. The fractions with the both diastereomers were collected and run through the silica gel column again to fully isolate the desired product. In addition to comparing the polarity of the diastereomers via elution time, the purity of the diastereomers was further confirmed by comparing the melting point of each compound; (3*S*,2'*S*)-3-(2'-methoxy-2'-phenyl-)acetamido-2-thiophenone (containing L-homocysteine thiolactone) had a melting point of 160-164°C (literature value: 161-163°C<sup>57</sup>) whereas (3*R*,2'*S*)-3-(2'-methoxy-2'-phenyl-)acetamido-2-thiophenone (containing D-homocysteine thiolactone) had a melting point of 110-115°C (literature value: 109-111°C<sup>57</sup>). Once the D-homocysteine thiolactone head-group was isolated and recrystallized in 2-propanol, its stereo purity was confirmed by optical rotation measurement  $[\alpha]_D^{25}$  -36.3 (0.05 mg/mL in H<sub>2</sub>O) (literature value: -21.7<sup>57</sup>).

#### *N*-Acyl-D-Homocysteine Thiolactone (Figure 20, Chapter 2)

The DCC-coupled reaction resulted in colorless mixture with white cloudy urea precipitate, which was easily removed via filtration with celite. Butyric acid was sufficiently polar to yield clean *N*-Butanoyl-D-homocysteine thiolactone through a series of aqueous washes with water, HCl (2M; 3x10 mL), NaHCO<sub>3</sub> (saturated; 3x10 mL), and brine (saturated; 3x10 mL). However, carboxylic acids with tails of six carbons or longer were not polar enough to be removed by aqueous washes alone, requiring purification via

silica gel column chromatography. The polarity between the *N*-acyl-D-homocysteine thiolactones and their corresponding carboxylic acids were close enough that two runs through the column were required to obtain a pure product.

#### *N*-(3-Oxoacyl)-D-Homocysteine Thiolactone (Figure 21, Chapter 2)

Meldrum's acid acylation reaction resulted in a colorless mixture with white cloudy urea precipitate, which was removed via celite filtration, which yielded a pale-yellow flake-like product which was stored at -20 °C to protect the temperature sensitive Meldrum's acid. Refluxing the acylated Meldrum's acid with the D-homocysteine thiolactone head-group opened the Meldrum's acid ring and attached the 3-oxoacyl tail to the headgroup. The polarity of the *N*-(3-Oxoacyl)-D-homocysteine thiolactones and their corresponding carboxylic acids were close enough that two runs through the silica gel column were required to obtain a pure product.

#### Spectral Data

See Appendix for all Mass Spectrometry (Appendix A), NMR (Appendix B), and UV-vis spectrophotometer (Appendix C) spectra.

### **AHL Analog Kinetics**

#### Background rate

As reported previously, non-specific reduction of DCPIP is a major limitation of the DCPIP colorimetric assay, which is compounded by significant levels of contamination in commercially available SAM-Cl.<sup>53</sup> To circumvent the issue, the reaction mixture, except the enzyme, was incubated with DCPIP and the decrease in absorbance at 600 nm was observed. The rate of decrease of absorbance flattens around 600 s (10 min) and the background rate in the 600-900 s range is equivalent of 0.013



$\mu\text{M}/\text{min}$ , about 5% of the lowest enzyme rate observed in this project (Figure 26).

Therefore, to minimize background rate interference, the reaction mixture was incubated with DCPIP for 10 min before initiation with the enzyme.

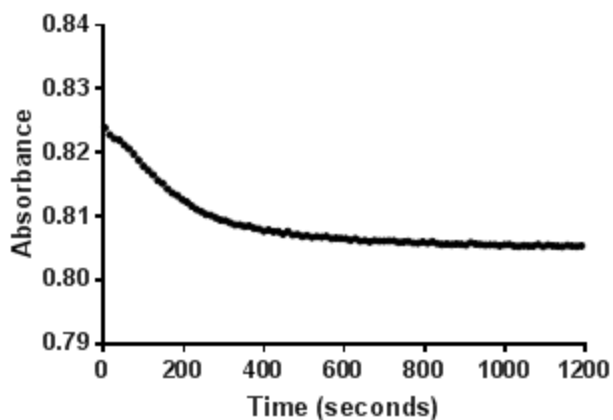


**Figure 26. DCPIP background rate progress curve.** The 100  $\mu\text{L}$  reaction mixture was composed of HEPES buffer (100 mM, pH 7.3), SAM (300  $\mu\text{M}$ ), butanoyl-ACP (30  $\mu\text{M}$ ), DCPIP (30  $\mu\text{M}$ ), and water. The absorbance at 600 nm was observed for 1200 s (20 min). The background rate flattens out at 600 s (10 min).

#### The Effects of AHL analogs on RhII enzymatic rate

Previous studies have shown that RhII activity is unaffected by butanoyl-homoserine lactone (C4-HSL; compound 1), its native *N*-acyl-homoserine lactone (AHL) product.<sup>36</sup> To explore the components of the AHL structure that could be modified to affect RhII activity, the first set of AHL analogs were designed to test the effects of alterations to the headgroup on RhII enzymatic rate (Figure 27). The L-homoserine lactone headgroup was modified in the lactone ring (compounds: 2-4, 8-12), the chirality (compounds: 5, 12), and the tail-headgroup linkage (compounds: 6, 7, 10-12). While most derivatives failed to effect RhII, a change in the chirality and linkage (compounds 5 and 12) in AHL inhibited RhII. Although analog 8, the thiolactone derivative, did not inhibit RhII, work from our collaborators have found thiolactone analogs to have

significant antagonistic and agonistic effects on QS receptor proteins; therefore, we were interested in exploring thiolactone analogs in an effort to discover compounds that could inhibit both RhII (AHL synthase) and RhIR (AHL receptor) simultaneously.<sup>43</sup> The initial study and previous findings prompted us to further expand the analog libraries with alterations to the headgroup stereocenter, sulfonamide linkage between the headgroup and the aliphatic chain, and thiolactone ring headgroup in the search for better RhII inhibitors. (for kinetics data, see Appendix, Figure C1)

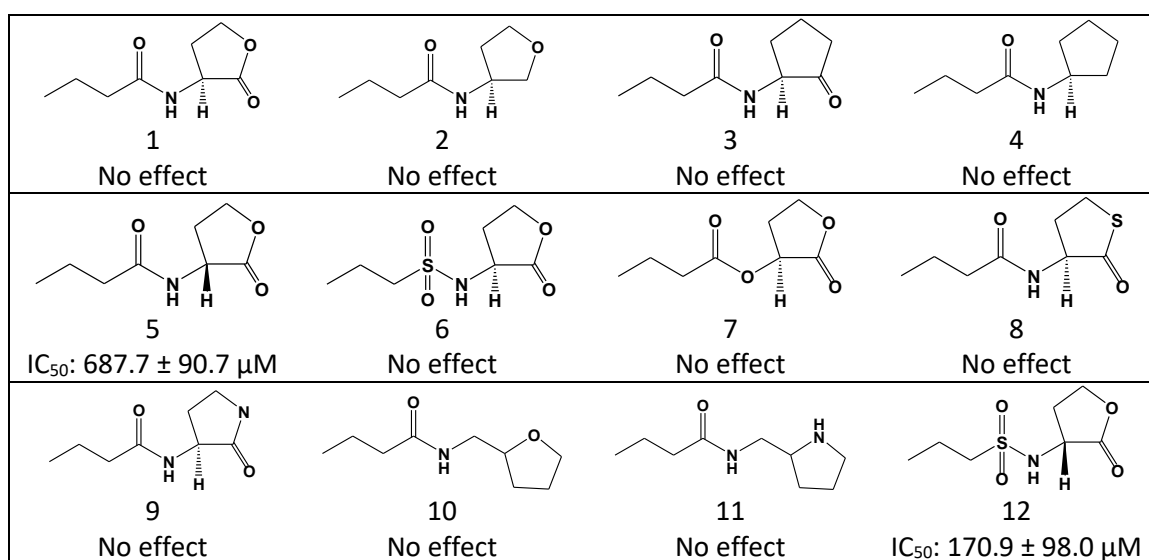


**Figure 27. Initial set of AHL-analogs and their effects.** The initial rates of RhII with 300  $\mu M$  of SAM and 14  $\mu M$  of C4-ACP in the presence of 0-20 mM of the AHL analogs were observed. Only the chiral and linkage changes (compounds 5 and 12) caused inhibition. (Appendix Figure C1)

#### Acyl-L-homoserine lactone (L-HSL)

In many QS receptor studies, modifications to the acyl-chain had significant antagonistic and agonistic effects on the receptor.<sup>43, 59</sup> To determine whether the same is true for RhII, the native headgroup, L-HSL, was acylated with various acyl, 3-oxoacyl, and 3-hydroxyacyl-chains (compounds 1,13-27; Figure 28). Regardless of the

modification to the hydrocarbon chain, none of the sixteen analogs with the L-HSL headgroup moiety inhibited RhII. (Appendix Figure C2)

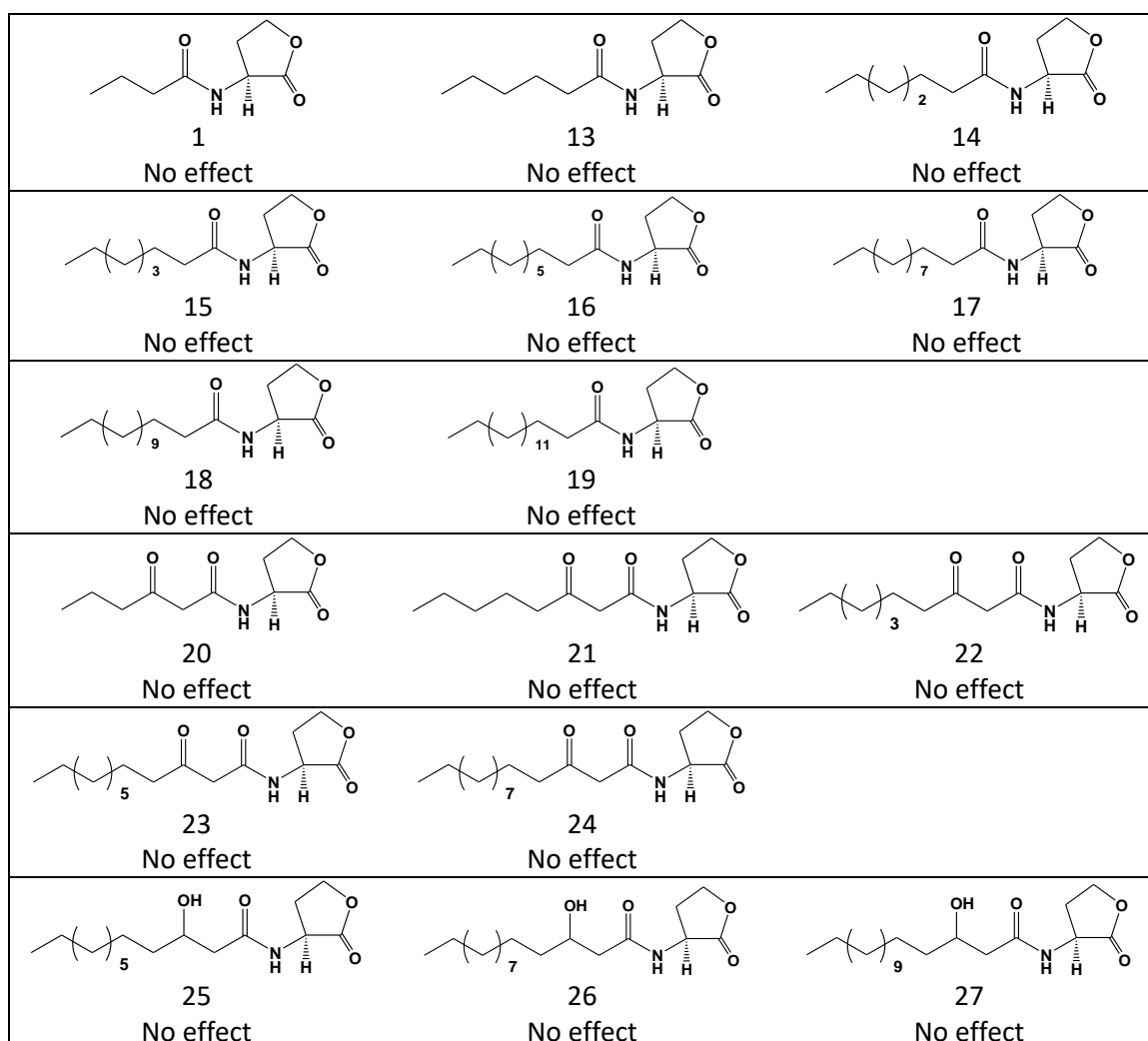


**Figure 28.** Effects of acyl-L-homoserine lactones, 3-oxoacyl- and 3-hydroxyacyl-L-homoserine lactones on RhII initial rate. The initial rates of RhII in the presence of 0-2 mM of acyl-L-homoserine lactones of various acyl-chain lengths were observed. Acyl-L-homoserine lactones with chains between 4 and 16 carbons long did not inhibit RhII. (Appendix Figure C2)

#### Acyl-D-homoserine lactone (D-HSL)

While none of the eight acyl-L-HSLs (compounds: 1, 13-19) inhibited RhII, two analogs out of seven acyl-D-HSLs were found to inhibit the enzyme: compounds 5,  $IC_{50}$ :  $687.7 \pm 90.7 \mu\text{M}$ , and compound 31,  $IC_{50}$ :  $20.2 \pm 10.1 \mu\text{M}$  (Figure 29). Interestingly,

while compound 5 has a butanoyl tail, which is the native acyl-chain for the RhI QS system, compound 31 has a phenylbutanoyl chain, which should be too large to bind to RhII acyl-chain binding pocket. (Appendix Figure C3)

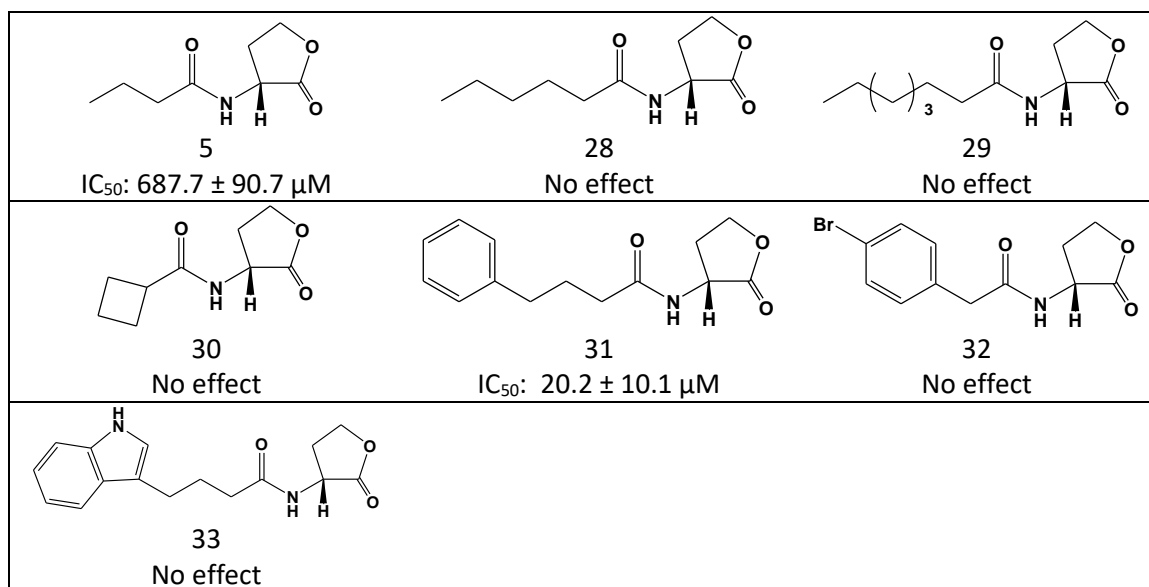


**Figure 29. Effects of acyl-D-homoserine lactones.** The initial rates of RhII in the presence of 0-2 mM of acyl-D-homoserine lactones of various acyl-chain lengths were observed. Of these compounds, acyl-D-homoserine lactones with butanoyl and butyl-phenyl chain (compounds 5 and 31) inhibited RhII, with the longer/bulkier compound 31 having lower  $IC_{50}$  value ( $20.2 \pm 10.1 \mu M$  vs.  $687.7 \pm 90.7 \mu M$ ). (Appendix Figure C3)

### 3-oxoacyl-D-HSL

However, the more interesting pattern emerges with 3-oxoacyl-D-HSL derivatives (Figure 30). While compound 35, medium chain-length analog (3-oxoC8-D-HSL), inhibited RhII ( $IC_{50}: 282.0 \pm 34.1 \mu M$ ), a shorter chain derivative, compound 34 (3-oxoC6-D-HSL), activated RhII ( $EC_{50}: 224.4 \pm 55 \mu M$ ). This discovery of an activator, suggests that the small molecule modulators are perhaps binding to an allosteric or nonspecific binding site. The presence of a nonspecific binding site could explain how compound 31, with its large tail, binds with and inhibits RhII. (Appendix Figure C4)

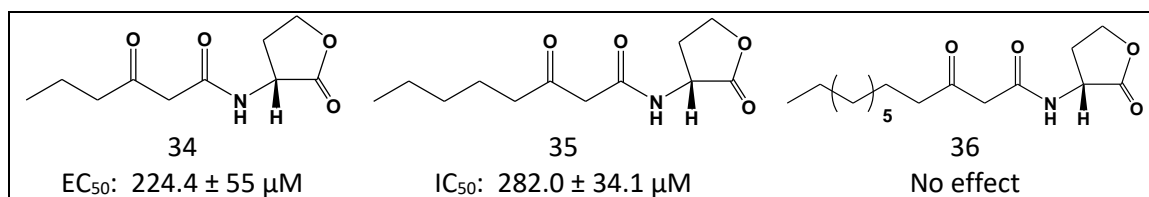


**Figure 30. Effects of 3-oxoacyl-D-homoserine lactones.** The initial rates of RhII in the presence of 0-2 mM of 3-oxoacyl-D-homoserine lactones of various acyl-chain lengths were observed. Of these compounds, acyl-D-homoserine lactones with hexanoyl chain (compound 34) activated RhII initial rate (EC<sub>50</sub>: 224.4 ± 55 μM) whereas the one with octanoyl chain (compound 35) inhibited RhII (IC<sub>50</sub>: 282.0 ± 34.1 μM) and the one with dodecanoyl chain did not affect RhII enzyme rate. (Appendix Figure C4)

### Acyl-sulfonamide-DL-HSL

Unlike the pattern found with acyl-HSLs, RhII inhibitors were found from both L and D sulfonamide derivatives (Figure 31). Compound 12, a sulfonamide-D-HSL analog, was found to be a more potent inhibitor than compound 37, a sulfonamide-L-HSL analog, with IC<sub>50</sub> values of 170.9 ± 98.0 μM vs. 345.3 ± 79.3 μM, respectively. However, no other variations in the aliphatic chain with sulfonamide linkage was found to inhibit RhII. (Appendix Figure C5)

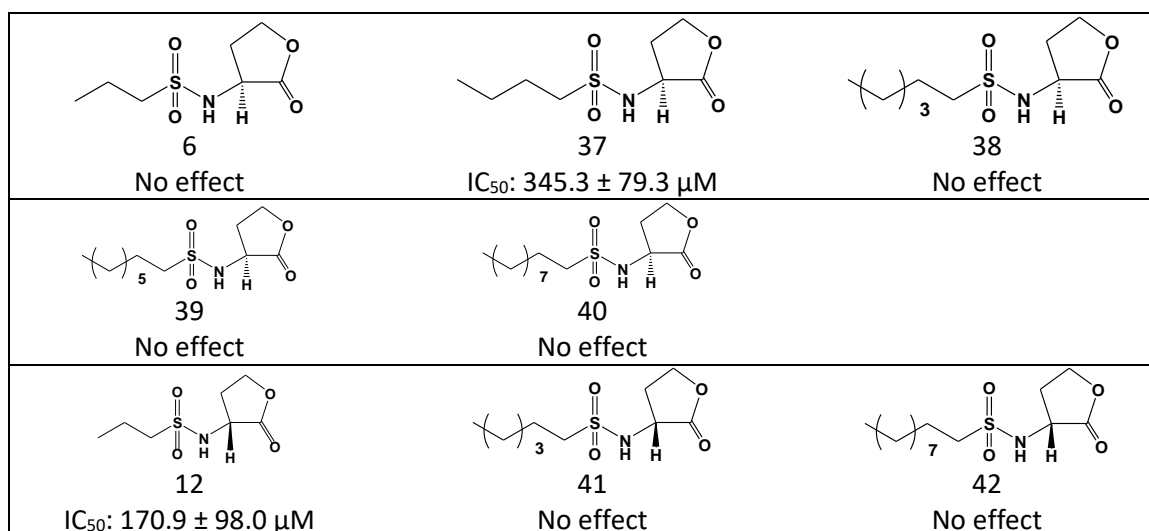


**Figure 31. Effects of L and D sulfonamides.** The initial rates of RhII in the presence of 0-2 mM of L and D sulfonamide-homoserine lactones of various chain lengths were observed. The compounds with the short chains, butylsulfonamide-L-homoserine lactone (compound 37) and propylsulfonamide-D-homoserine lactone (compound 12), inhibited RhII with IC<sub>50</sub> values of 345.3 ± 79.3 μM and 170.9 ± 98.0 μM, respectively. (Appendix Figure C5)

### Acyl- and 3-oxoacyl-L-homocysteine thiolactone

Although compound 8 did not inhibit RhII, expansion of the hydrocarbon tail library yielded two inhibitors: compounds 46 and 55 with  $IC_{50}$  values of  $387.3 \pm 88.6 \mu\text{M}$  and  $621.2 \pm 49.5 \mu\text{M}$ , respectively (Figure 32). Again, contrary to initial expectations, it is the long-chain analogs that inhibit RhII while the short-chain derivatives fail to effect RhII activity. Furthermore, this is the first category of compounds with a L-stereocenter headgroup in which multiple inhibitors were discovered. (Appendix Figure C6)

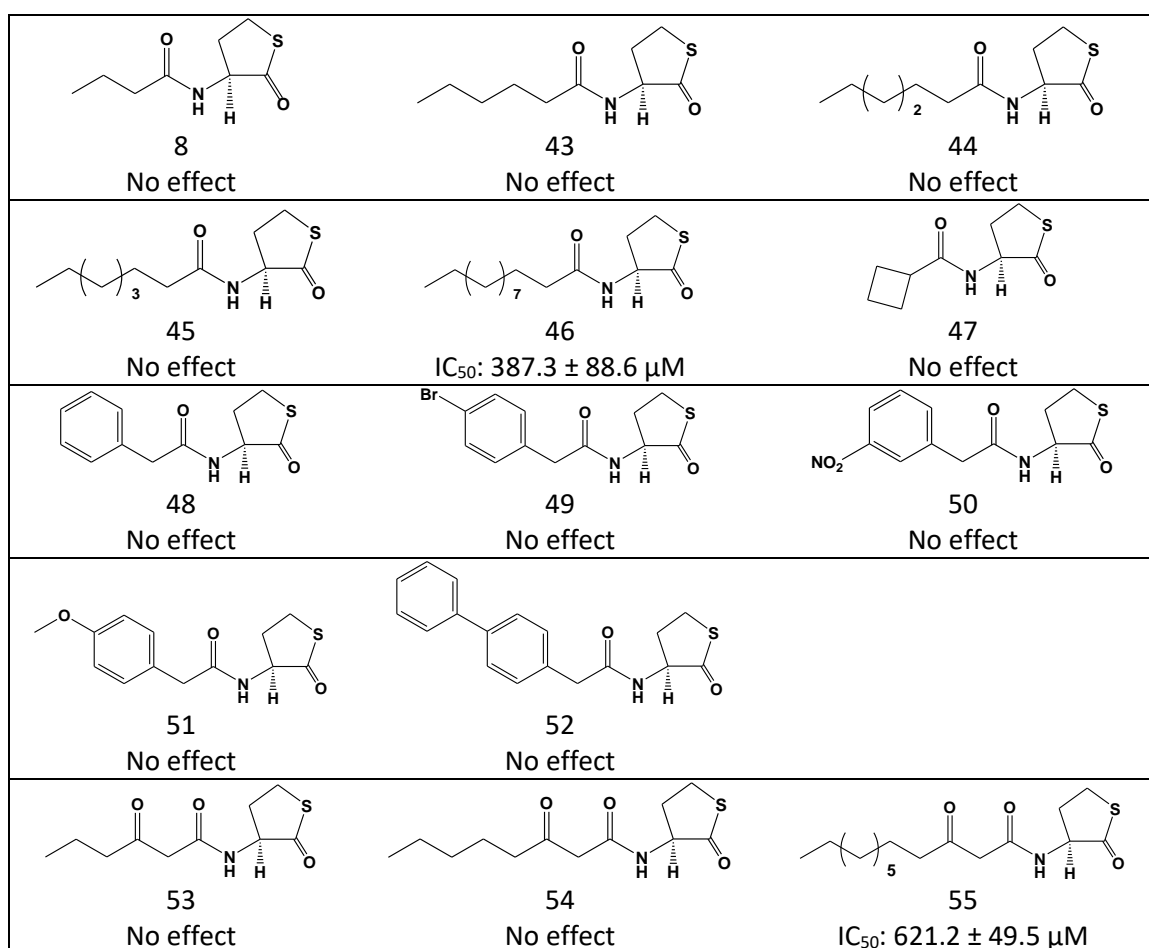


**Figure 32.** Effects of acyl- and 3-oxoacyl-L-homocysteine thiolactones. The initial rates of RhII in the presence of 0-2 mM of acyl- and 3-oxoacyl-L-homocysteine thiolactones of various acyl-chain lengths were observed. Of these compounds, only C12-L-homocysteine thiolactone and 3-oxo-C12-L-homocysteine thiolactone (compounds 46 and 55), the ones with the longest straight chain, inhibited RhII. Of these two compounds, one with the acyl-chain had lower  $IC_{50}$  value than the one with the 3-oxoacyl-chain ( $IC_{50}$ :  $387.3 \pm 88.6 \mu\text{M}$  vs.  $621.2 \pm 49.5 \mu\text{M}$ ). (Appendix Figure C6)

### Acyl- and 3-oxoacyl-D-thiolactone

Following the pattern found with L- and D-HSL derivatives, D-thiolactone analogs produced much more potent inhibitors than L-thiolactones (Figure 33). Compared with IC<sub>50</sub> value of 387.3 ± 88.6 μM for compound 46 (C12-L-thiolactone), compound 60 (C12 D-thiolactone) had IC<sub>50</sub> value of 11.4 ± 1.5 μM, a 34-fold decrease. And whereas compound 55 (3-oxoC12-L-thiolactone) had IC<sub>50</sub> value of 621.2 ± 49.5 μM, compound 64 (3-oxoC12-D-thiolactone) was found to have a much lower IC<sub>50</sub> value 127.4 ± 70.2 μM, close to 5-fold decrease. However, the most interesting phenomena occurred with short and medium-chain derivatives. As seen with 3-oxoacyl-D-HSLs, which were found to be activating with a shorter chain and inhibiting with a longer chain, 3-oxoC6, 3-oxoC8, and 3-oxoC10-D-thiolactones (compounds 61-63) activated while 3-oxo C12-D-thiolactone (compound 64) inhibited RhII. Interestingly, as the chain lengthened from 3-oxoC6 to 3-oxoC8 and 3-oxoC10, the activation potency increased indicated by EC<sub>50</sub> values decreasing 1506 ± 109.9 μM, 854.5 ± 74.4 μM, and 57.1 ± 22.7 μM. (Appendix Figure C7)

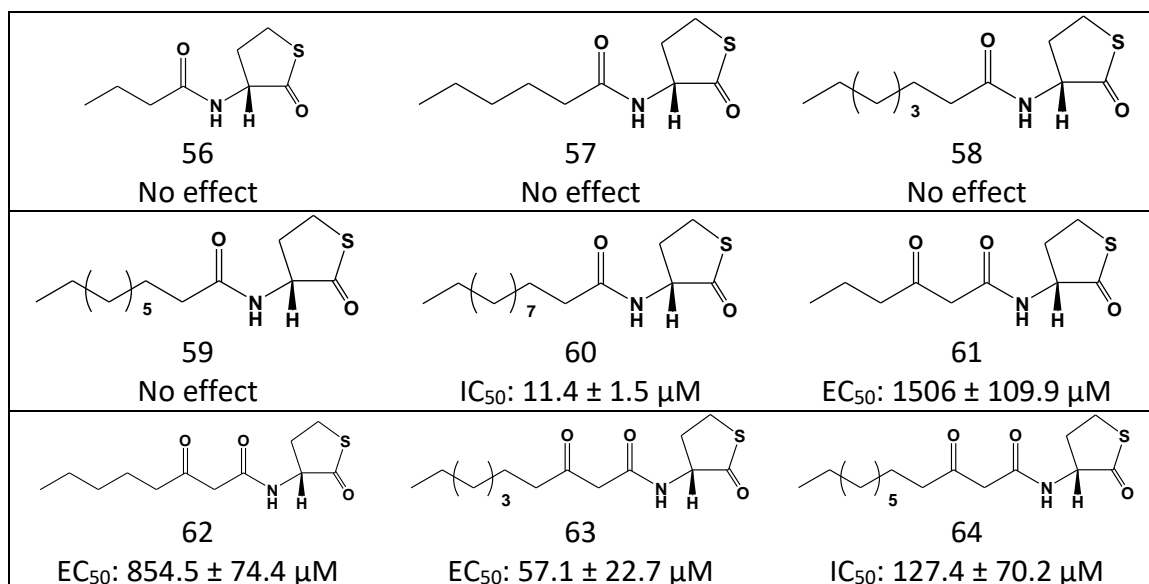


**Figure 33. Effects of acyl- and 3-oxoacyl-D-homocysteine thiolactones.** The initial rates of RhII in the presence of 0-2 mM of acyl- and 3-oxoacyl-D-homocysteine thiolactones of various acyl-chain lengths were observed. Of these compounds, dodecanoyl-D-homocysteine thiolactone and 3-oxo-dodecanoyl-L-homocysteine thiolactone (compounds 60 and 64), the ones with the longest straight chain, inhibited RhII. As with their L-counterpart, one with the acyl-chain had lower  $IC_{50}$  value than the one with the 3-oxoacyl-chain ( $IC_{50}: 11.4 \pm 1.5 \mu M$  vs.  $127.4 \pm 70.2 \mu M$ ). The shorter-chain 3-oxoacyl-D-homocysteine thiolactones (compounds 61-63) activated RhII activity, with the  $EC_{50}$  values decreasing as the carbon chain lengthened. (Appendix Figure C7)

#### Acyl-Cyclopentanamide

Since thiolactone derivatives inhibited and activated RhII to a greater degree than lactone analogs, the effects of cyclopentyl headgroup was tested to explore further increase in headgroup hydrophobicity (compounds 4, 65-68; Figure 34). However, no cyclopentyl derivatives effected RhII activity. (Appendix Figure C8)



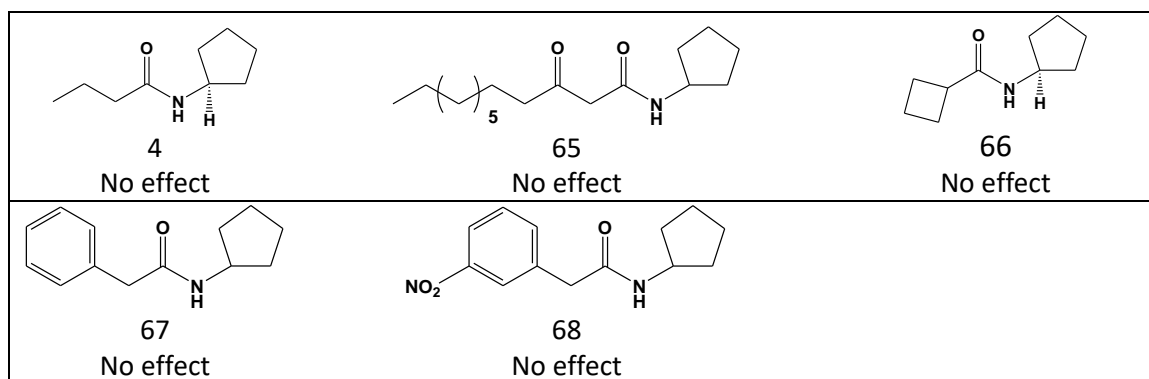


**Figure 34. Effects of acyl-cyclopentanamide on RhII activity.** The initial rates of RhII-catalyzed C4-HSL synthesis were similar with and without acyl-cyclopentanamides, suggesting no inhibitory effect of this class of molecules on RhII activity. (Appendix Figure C8)

#### Non-lactone derivatives

While cyclopentyl derivatives tested the effects of nonpolar headgroups, various non-lactone analogs were designed to test headgroups of various configurations and hydrophilicity (compounds 2, 3, 9-11, 69-73; Figure 35). None of these non-lactone compounds inhibited RhII. (Appendix Figure C9)

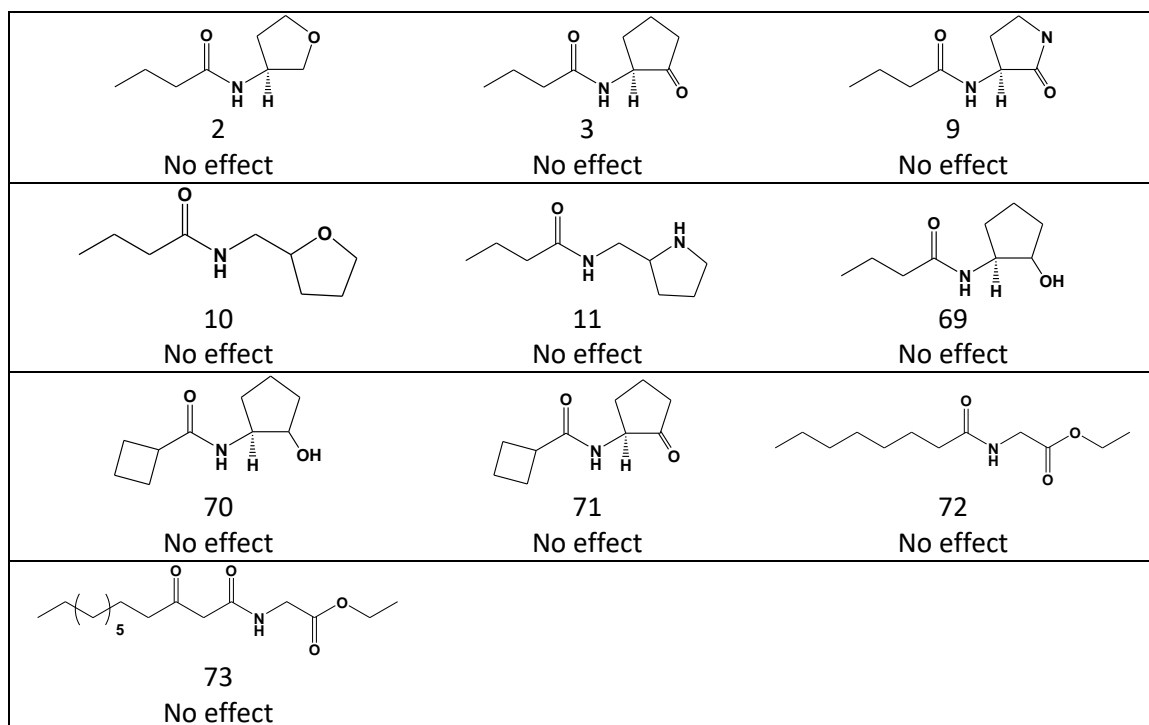


**Figure 35. Effects of non-lactone AHL analogs on RhII activity.** The initial rates of RhII in the presence of 0-2 mM of various non-lactone AHL analogs were observed and none of them inhibited RhII. (Appendix Figure C9)

### Headgroup vs Tail chain effects

Thus far, only lactone and thiolactone derivatives modulated RhII rate (activation and inhibition), and the variation in the acyl-chain enhanced the effect. To check if the inhibitory effects observed for lactone and thiolactone derivatives described above was caused by nonspecific binding of headgroup or fatty acid to the synthase enzyme, the initial rate of RhII was observed in the presence of the headgroup (L-HSL, D-HSL, L-thiolactone, and D-thiolactone; compounds 74-77), the fatty acid chain tail (butyric, hexanoic, octanoic, decanoic, and dodecanoic acid; compounds 78-82), or both (D-thiolactone + dodecanoic acid, compounds 77 + 82, corresponding to compound 60; Figure 36). None of these kinetic assays resulted in the inhibition of RhII, suggesting that both the headgroup and the aliphatic tail moieties must be covalently linked to each other to observe the inhibition/activation effects described above. (Appendix Figure C10)

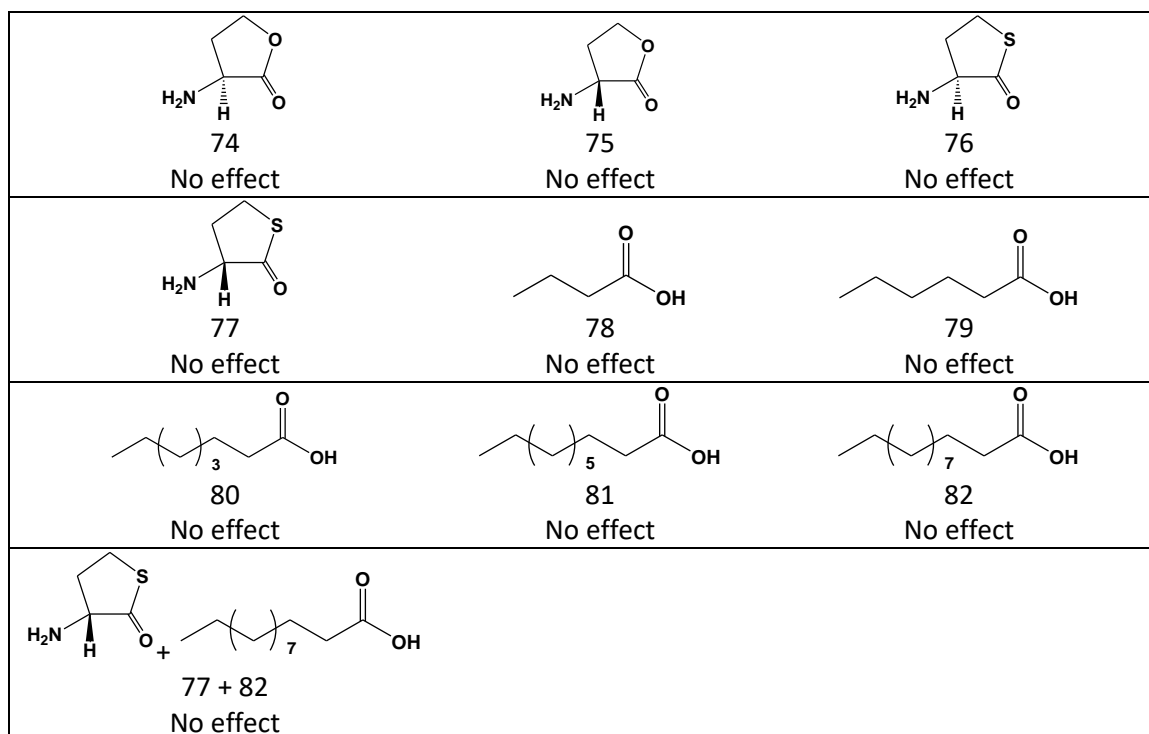


**Figure 36. Effects of headgroup and tail moieties in isolation on RhII initial rate.** the initial rates of RhII in the presence of 0-2 mM of L and D homoserine lactone and homocysteine thiolactone headgroups and various carboxylic acid tail groups were observed. Furthermore, the initial rates of RhII were observed in the presence of 0-2 mM of both compounds 77 and 82, which was analogous to compound 60 which did inhibit RhII. None of these compounds inhibited RhII, indicating that neither the acyl-chain nor the headgroup alone has sufficient binding affinity to RhII to cause inhibition. (Appendix Figure C10)

#### Determining the mode of inhibition

As described in chapter 1, RhII is an ordered bi-ter enzyme with C4-ACP binding second and C4-L-HSL released second (Figure 37). AHL analogs are expected to compete for C4-L-HSL binding site. As such, C4-ACP and AHL analogs bind to different RhII forms (C4-ACP to EA form and analogs to ER form), which would cause intercept-effect in a double reciprocal plot (Chapter 1, p. 21). Furthermore, C4-ACP binding and C4-L-HSL release are separated by a product release step in both the forward and reverse directions; therefore, C4-ACP binding and AHL analog binding are irreversibly connected, which would be manifested by a lack of slope-effect in a double

reciprocal plot (Chapter 1, p. 20). Intercept-effect without slope-effect would produce a set of parallel lines, indicative of uncompetitive inhibition.



**Figure 37. Cleland diagram of RhII catalyzed reaction.** “E” denotes RhII while “A,” “B,” “P,” “Q,” and “R” represents SAM, C4-ACP, holo-ACP, C4-L-HSL, and MTA, respectively.

The Lineweaver-Burk plot of initial RhII rate versus variable C4-ACP concentrations at various fixed C12-D-thiolactone (Figure 38a) or 3-oxoC12-D-thiolactone (Figure 38b) concentrations show a set of parallel lines, indicative of uncompetitive-mode of inhibition which supports the initial expectation that AHL analogs are binding to C4-L-HSL binding site (ER enzyme conformation in Figure 31 above). Further analysis using the Akaike’s method (AIC; see equations 24, 25), confirms that all the inhibition data is best fitted by uncompetitive inhibition model (Table 10). Moreover, as predicted by the trend in  $IC_{50}$  values, C12-D-thiolactone ( $K_i$ :  $86.2 \pm 9.6 \mu\text{M}$ ) has higher binding affinity than 3-oxoC12-D-thiolactone ( $K_i$ :  $431.6 \pm 30.8 \mu\text{M}$ ) (Table 11).

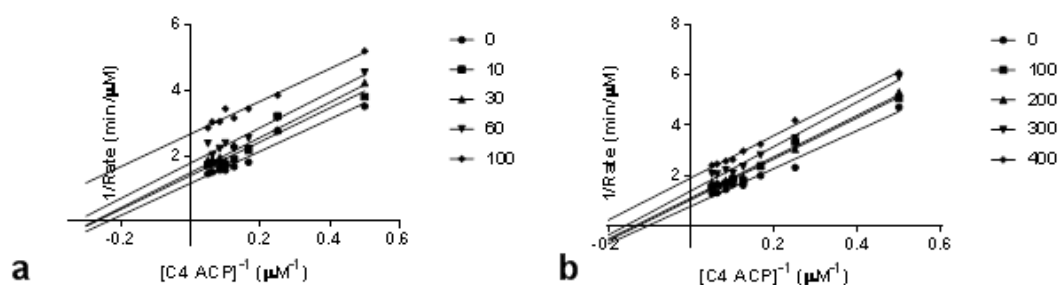


**Figure 38. Double Reciprocal Plot of RhII activity with varying C4-ACP concentrations and various fixed AHL analog concentrations.** Double reciprocal of the initial rate of RhII against C4-ACP concentration in the presence of various fixed concentrations of (a) compound 60 (C12-D-thiolactone) and (b) compound 64 (3-oxoC12-D-thiolactone) was plotted. The fixed AHL analog concentrations were chosen to be 0, below the  $IC_{50}$  value, around the  $IC_{50}$  value, and two above the  $IC_{50}$  value. While keeping the AHL analog concentration fixed, C4-ACP concentration was varied from 2 to 20  $\mu$ M. The inverse of the initial rate was plotted against inverse of the C4-ACP concentration which revealed a set of parallel lines, indicative of uncompetitive mode of inhibition.

**Table 10. Determining best fit model for the mode of inhibition using AIC**

Analog	Best fit	U <sup>a</sup> vs C <sup>b</sup>	U vs M <sup>c</sup>	U vs N <sup>d</sup>
60	Uncompetitive	>99.99% U	78.81% U	95.84% U
64	Uncompetitive	>99.99% U	54.69% U	68.30% U
a = Uncompetitive mode of inhibition				
b = Competitive mode of inhibition				
c = Mixed mode of inhibition				
d = Noncompetitive mode of inhibition				

**Table 11. Effect of AHL analogs on RhII initial enzyme rate with variable C4-ACP concentration.**

Analog	$IC_{50}$ ( $\mu$ M)	$K_i$ ( $\mu$ M)	Mode of Inhibition
60	$11.4 \pm 1.5$	$86.2 \pm 9.6$	Uncompetitive
64	$127.4 \pm 70.2$	$431.6 \pm 30.8$	Uncompetitive

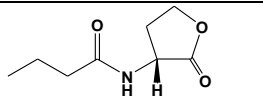
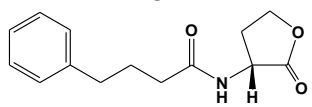
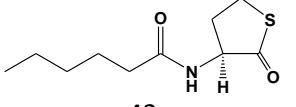
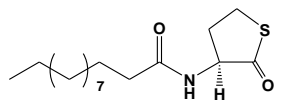
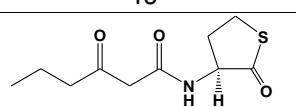
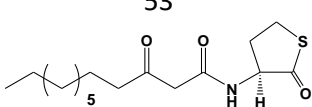
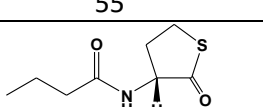
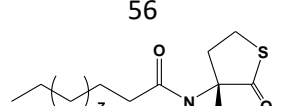
### AHL analog Trends

#### Chain length effect

RhII inhibition was primarily observed with D-HSL, L-thiolactone, and D-thiolactone headgroups. With each headgroup, a short-chain derivative resulted in no or

weak inhibition while a long or bulky-chain analog displayed much more potent inhibitory effects (Table 12). Moreover, if the short-chain analog does inhibit, it achieves greater maximum inhibition (maximum % inhibition). This pattern of long-chain derivatives having lower  $IC_{50}$  is highly surprising. The acyl-chain moiety is expected to bind in the small acyl-chain binding pocket of RhII, specific for a butanoyl chain of the C4-ACP native substrate, used by its native substrate/product. In the absence of the crystal structure of RhII, this phenomenon can be explained by several hypotheses: (1) both the  $k_{on}$  and  $k_{off}$  values could be higher for longer chains or (2) the longer acyl-chains are binding to a nonspecific or an alternate acyl-chain binding site with higher affinity than the acyl-chain binding pocket. This acyl-chain length pattern of longer chains better inhibiting RhII can be further studied by analyzing RhII enzymatic rate with nonnative acyl-ACP substrates and the inhibition patterns of inhibitors of various hydrocarbon tail length. Acyl carrier protein (ACP) engulfs the acyl-chain until the proteins binds to the appropriate enzyme active site and then releases the acyl-chain. Therefore, any acyl-chain binding site must be specific and close to ACP binding site. Long-chain acyl-ACP substrates undergo RhII catalysis with decreasing  $K_m$  as the acyl-chain length is increased (see “Determining Kinetic Constants with various Acyl-ACPs” section below). Similar pattern (decrease in  $K_i$  and  $IC_{50}$  with increase in acyl-chain length) was observed with longer chain alkyl-ACPs and alkyl-CoAs, thus ruling out inhibition due to nonspecific binding for long-chain analogs. Therefore, the acyl-chain must bind at or somewhere close to the acyl-chain binding pocket in RhII.

**Table 12. Trends with variations in the acyl-chain length/size.**

Compound	IC <sub>50</sub> (μM) % Inhibition	IC <sub>50</sub> Trends <sup>a</sup>
 5	687.7 ± 90.7 40%	Weaker
 31	20.2 ± 10.1 25%	Stronger
 43	None 0%	No Inhibition
 46	387.3 ± 88.6 60%	Weak Inhibition
 53	None 0%	No Inhibition
 55	621.2 ± 49.5 60%	Weak Inhibition
 56	None 0%	No Inhibition
 60	11.4 ± 1.5 40%	Weak Inhibition
a = On a relative scale		

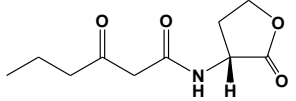
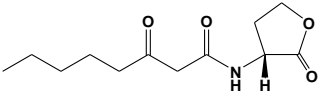
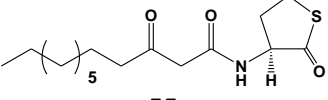
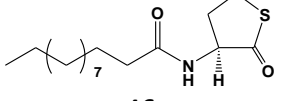
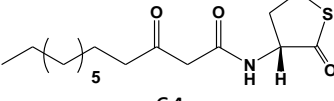
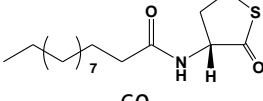
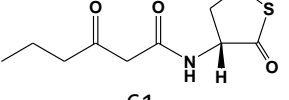
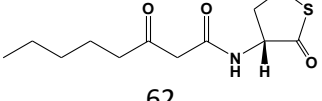
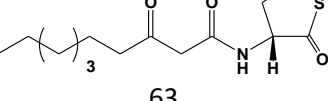
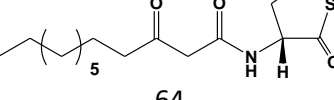
Acyl-chain vs 3-oxoacyl-chain effects

A very interesting pattern develops with 3-oxoacyl-chain derivatives (Table 13). Compared with their acyl-chain counterparts, 3-oxoacyl analogs have much less inhibitory characteristics, indicated by their significantly higher IC<sub>50</sub> values (621.2 ± 49.5 μM vs 387.3 ± 88.6 μM for compounds 55 and 46, respectively; and 127.4 ± 70.2 μM vs 11.4 ± 1.5 μM for compounds 64 and 60, respectively). Furthermore, varying the chain

length significantly alters its behavior. As discussed above, shortening the chain seems to decrease the inhibitory characteristics of the analog. The decrease in the inhibitory characteristic due to having a carbonyl at the C3 position combined with the short-chain effect appears to have a synergistic result of activating RhII activity. While 3-oxoC8-D-HSL (compound 35) inhibited RhII with  $IC_{50}$  value of  $282.0 \pm 34.1 \mu\text{M}$ , shortening the 3-oxoacyl-chain to 3-oxoC6 chain (compound 34) caused the derivative to activate RhII with  $EC_{50}$  value of  $224.4 \pm 55 \mu\text{M}$ . The same pattern holds true with 3-oxoacyl-D-thiolactone analogs. While 3-oxoC12-D-thiolactone, the long-chain derivative, inhibited RhII with  $IC_{50}$  value of  $127.4 \pm 70.2 \mu\text{M}$ , shorter chain analogs activated RhII. However, until the long-chain effect caused 3-oxoC12-D-thiolactone (compound 64) to be an inhibitor, lengthening the chain from 3-oxoC6-D-thiolactone (compound 61) to 3-oxoC8-D-thiolactone (compound 62) and then to 3-oxoC10-D-thiolactone (compound 63) heightened RhII activation, shown by decreasing  $EC_{50}$  values of  $1506 \pm 109.9 \mu\text{M}$ ,  $854.5 \pm 74.4 \mu\text{M}$ , and  $57.1 \pm 22.7 \mu\text{M}$ , respectively. Although the  $EC_{50}$  values decrease as the chain length increase, the maximum activation also decrease as the chain lengthens. Activation is usually indicative of a presence of an allosteric site. Moreover, if the 3-oxoacyl-chains bind to and occupy the RhII acyl-chain binding pocket, it is inconceivable that the acyl-chain from C4-ACP can also bind to the acyl-chain binding pocket, further supporting hypothesis 2.



**Table 13. Patterns in varying effects of acyl- and 3-oxoacyl-chain derivatives.**

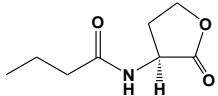
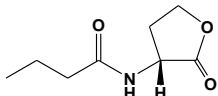
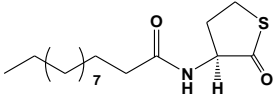
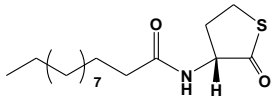
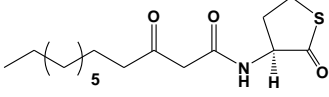
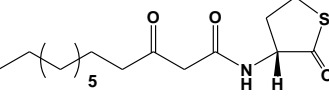
Compound	IC <sub>50</sub> /EC <sub>50</sub> (μM) % Inhibition/Activation	IC <sub>50</sub> and EC <sub>50</sub> Trends <sup>a</sup>
 34	EC <sub>50</sub> : 224.4 ± 55 100% A	Activation
 35	IC <sub>50</sub> : 282.0 ± 34.1 60% I	Inhibition
 55	IC <sub>50</sub> : 621.2 ± 49.5 60% I	Weaker Inhibition
 46	IC <sub>50</sub> : 387.3 ± 88.6 60% I	Stronger Inhibition
 64	IC <sub>50</sub> : 127.4 ± 70.2 50% I	Weaker Inhibition
 60	IC <sub>50</sub> : 11.4 ± 1.5 30% I	Stronger Inhibition
 61	EC <sub>50</sub> : 1506 ± 109.9 100% A	Weak Activation
 62	EC <sub>50</sub> : 854.5 ± 74.4 60% A	
 63	EC <sub>50</sub> : 57.1 ± 22.7 40% A	Strong Activation
 64	IC <sub>50</sub> : 127.4 ± 70.2 50% I	Inhibition

a = On a relative scale

### Headgroup chirality effect

The D-stereocenter derivatives were found to have much greater effect on RhII enzymatic rate than their L-stereocenter counterparts (Table 14). While the native AHL product, C4-L-HSL, did not inhibit RhII, change of the headgroup chirality to C4-D-HSL transformed it to a weak inhibitor. Whereas both C12-L-thiolactone (compound 60) and 3-oxoC12-L-thiolactone (compound 64) both inhibited RhII, the IC<sub>50</sub> value dropped by 34-fold and 5-fold, respectively for their corresponding D-stereocenter counter parts (compounds 46 vs 60 and 55 vs 64).

**Table 14. Effects of varying the headgroup chirality from L to D stereoisomer.**

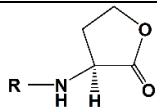
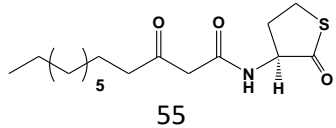
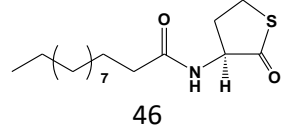
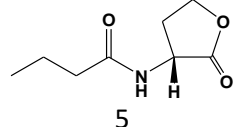
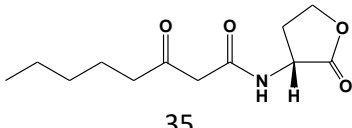
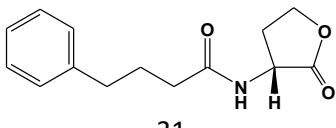
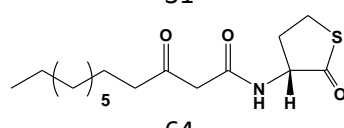
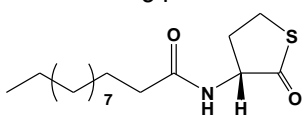
Compound	IC <sub>50</sub> (μM) % Inhibition	IC <sub>50</sub> Trends <sup>a</sup>
 1	None 0%	No Inhibition
 5	687.7 ± 90.7 40%	Weak Inhibition
 46	387.3 ± 88.6 60%	Weaker Inhibition
 60	11.4 ± 1.5 30%	Stronger Inhibition
 55	621.2 ± 49.5 60%	Weaker Inhibition
 64	127.4 ± 70.2 50%	Stronger Inhibition

a = On a relative scale

### Headgroup hydrophilicity effect

Reducing the hydrophilicity of the headgroup by replacing homoserine lactone with homocysteine thiolactone head made a marked increase in the magnitude of the effect on RhII inhibition and activation (Table 15). While no L-HSL derivatives inhibited RhII, C12-L-thiolactone and 3-oxo-C12-L-thiolactone were shown to be inhibitors of the AHL synthase. With D-HSL derivatives, IC<sub>50</sub> values ranged from 687.7 to 20.2 μM (compounds 5 and 31), which was significantly reduced to 127.4 to 11.4 μM (compounds 64 and 60) by replacing D-HSL with a more hydrophobic D-thiolactone headgroup.

**Table 15. The effect of headgroup hydrophobicity on RhII inhibition.**

Compound	IC <sub>50</sub> (μM) % Inhibition	IC <sub>50</sub> Trends <sup>a</sup>
 All 3-oxoacyl-/3-hydroxyacyl/acyl-L-HSL	No effect 0%	No Inhibition
 55	621.2 ± 49.5 60%	Weaker Inhibition
 46	387.3 ± 88.6 60%	Stronger Inhibition
 5	687.7 ± 90.7 40%	Weaker Inhibition
 35	282.0 ± 34.1 60%	Weaker Inhibition
 31	20.2 ± 10.1 25%	Weaker Inhibition
 64	127.4 ± 70.2 60%	Weaker Inhibition
 60	11.4 ± 1.5 60%	Stronger Inhibition
a = On a relative scale		

### Determining Kinetic Constants with various Acyl-ACPs

To determine the effect of the acyl-chain variation on acyl-ACP substrate catalytic efficiencies, RhII activity was assayed with butanoyl-ACP (compound 83; Chapter 1, Table 6), the native substrate, and then with four long-chain substrates: C6-ACP, C8-ACP, C10-ACP, and C12-ACP (compounds 84-87). The reaction setup was

based on published reaction conditions for previous studies on RhlII with its native C4-ACP substrate. The acyl-ACP was the variable substrate while SAM was kept to 300  $\mu\text{M}$  (Figure 39). As expected, the highest initial enzyme rate was achieved with the native substrate, C4-ACP, with a  $k_{\text{cat}}$  value of  $3 \pm 0.3 \text{ min}^{-1}$ . This was followed by  $k_{\text{cat}}$  values of  $0.86 \pm 0.03 \text{ min}^{-1}$ ,  $0.64 \pm 0.02 \text{ min}^{-1}$ ,  $0.39 \pm 0.01 \text{ min}^{-1}$ , and  $0.61 \pm 0.01 \text{ min}^{-1}$  for C6-, C8-, C10-, and C12-ACPs, respectively. The  $K_{\text{m}}$  value for the native product was found to be  $7 \pm 2 \mu\text{M}$ . Typically, non-native substrates have higher  $K_{\text{m}}$  value than that of the native substrate.<sup>22</sup> However, contrary to expectation, the  $K_{\text{m}}$  value decreased as the acyl-chain lengthened:  $1.2 \pm 0.2 \mu\text{M}$  for C6-ACP,  $0.21 \pm 0.06 \mu\text{M}$  for C8-ACP,  $0.16 \pm 0.03 \mu\text{M}$  for C10-ACP, and  $0.26 \pm 0.05 \mu\text{M}$  for C12-ACP. Although both  $K_{\text{m}}$  and  $k_{\text{cat}}$  values both decreased,  $K_{\text{m}}$  dropped more precipitously, causing the catalytic efficiency, determined by  $k_{\text{cat}}/K_{\text{m}}$ , to be much greater for the non-native substrate than that of the native substrate as summarized in Table 16 (Figure 40).

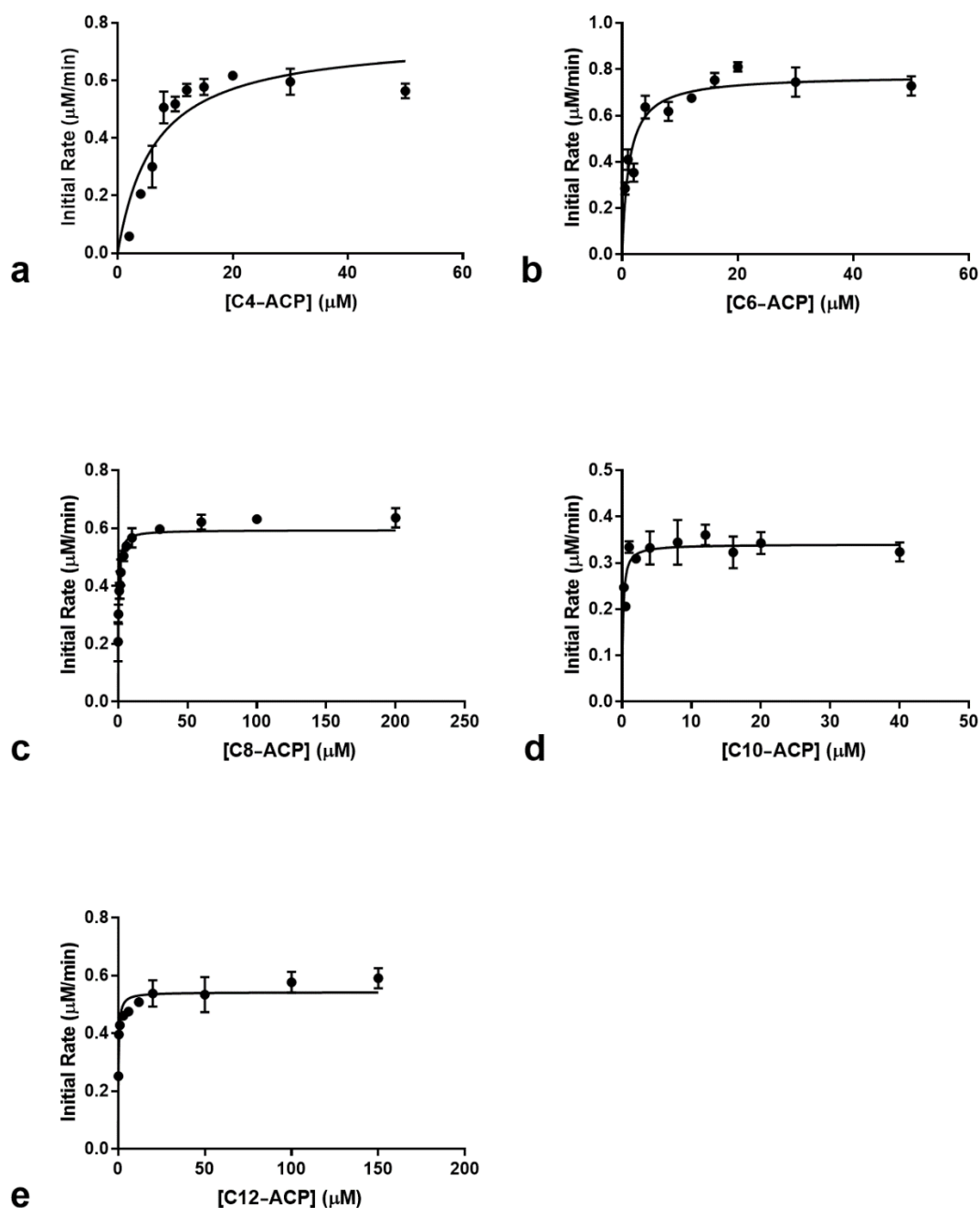


**Figure 39. Substrate-velocity curves of RhlI with native and nonspecific acyl-ACP substrates.** RhlI initial rates as a function of acyl-ACP substrate concentration at fixed 300 μM SAM. (a) varying [C4-ACP] and 0.3 μM RhlI, (b) varying [C6-ACP] and 0.9 μM RhlI, (c) varying [C8-ACP] and 0.9 μM RhlI, (d) varying [C10-ACP] and 0.9 μM RhlI, and (e) varying [C12-ACP] and 0.9 μM RhlI. As the acyl-chain length of acyl-ACP increases,  $V_{\max}$  is reached at lower acyl substrate concentrations, indicative of decreasing  $K_m$  values.

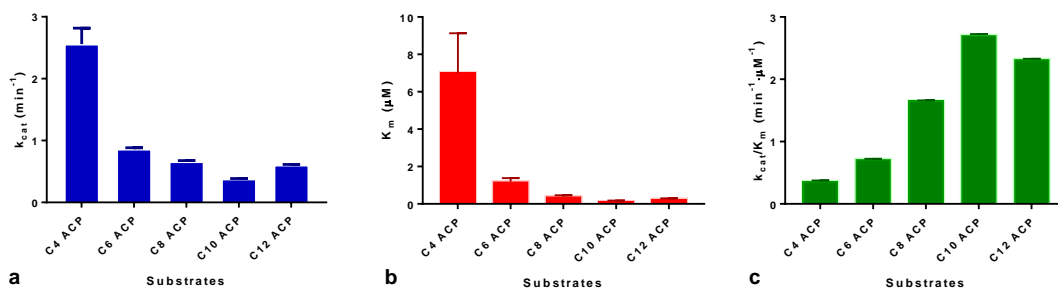


**Figure 40.** Trends in  $k_{cat}$ ,  $K_m$ , and  $k_{cat}/K_m$  values of RhII with various acyl substrates. As the acyl-chain deviates further from the native substrate, both the (a)  $k_{cat}$  and the (b)  $K_m$  values decrease. However,  $K_m$  drops much faster than  $k_{cat}$ , which leads to (c) the catalytic efficiency,  $k_{cat}/K_m$ , to rise with longer acyl moiety.

**Table 16.** RhII initial enzyme rate with various acyl-ACP substrates

Acyl-ACP	[RhII] (μM)	$k_{cat}$ (min <sup>-1</sup> )	$K_m$ (μM)	$k_{cat}/K_m$ (μM <sup>-1</sup> min <sup>-1</sup> )	$k_{cat}/K_m$ (Relative) <sup>a</sup>
C4-ACP	0.3	2.6 ± 0.3	7 ± 2	0.36 ± 0.01	100.0
C6-ACP	0.9	0.86 ± 0.02	1.2 ± 0.2	0.719 ± 0.003	197.4
C8-ACP	0.9	0.66 ± 0.02	0.40 ± 0.06	1.655 ± 0.006	454.1
C10-ACP	0.9	0.378 ± 0.009	0.14 ± 0.04	2.71 ± 0.02	743.2
C12-ACP	0.9	0.60 ± 0.01	0.26 ± 0.03	2.324 ± 0.006	637.6

a = [( $k_{cat}/K_m$ )/0.36]

Crystal structures have shown many AHL synthases to have similar structure, all having specific ACP binding site, SAM binding site, and acyl-chain binding pocket.<sup>60-63</sup> The acyl-chain binding pocket is easily recognizable by its V-cleft shape, which has a definite spatial limitation to only accommodate acyl-chains of specific size. Moreover, previous studies from the Nagarajan laboratory have shown that variations in the acyl-chain from the native substrate significantly reduce the enzymatic rate of AHL synthases.<sup>22, 60</sup> This pattern of behavior allows the bacteria to discriminate against the synthesis of wrong signals, conserve resources, and increase the signal-to-noise ratio of its own signal molecules. Therefore, the higher catalytic efficiency non-native acyl substrate with RhII poses a serious conundrum. One possible cause for this phenomenon

could be with the ACP protein. *Pseudomonas aeruginosa* genome codes for three different acyl carrier proteins: ACP1, ACP2, and ACP3.<sup>51</sup> RhII has been shown to react with C4-ACP1 and C4-ACP2 substrates with comparable catalytic efficiency but with much greater catalytic efficiency than *E. coli* ACP-using substrate, which, in turn, has much higher catalytic efficiency than C4-ACP3. However, this work was conducted using *E. coli* ACP since *P. aeruginosa* ACPs and *E. coli* ACP share similar sequences and to provide a common reference point to compare various AHL synthases (Figure 41). Mair Churchill's work with LasI (another AHL synthase found in *P. aeruginosa*) showed that when LasI is expressed in *E. coli* with access to *E. coli* ACP only, the amount of non-native AHL products is significantly higher than when LasI is expressed in *P. aeruginosa* (Figure 42).<sup>64</sup> Additionally, alkyl-CoA inhibition test (see [Alkyl-CoA inhibition](#) section below) also seems to indicate that the ACP moiety plays an important role in binding with RhII. Therefore, the pattern of higher catalytic efficiency with longer-chain acyl-ACP could be an artifact of using a non-native ACP and could be removed by using *P. aeruginosa* ACP. Nevertheless, regardless of the ACP-effect, that RhII can accommodate long acyl-chain is surprising. As noted above, this phenomenon can be explained if longer acyl-chains have higher  $k_{off}$  rate (hypothesis 1) or if RhII has an allosteric site with equal or higher affinity for acyl-chains of various length than the acyl-chain binding pocket (hypothesis 2). Under hypothesis 1, the increasing catalytic efficiencies with longer acyl-chains could be due to higher  $k_{on}$  rate while the decreasing  $k_{cat}$  rate could be caused by higher  $k_{off}$  value. If hypothesis 2 is correct, it is possible that the allosteric site promotes binding while the acyl-chain binding pocket promotes reaction catalysis, analogous to kinetic vs. thermodynamic controls of reaction. The



feasibility of these proposals was examined by analyzing the inhibition patterns of inhibitors of various hydrocarbon tail length.

```

P.a. ACP1  -MSTIEERVKKIVAEQLGVKEEEVTNSASFVEDLGADSLDTVELVMALEE
P.a. ACP3  -MDDIETRVRKLVAAARFGVEECDIRLDSDFRNDFGAESLEVVELVMALEA
P.a. ACP3  MPNDMEDHLLTVLSVASGVPKEEISRDS-RMEDLAFDSLTVVSELSLKLKRLK
E.c. ACP   -MSTIEERVKKIIGEQLGVKQEEVTNNASFVEDLGADSLDTVELVMALEE
          . : *  ::  ....  **  :  ::  .:  : * . . : * * .  **  :  * .

P.a. ACP1  EFETEIPDE-KEKITTVQEAIDYIVAHQQ-
P.a. ACP3  EFGVEIADDDAERIETVRQAIDYLEEAVPT
P.a. ACP3  EFGVTGVDDDELDDLETVDLQFQVVEKHRAA
E.c. ACP   EFDTEIPDEEAEKITTVQAIDYINGHQA-
          ** .  * :  : : * *  : : :

```

**Figure 41.** Alignment of amino acid sequence of *P. aeruginosa* ACP1, ACP3, and *E. coli* ACP. The conserved residues are noted with an asterisk (\*), mostly conserved residues with a colon (:), and semi-conserved residues with a period (.).

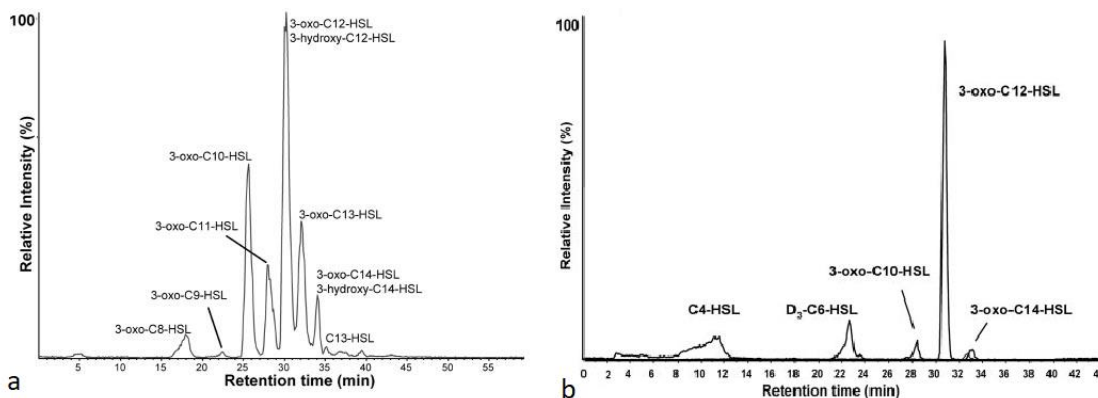


**Figure 42.<sup>64</sup>** Various AHL products of LasI. AHL profiles of (a) *E. coli* strain and (b) *P. aeruginosa* strain were determined by liquid chromatography-mass spectrometry (LC-MS). With access to native *P. aeruginosa* ACP, 3-oxoC12 HSL is the major AHL product with limited amount of other AHLs. However, with *E. coli* ACP, there are significant amounts of non-native AHL formation, signifying that ACP plays a significant role in acyl-ACP specificity found in AHL synthases.

### Alkyl-ACP Inhibition

The effect of hydrocarbon chain length was tested using alkyl-ACPs, also known as inert-ACP or IACP. The removal of the carbonyl group from acyl-ACP converts the

highly reactive thioester bond to relatively nonreactive thioether bond, making alkyl-ACPs inactive analogs of acyl-ACP (Figure 43). The  $IC_{50}$  values of butyl-, hexyl-, octyl-, and decyl-ACPs (compounds 88-91; Chapter 1, Table 6) with RhII were determined to be  $9.9 \pm 4 \mu\text{M}$ ,  $0.74 \pm 0.4 \mu\text{M}$ ,  $0.068 \pm 0.02 \mu\text{M}$ , and  $0.102 \pm 0.04 \mu\text{M}$ , respectively (Table 17; Figure 44). Although the  $IC_{50}$  values decrease as the alkyl chain lengthens, the maximum inhibition (indicated by %Rate) also decrease from 50% inhibition with C4-IACP to 20% inhibition with all other IACPs (Table 17). This pattern of partial inhibition suggests the presence of less active form of enzyme, indicative of allosteric inhibition.

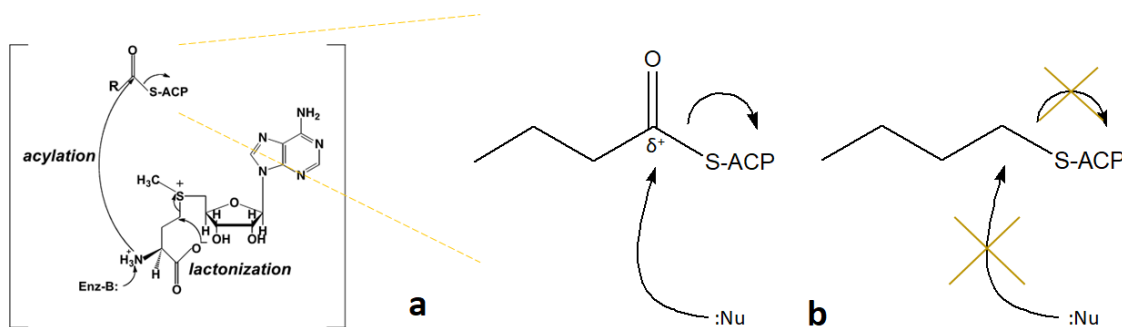


**Figure 43. Designing inactive acyl-ACP analog.** (a) In acyl-ACP, the carbonyl group is a part of unstable thioester bond and creates a zone of electronegativity suitable for nucleophilic attack. However, (b) the removal of the carbonyl group in alkyl-ACP forms relatively stable thioether bond unfavorable to nucleophilic attack, thus forming inert-ACP (IACP) analog of the acyl substrate.

**Table 17. Effect of IACP on RhII initial enzyme rate.**

IACP	$IC_{50}$ ( $\mu\text{M}$ )	% Inhibition	$K_i$ ( $\mu\text{M}$ )
<b>C4-IACP</b>	$9.9 \pm 4$	50	$15.9 \pm 0.9$
<b>C6-IACP</b>	$0.74 \pm 0.4$	20	$10.6 \pm 1.1$
<b>C8-IACP</b>	$0.058 \pm 0.02$	20	$6.5 \pm 0.7$
<b>C10-IACP</b>	$0.102 \pm 0.04$	20	$4.8 \pm 0.3$

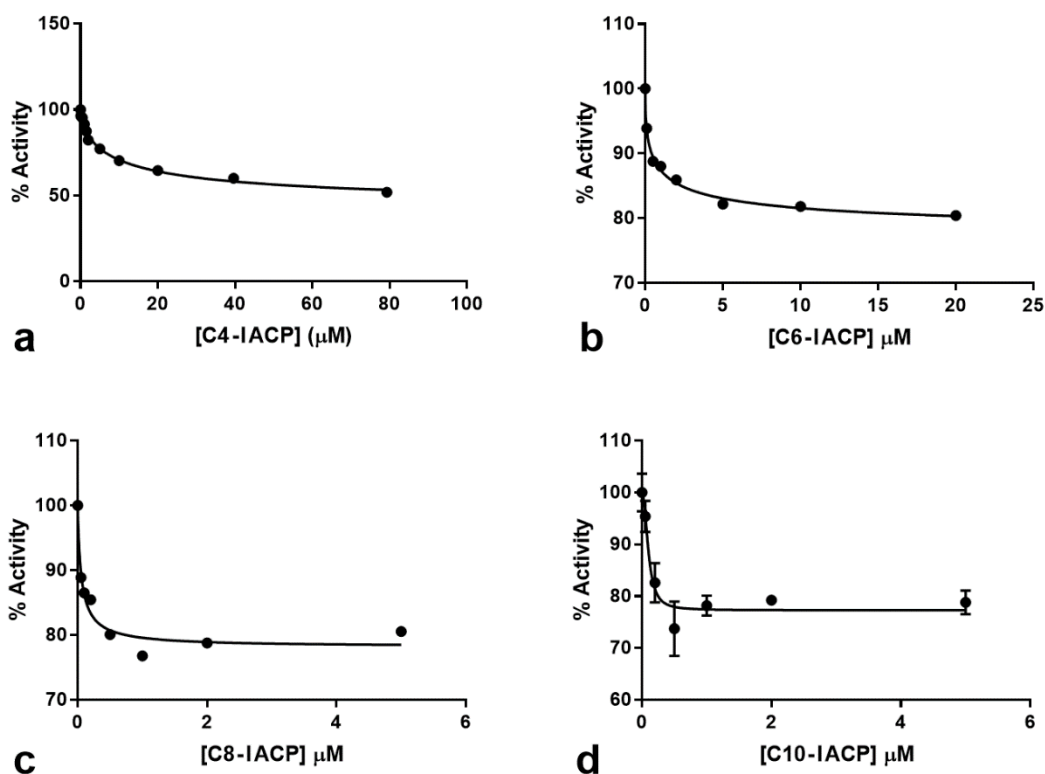


**Figure 44. IC<sub>50</sub> test of various IACPs.** The initial rate of RhII with 300 μM of SAM and 14 μM of C4-ACP in the presence of varying concentrations of (a) C4-, (b) C6-, (c) C8-, and (d) C10-IACPs were determined. Whereas C4-IACP, the native substrate analog, achieved the maximum inhibition (~50% inhibition compared to ~20% for all others), other IACPs reached minimum activity at much lower inhibitor concentration.

Given that these four IACPs all inhibit RhII, the mode of inhibition of these IACPs could shed light to how RhII copes with longer acyl-chains. Competitive inhibition would definitively indicate that the IACPs are competing with butanoyl-ACP for the same binding site and that RhII acyl-chain binding pocket can accommodate longer chains. On the contrary, uncompetitive mode of inhibition could be a result of the IACP binding after AHL departs from the active site (hypothesis 1) or it could signify that the IACP is not competing for the acyl-chain binding pocket and support the hypothesis of longer chains binding to nonspecific site. Similarly, noncompetitive inhibition could be a result of the inhibitor-free enzyme (EI) complex formed before

E·SAM complex formation (hypothesis 1) or if the inhibitor binding to the hypothetical alternate/allosteric acyl-chain binding site (hypothesis 2). Plotting the double reciprocal (Lineweaver-Burk plot) of initial RhII rate versus variable C4-ACP concentrations at various fixed IACP concentrations show a set of lines intersecting each other at the x-axis, indicative of noncompetitive-mode of inhibition (Figure 45). Further analysis using the Akaike's method (AIC; see equations 24, 25), confirms that all the inhibition data is best fitted by noncompetitive inhibition model (Table 16). This finding is especially surprising for C4 IACP, since its similarity with the native substrate, C4-ACP, led to the prediction that would competitively inhibit RhII activity. As predicted by the  $IC_{50}$  values,  $K_i$  values decrease as the alkyl-chain lengthened (Table 18). If the inhibition is due to alkyl-ACP binding to free RhII before SAM binding with RhII, the drop in the overall inhibition with longer alkyl chains could be due to higher  $k_{off}$  rate while the decrease in  $K_i$  ( $K_i = k_{off}/k_{on}$ ) could be a result of long-chain ACPs having even higher  $k_{on}$  rate. However, the noncompetitive mode of inhibition and the drop in both  $K_i$  and overall inhibition could be due to hydrocarbon chains binding with equal or higher affinity to an alternative acyl-chain binding sites than to the acyl-chain binding pocket. Although the alternative pocket is yet to be identified, inhibition data with IACPs and ICoAs (see "Alkyl-CoA Inhibition" section below) suggest that the acyl-chain binding pocket of the alternative binding site would most likely be close enough or overlap with the native acyl-chain pocket in RhII.

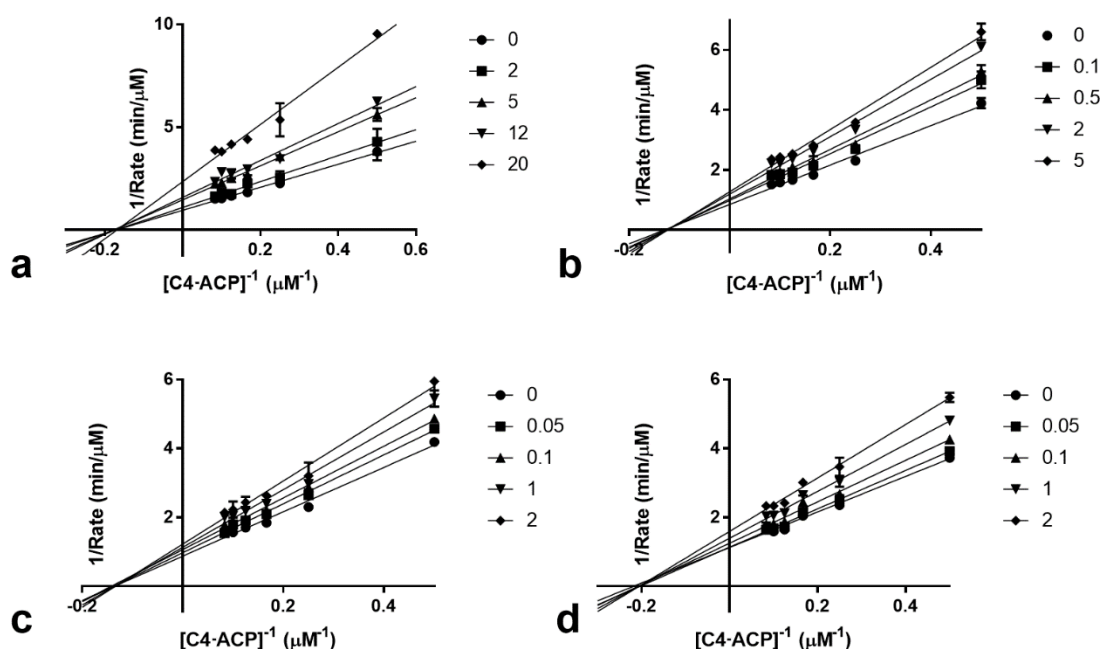


**Figure 45. Double Reciprocal Plot of RhII activity with varying C4-CP concentrations and various fixed IACP concentrations.** Double reciprocal of initial rate of RhII activity vs. C4-ACP concentration in the presence of various fixed concentrations of (a) C4-IACP, (b) C6-IACP, (c) C8-IACP, and (d) C10-IACP was plotted. The fixed IACP concentrations were chosen to be 0, below the  $IC_{50}$  value, around the  $IC_{50}$  value, and two above the  $IC_{50}$  value. While keeping the IACP concentration fixed, C4-ACP concentration was varied from 2 to 20  $\mu\text{M}$ . The inverse of the initial rate was plotted against inverse of the C4-ACP concentration which revealed a set of lines intersecting near the x-axis, indicative of noncompetitive mode of inhibition.

**Table 18. Determining best fit model for the mode of inhibition using AIC**

Analog	Mode	N <sup>a</sup> vs C <sup>b</sup>	N vs U <sup>c</sup>	N vs M <sup>d</sup>
C4-IACP	Noncompetitive	>99.99 N	99.99 N	67.00 N
C6-IACP	Noncompetitive	99.87 N	91.03 N	74.41 N
C8-IACP	Noncompetitive	99.87 N	82.48 N	75.70 N
C10-IACP	Noncompetitive	>99.99 N	96.94 N	75.72 N
a = Noncompetitive mode of inhibition				
b = Competitive mode of inhibition				
c = Uncompetitive mode of inhibition				
d = Mixed mode of inhibition				

A pure noncompetitive mode of inhibition could be a result of nonspecific, non-mechanistic enzyme deactivation. To determine whether IACP inhibition is a specific

effect, RhII was incubated with C4-IACP and C8-IACP for 0 to 60 min and the  $IC_{50}$  was taken at various time points. Preincubation of RhII with IACP did not significantly alter the inhibitory effects of IACPs, indicating that the inhibition was due to specific binding of IACP to RhII (Figure 46).

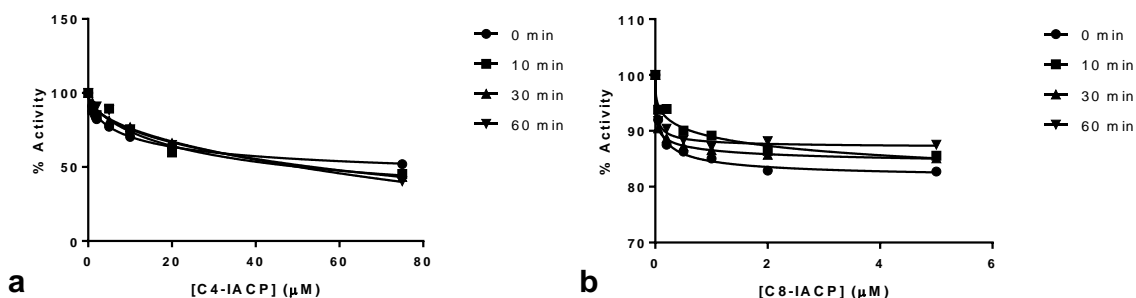


**Figure 46. Time-dependency of IACP inhibition.** RhII was preincubated with varying concentrations of (a) C4- and (b) C8-IACPs for 0 to 60 minutes. The AHL synthase reaction was initiated by the addition of RhII + IACP mixture to reaction mixtures consisting of 300  $\mu$ M SAM and 14  $\mu$ M C4-ACP. With both C4- and C8-IACP, the variations in RhII activity remained under 5% as incubation time changed from 0 to 60 minutes, eliminating the possibility of nonspecific, nonmechanistic inhibition of RhII by IACPs.

### Alkyl-CoA Inhibition

To differentiate the contribution of the hydrocarbon tail and the ACP moieties in binding affinity with RhII, inhibition of enzyme activity with butyl-, hexyl-, and octyl-CoAs (C4-, C6-, and C8-ICoAs; compounds 92-94, respectively; Chapter 1, Table 3) were investigated in greater detail. RhII initial rate was observed at a fixed C4-ACP concentration and variable ICoA concentrations (Figure 47). The  $IC_{50}$  values of the ICoAs were calculated from the data (Table 19). The  $IC_{50}$  values of ICoAs are about one hundred times greater than the  $IC_{50}$  values of corresponding IACPs:  $72.7 \pm 13$  vs  $0.74 \pm 0.4$   $\mu$ M for C6-ICoA and C6-IACP, respectively; and  $5.1 \pm 0.8$  vs  $0.058 \pm 0.02$   $\mu$ M for C8-ICoA and C8-IACP, respectively. However, the sub-10  $\mu$ M  $IC_{50}$  values for ICoAs

and IACPs are significantly lower than most of the  $IC_{50}$ 's obtained with AHL analogs and no inhibition achieved with fatty acid tail alone, suggesting that ACP-pantetheine (holo-ACP) moieties contribute significantly to the potency of the binding affinity. (Appendix Figure C15)

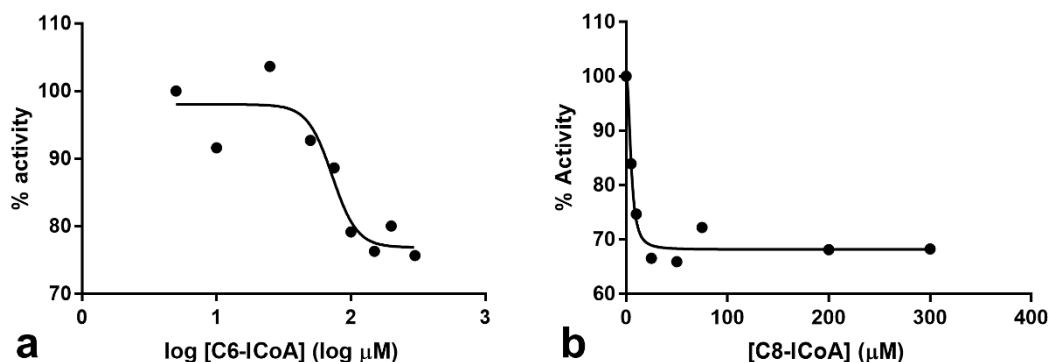


**Figure 47.**  $IC_{50}$  test of various ICoAs. The initial rate of RhII with 300  $\mu\text{M}$  of SAM and 14  $\mu\text{M}$  of C4-ACP in the presence of varying concentrations of (a) C6- and (b) C8-ICoAs were determined.

**Table 19.** Effect of ICoA on RhII initial enzyme rate with fixed C4 -ACP concentration.

ICoA	$IC_{50}$ ( $\mu\text{M}$ )
C4-ICoA	None up to 1 mM
C6-ICoA	$72.7 \pm 13$
C8-ICoA	$5.1 \pm 0.8$

### Conclusion

This project represents the first effort to use AHL-based small molecules as modulators of AHL-synthases.

We hypothesize that acyl-homoserine lactone based inhibitors would be quorum sensing-specific inhibitors binding to both acyl-chain binding pocket and SAM binding site. By varying headgroup polarity and chirality along with acyl-chain size and

substitution, we have identified key characteristics to improve inhibition and activation (Figure 48). A long or bulky acyl-chain with headgroup of increased hydrophobicity and D-stereocenter is required to inhibit RhII. A slightly more hydrophobic headgroup with D-stereocenter acylated with 3-oxoacyl-chain of medium-long length (6-10 carbons long) yielded the best activators of RhII. We also found that the fatty acid tail group and the headgroup cannot independently inhibit RhII activity. Second generation of AHL-based modulators of RhII activity could include bicyclic headgroups with various substitutions to better fine-tune the levels of hydrophobicity and probe yet-to-be-identified characteristics of the headgroup binding sites.

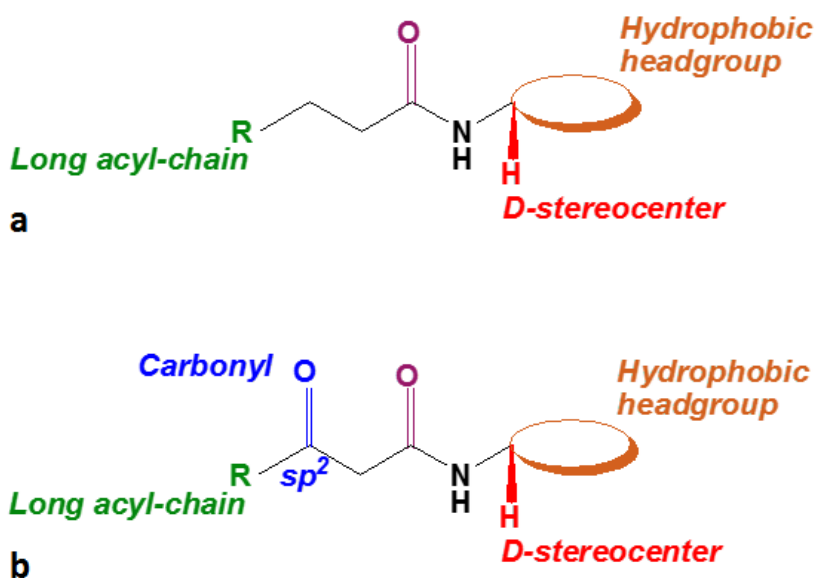


**Figure 48. Moieties of interest for improved AHL-based RhII modulators.** Inhibitors (a): hydrophobic headgroup with D-stereocenter acylated with long chain; Activators (b): long 3-oxoacyl-chain attached to hydrophobic headgroup with D-stereocenter.

The discovery of AHL-based small molecule inhibitors of RhII is promising.

Since antibiotic resistance is often a QS-controlled phenotype, QS inhibitor with limited potency could be used as a combination drug to reduce antibiotic resistance to further the



usability of currently available drugs. Furthermore, if AHL analogs could target both RhII and RhIR, its inhibition potency could be significantly heightened to make it a viable QS inhibitor. Therefore, despite the failure of the current library of AHL analogs to inhibit RhII with sub-micromolar  $IC_{50}$ , AHL-based modulators of quorum sensing merit further research.

However, focusing strictly on AHL synthase inhibition, AHL-analogs were heavily outcompeted. Although targeting acyl-chain and SAM binding sites with AHL analogs allow for QS-specific modulation, fatty-acid, IACP, and ICoA inhibition data suggest that much greater binding energy is associated with the pantetheine and ACP binding sites (Figure 49). To maximize both specificity and potency, the next generation of AHL synthase inhibitors could be designed to target SAM binding site with ACP or pantetheine binding sites.

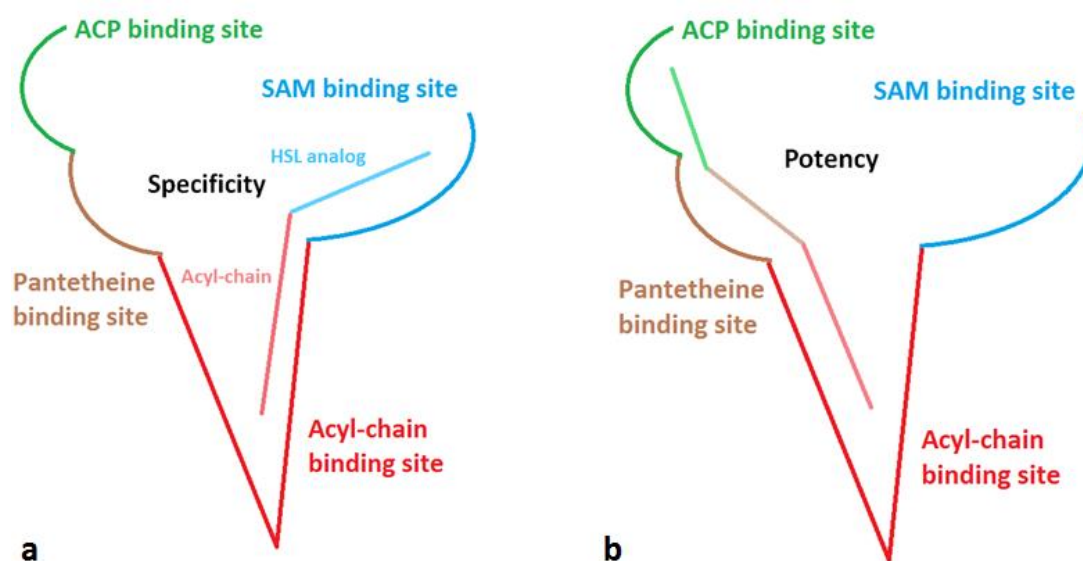


**Figure 49. Specificity vs. Potency in targeting RhII.** Acyl-ACP and SAM are commonly used substrates in human enzymes; therefore, (a) by targeting both acyl-chain binding pocket and SAM binding site, AHL-synthase-specific inhibitor could be designed. However, this study has demonstrated that (b) the pantetheine and ACP binding sites need to be targeted for more potent inhibition of RhII.

We proposed two hypotheses to explain the trends we see with aliphatic-chain length and RhII activity. As the acyl-chain length increases, the  $IC_{50}$ ,  $K_i$ , and percent inhibition all decrease for AHL-based RhII inhibitors while  $K_m$  and  $k_{cat}$  decreases for corresponding acyl-ACP substrates. The decrease in  $K_m$  was much steeper than the decrease in  $k_{cat}$  for longer-chain acyl-ACP substrates, leading to an increase in catalytic efficiencies for longer-chain non-native substrates relative to C4-ACP. In addition, as the alkyl-chain length increases, inhibition increase as observed by significant decreases in  $IC_{50}$  and  $K_i$  values for the longer-chain analogs; however, the percent inhibition also decreased. This acyl-chain pattern could be due to higher  $k_{off}$  rate and even higher  $k_{on}$  rate for longer-chain compounds binding to RhII. Higher  $k_{off}$  rate would cause less potent effect (lower overall inhibition) while higher  $k_{on}$  rate would cause the  $K_i$  value to decrease, indicative of higher binding affinity. However, this trend could be caused by the presence of an alternative acyl-chain binding site (or allosteric site). That all the inhibitors discovered in this study were partial inhibitors suggests allosteric inhibition. This proposal of a possible alternate acyl-chain binding site is further supported by the presence of activators. If the 3-oxoacyl-chains of the activators were to bind with the acyl-chain binding pocket, as indicated by hypothesis 1, it would inhibit C4-ACP binding; however, under hypothesis 2, the 3-oxoacyl-chains would bind with the alternate site. The binding could cause changes to RhII tertiary structure and form a structural configuration more favorable for catalysis to occur. Furthermore, hypothesis 2 raises another question: how could long-chain derivatives binding to one allosteric site cause both activating and inhibiting behaviors? We hypothesize that these effects could be due to either a) the carbonyl at the C3 position alters the mode of binding for activators

compared with inhibitors; or (b) there could be more than one allosteric site, one for inhibition and another for activation. Co-crystal structures of activators and inhibitors complexed with RhII should provide light on some of these unanswered questions. Although we have not found a submicromolar inhibitor for AHL synthase in this thesis yet, our research efforts on AHL derivatives as potential quorum sensing modulators should open new doors to develop quorum sensing specific inhibitors for pathogenic bacteria. In conclusion, the combination of scarcity of antibacterials in the drug pipeline, increasing resistance to antibiotics, and favorable pharmaceutical qualities of AHL derivatives as novel antivirulent molecules merit further research in this area.

## REFERENCES

1. Michaelidis, C. I.; Fine, M. J.; Lin, C. J.; Linder, J. A.; Nowalk, M. P.; Shields, R. K.; Zimmerman, R. K.; Smith, K. J., The hidden societal cost of antibiotic resistance per antibiotic prescribed in the United States: an exploratory analysis. *BMC Infect Dis* **2016**, *16* (1), 655.
2. Obama, B., Executive Order -- Combating Antibiotic-Resistant Bacteria. House, T. W., Ed. U.S.A., 2014.
3. Chan, M. WHO Director-General addresses G7 health ministers meeting on antimicrobial resistance. <http://www.who.int/dg/speeches/2015/g7-antimicrobial-resistance/en/> (accessed August 8, 2017).
4. Baym, M.; Lieberman, T. D.; Kelsic, E. D.; Chait, R.; Gross, R.; Yelin, I.; Kishony, R., Spatiotemporal microbial evolution on antibiotic landscapes. *Science* **2016**, *353* (6304), 1147-51.
5. Clatworthy, A. E.; Pierson, E.; Hung, D. T., Targeting virulence: a new paradigm for antimicrobial therapy. *Nat Chem Biol* **2007**, *3* (9), 541-8.
6. Ventola, C. L., The antibiotic resistance crisis: part 1: causes and threats. *P T* **2015**, *40* (4), 277-83.
7. Piddock, L. J., The crisis of no new antibiotics--what is the way forward? *Lancet Infect Dis* **2012**, *12* (3), 249-53.
8. Dwidar, M.; Monnappa, A. K.; Mitchell, R. J., The dual probiotic and antibiotic nature of *Bdellovibrio bacteriovorus*. *BMB Rep* **2012**, *45* (2), 71-8.
9. Shanks, R. M.; Kadouri, D. E., Predatory prokaryotes wage war against eye infections. *Future Microbiol* **2014**, *9* (4), 429-32.
10. Loc-Carrillo, C.; Abedon, S. T., Pros and cons of phage therapy. *Bacteriophage* **2011**, *1* (2), 111-114.
11. Toke, O., Antimicrobial peptides: new candidates in the fight against bacterial infections. *Biopolymers* **2005**, *80* (6), 717-35.
12. Citorik, R. J.; Mimee, M.; Lu, T. K., Sequence-specific antimicrobials using efficiently delivered RNA-guided nucleases. *Nat Biotechnol* **2014**, *32* (11), 1141-5.
13. Hentzer, M.; Givskov, M., Pharmacological inhibition of quorum sensing for the treatment of chronic bacterial infections. *J Clin Invest* **2003**, *112* (9), 1300-7.
14. Totsika, M., Benefits and Challenges of Antivirulence Antimicrobials at the Dawn of the Post-Antibiotic Era. *Current Medicinal Chemistry* **2016**, *6* (1), 30-37.
15. Fuqua, C.; Winans, S. C.; Greenberg, E. P., Census and consensus in bacterial ecosystems: the LuxR-LuxI family of quorum-sensing transcriptional regulators. *Annu Rev Microbiol* **1996**, *50*, 727-51.
16. Fuqua, C.; Greenberg, E. P., Self perception in bacteria: quorum sensing with acylated homoserine lactones. *Curr Opin Microbiol* **1998**, *1* (2), 183-9.
17. Bassler, B. L.; Losick, R., Bacterially speaking. *Cell* **2006**, *125* (2), 237-46.

18. Geske, G. D.; O'Neill, J. C.; Blackwell, H. E., Expanding dialogues: from natural autoinducers to non-natural analogues that modulate quorum sensing in Gram-negative bacteria. *Chem Soc Rev* **2008**, *37* (7), 1432-47.
19. Gerdt, J. P.; Blackwell, H. E., Competition studies confirm two major barriers that can preclude the spread of resistance to quorum-sensing inhibitors in bacteria. *ACS Chem Biol* **2014**, *9* (10), 2291-9.
20. Chen, C. C.; Riadi, L.; Suh, S. J.; Ohman, D. E.; Ju, L. K., Degradation and synthesis kinetics of quorum-sensing autoinducer in *Pseudomonas aeruginosa* cultivation. *J Biotechnol* **2005**, *117* (1), 1-10.
21. Camilli, A.; Bassler, B. L., Bacterial small-molecule signaling pathways. *Science* **2006**, *311* (5764), 1113-6.
22. Montebello, A. N.; Brecht, R. M.; Turner, R. D.; Ghali, M.; Pu, X.; Nagarajan, R., Acyl-ACP substrate recognition in *Burkholderia mallei* BmaI1 acyl-homoserine lactone synthase. *Biochemistry* **2014**, *53* (39), 6231-42.
23. Miller, M. B.; Bassler, B. L., Quorum sensing in bacteria. *Annu Rev Microbiol* **2001**, *55*, 165-99.
24. Rutherford, S. T.; Bassler, B. L., Bacterial quorum sensing: its role in virulence and possibilities for its control. *Cold Spring Harb Perspect Med* **2012**, *2* (11).
25. Pereira, C. S.; Thompson, J. A.; Xavier, K. B., AI-2-mediated signalling in bacteria. *FEMS Microbiol Rev* **2013**, *37* (2), 156-81.
26. Lowery, C. A.; Salzameda, N. T.; Sawada, D.; Kaufmann, G. F.; Janda, K. D., Medicinal chemistry as a conduit for the modulation of quorum sensing. *J Med Chem* **2010**, *53* (21), 7467-89.
27. Gómez-Garzón, C.; Dussán, J., Evidence-based validation of quorum quenching from *Lysinibacillus sphaericus* and *Geobacillus* sp. in bioremediation of oil sludge. *Can J Microbiol* **2016**, 1-9.
28. Praneenarat, T.; Palmer, A. G.; Blackwell, H. E., Chemical methods to interrogate bacterial quorum sensing pathways. *Org Biomol Chem* **2012**, *10* (41), 8189-99.
29. Jimenez, P. N.; Koch, G.; Thompson, J. A.; Xavier, K. B.; Cool, R. H.; Quax, W. J., The multiple signaling systems regulating virulence in *Pseudomonas aeruginosa*. *Microbiol Mol Biol Rev* **2012**, *76* (1), 46-65.
30. Ni, N.; Li, M.; Wang, J.; Wang, B., Inhibitors and antagonists of bacterial quorum sensing. *Med Res Rev* **2009**, *29* (1), 65-124.
31. Geske, G. D.; Wezeman, R. J.; Siegel, A. P.; Blackwell, H. E., Small molecule inhibitors of bacterial quorum sensing and biofilm formation. *J Am Chem Soc* **2005**, *127* (37), 12762-3.
32. Borlee, B. R.; Geske, G. D.; Blackwell, H. E.; Handelsman, J., Identification of synthetic inducers and inhibitors of the quorum-sensing regulator LasR in *Pseudomonas aeruginosa* by high-throughput screening. *Appl Environ Microbiol* **2010**, *76* (24), 8255-8.
33. Geske, G. D.; O'Neill, J. C.; Miller, D. M.; Wezeman, R. J.; Mattmann, M. E.; Lin, Q.; Blackwell, H. E., Comparative analyses of N-acylated homoserine lactones reveal unique structural features that dictate their ability to activate or inhibit quorum sensing. *Chembiochem* **2008**, *9* (3), 389-400.

34. Pearson, J. P.; Feldman, M.; Iglewski, B. H.; Prince, A., *Pseudomonas aeruginosa* cell-to-cell signaling is required for virulence in a model of acute pulmonary infection. *Infect Immun* **2000**, *68* (7), 4331-4.
35. Val, D. L.; Cronan, J. E., In vivo evidence that S-adenosylmethionine and fatty acid synthesis intermediates are the substrates for the LuxI family of autoinducer synthases. *J Bacteriol* **1998**, *180* (10), 2644-51.
36. Parsek, M. R.; Val, D. L.; Hanzelka, B. L.; Cronan, J. E.; Greenberg, E. P., Acyl homoserine-lactone quorum-sensing signal generation. *Proc Natl Acad Sci U S A* **1999**, *96* (8), 4360-5.
37. Lindemann, A.; Pessi, G.; Schaefer, A. L.; Mattmann, M. E.; Christensen, Q. H.; Kessler, A.; Hennecke, H.; Blackwell, H. E.; Greenberg, E. P.; Harwood, C. S., Isovaleryl-homoserine lactone, an unusual branched-chain quorum-sensing signal from the soybean symbiont *Bradyrhizobium japonicum*. *Proc Natl Acad Sci U S A* **2011**, *108* (40), 16765-70.
38. Christensen, Q. H.; Brecht, R. M.; Dudekula, D.; Greenberg, E. P.; Nagarajan, R., Evolution of acyl-substrate recognition by a family of acyl-homoserine lactone synthases. *PLoS One* **2014**, *9* (11), e112464.
39. Friedel, H. A.; Goa, K. L.; Benfield, P., S-adenosyl-L-methionine. A review of its pharmacological properties and therapeutic potential in liver dysfunction and affective disorders in relation to its physiological role in cell metabolism. *Drugs* **1989**, *38* (3), 389-416.
40. Chan, D. I.; Vogel, H. J., Current understanding of fatty acid biosynthesis and the acyl carrier protein. *Biochem J* **2010**, *430* (1), 1-19.
41. Bunkoczi, G.; Pasta, S.; Joshi, A.; Wu, X.; Kavanagh, K. L.; Smith, S.; Oppermann, U., Mechanism and substrate recognition of human holo ACP synthase. *Chem Biol* **2007**, *14* (11), 1243-53.
42. Avila, M. A.; García-Trevijano, E. R.; Lu, S. C.; Corrales, F. J.; Mato, J. M., Methylthioadenosine. *Int J Biochem Cell Biol* **2004**, *36* (11), 2125-30.
43. McInnis, C. E.; Blackwell, H. E., Thiolactone modulators of quorum sensing revealed through library design and screening. *Bioorg Med Chem* **2011**, *19* (16), 4820-8.
44. Moore, J. D.; Rossi, F. M.; Welsh, M. A.; Nyffeler, K. E.; Blackwell, H. E., A Comparative Analysis of Synthetic Quorum Sensing Modulators in *Pseudomonas aeruginosa*: New Insights into Mechanism, Active Efflux Susceptibility, Phenotypic Response, and Next-Generation Ligand Design. *J Am Chem Soc* **2015**, *137* (46), 14626-39.
45. Stacy, D. M.; Welsh, M. A.; Rather, P. N.; Blackwell, H. E., Attenuation of quorum sensing in the pathogen *Acinetobacter baumannii* using non-native N-Acyl homoserine lactones. *ACS Chem Biol* **2012**, *7* (10), 1719-28.
46. CDC *Pseudomonas aeruginosa* in Healthcare Settings. <https://www.cdc.gov/hai/organisms/pseudomonas.html> (accessed August 8, 2017).
47. Deretic, V., *Pseudomonas aeruginosa* Infections. In *Persistent Bacterial Infections*, Nataro, J. P.; Blaser, M. J.; Cunningham-Rundles, S., Eds. ASM Press: Washington DC, 2000; pp 305-326.
48. Welsh, M. A.; Eibergen, N. R.; Moore, J. D.; Blackwell, H. E., Small molecule disruption of quorum sensing cross-regulation in *pseudomonas aeruginosa* causes

- major and unexpected alterations to virulence phenotypes. *J Am Chem Soc* **2015**, *137* (4), 1510-9.
49. Gupta, R. K.; Harjai, K.; Chhibber, S., Rhl quorum sensing affects the virulence potential of *Pseudomonas aeruginosa* in an experimental urinary tract infection. *Antonie van Leeuwenhoek* **2016**, *109* (12), 1535-1544.
50. Eibergen, N. R.; Moore, J. D.; Mattmann, M. E.; Blackwell, H. E., Potent and Selective Modulation of the RhlR Quorum Sensing Receptor by Using Non-native Ligands: An Emerging Target for Virulence Control in *Pseudomonas aeruginosa*. *Chembiochem* **2015**, *16* (16), 2348-56.
51. Raychaudhuri, A.; Jerga, A.; Tipton, P. A., Chemical mechanism and substrate specificity of RhlI, an acylhomoserine lactone synthase from *Pseudomonas aeruginosa*. *Biochemistry* **2005**, *44* (8), 2974-81.
52. Raychaudhuri, A.; Tullock, A.; Tipton, P. A., Reactivity and reaction order in acylhomoserine lactone formation by *Pseudomonas aeruginosa* RhlI. *Biochemistry* **2008**, *47* (9), 2893-8.
53. Shin, D.; Frane, N. D.; Brecht, R. M.; Keeler, J.; Nagarajan, R., A Comparative Analysis of Acyl-Homoserine Lactone Synthase Assays. *Chembiochem* **2015**, *16* (18), 2651-9.
54. Equation: [Inhibitor] vs. response -- Variable slope. [https://www.graphpad.com/guides/prism/7/curve-fitting/index.htm?reg\\_dr\\_inhibit\\_variable\\_2.htm](https://www.graphpad.com/guides/prism/7/curve-fitting/index.htm?reg_dr_inhibit_variable_2.htm) (accessed August 8, 2017).
55. Equation: [Agonist] vs. response -- Variable slope. [https://www.graphpad.com/guides/prism/7/curve-fitting/index.htm?reg\\_dr\\_stim\\_variable\\_2.htm](https://www.graphpad.com/guides/prism/7/curve-fitting/index.htm?reg_dr_stim_variable_2.htm) (accessed August 8, 2017).
56. **Ammonium Sulfate Calculator.** <http://www.encorbio.com/protocols/AM-SO4.htm> (accessed August 08, 2017).
57. Shinohara, Y.; Hasegawa, H.; Hashimoto, T.; Ichida, K., Synthesis of optically active deuterium-labeled homocysteine thiolactone *Journal of Labelled Compounds and Radiopharmaceuticals* **2010**, *53* (8).
58. Chhabra, S. R.; Harty, C.; Hooi, D. S.; Daykin, M.; Williams, P.; Telford, G.; Pritchard, D. I.; Bycroft, B. W., Synthetic analogues of the bacterial signal (quorum sensing) molecule N-(3-oxododecanoyl)-L-homoserine lactone as immune modulators. *J Med Chem* **2003**, *46* (1), 97-104.
59. Mattmann, M. E.; Blackwell, H. E., Small molecules that modulate quorum sensing and control virulence in *Pseudomonas aeruginosa*. *J Org Chem* **2010**, *75* (20), 6737-46.
60. Dong, S. H.; Frane, N. D.; Christensen, Q. H.; Greenberg, E. P.; Nagarajan, R.; Nair, S. K., Molecular basis for the substrate specificity of quorum signal synthases. *Proc Natl Acad Sci U S A* **2017**, *114* (34), 9092-9097.
61. Watson, W. T.; Minogue, T. D.; Val, D. L.; von Bodman, S. B.; Churchill, M. E., Structural basis and specificity of acyl-homoserine lactone signal production in bacterial quorum sensing. *Mol Cell* **2002**, *9* (3), 685-94.
62. Chung, J.; Goo, E.; Yu, S.; Choi, O.; Lee, J.; Kim, J.; Kim, H.; Igarashi, J.; Suga, H.; Moon, J. S.; Hwang, I.; Rhee, S., Small-molecule inhibitor binding to an N-acyl-homoserine lactone synthase. *Proc Natl Acad Sci U S A* **2011**, *108* (29), 12089-94.

63. Gould, T. A.; Schweizer, H. P.; Churchill, M. E., Structure of the *Pseudomonas aeruginosa* acyl-homoserine lactone synthase LasI. *Mol Microbiol* **2004**, *53* (4), 1135-46.
64. Gould, T. A.; Herman, J.; Krank, J.; Murphy, R. C.; Churchill, M. E., Specificity of acyl-homoserine lactone synthases examined by mass spectrometry. *J Bacteriol* **2006**, *188* (2), 773-83.



## APPENDIX A

## Mass Spectra

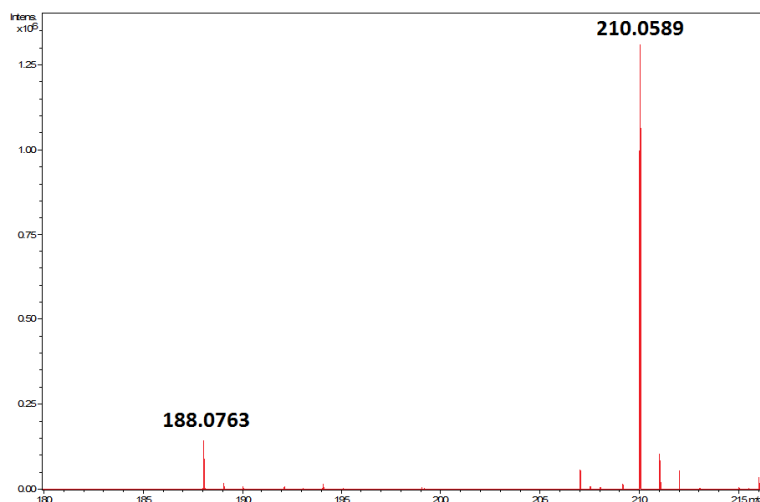


**Figure A1. Mass Spectrum of Compound 56**  
C8H13NO2S

Expected m/z [ $M + H^+$ ]: 188.0734, observed: 188.0763; relative mass error: 15.28 ppm;  
Expected m/z [ $M + Na^+$ ]: 210.0554, observed: 210.0589; relative mass error: 16.81 ppm

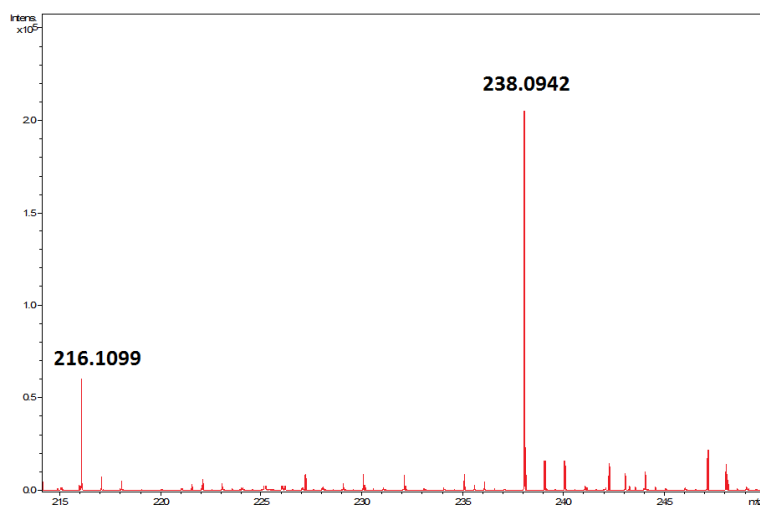


**Figure A2. Mass Spectrum of Compound 57**  
C10H17NO2S

Expected m/z [ $M + H^+$ ]: 216.1047, observed: 216.1099; relative mass error: 23.94 ppm;  
Expected m/z [ $M + Na^+$ ]: 238.0867, observed: 238.0942; relative mass error: 31.63 ppm

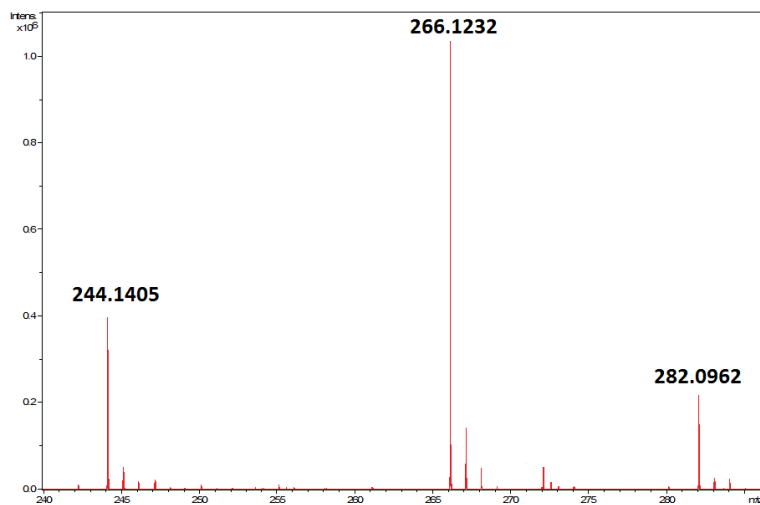
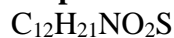


**Figure A3. Mass spectrum of Compound 58**



Expected m/z [ $M + H^+$ ]: 244.1360, observed: 244.1405; relative mass error: 18.32 ppm;  
Expected m/z [ $M + Na^+$ ]: 266.1180, observed: 266.1232; relative mass error: 19.66 ppm;  
Expected m/z [ $M + K^+$ ]: 282.0919, observed: 282.0962; relative mass error: 15.21 ppm

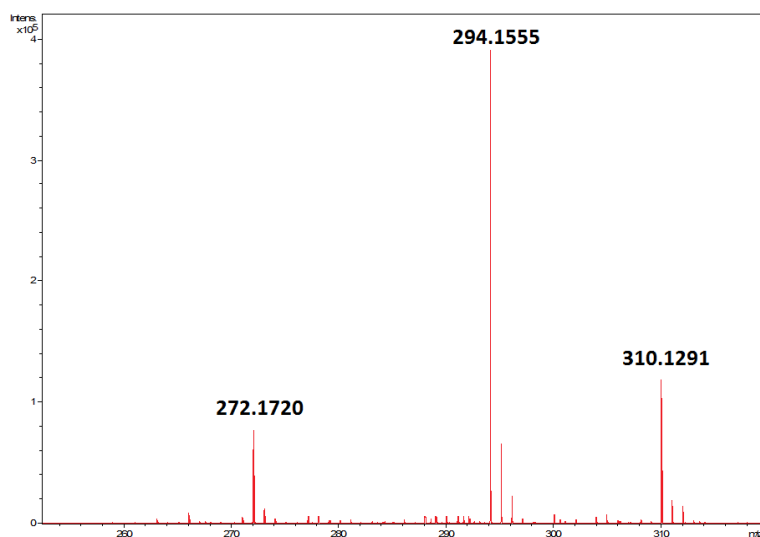
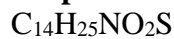


**Figure A4. Mass Spectrum of Compound 59**



Expected m/z [ $M + H^+$ ]: 272.1673, observed: 272.1720; relative mass error: 17.17 ppm;  
Expected m/z [ $M + Na^+$ ]: 294.1493, observed: 294.1555; relative mass error: 21.18 ppm;  
Expected m/z [ $M + K^+$ ]: 310.1291, observed: 310.1291; relative mass error: 19.00 ppm

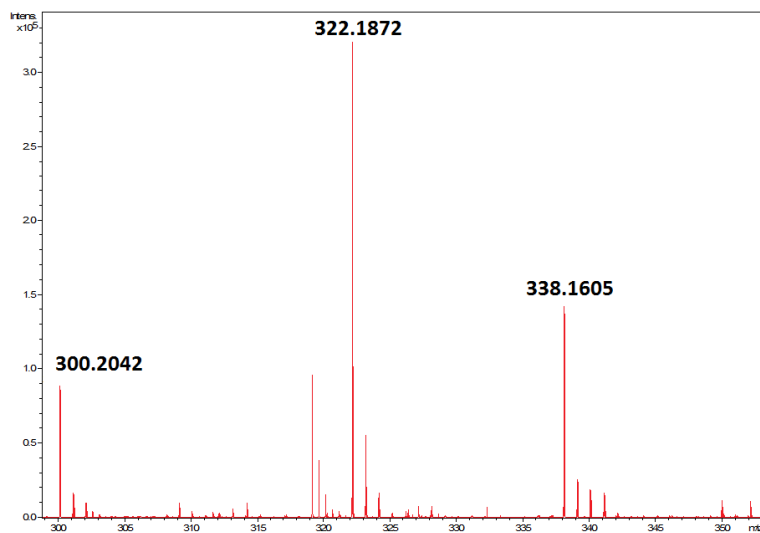
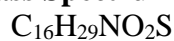


**Figure A5. Mass Spectrum of Compound 60**



Expected m/z [ $M + H^+$ ]: 300.1986, observed: 300.2042; relative mass error: 18.56 ppm;  
 Expected m/z [ $M + Na^+$ ]: 322.1806, observed: 322.1872; relative mass error: 20.58 ppm;  
 Expected m/z [ $M + K^+$ ]: 338.1545, observed: 338.1605; relative mass error: 17.72 ppm

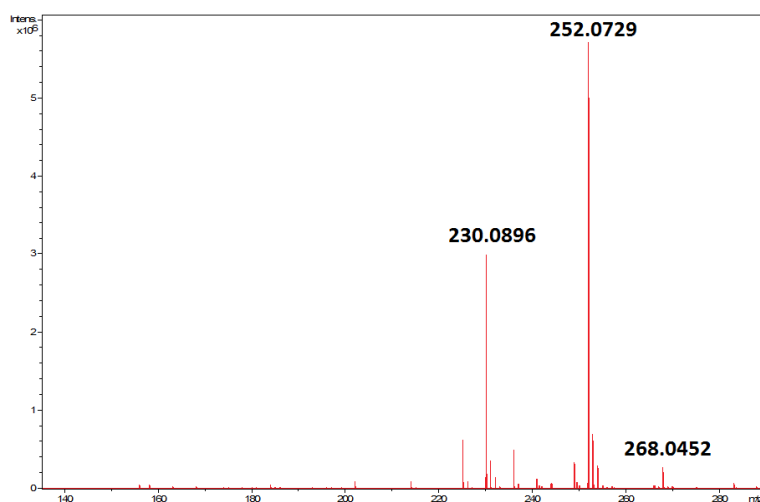
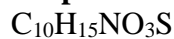


**Figure A6. Mass Spectrum of Compound 61**



Expected m/z [ $M + H^+$ ]: 230.0845, observed: 230.0896; relative mass error: 21.99 ppm;  
 Expected m/z [ $M + Na^+$ ]: 252.0665, observed: 252.0729; relative mass error: 25.46 ppm;  
 Expected m/z [ $M + K^+$ ]: 268.0404, observed: 268.0452; relative mass error: 17.83 ppm

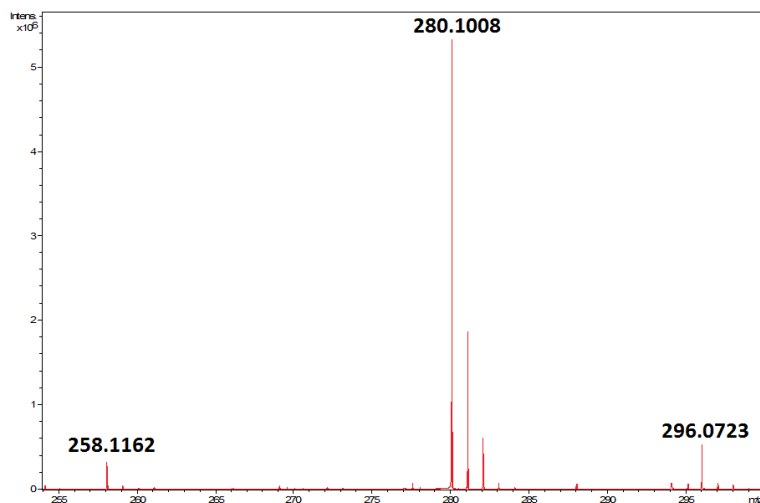
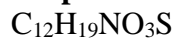


**Figure A7. Mass Spectrum of Compound 62**



Expected m/z [ $M + H^+$ ]: 258.1158, observed: 258.1162; relative mass error: 1.39 ppm;  
Expected m/z [ $M + Na^+$ ]: 280.0978, observed: 280.1008; relative mass error: 10.77 ppm;  
Expected m/z [ $M + K^+$ ]: 296.0717, observed: 296.0723; relative mass error: 1.95 ppm

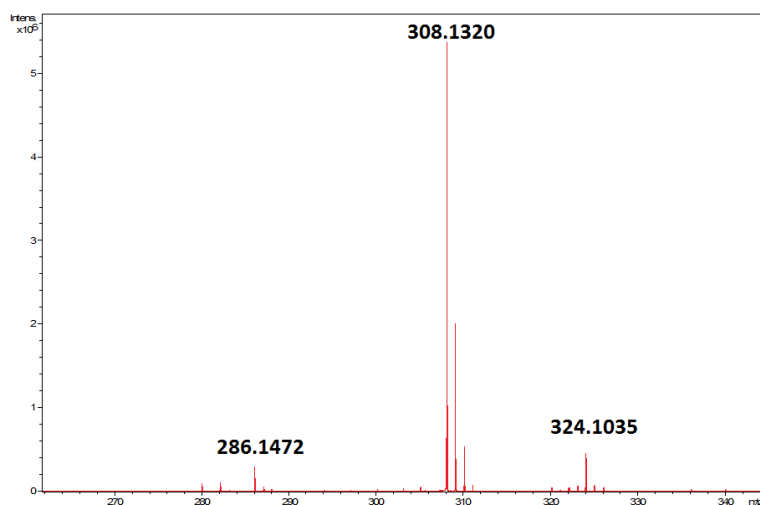
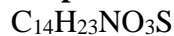


**Figure A8. Mass Spectrum of Compound 63**



Expected m/z [ $M + H^+$ ]: 286.1471, observed: 286.1472; relative mass error: 0.21 ppm;  
Expected m/z [ $M + Na^+$ ]: 308.1291, observed: 308.1320; relative mass error: 9.46 ppm;  
Expected m/z [ $M + K^+$ ]: 324.1030, observed: 324.1035; relative mass error: 1.47 ppm

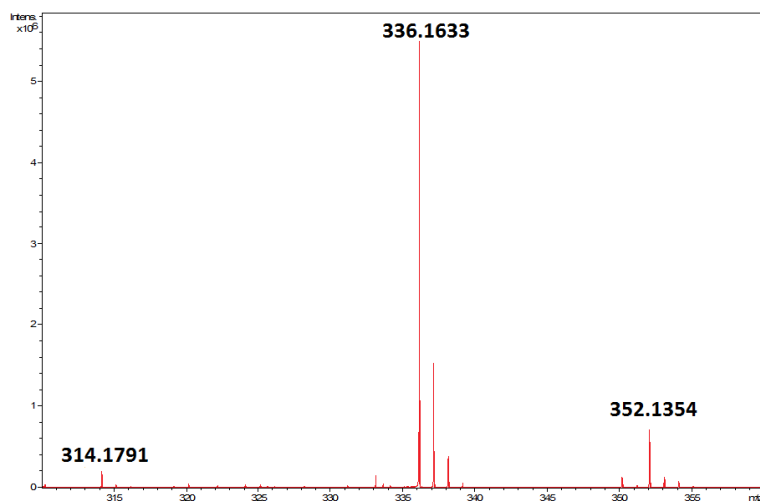
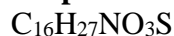


**Figure A9. Mass Spectrum of Compound 64**



Expected m/z  $[\text{M} + \text{H}^+]$ : 314.1784, observed: 314.1791; relative mass error: 2.10 ppm;  
 Expected m/z  $[\text{M} + \text{Na}^+]$ : 336.1604, observed: 336.1633; relative mass error: 8.68 ppm;  
 Expected m/z  $[\text{M} + \text{K}^+]$ : 352.1343, observed: 352.1354; relative mass error: 3.06 ppm

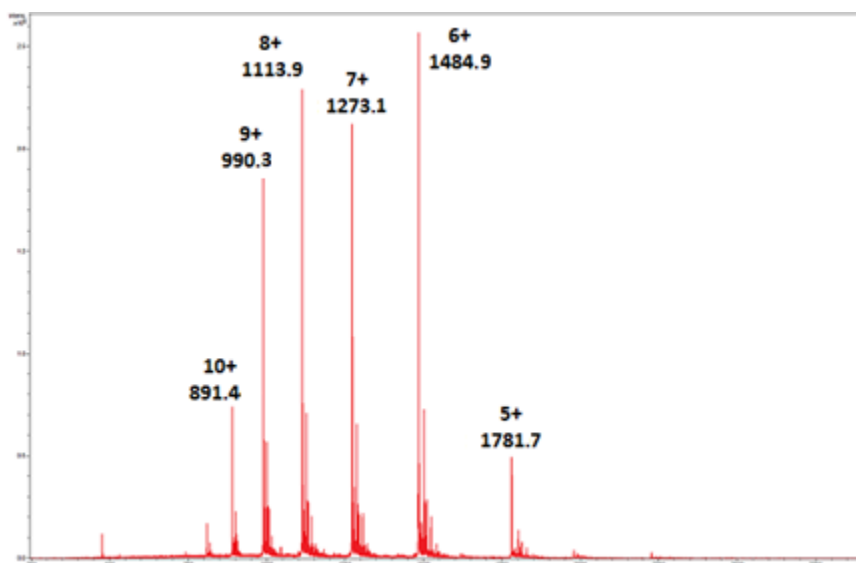


**Figure A10. Mass Spectrum of Compound 88**

Expected m/z  $[\text{M} + 5\text{H}^+]$ : 1781.9, observed: 1781.7;  
 Expected m/z  $[\text{M} + 6\text{H}^+]$ : 1485.1, observed: 1484.9;  
 Expected m/z  $[\text{M} + 7\text{H}^+]$ : 1273.1, observed: 1273.1;  
 Expected m/z  $[\text{M} + 8\text{H}^+]$ : 1114.1, observed: 1113.9;  
 Expected m/z  $[\text{M} + 9\text{H}^+]$ : 990.4, observed: 990.3;  
 Expected m/z  $[\text{M} + 10\text{H}^+]$ : 891.5, observed: 891.4

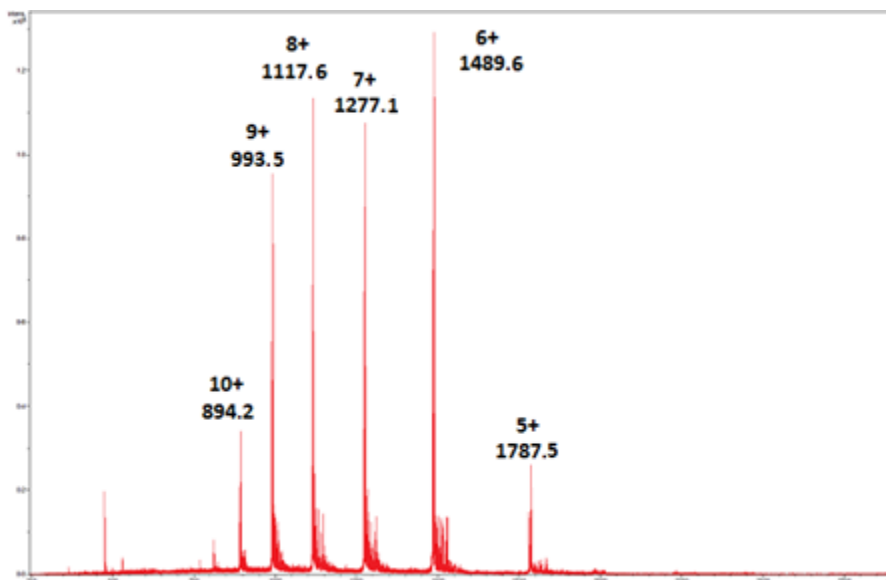


**Figure A11. Mass Spectrum of Compound 89**

Expected m/z  $[M + 5H^+]$ : 1787.5, observed: 1787.5;  
 Expected m/z  $[M + 6H^+]$ : 1489.8, observed: 1489.6;  
 Expected m/z  $[M + 7H^+]$ : 1277.1, observed: 1277.1;  
 Expected m/z  $[M + 8H^+]$ : 1117.6, observed: 1117.6;  
 Expected m/z  $[M + 9H^+]$ : 993.5, observed: 993.5;  
 Expected m/z  $[M + 10H^+]$ : 894.3, observed: 894.2

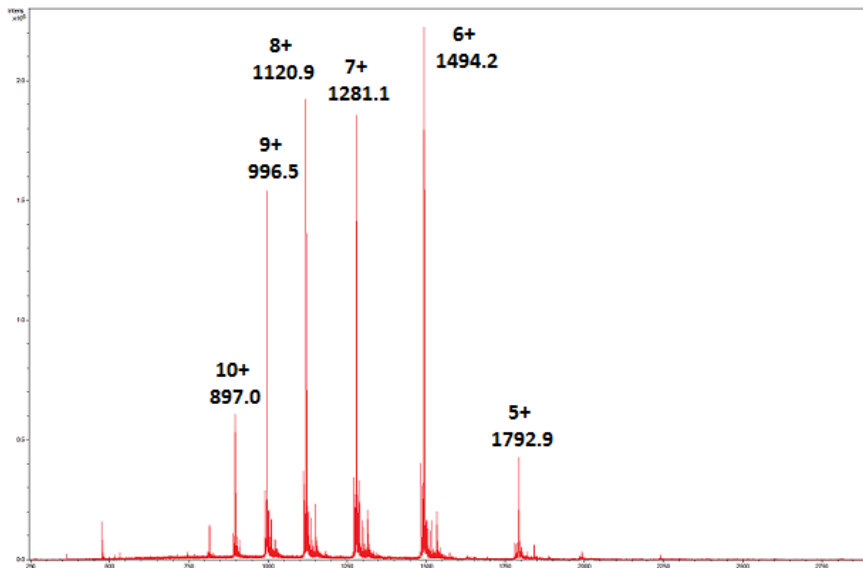


**Figure A12. Mass Spectrum of Compound 90**

Expected m/z  $[M + 5H^+]$ : 1793.1, observed: 1792.9;  
 Expected m/z  $[M + 6H^+]$ : 1494.5, observed: 1494.2;  
 Expected m/z  $[M + 7H^+]$ : 1281.1, observed: 1281.1;  
 Expected m/z  $[M + 8H^+]$ : 1121.1, observed: 1120.9;  
 Expected m/z  $[M + 9H^+]$ : 996.6, observed: 996.5;  
 Expected m/z  $[M + 10H^+]$ : 897.1, observed: 897.0

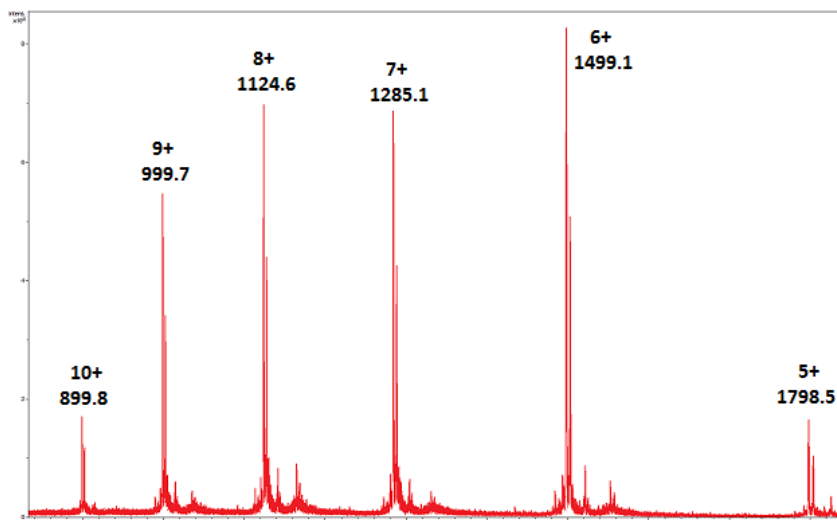


**Figure A13. Mass Spectrum of Compound 91**

Expected  $m/z$   $[M + 5H^+]$ : 1798.7, observed: 1798.5;  
 Expected  $m/z$   $[M + 6H^+]$ : 1499.1, observed: 1499.1;  
 Expected  $m/z$   $[M + 7H^+]$ : 1285.1, observed: 1285.1;  
 Expected  $m/z$   $[M + 8H^+]$ : 1124.6, observed: 1124.6;  
 Expected  $m/z$   $[M + 9H^+]$ : 999.8, observed: 999.7;  
 Expected  $m/z$   $[M + 10H^+]$ : 899.9, observed: 899.8

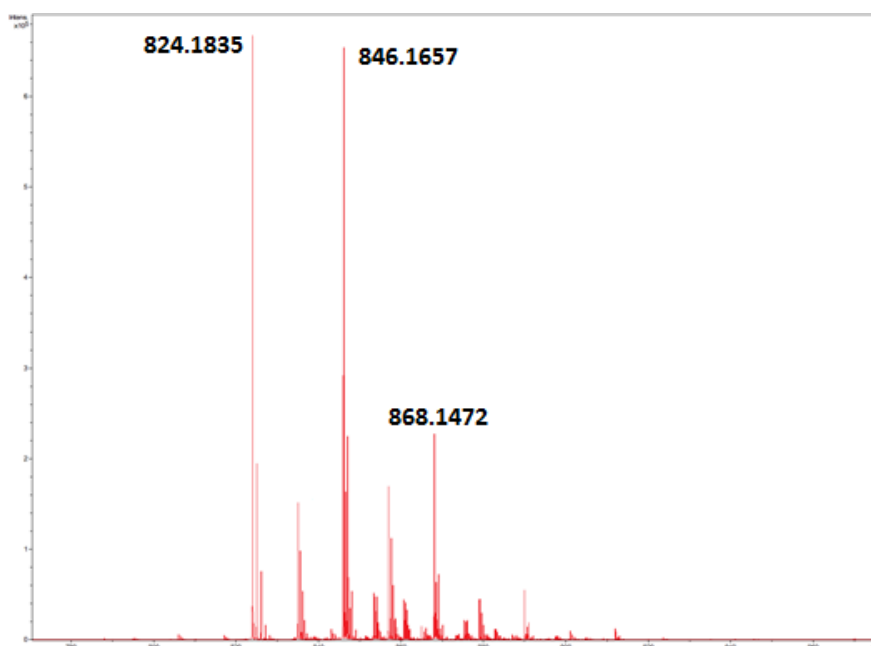
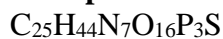


**Figure A14. Mass Spectrum of Compound 92**



Expected  $m/z$   $[M + H^+]$ : 824.1851, observed: 824.1835; relative mass error: -1.92 ppm;  
 Expected  $m/z$   $[M + Na^+]$ : 846.1670, observed: 846.1657; relative mass error: -1.57 ppm;  
 Expected  $m/z$   $[M + 2Na^+ - H^+]$ : 868.1490, observed: 868.1472; relative mass error: -2.04 ppm



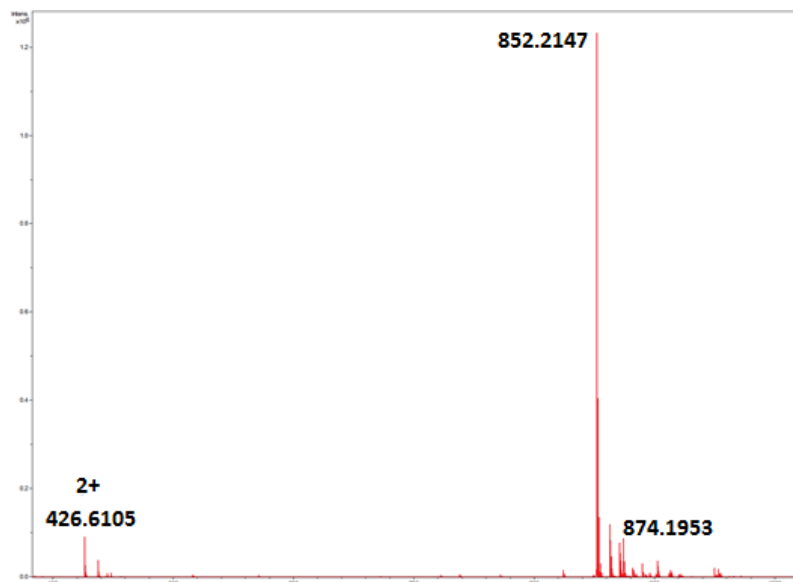
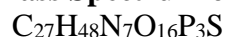


**Figure A15. Mass Spectrum of Compound 93**



Expected  $m/z$  [ $M + H^+$ ]: 852.2164, observed: 852.2147; relative mass error: -1.98 ppm;  
Expected  $m/z$  [ $M + Na^+$ ]: 874.1983, observed: 874.1953; relative mass error: -3.47 ppm;  
Expected  $m/z$  [ $M + 2H^+$ ]: 426.6118, observed: 426.6105; relative mass error: -3.12 ppm

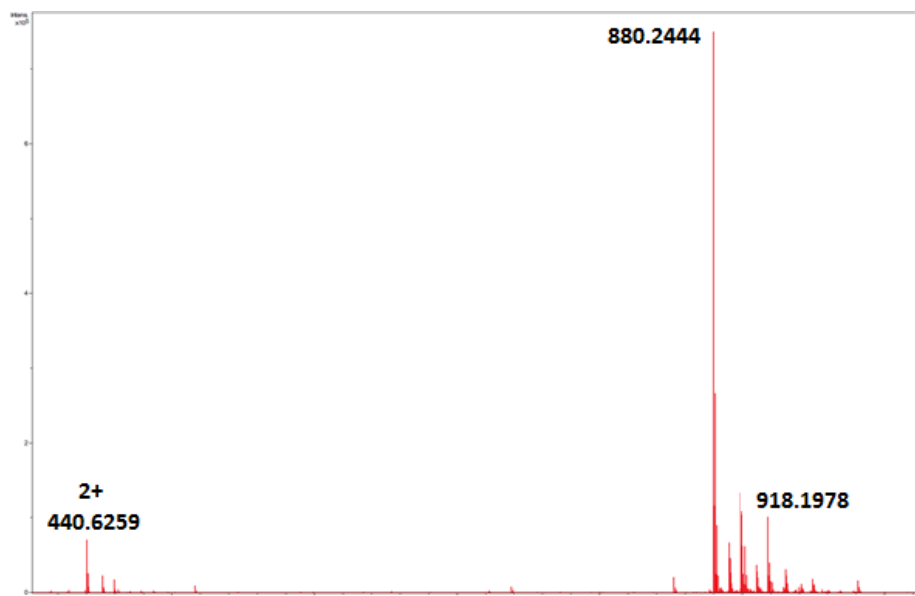
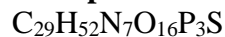


**Figure A16. Mass Spectrum of Compound 94**



Expected  $m/z$  [ $M + H^+$ ]: 880.2477, observed: 880.2444; relative mass error: -3.73 ppm;  
Expected  $m/z$  [ $M + K^+$ ]: 918.2036, observed: 918.1978; relative mass error: -6.28 ppm;  
Expected  $m/z$  [ $M + 2H^+$ ]: 440.6275, observed: 440.6259; relative mass error: -3.59 ppm

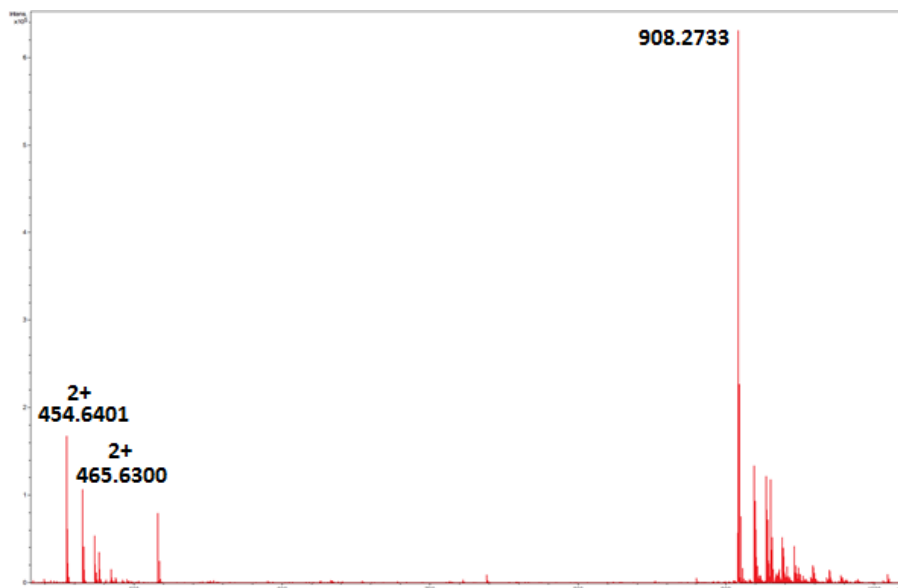
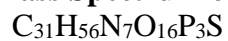


**Figure A17. Mass Spectrum of Compound 95**



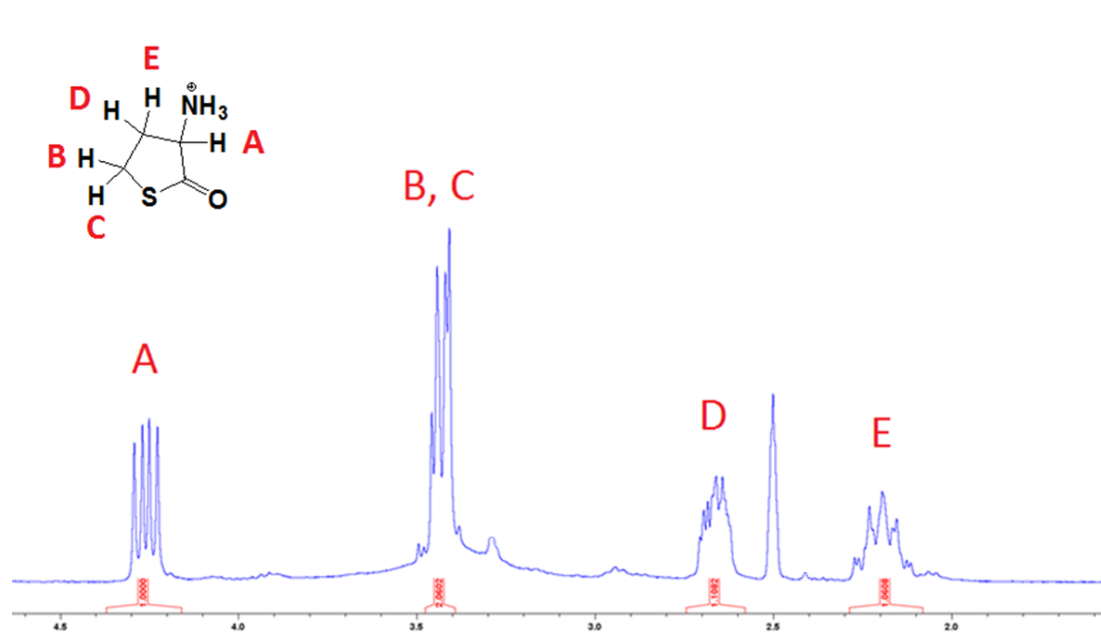
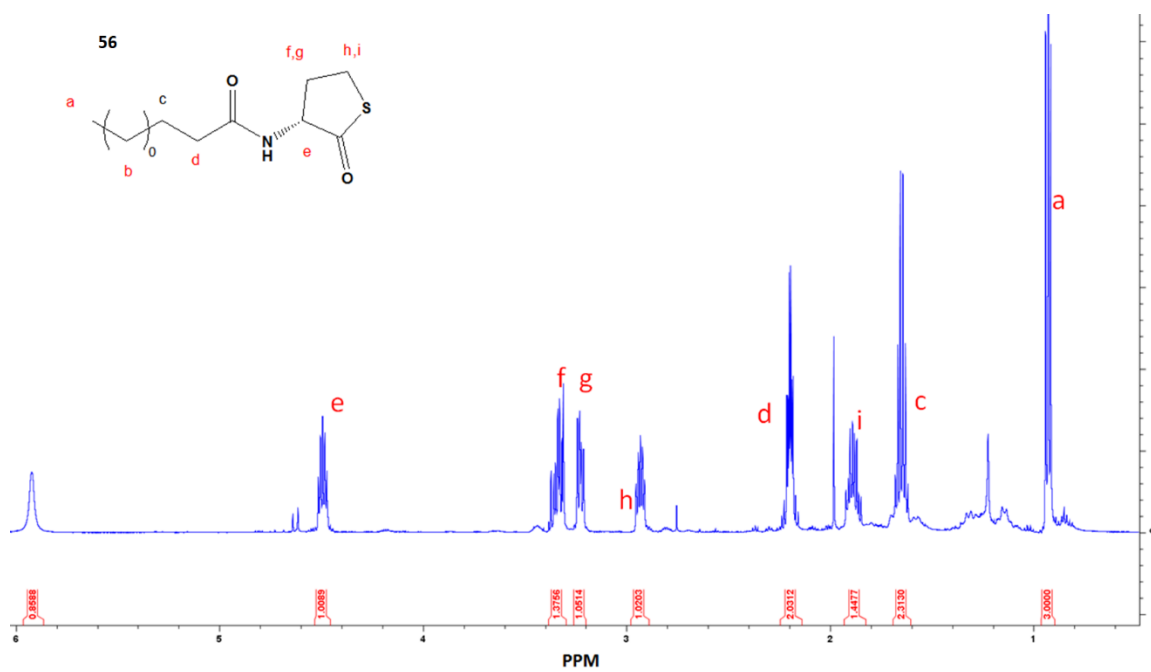
Expected  $m/z$   $[M + H^+]$ : 908.2790, observed: 9083.2733; relative mass error: -6.26 ppm;

Expected  $m/z$   $[M + 2H^+]$ : 454.6431, observed: 454.6401; relative mass error: -6.67 ppm;

Expected  $m/z$   $[M + H^+ + Na^+]$ : 465.6345, observed: 465.6300; relative mass error: -9.62 ppm

APPENDIX B

## NMR spectra

Figure B1. D-homocysteine thiolactone <sup>1</sup>H NMRFigure B2. Compound 56 <sup>1</sup>H NMR

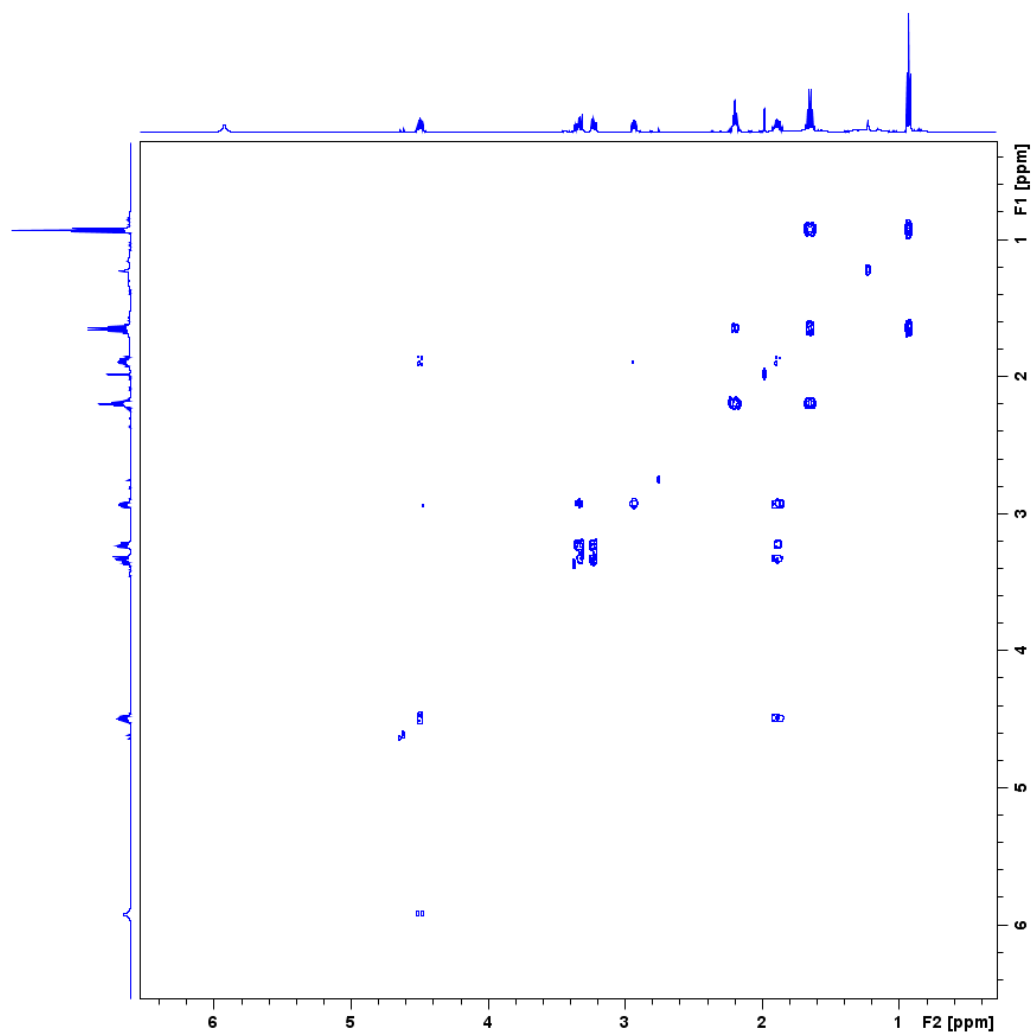


Figure B3. Compound 56 COSY NMR

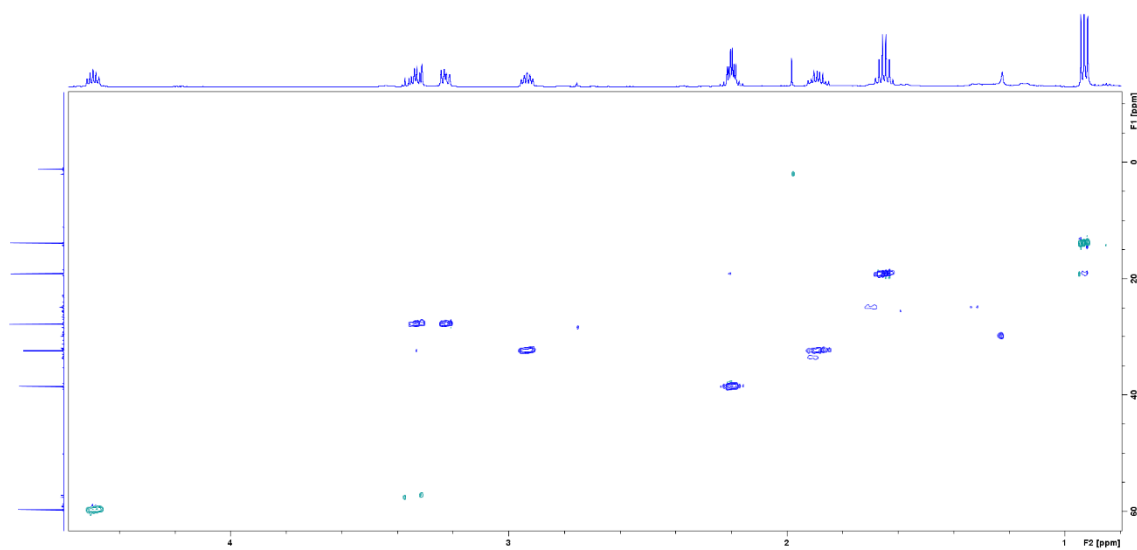


Figure B4. Compound 56 HSQC NMR

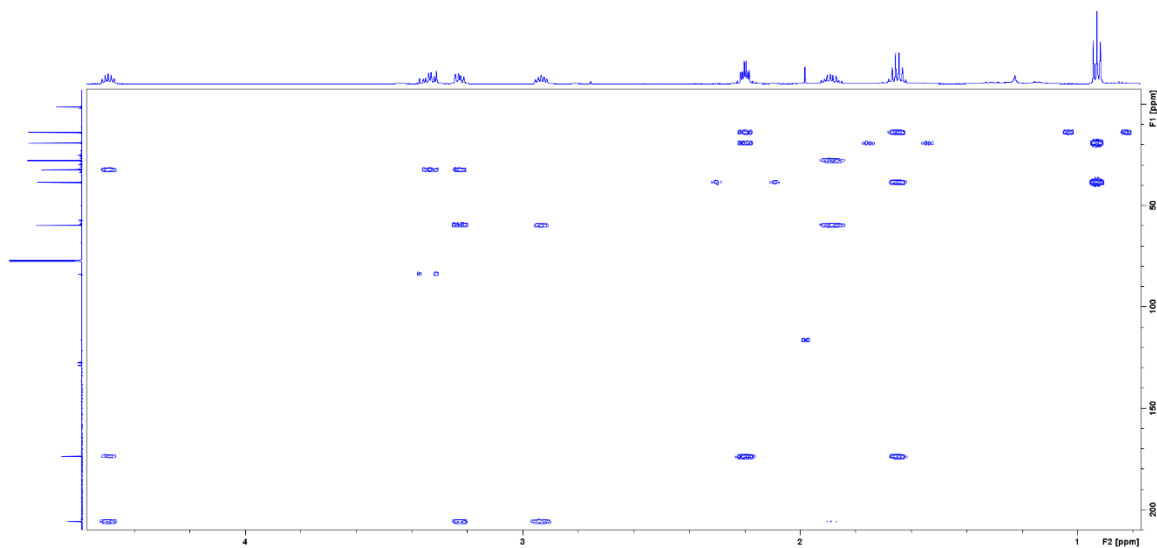


Figure B5. Compound 56 HMBC NMR

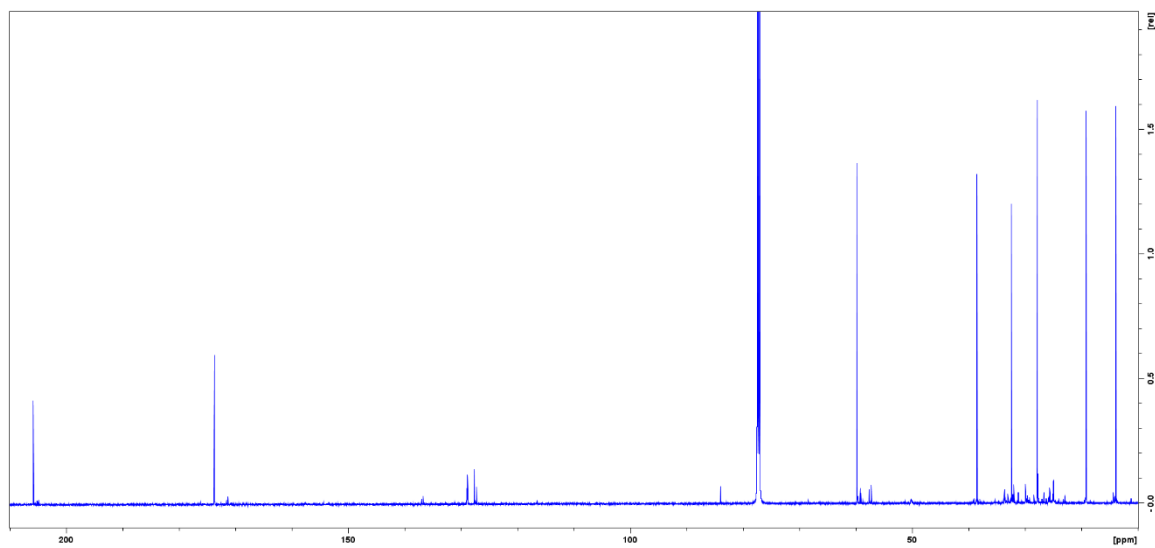


Figure B6. Compound 56 <sup>13</sup>C NMR

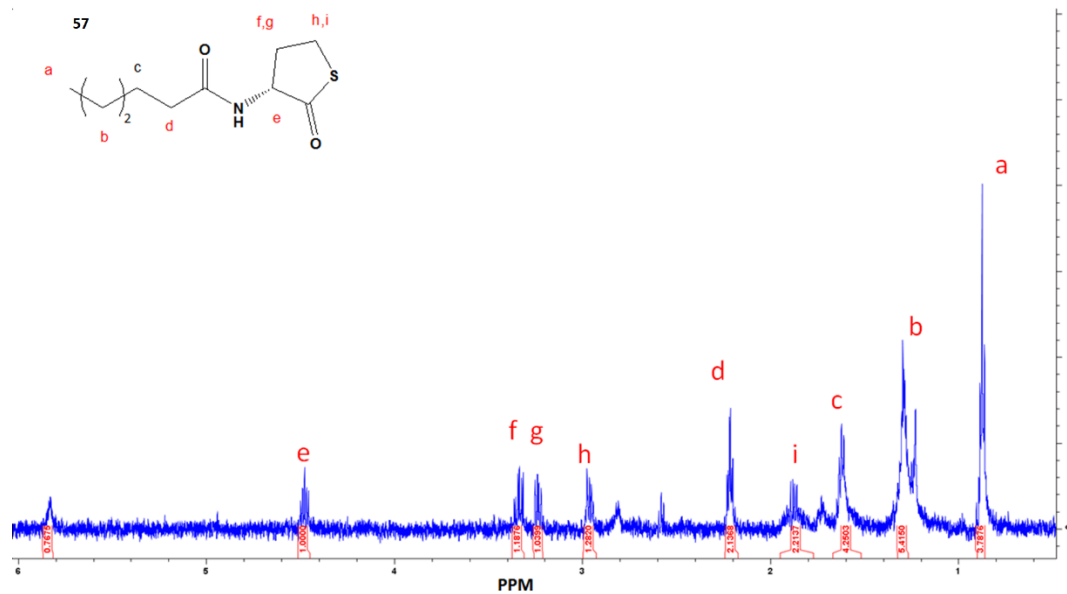


Figure B7. Compound 57  $^1\text{H}$  NMR

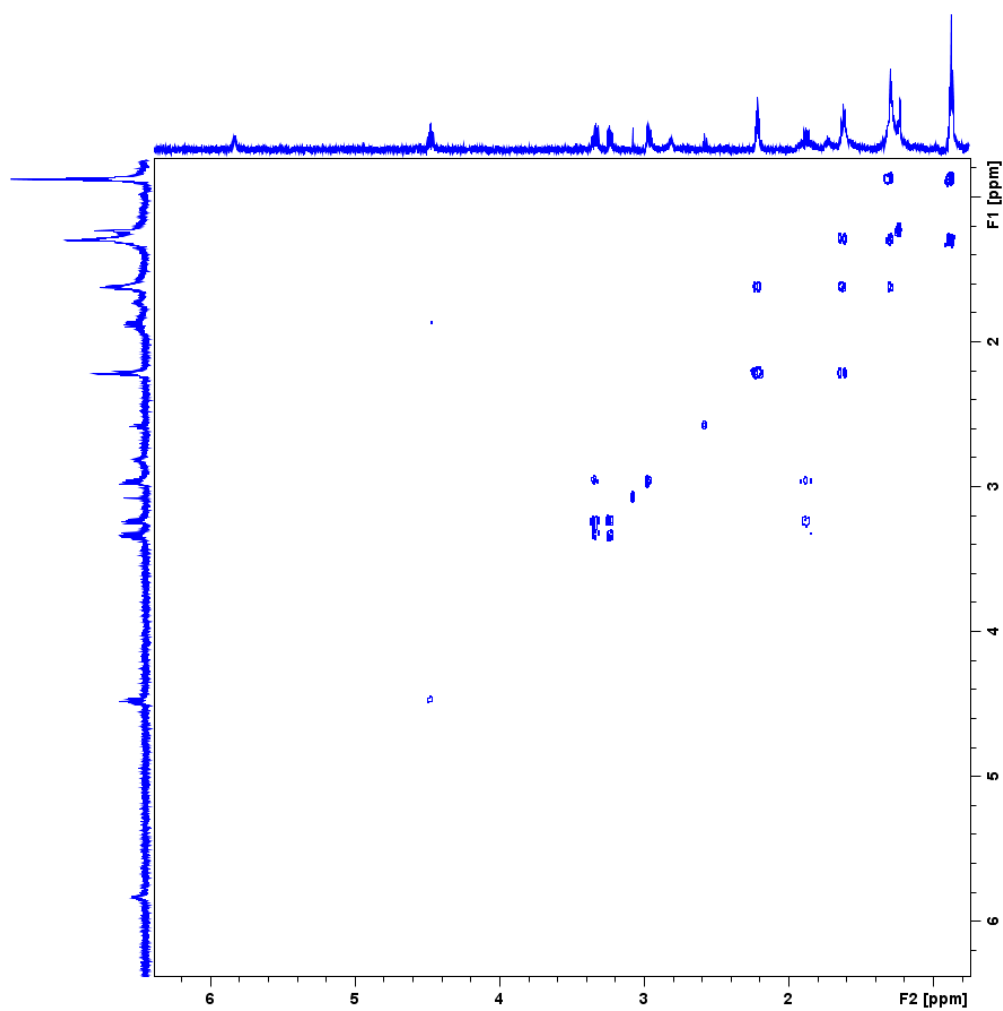
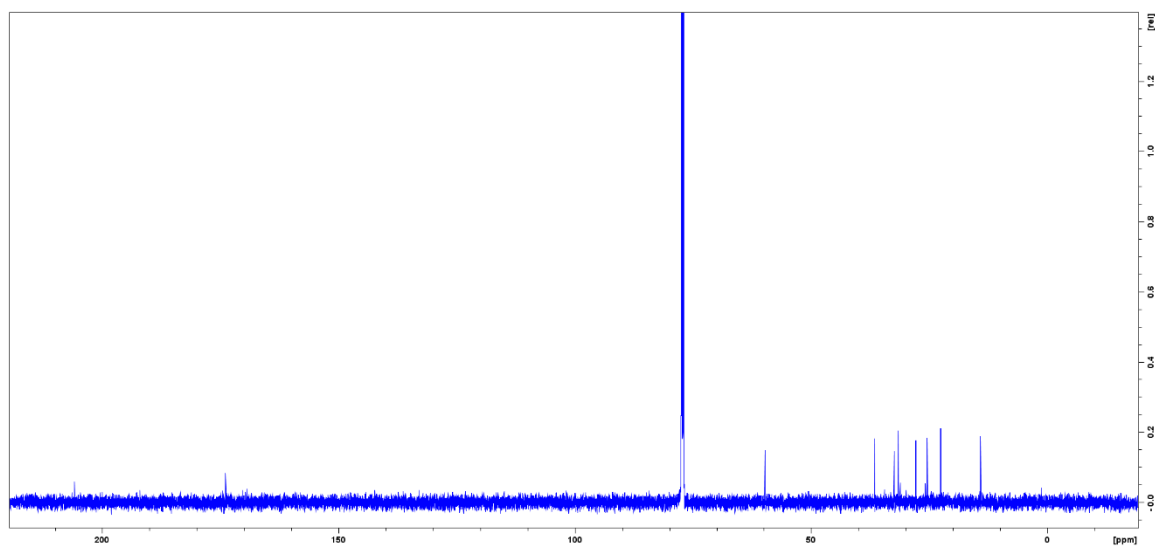
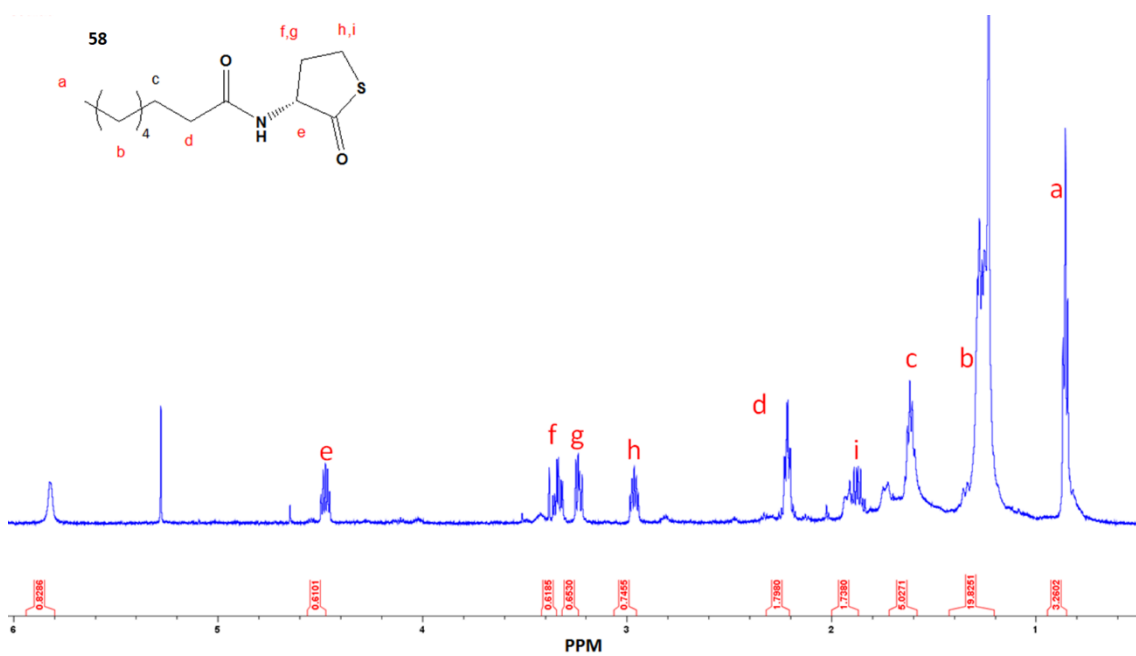


Figure B8. Compound 57 COZY NMR

Figure B9. Compound 57  $^{13}\text{C}$  NMRFigure B10. Compound 58  $^1\text{H}$  NMR



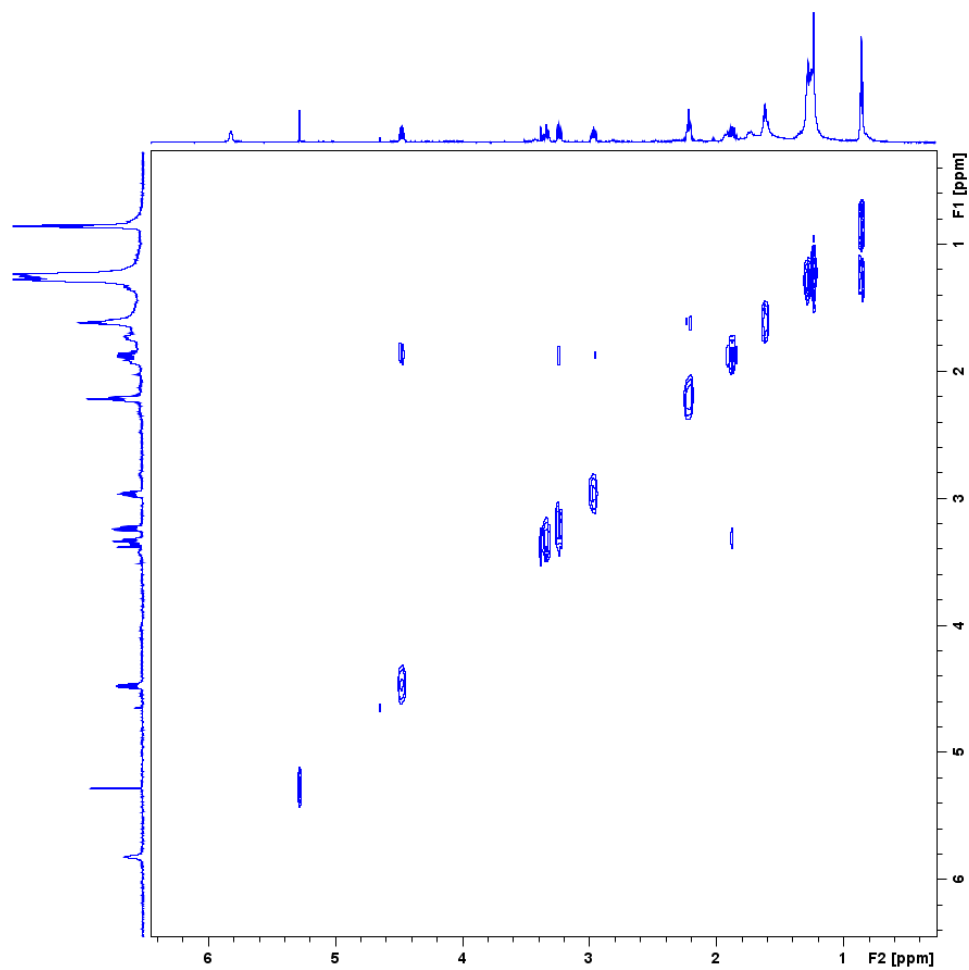


Figure B11. Compound 58 COSY NMR

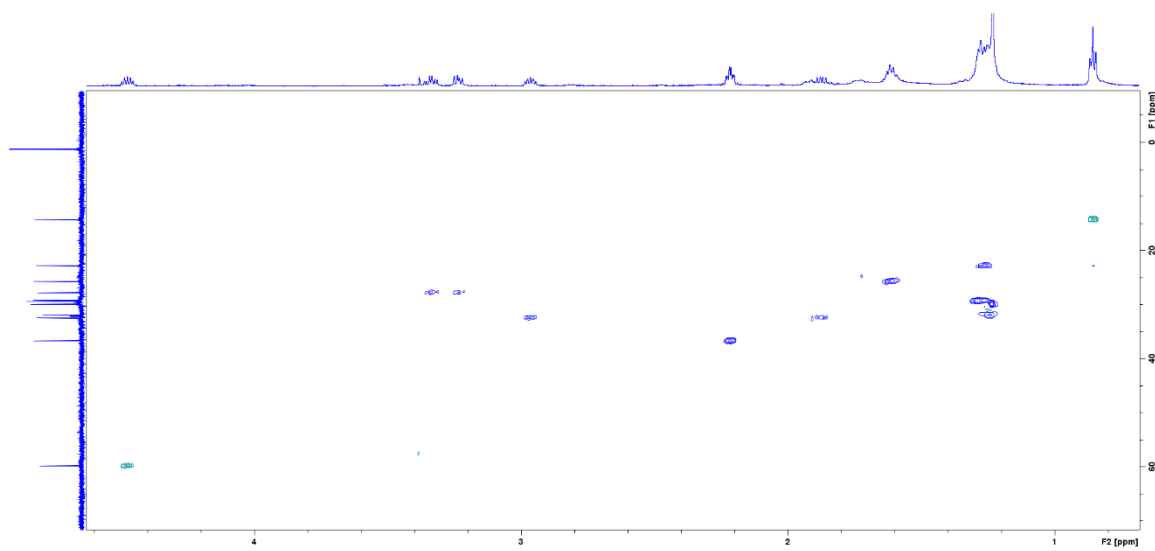


Figure B12. Compound 58 HSQC NMR

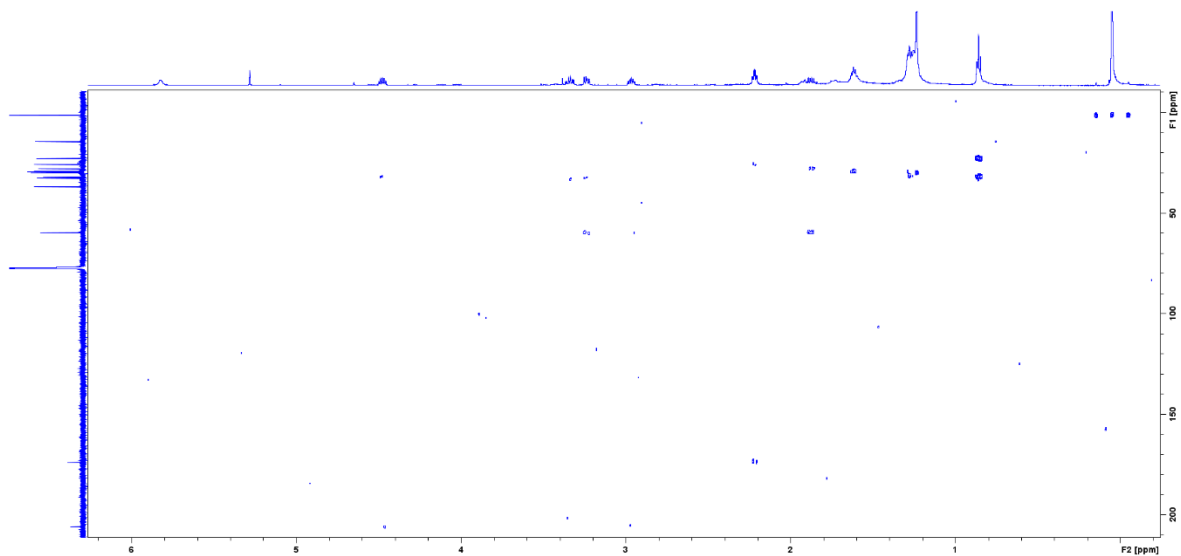


Figure B13. Compound 58 HMBC NMR

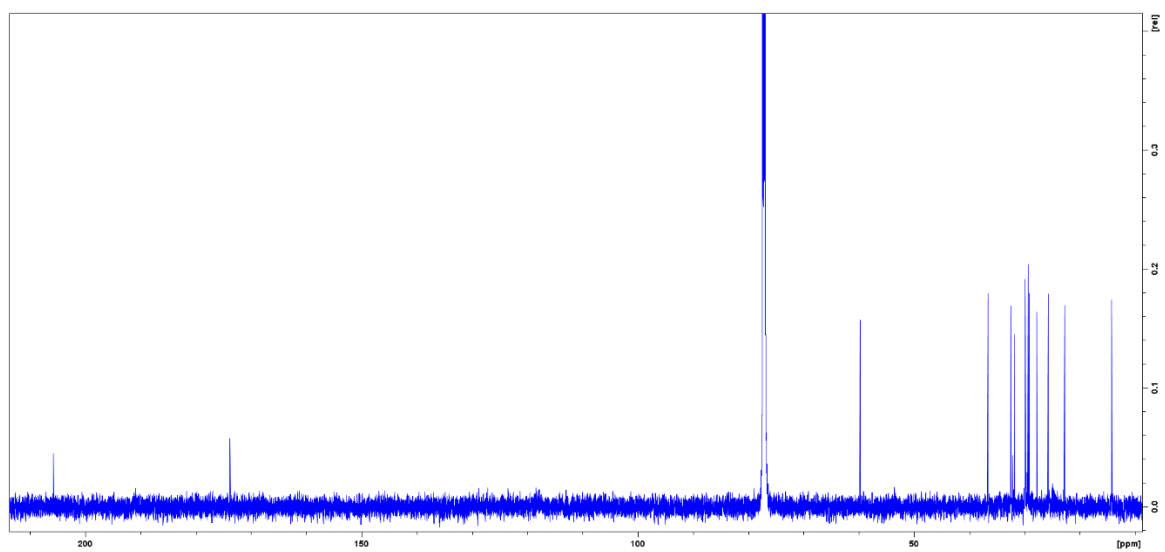


Figure B14. Compound 58  $^{13}\text{C}$  NMR

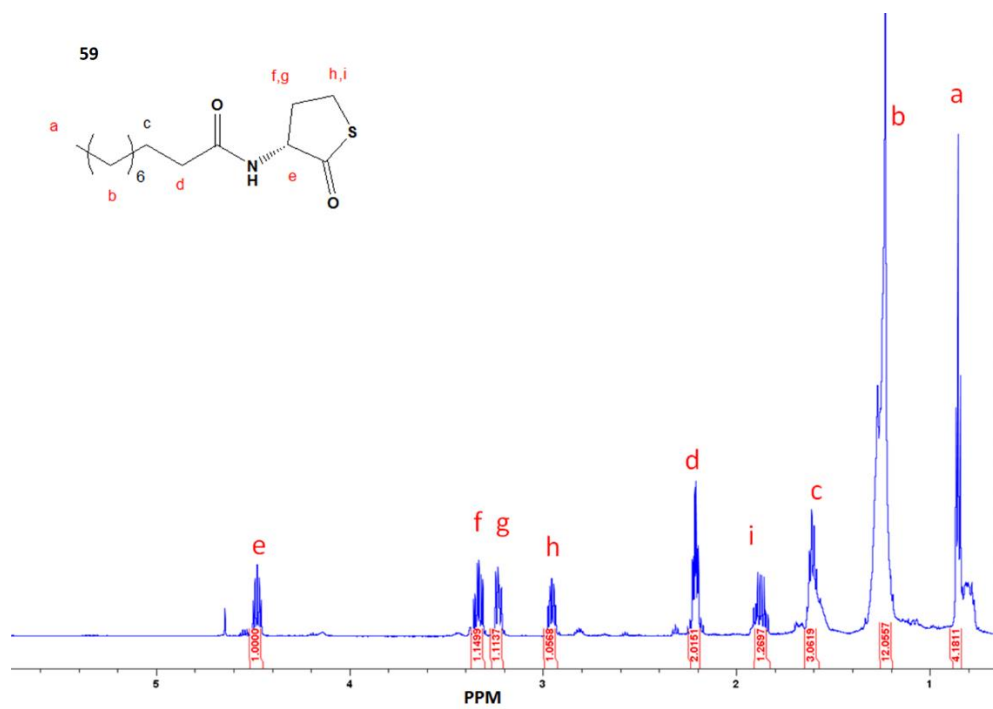
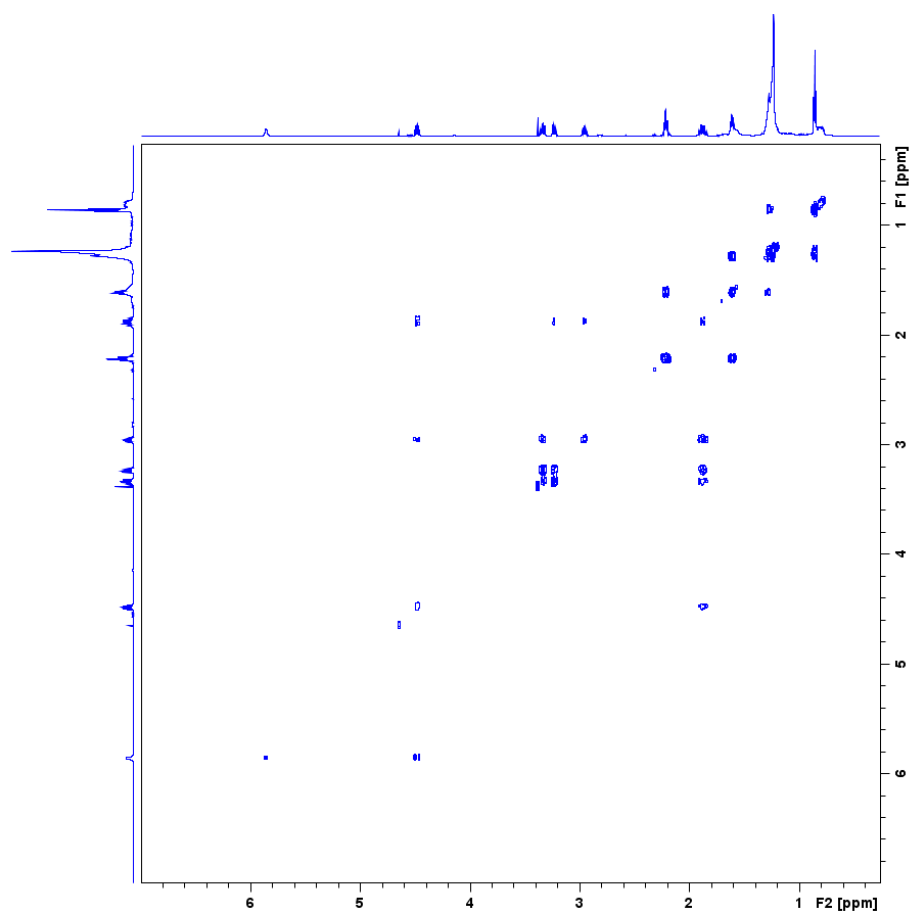
Figure B15. Compound 59  $^1\text{H}$  NMR

Figure B16. Compound 59 COSY NMR

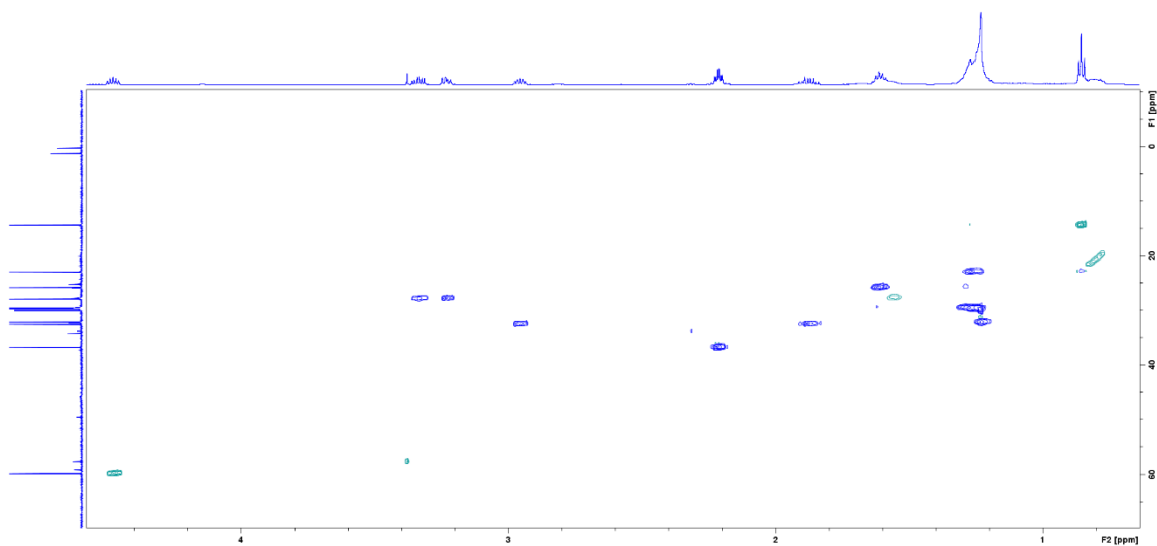


Figure B17. Compound 59 HSQC NMR

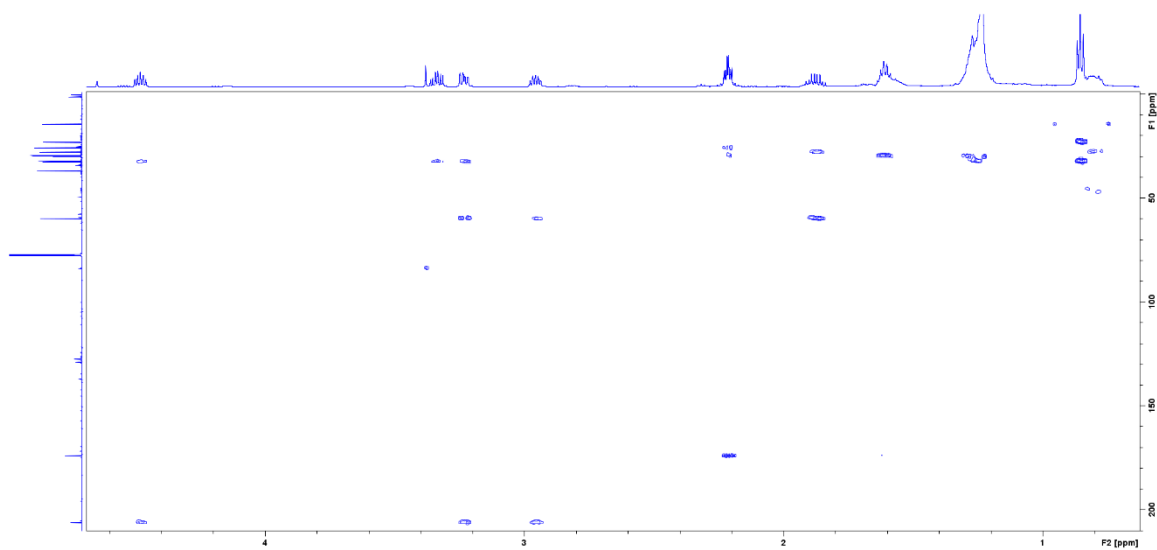


Figure B18. Compound 59 HMBC NMR

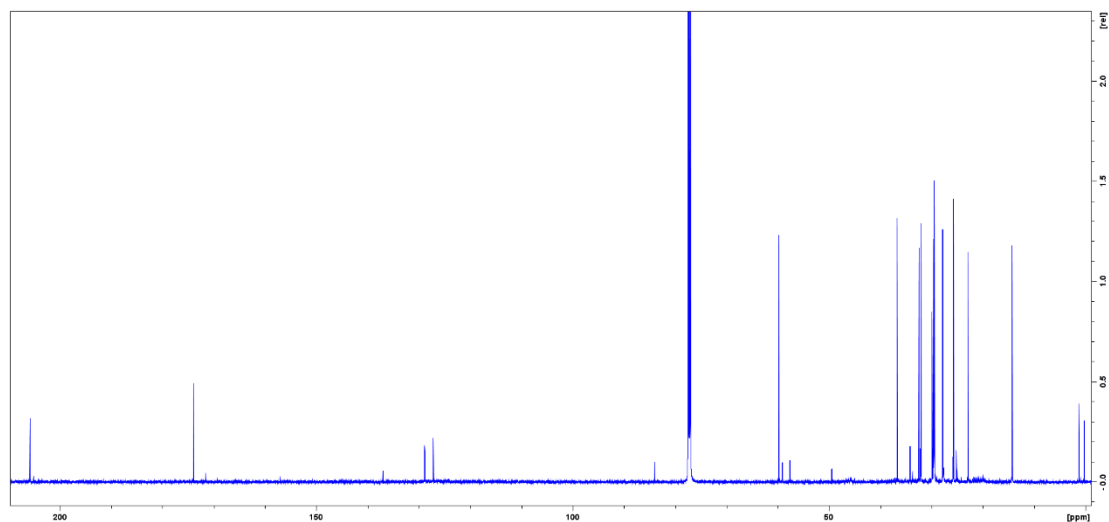


Figure B19. Compound 59  $^{13}\text{C}$  NMR

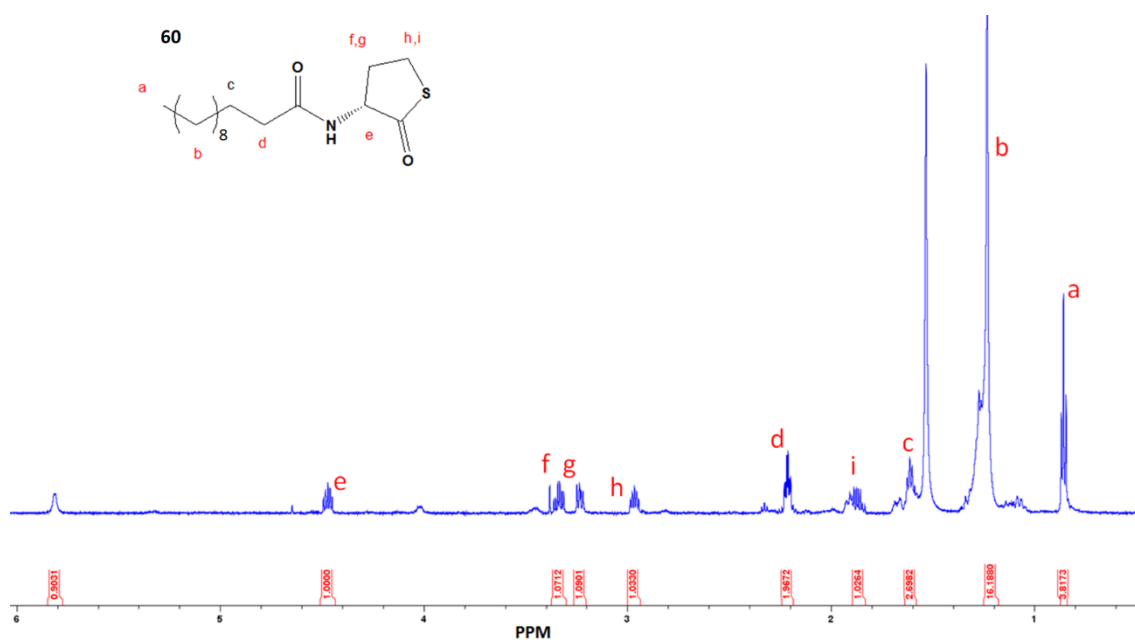


Figure B20. Compound 60  $^1\text{H}$  NMR

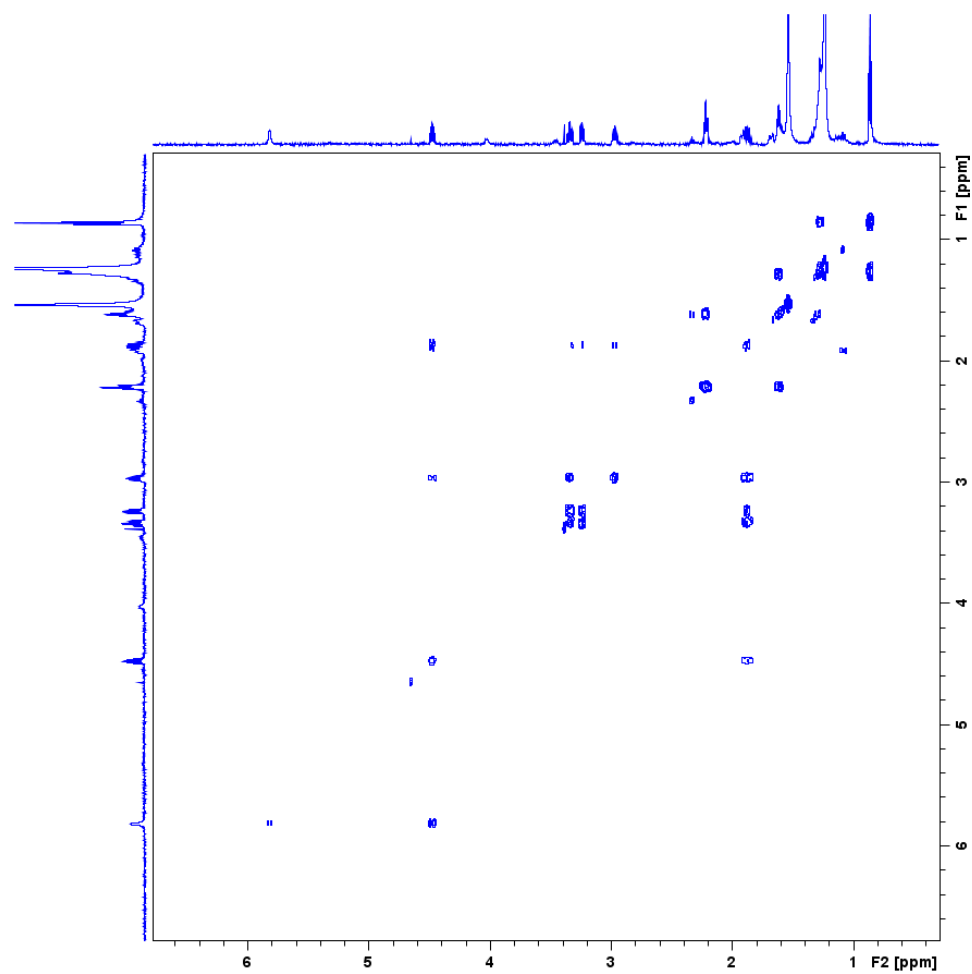


Figure B21. Compound 60 COSY NMR

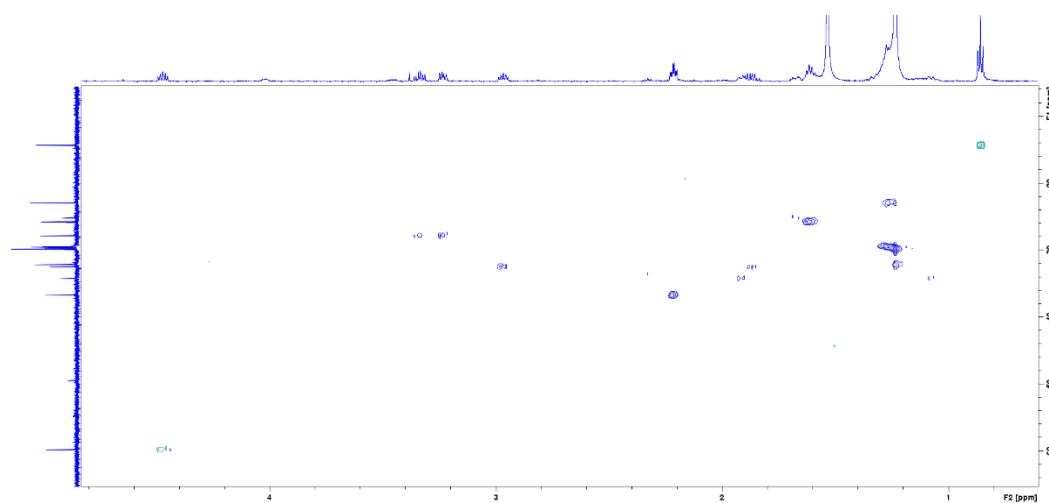


Figure B22. Compound 60 HSQC NMR

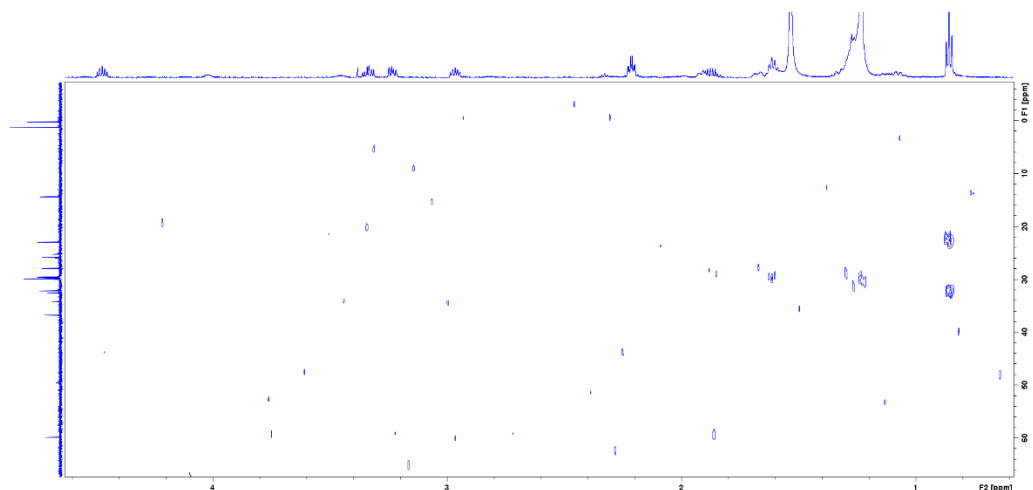


Figure B23. Compound 60 HMBC NMR

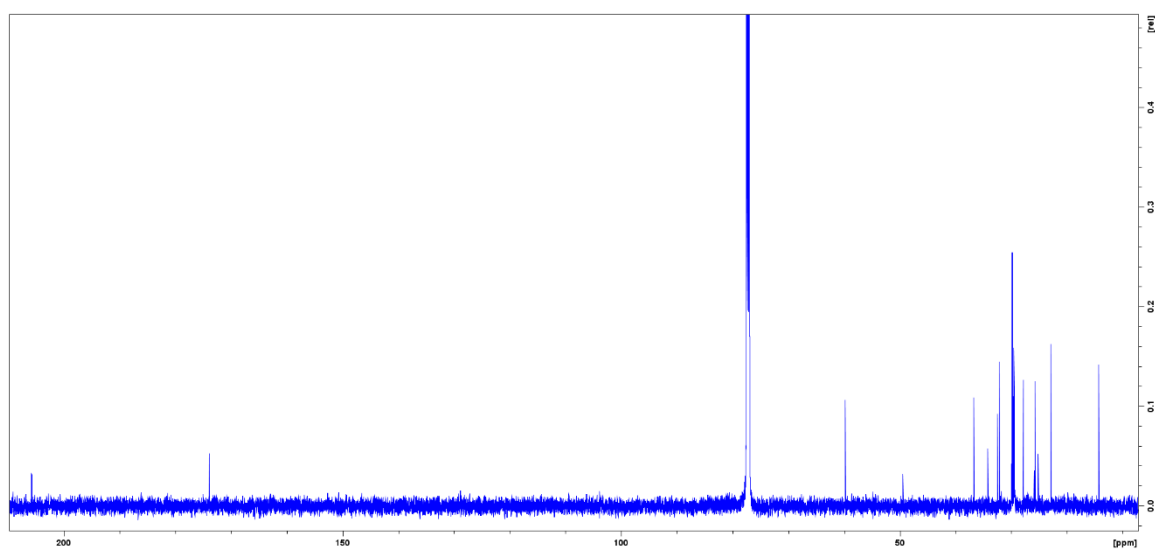
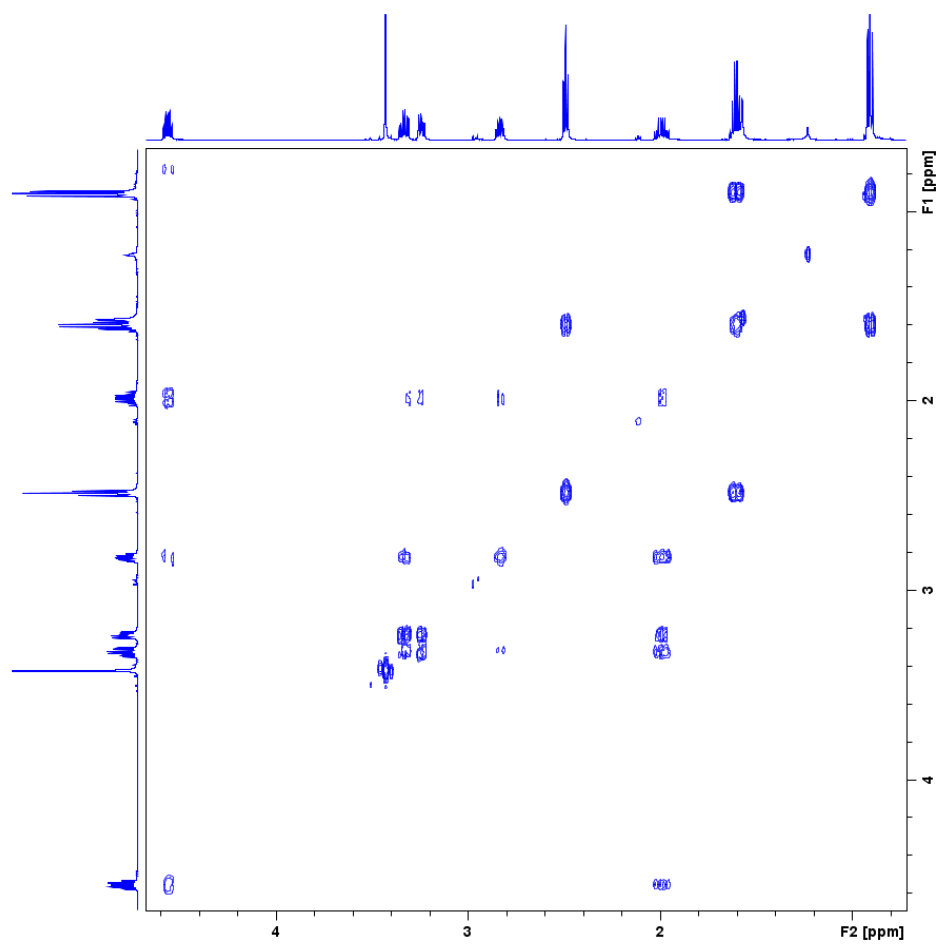
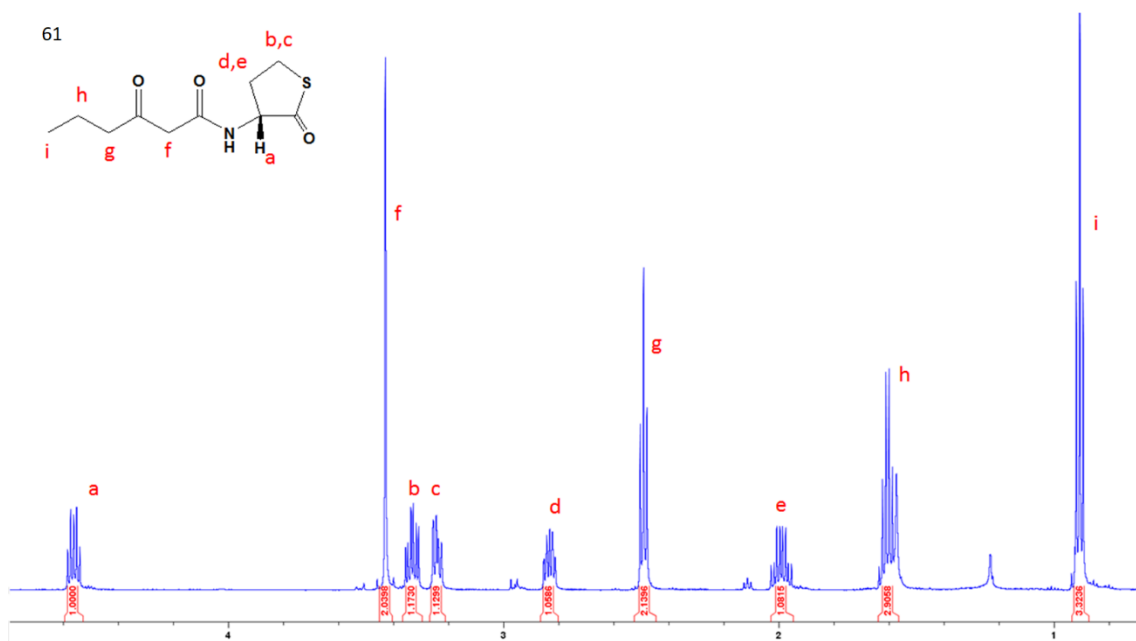


Figure B24. Compound 60 <sup>13</sup>C NMR





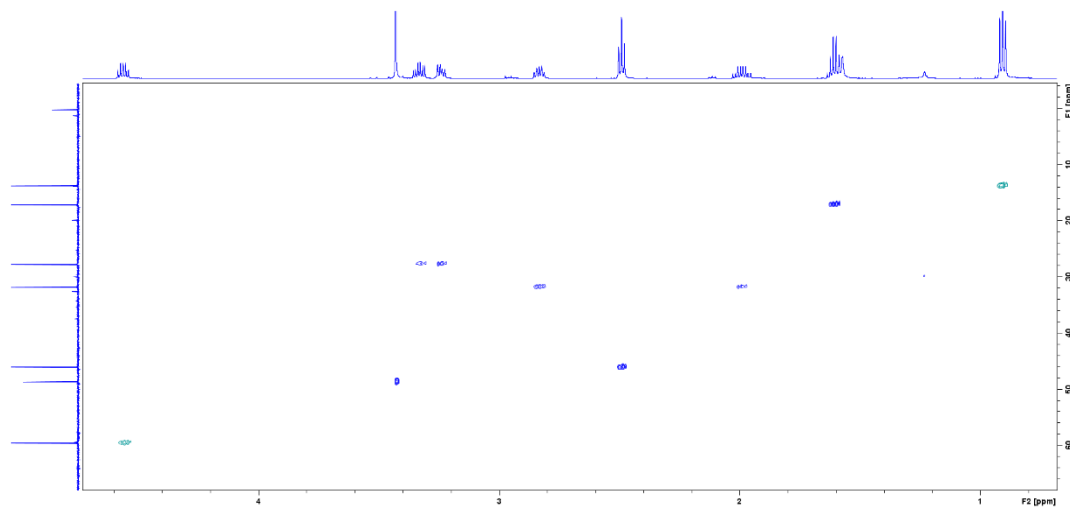


Figure B27. Compound 61 HSQC NMR

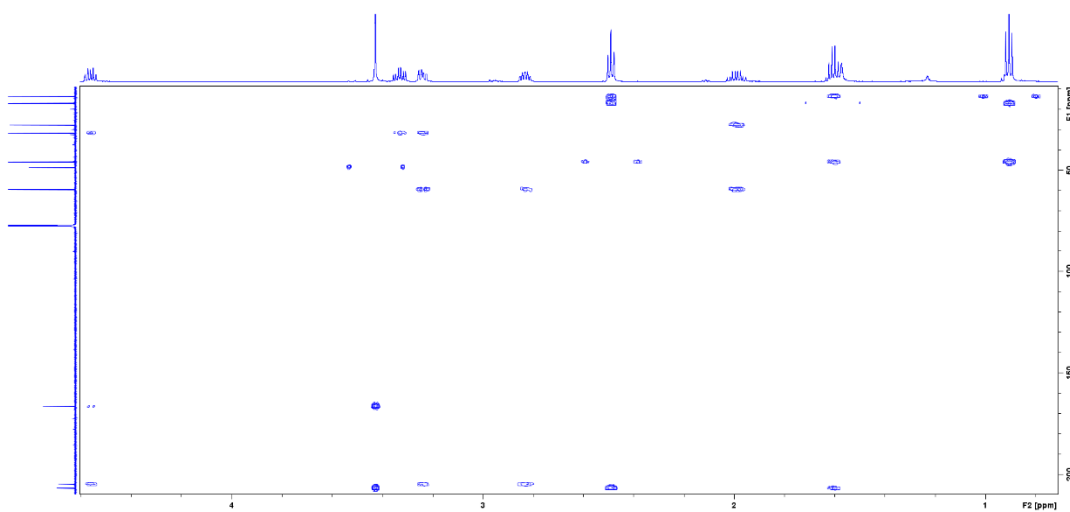


Figure B28. Compound 61 HMBC NMR

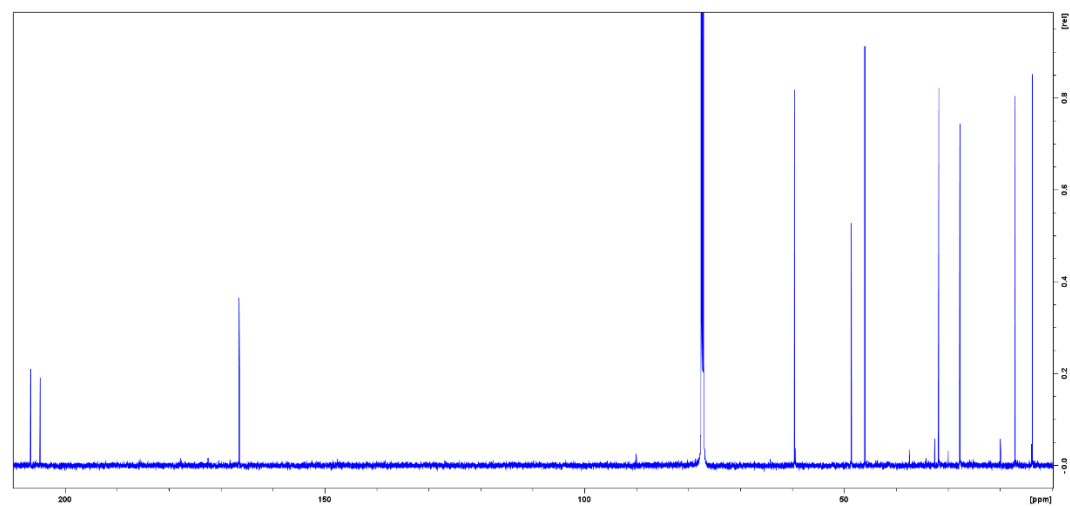


Figure B29. Compound 61  $^{13}\text{C}$  NMR

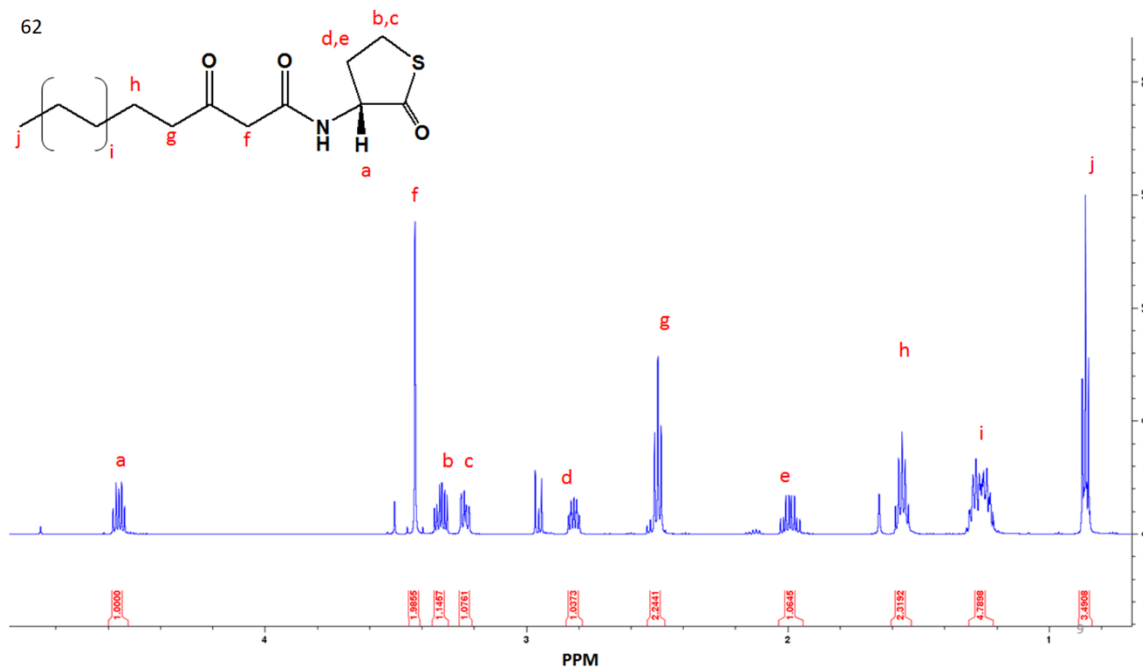


Figure B30. Compound 62  $^1\text{H}$  NMR

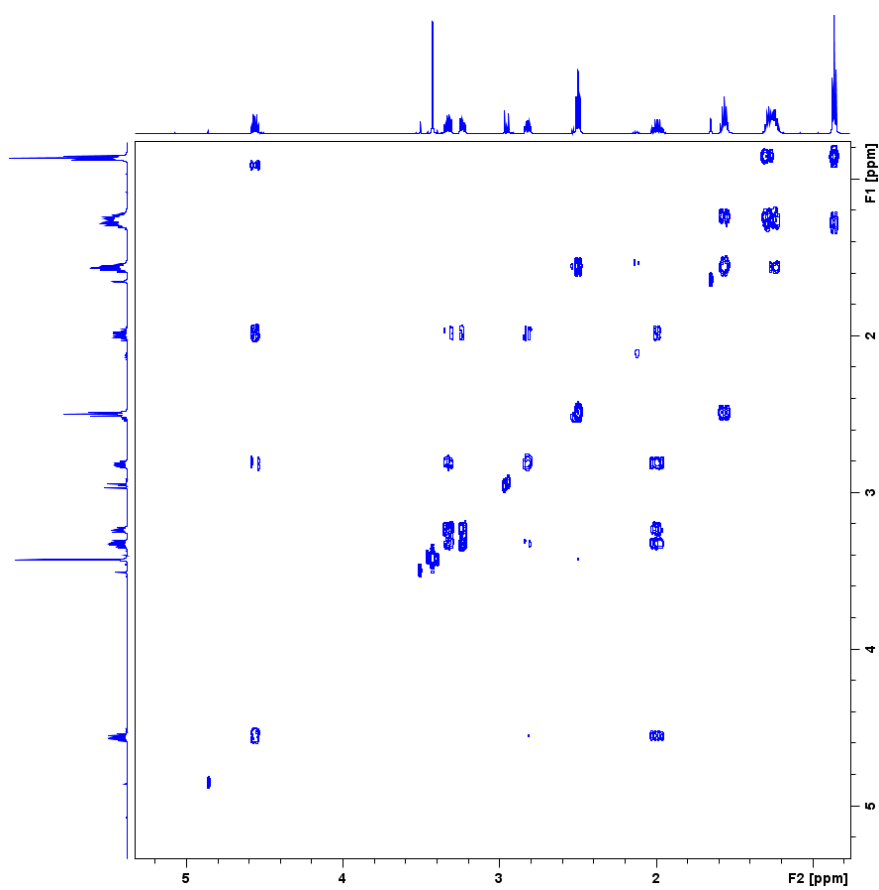


Figure B31. Compound 62 COSY NMR

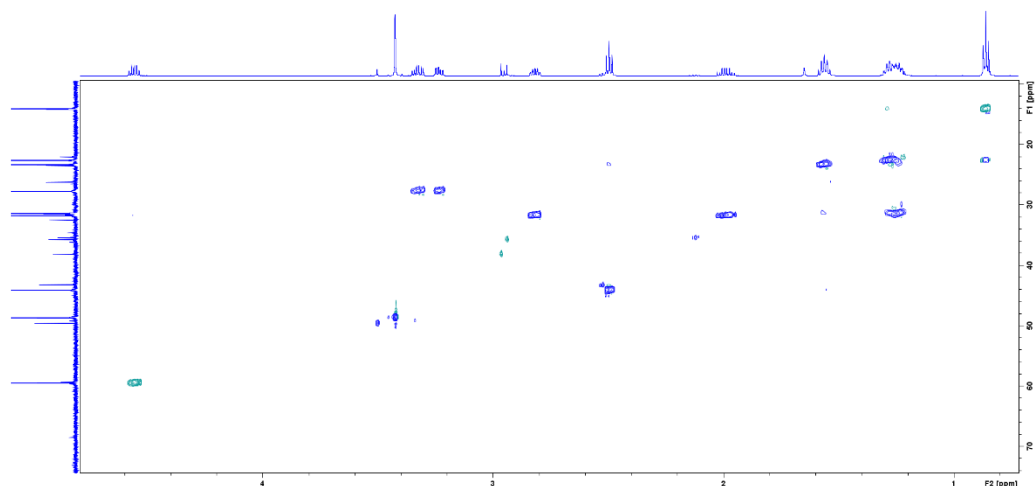


Figure B32. Compound 62 HSQC NMR

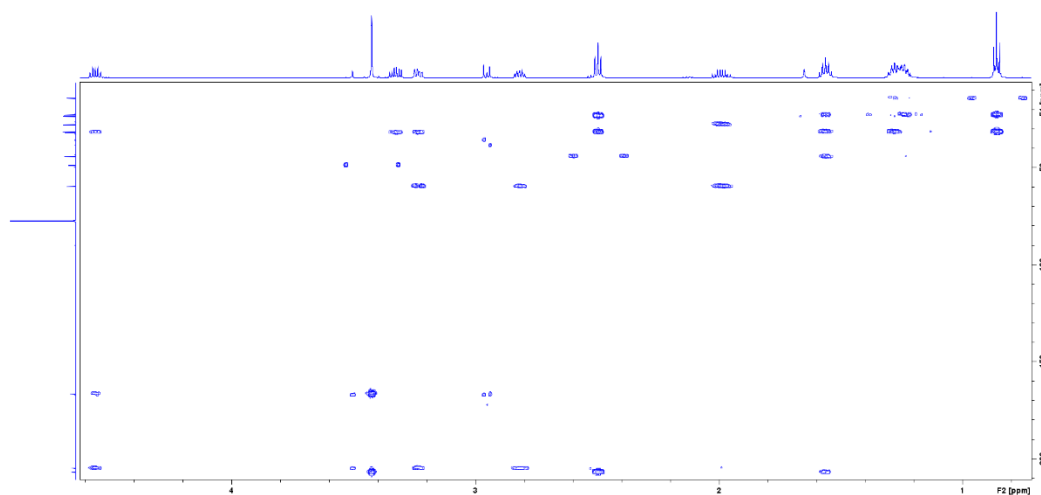


Figure B33. Compound 62 HMBC NMR

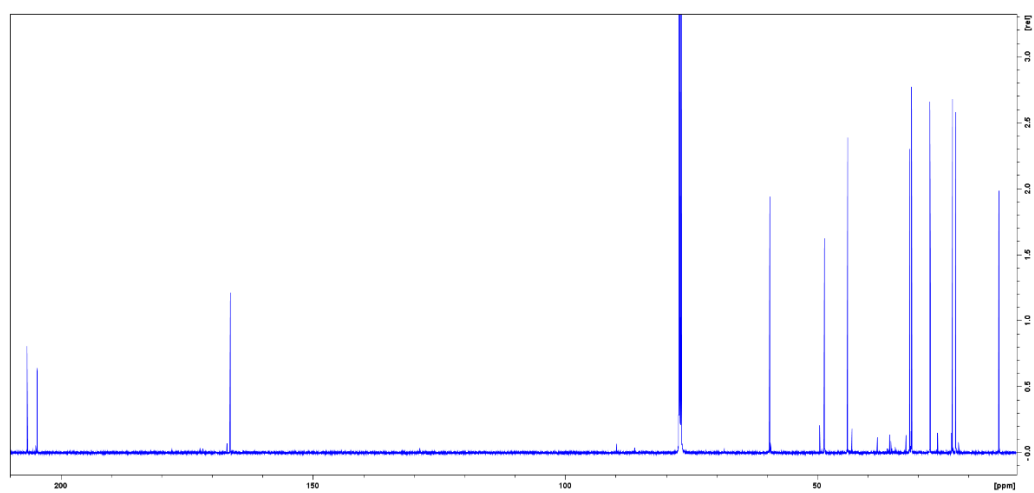


Figure B34. Compound 62 <sup>13</sup>C NMR

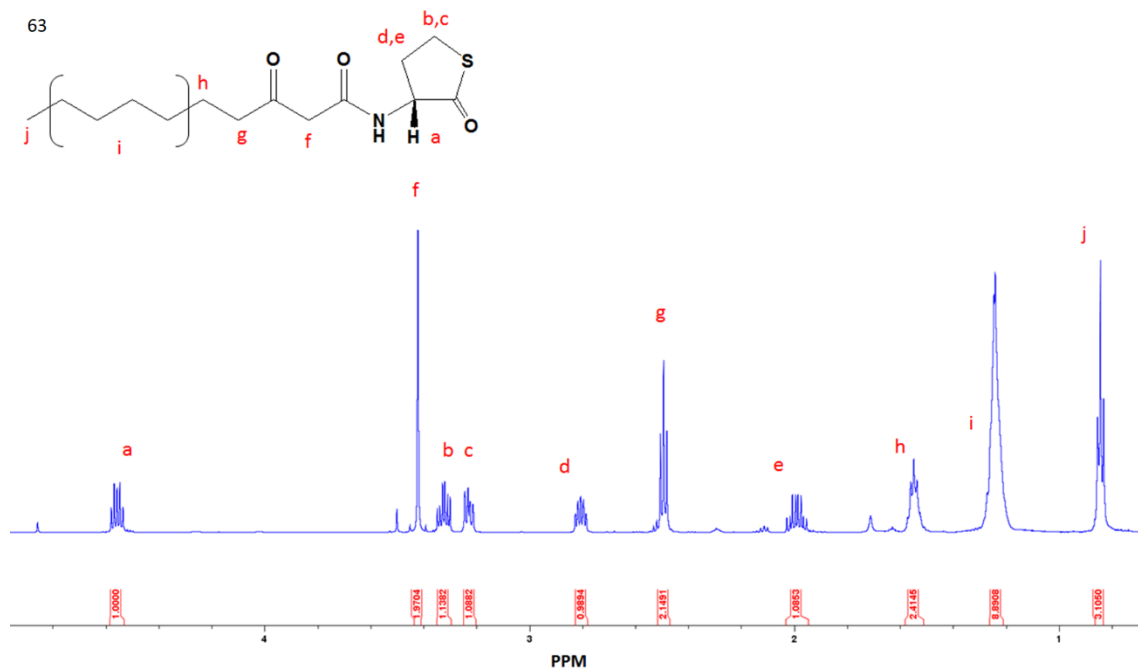


Figure B35. Compound 63 <sup>1</sup>H NMR

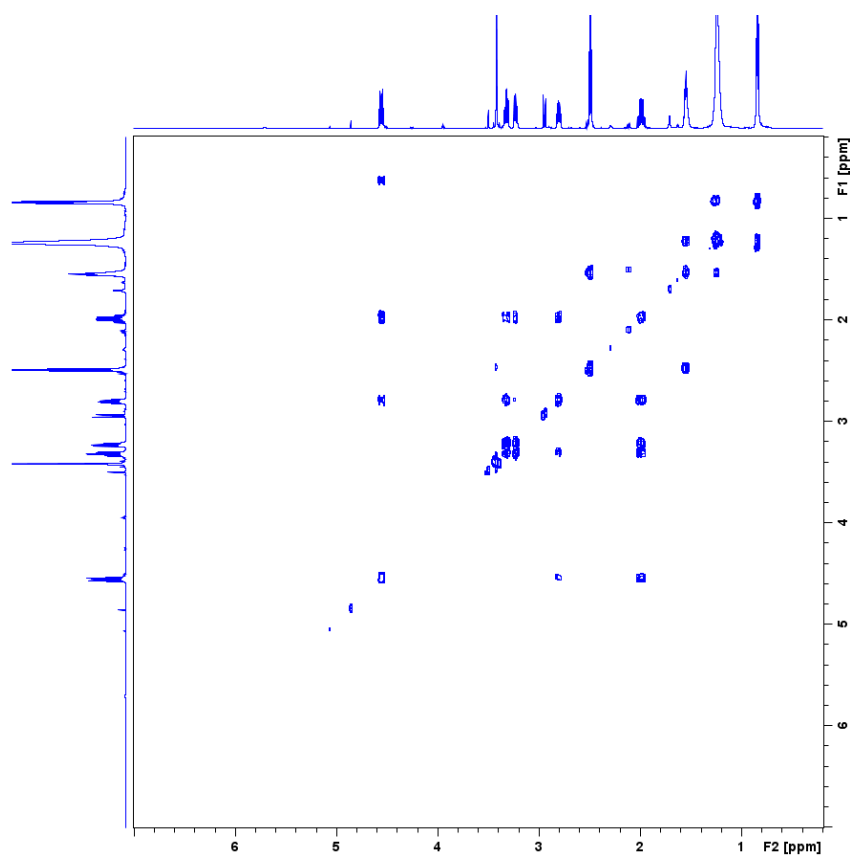


Figure B36. Compound 63 COSY NMR

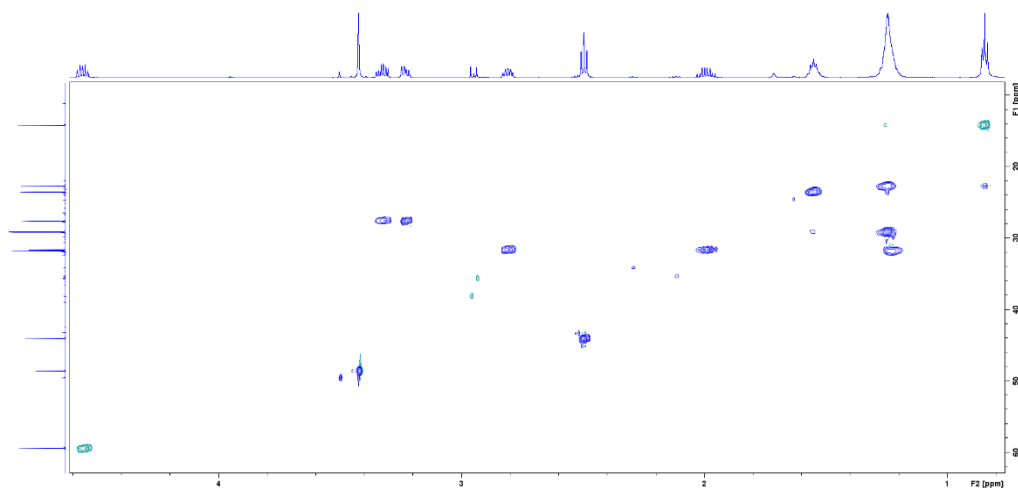


Figure B37. Compound 63 HSQC NMR

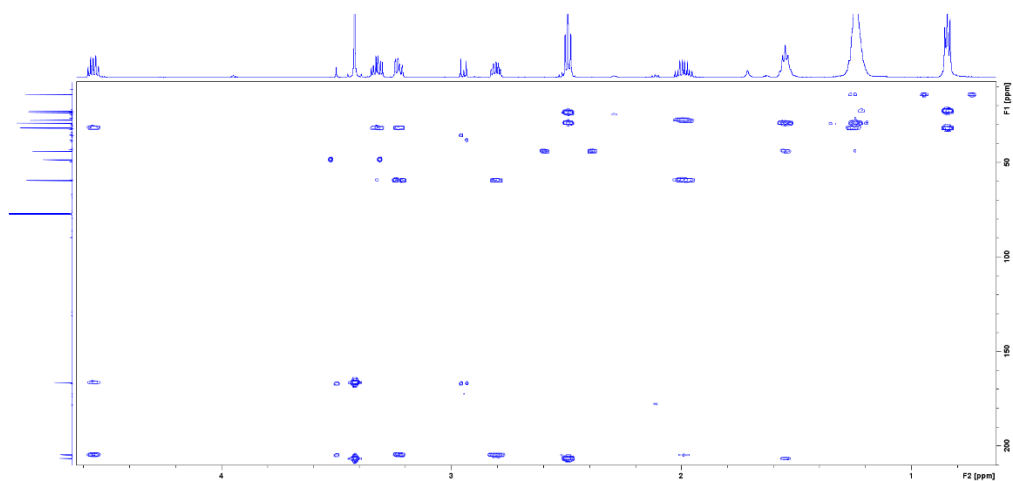


Figure B38. Compound 63 HMBC NMR

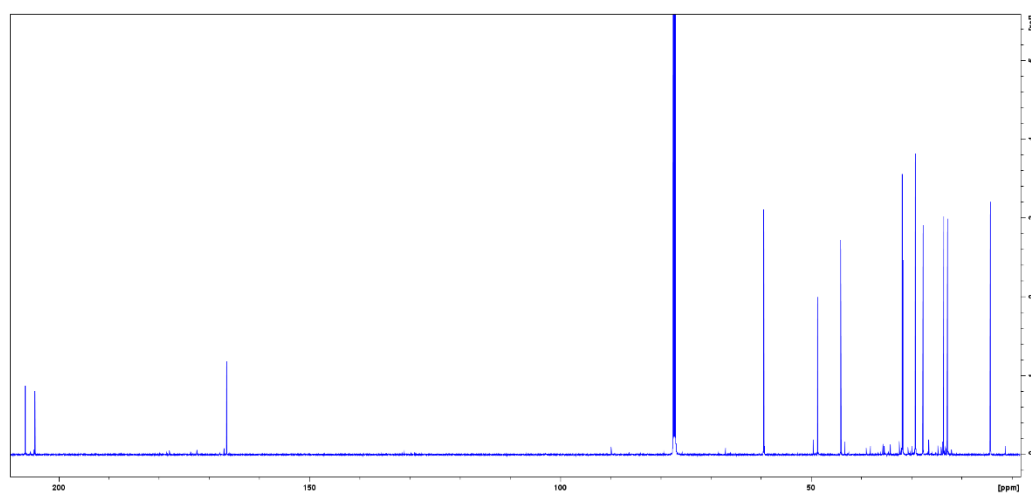


Figure B39. Compound 64  $^{13}\text{C}$  NMR

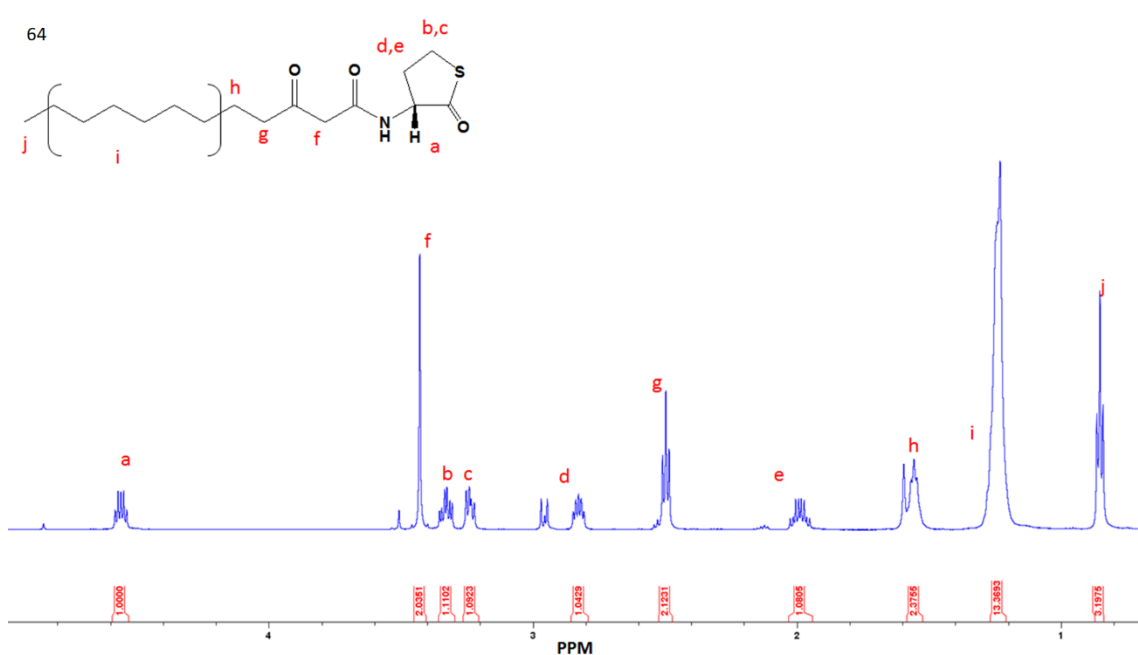


Figure B40. Compound 64 <sup>1</sup>H NMR

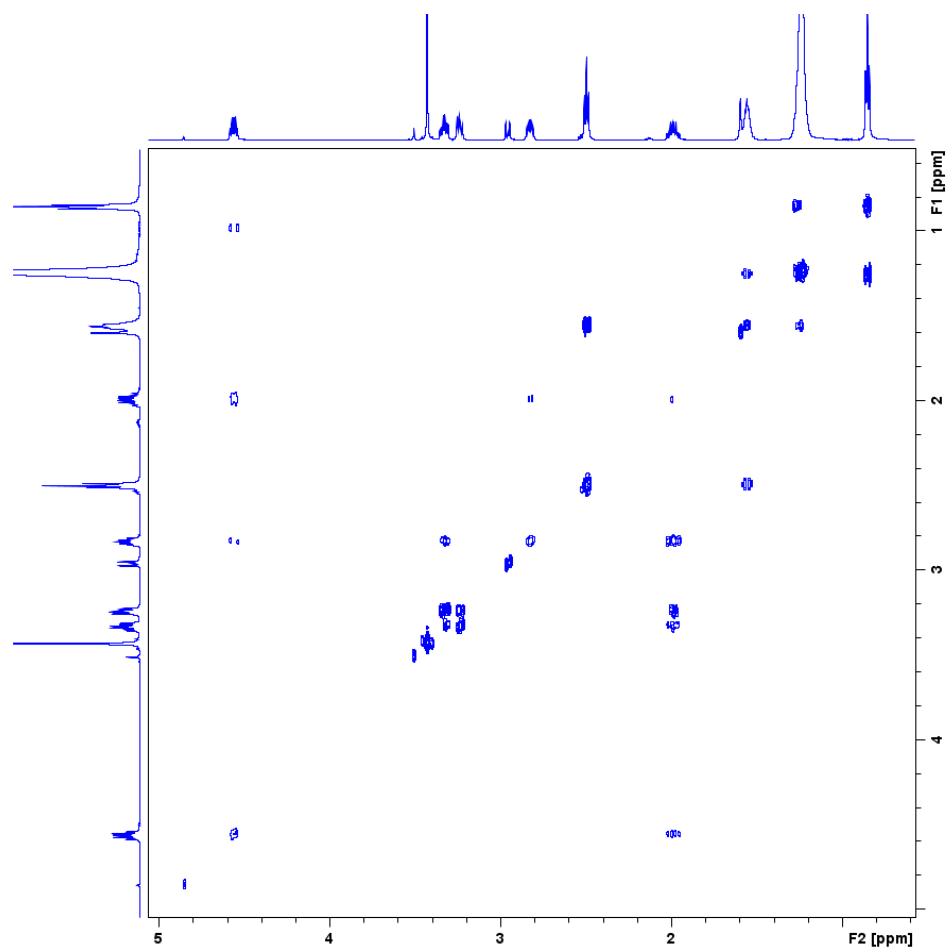


Figure B41. Compound 64 COSY NMR

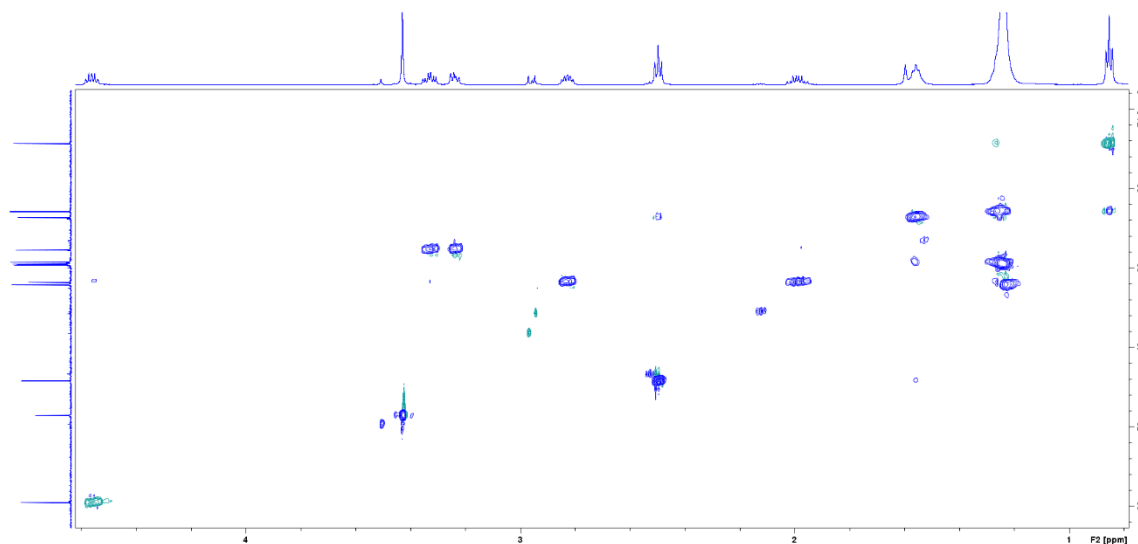


Figure B42. Compound 64 HSQC NMR

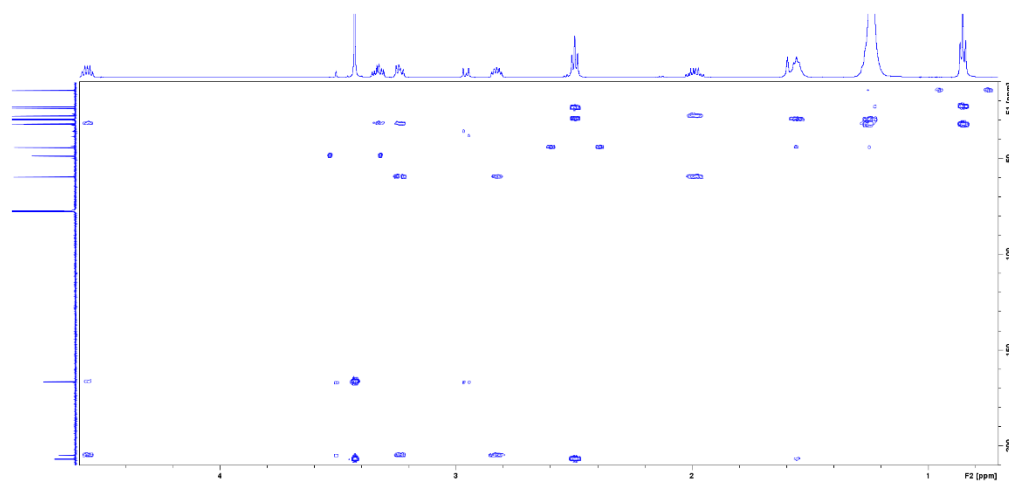


Figure B43. Compound 64 HMBC NMR

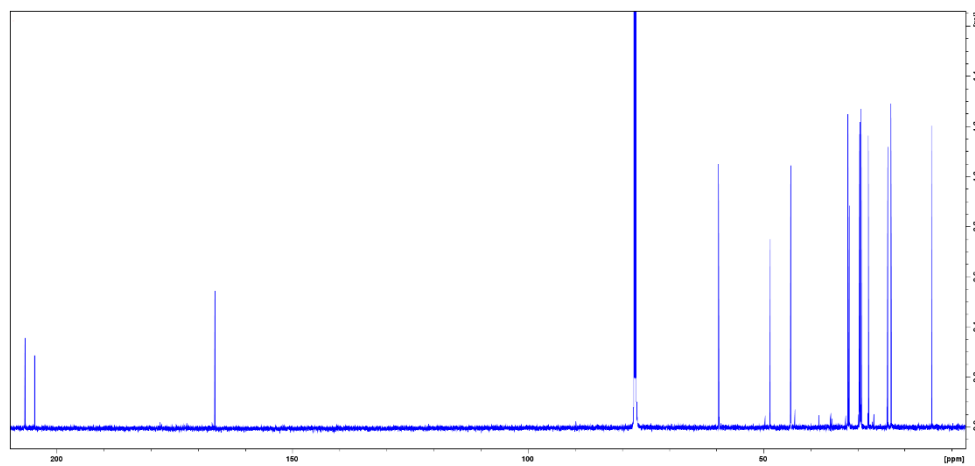
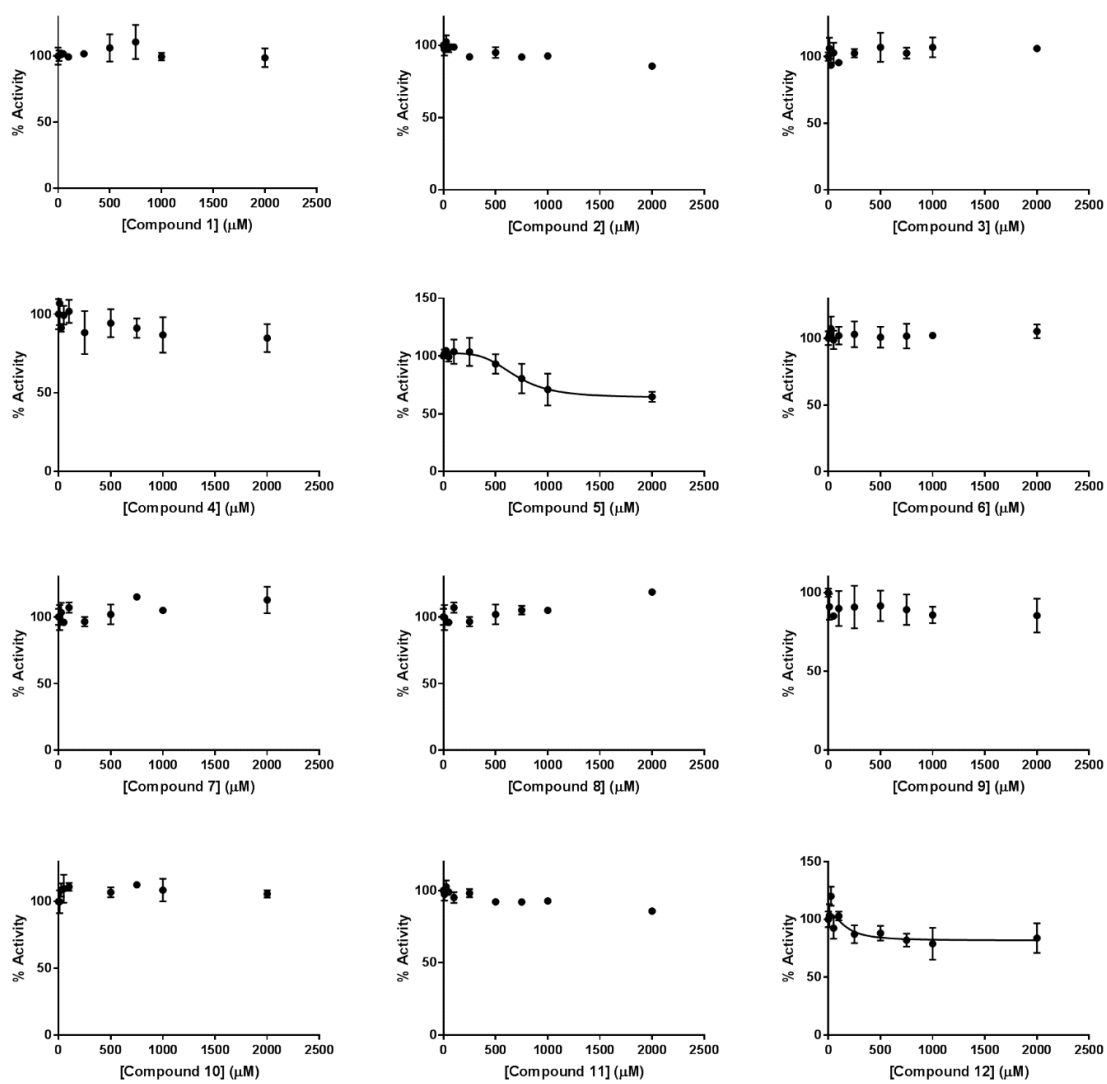


Figure B44. Compound 64 <sup>13</sup>C NMR

APPENDIX C



## UV-Vis Spectra



**Figure C1. IC<sub>50</sub> of First generation of AHL analogs.**  
(Corresponds to Figure 27, Chapter 3)

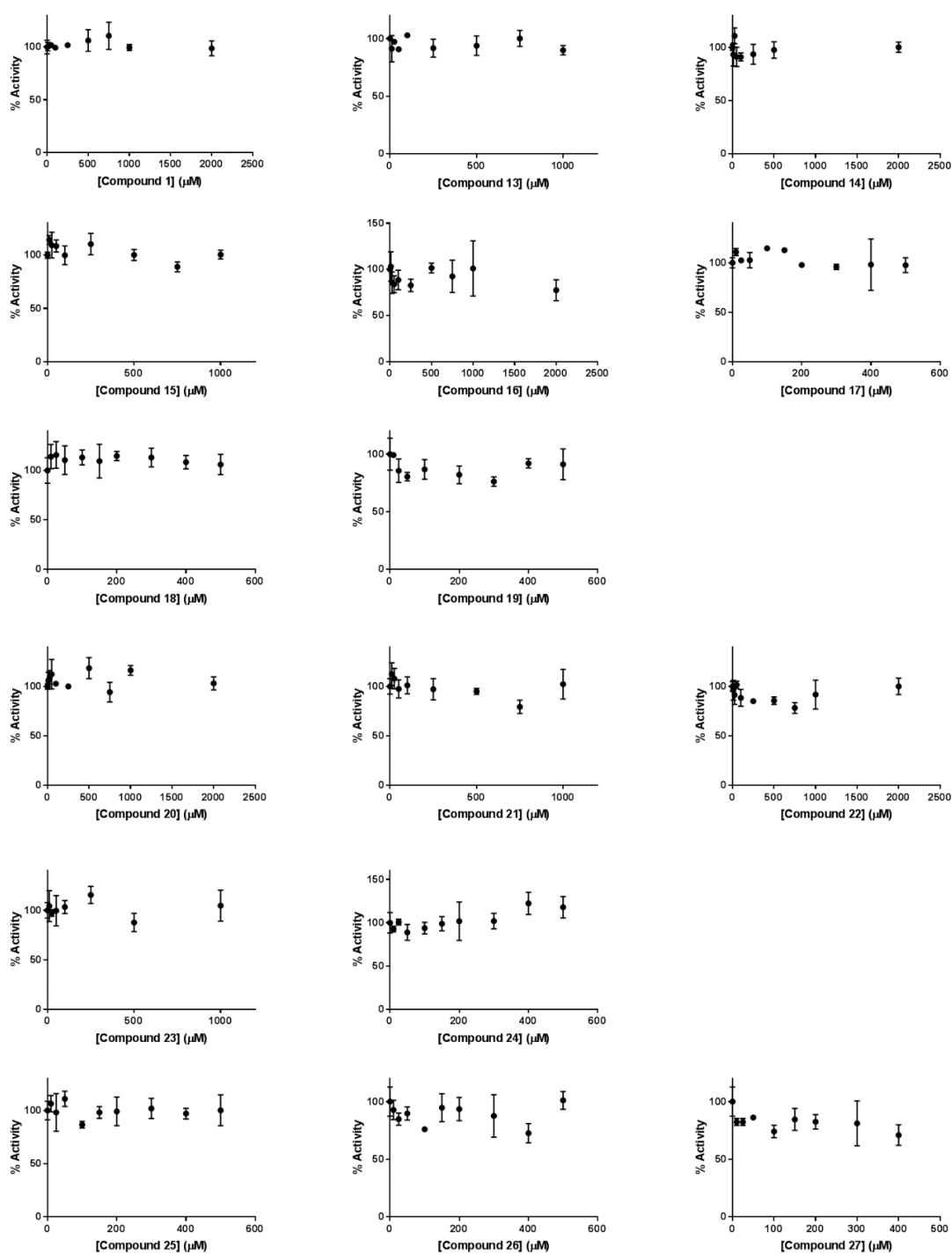


**Figure C2. IC<sub>50</sub> of L-HSL derivatives.**  
(Corresponds to Figure 28, Chapter 3)

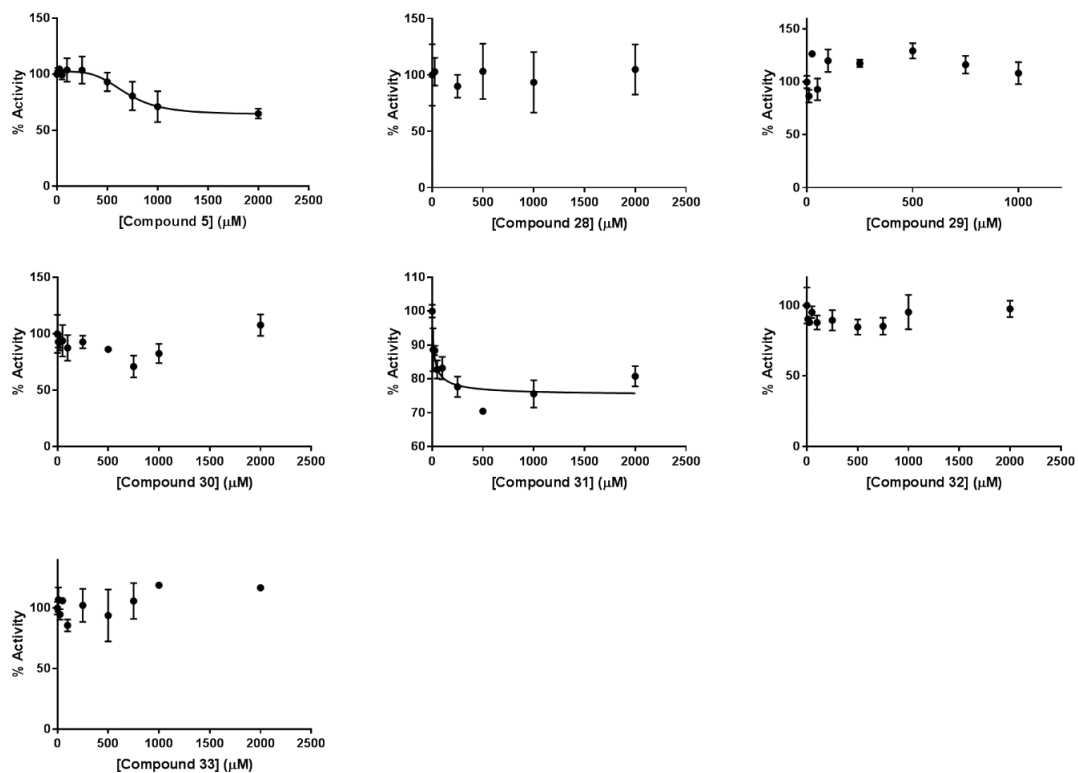


**Figure C3. IC<sub>50</sub> of acyl-D-HSL analogs.**  
(Corresponds to Figure 29, Chapter 3)

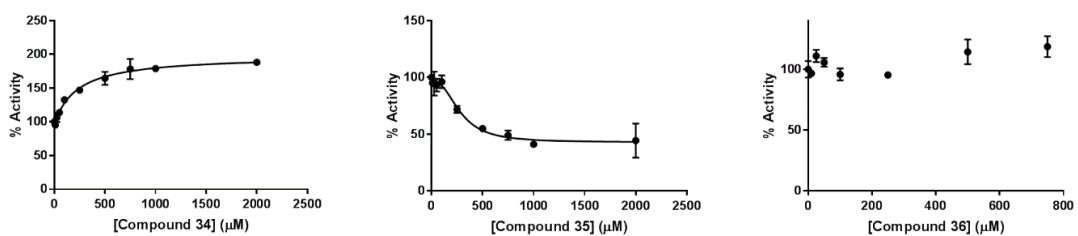


**Figure C4. IC<sub>50</sub> and EC<sub>50</sub> of 3-oxoacyl-D-HSL analogs.**  
(Corresponds to Figure 30, Chapter 3)

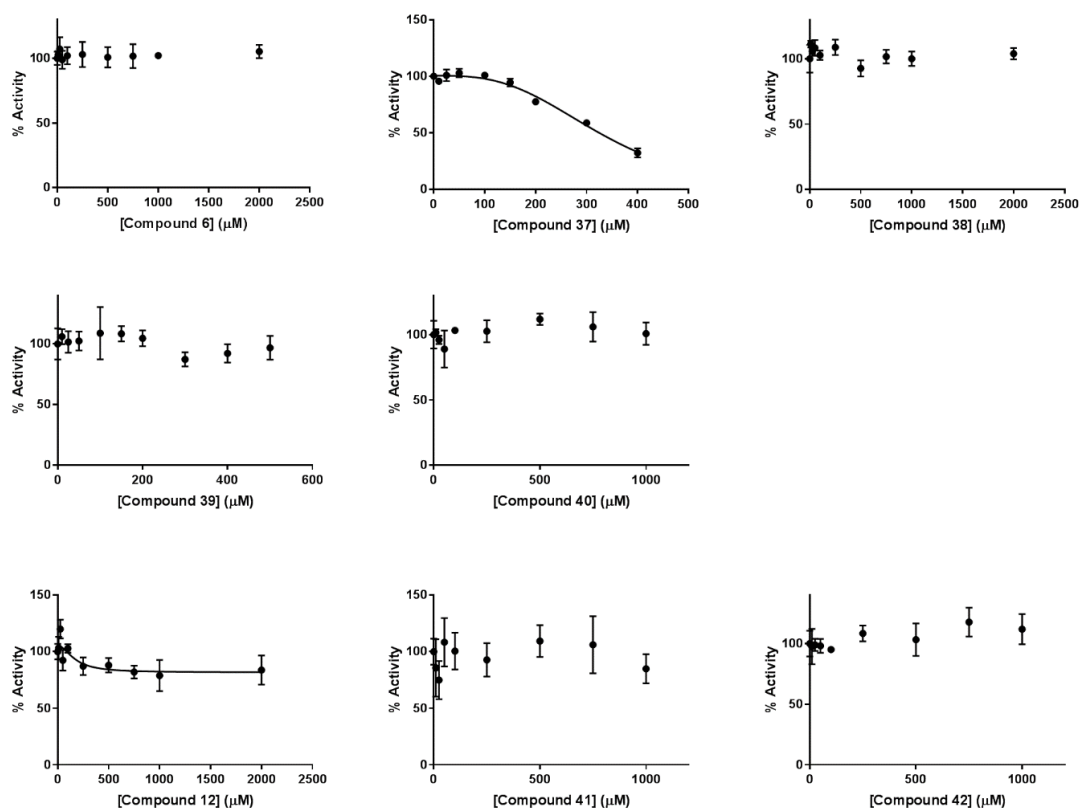


**Figure C5. IC<sub>50</sub> of DL-sulfonamide analog.**  
(Corresponds to Figure 31, Chapter 3)

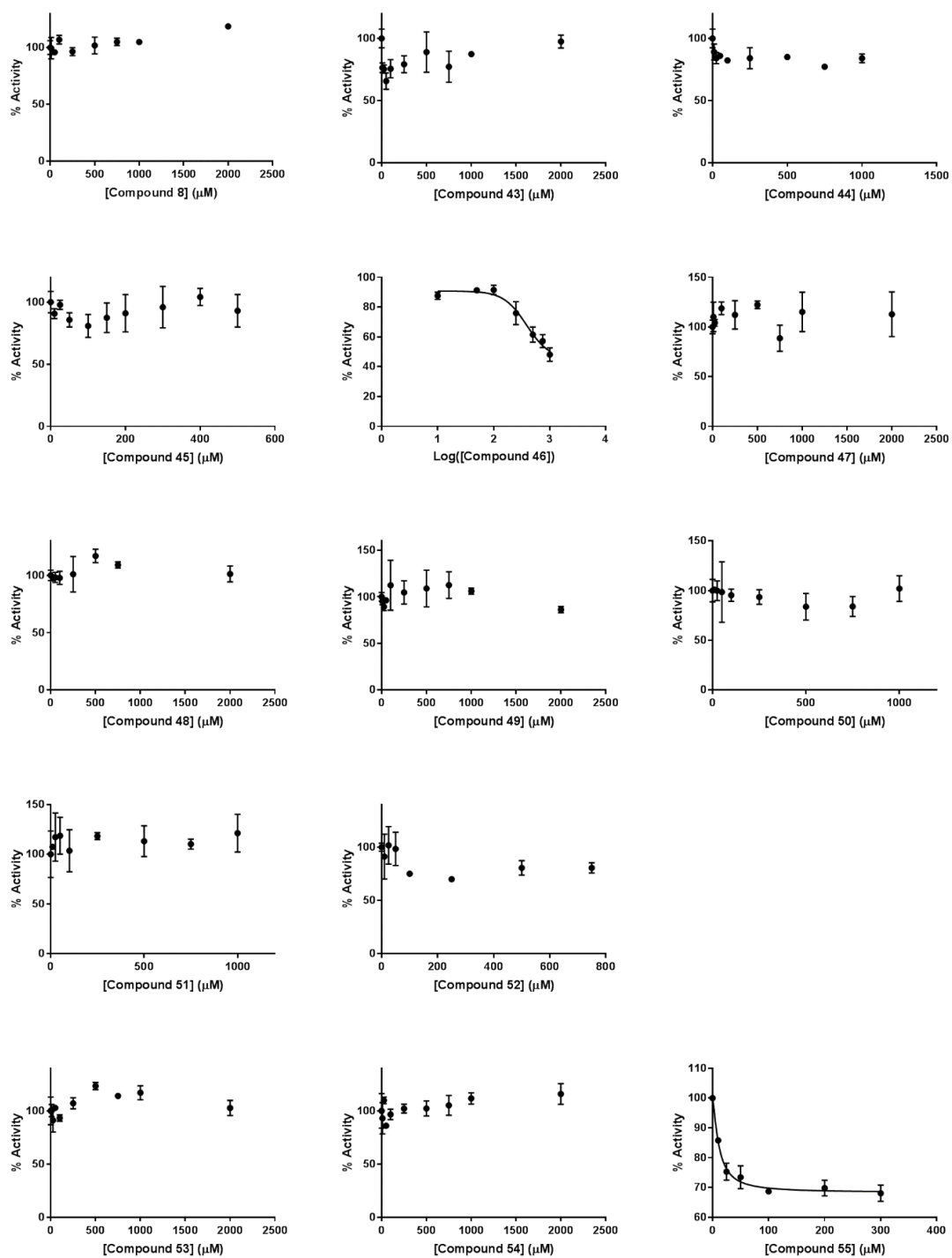


**Figure C6.** IC<sub>50</sub> of acyl- and 3-oxoacyl-L-homocysteine thiolactones.  
(Corresponds to Figure 32, Chapter 3)

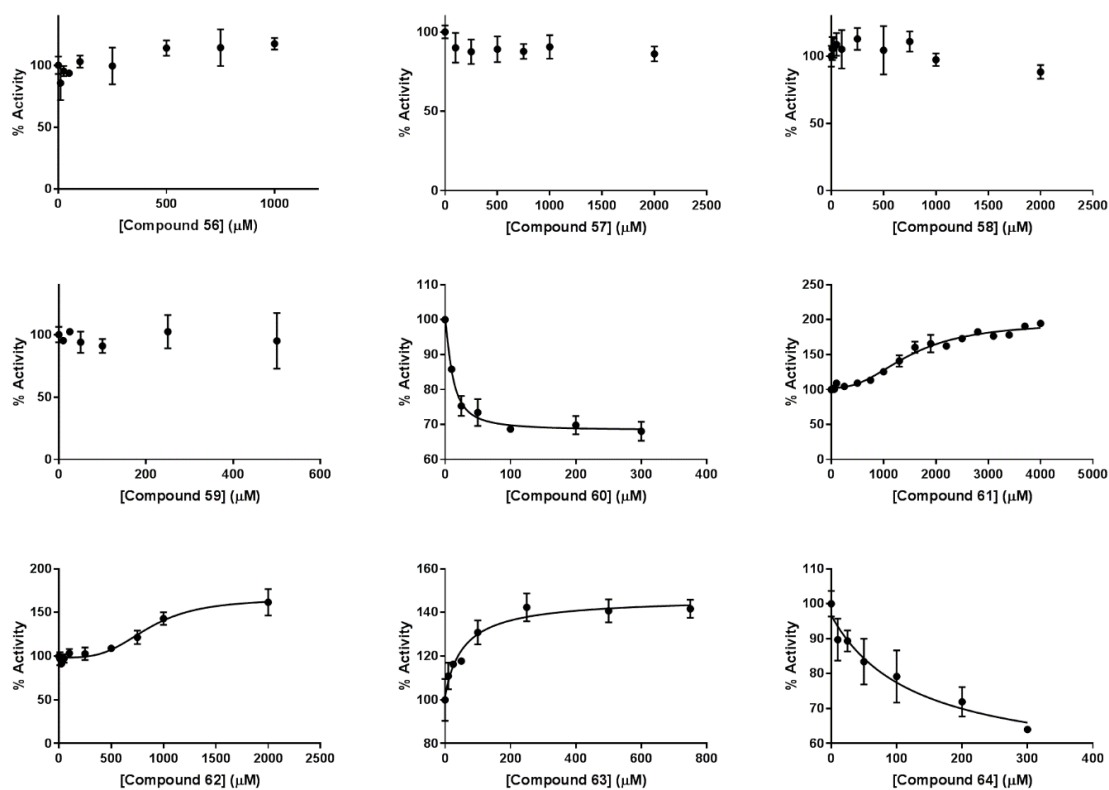


**Figure C7.**  $\text{IC}_{50}$  and  $\text{EC}_{50}$  of acyl- and 3oxoacyl-D-homocysteine thiolactones. (Corresponds to Figure 33, Chapter 3)

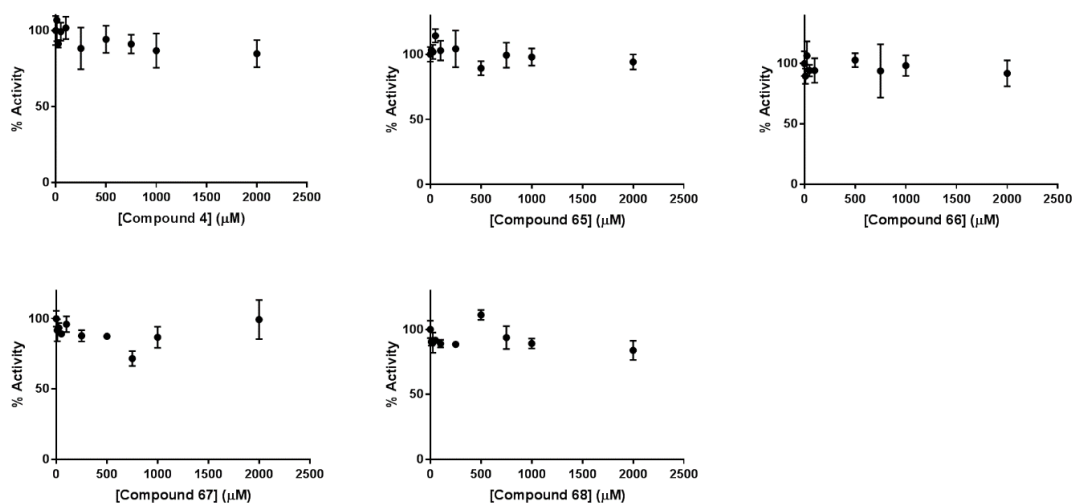


**Figure C8.**  $\text{IC}_{50}$  of cyclopentyl derivatives. (Corresponds to Figure 34, Chapter 3)

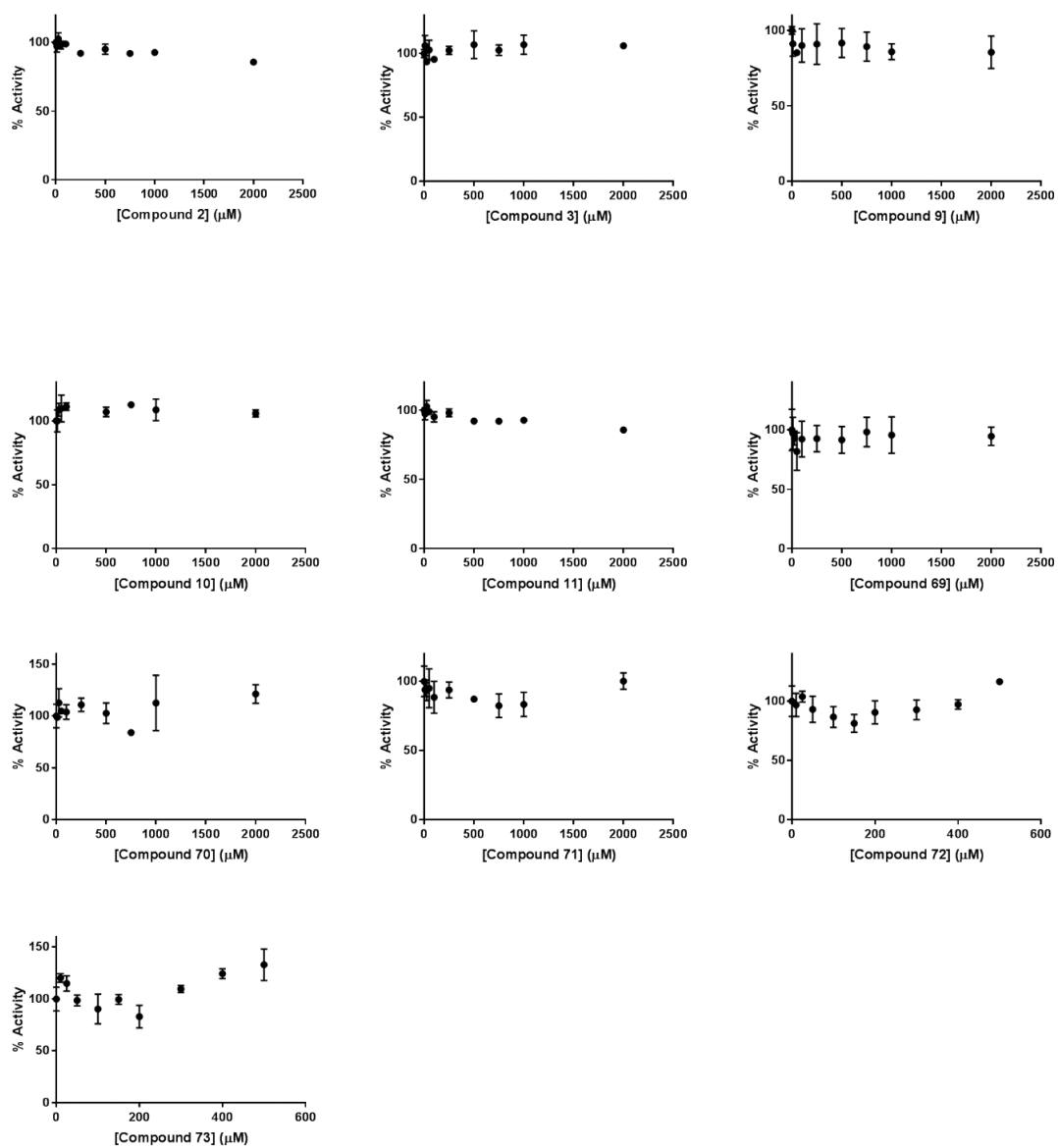


**Figure C9. IC<sub>50</sub> of non-lactone AHL analogs.**  
(Corresponds to Figure 35, Chapter 3)

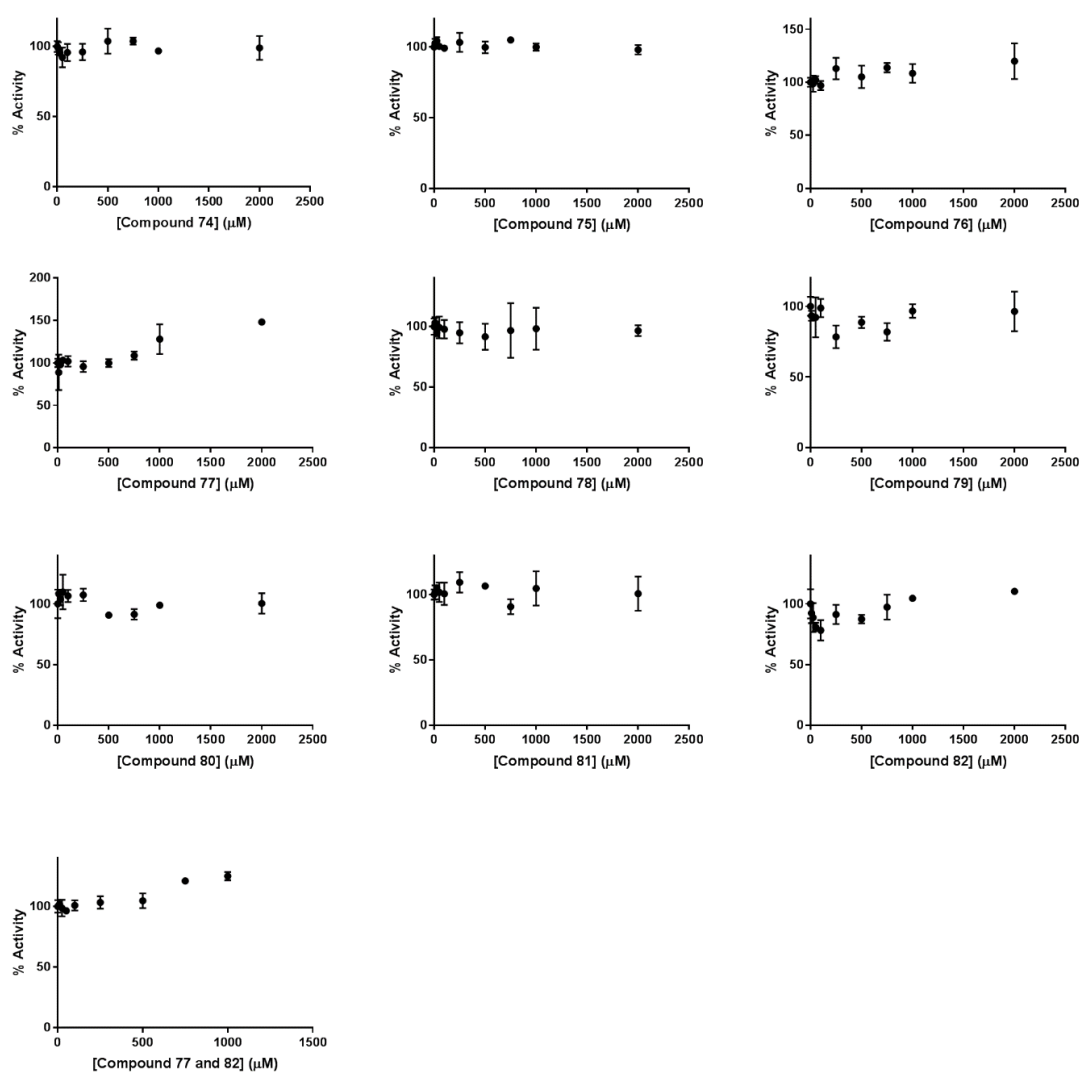


**Figure C10. IC<sub>50</sub> of headgroup and tail moieties.**  
(Corresponds to Figure 36, Chapter 3)



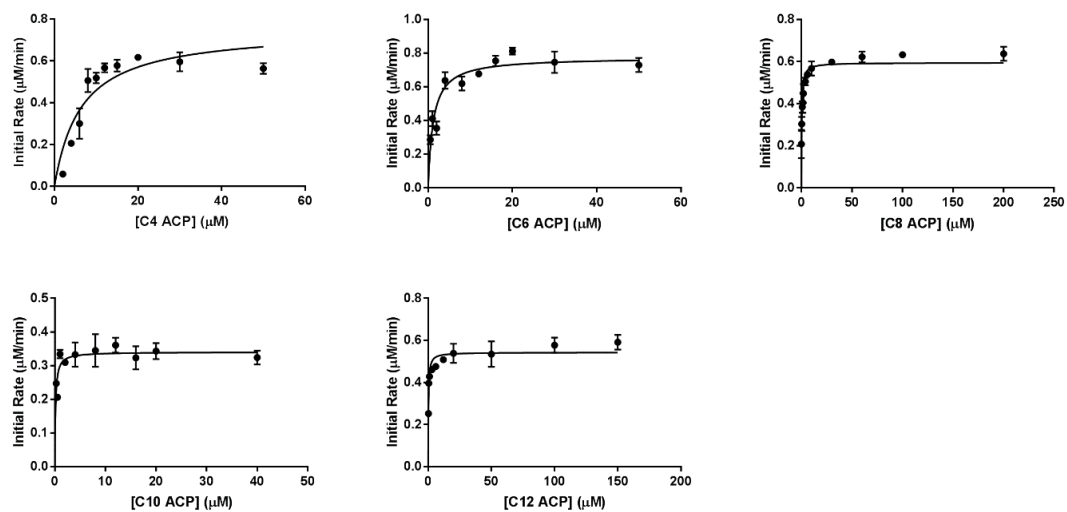


**Figure C11.** Substrate-velocity curve of RhlI with various acyl-ACP substrates.

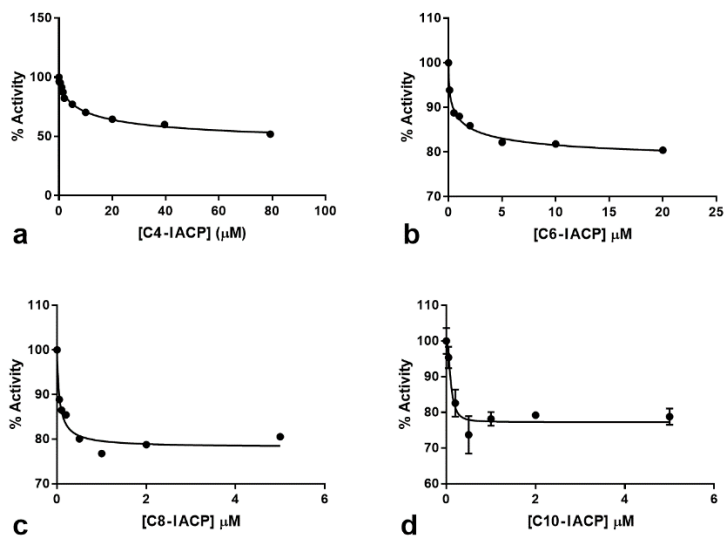


**Figure C12.** IC<sub>50</sub> of various alkyl-ACPs.  
(a) C4-IACP, (b) C6-IACP, (c) C8-IACP, (d) C10-IACP

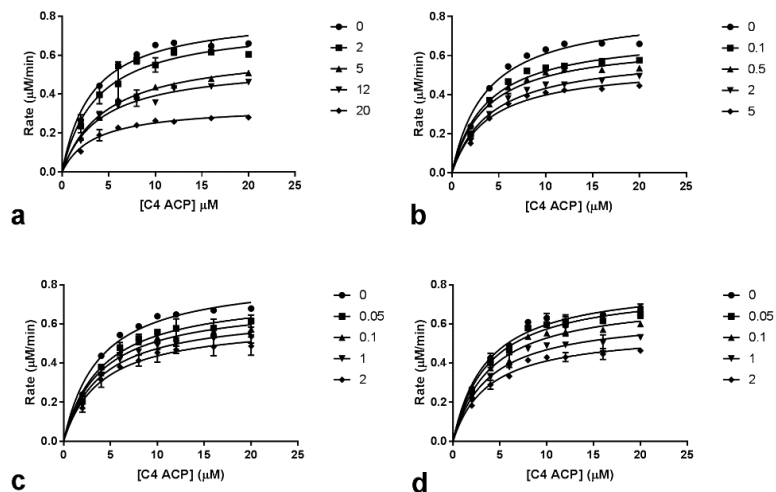


**Figure C13. RhII Inhibition assays with various alkyl-ACPs.**  
 (a) C4-IACP, (b) C6-IACP, (c) C8-IACP, (d) C10-IACP

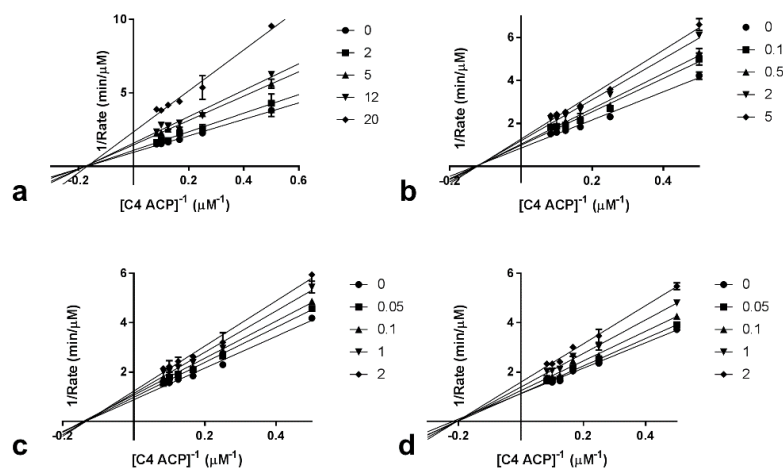


**Figure C14. Double reciprocal plot for RhII inhibition with various alkyl-ACPs.**  
 (a) C4-IACP, (b) C6-IACP, (c) C8-IACP, (d) C10-IACP

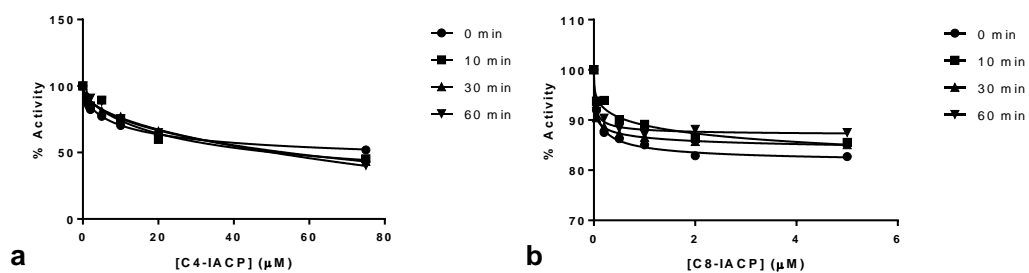


**Figure C15. IC<sub>50</sub> of IACPs at different time points**  
C4-IACP and (b) C8-IACP

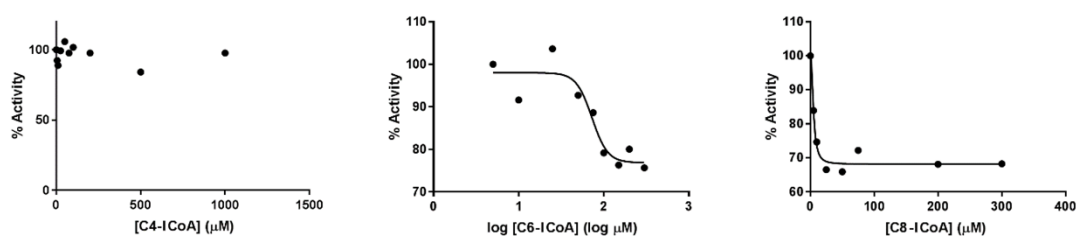


**Figure C16. IC<sub>50</sub> of ICoA derivatives.**

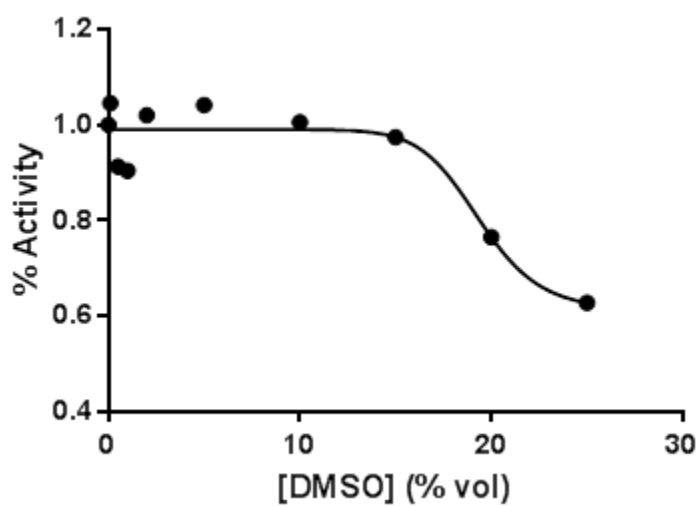


**Figure C17. DMSO Inhibition**  
RhII activity was not inhibited up to 10% DMSO (by volume)